ISSN 1349-0087

SPring-8 Research Frontiers

2005

CONTENTS 2005

Note: The principal publication(s) concerning each article is indicated with all authors' names in italics in the list of references.

Editor's Note

SPring-8 Research Frontiers describes the remarkable scientific achievements being made at SPring-8 as well as developments in the accelerator and beamlines and the status of the facility. This eighth issue "2005" covers advances made during two consecutive research terms, the second half of 2004 and the first half of 2005.

The quality of scientific activities at SPring-8 is being enhanced owing to the introduction of the top-up operation, the upgrading of the experimental apparatuses and others. This is reflected in this issue as an increase in volume. It is also to be noted that the section of Industrial Applications has becomes prosperous since the number of relevant experiments exceeds 20% of the entire use.

The section "Project XFEL" is newly created, because R&D for the XFEL (X-ray Free Electron Laser) project started in 2006 at RIKEN and the XFEL is planned to be completed in 2010 at the SPring-8 campus.

Finally note that the principal publication(s) concerning each article is indicated with all authors' names in italics in the list of references.

We invited nine specialists from the Proposal Review Committee to serve as the Editing Coordinators for their respective research fields:

Life Science: Structural Biology - Prof. Keiichi Fukuyama (Osaka University)
Life Science: Medical Biology - Prof. Fumihiko Kajiya (Kawasaki Medical School / Okayama University)
Materials Science: Structure - Prof. Satoshi Sasaki (Tokyo Institute of Technology)
Materials Science: Electronics & Magnetic Properties - Prof. Takashi Takahashi (Tohoku University)
Chemical Science - Prof. Kiyotaka Asakura (Hokkaido University)
Earth & Planetary Science - Prof. Takehiko Yagi (The University of Tokyo)
Environmental Science - Dr. Masayuki Kunugi (National Institute for Environmental Studies)
Industrial Applications - Prof. Junji Matsui (Center for Advanced Science and Technology)
Instrumentation & Methodology - Prof. Yasushi Kagoshima (University of Hyogo)

We would like to express our most sincere appreciation to the Editing Coordinators for their efforts in preparing the introductory overview and providing comments on each research field. We would also like to express our gratitude to the users and staff members of SPring-8 for contributing their reports to SPring-8 Research Frontiers.

SPring-8 Research Frontiers will be sent on request. Its full text is also available on the SPring-8 website: http://www.spring8.or.jp/

Preface

In 2005, the ratio of industrial use exceeded 20% for the first time. This ratio is outstanding among the major synchrotron radiation facilities in the world. The contribution to the industry was a central promise to the Government and industries in the planning and construction stages of SPring-8. By the way, a remarkable feature of the industrial use at SPring-8 is that it is not dominated by the pharmaceutical industry as is in other facilities but it covers broad categories of industries: electronics, materials, automobile, etc.

The top-up operation of the machine started in 2005 as mentioned in Beam Performance section of this issue. We believe that it brought big merits to the users, especially to the advanced users. Everybody seems to be satisfied: neither complaints nor claims have been submitted.

SPring-8 has resumed the planning of new beamlines for which the Ring has 13 vacancies. SPring-8 is still the unique machine for the frontier research although it is 9 years old. It is still an important task of SPring-8 to explore the leading edge of synchrotron radiation sciences. Considering that the number of mid-sized facilities suitable to the common analysis is increasing, SPring-8 should be conscious of the utilization that fits the unique high-end properties of SPring-8.

A next-generation machine at a site of SPring-8 will be a SASE XFEL* which RIKEN is developing in cooperation with JASRI. The report of this FEL project is included in the Research Frontiers from this issue. In future, we will have both the Ring and the FEL, which will be managed in common.

*Self-Amplified-Spontaneous-Emission Free-Electron Laser

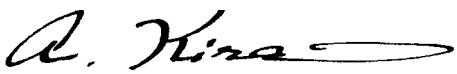

Akira Kira
Director General
SPring-8 / JASRI

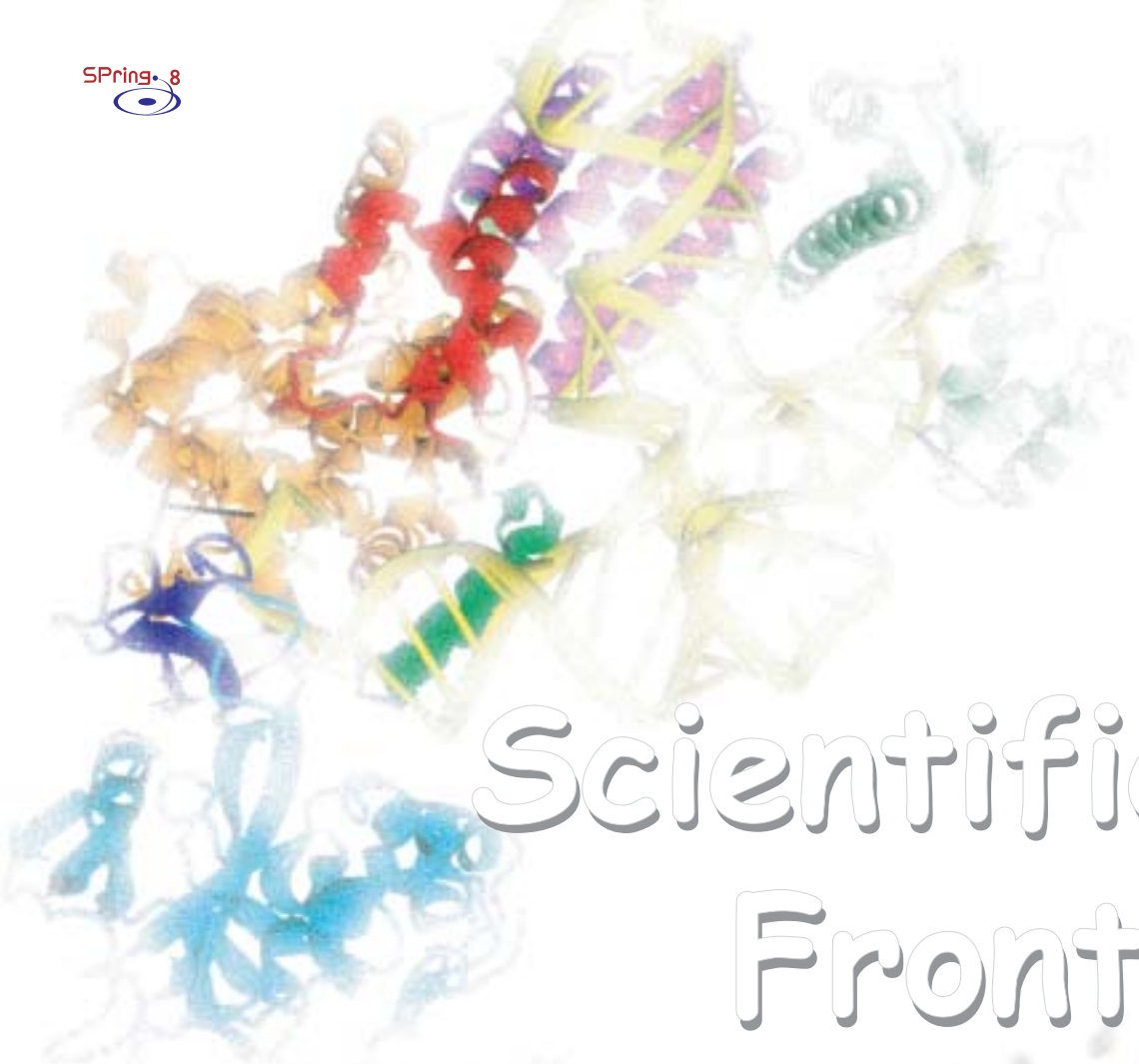

Scientific Frontiers

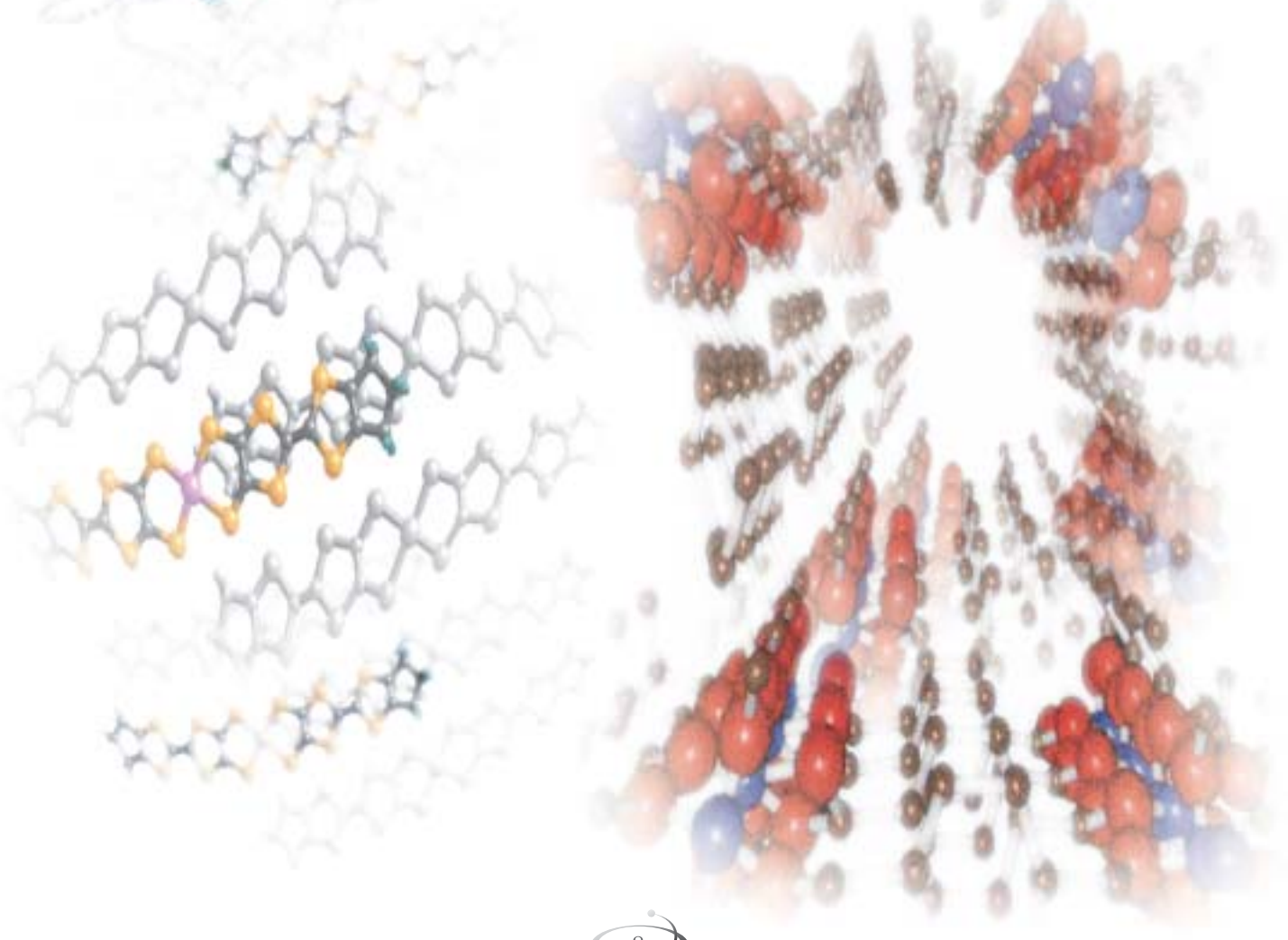

Life Science
Structural Biology

Many exciting structures of biological macromolecules were determined using beamlines for Life Science at SPring-8 in 2005. The determination of precise three-dimensional structures had great impact on studies in structural biology by revealing the molecular mechanisms of the biological functions. Protein crystallography and small-angle X-ray scattering (SAXS) become increasingly powerful methods using synchrotron radiation. The Protein 3000 project, which aims at determining a number of protein structures with biological significance, has been promoted with the use of the beamlines at SPring-8. For efficient operation, the functions of beamlines BL38B1 and BL40B2 were rearranged; BL38B1 was renamed Structural Biology III fully dedicated to protein crystallography and BL40B2 Structural Biology II focussing on SAXS.

All the beamlines for Life Science operated satisfactorily last year, and a number of new structures of biologically important molecules were reported. Here selected are representative papers published by SPring-8 users. The first three papers focus on the assembly of proteins or complexes. The structure of the bacterial flagellar hook and its joint mechanism are presented on the basis of the accurate crystal structure of its fragment protein and electron cryomicroscopic analysis. The structure of giant hemoglobin from beard worm (400 kDa) reveals a hierarchic assembly of four globin chains whereas that of P-protein of the glycine cleavage system (200kDa) shows how the active site is constituted in the a_2b_2 tetramer. The subsequent three papers describe the structures of DNA and proteins that interact with DNA/RNA. Using the Z-DNA binding protein, the structural analysis of a designed 15 base pair dsDNA successfully showed the junction structure between Z-DNA and B-DNA. In the FEN1-PCNA complex, an interesting motion of the protein is observed, which may be necessary for DNA processing whereas the structure of leucyl-tRNA synthetase-$tRNA^{Leu}$ complex provides the basis for proofreading between amino acid and tRNA. The precise structures of phytobilin synthesis enzyme and glucooligosaccharide oxidase enabled the clarification of the mechanisms of catalytic reactions. In acyl-coa thioesterase PaaI, an interesting structural change is discussed in relation to the reactivity of oligomeric enzyme. Taking advantage of *in situ* observations of SAXS, the last paper deals with the influence of humidity on the thickness of the cell membrane complex, and whisker diameter analyzed using the microbeam of BL40XU.

Keiichi Fukuyama
Department of Biological Sciences
Osaka University

Universal Joint Mechanism of the Bacterial Flagellar Hook

Bacteria swim by rotating helical flagellar filaments, which are about 15 μm long and 120-250 Å in diameter. A membrane-embedded rotary motor at the base of each filament drives the helical propeller at hundreds of revolutions per second. To be able to rotate the filament off axis of the motor, the filament is connected to the motor by a short filament called the hook, which works as a universal joint. It has a relatively well-defined length of 55 nm and is made by polymerization of about 130 molecules of a 41 kDa protein, FlgE. To understand the universal joint mechanism we solved its high-resolution structure. Because FlgE polymerizes we over-expressed, purified and crystallized a 31.2 kDa fragment, FlgE31, made of segment G71-S363 [1] and solved the crystal structure at 1.8 Å resolution [2]. FlgE31 contains two domains, D1 and D2 (Fig. 1). D1 is made of an N-terminal segment, Gly71 - Ala144, and a C-terminal segment, Pro285 - Ser363. The fold can be described as randomly oriented β-strands. D2 is made of a central segment, Ala145 - Lys284, and can be described as an irregular β-barrel.

An atomic model of the straight hook was then built by docking the crystal structure of FlgE31 into the density map of the straight hook obtained by electron cryomicroscopy. Because domain D0 of FlgE missing in the crystal structure is known to form the inner core portion of the hook, domains D1 and D2 were docked to the middle and external parts of the hook, respectively (Fig. 2). Each domain was separately docked, manually connected and then refined by a real-space refinement program [3]. The model shows strong interactions between D2 domains along the 6-start helix on the surface, but the axial interactions along the 11-start helix are between domain D2 of the lower subunit and a triangular loop (Thr 116 - Pro 135) of domain D1 of the upper subunit [2]. This mesh structure of the tube wall explains why the hook is rigid against twisting.

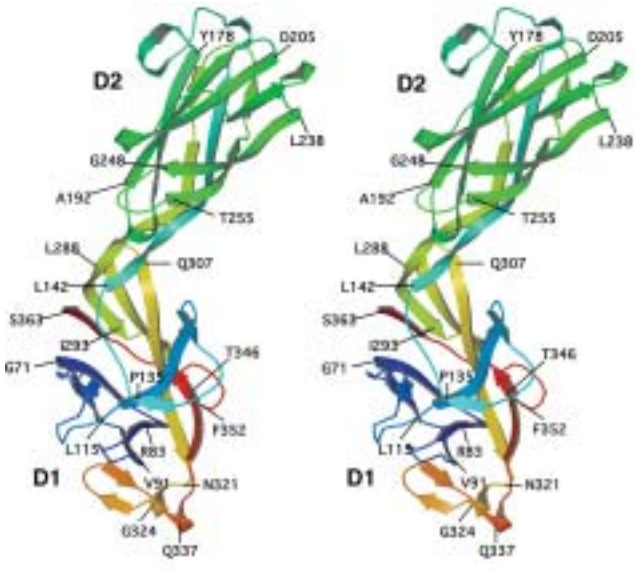

Fig. 1. Stereo view of the Cα backbone trace of FlgE31. The chain is color-coded from blue to red, going through the rainbow color from the N- to C-terminus.

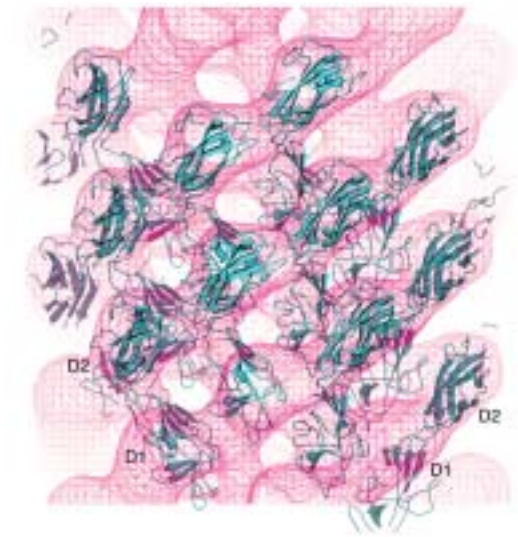

Fig. 2. Docking of the FlgE31 atomic model into two outer domains of hook. Side view.

The hook at work is highly curved and it is part of a supercoil. This implies that the repeat distance of protofilaments on the inner side of the curve must be shorter than those on the outer side. We built an atomic model of a supercoiled hook by continuously deforming the helical lattice of the straight hook so that the hook axis follows a right-handed helix with a pitch of 950 Å and a diameter of 350 Å as observed by electron microscopy (Fig. 3(a)). Subunits located on the inner side are axially more packed than those located on the outer surface (Figs. 3(c), 3(d)). The

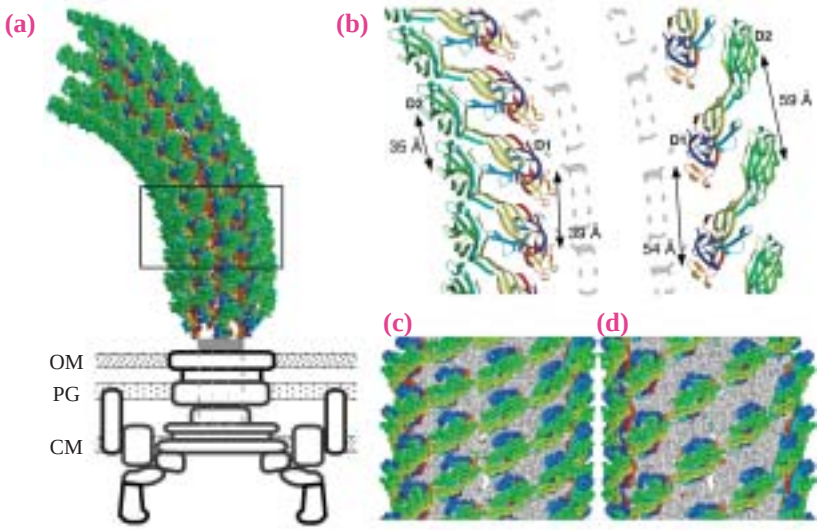

Fig. 3. Atomic model of a supercoiled hook. **(a)** Atomic model of a coiled hook with schematic diagram of the basal body. **(b)** Magnified image of the coiled hook with the innermost and outermost protofilaments on the left and right, respectively. The inner core domains forming the central channel are represented by dotted grey lines. **(c)**, **(d)** Intermolecular packing arrangements of D2 on the inner side **(c)** and outer side **(d)** of the coiled hook. Only D2 is color-coded as in Fig. 1, while D1 is colored light grey.

difference in repeat distance is almost 1.7 times (Fig. 3(b)). During the rotation of the hook around its axis, the protofilaments will successively be compressed and extended a few hundreds times per second. To understand how this dynamic change is achieved we performed a molecular dynamic simulation of the extension and compression of a protofilament model made of three subunits with surrounding water molecules (Fig. 4). The bonding interactions between residues of the triangular loop of D1 and the inner face of D2 show multiple steps of exchange in bonding partners, resulting in a large slippage at this D1-D2 interface. The bending flexibility of the hook, which is essential for its universal joint function, is probably due to this stepwise axial sliding along with the flexibility in relative domain orientation (see Ref. [2]).

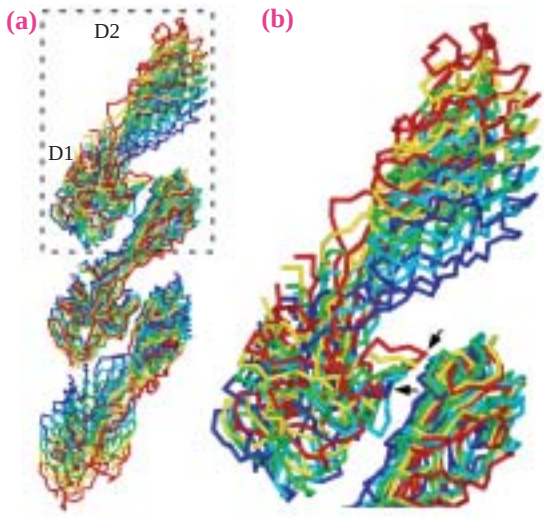

Fig. 4. Simulated extension and compression of a hook protofilament. Protofilament models at five different stages of simulated extension at 5 Å intervals are superimposed with different colors: dark blue, light blue, green, yellow, and red, from the most compressed to the most extended state. **(a)** Whole three subunits. **(b)** Magnified view of upper half. D2 at the top and D1 at the bottom have equal intervals (2.5 Å) along the vertical axis. The triangular loop of D1 and the surface of D2 have distinct side chain bonding partners depending on the state of extension or compression.

Fadel A. Samatey[a], Hideyuki Matsunami[a] and Keiichi Namba[a,b,*]

[a] Dynamic NanoMachine Project, ICORP, JST
[b] Graduate School of Frontier Bioscience, Osaka University

*E-mail: keiichi@fbs.osaka-u.ac.jp

References

[1] F.A. Samatey *et al.*: Acta Crystallogr. D **60** (2004) 2078.
[2] F.A. Samatey *et al.*: Nature **431** (2004) 1062.
[3] *T.R. Shaikh, D.R. Thomas, J.Z. Chen, F.A. Samatey, H. Matsunami, K. Imada, K. Namba and D.J. DeRosier: Proc. Natl. Acad. Sci. USA **102** (2005) 1023.*

Crystal Structure of Giant Hemoglobin from Beard Worm *Oligobra hia mashi oi*

Pogonophorans and vestimentiferans are marine animals that have no mouth or gut. Their nutrition is provided by endosymbiotic sulfur-oxidizing bacteria living inside their body. These animals live in sulfide-rich environments such as hydrothermal vents. Morphological, embryological and genetic studies suggest that pogonophorans, vestimentiferans, and annelids are closely related. All three groups have giant (400 kDa and/or 3500 kDa) extracellular hemoglobins (Hbs) that are remarkably different in their quaternary structure from well-known mammalian tetrameric assembly.

Pogonophorans have only a ~400 kDa Hb composed of ~24 globins in their blood [1]. Vestimentiferans have three types of Hb; hexagonal bilayer vascular V1 (~3500 kDa), vascular V2 (~400 kDa), and coelomic C1 (~400 kDa). Their molecular mass suggests pogonophoran Hbs are homologous to vestimentiferan V2 Hbs. It has been reported that both pogonophorans and vestimentiferans giant Hbs transport oxygen and sulfide simultaneously. Giant Hbs provide the host with oxygen and endosymbionts with sulfide. Sequence analyses of pogonophoran and vestimentiferan Hbs have shown that their putative sulfide-binding Cys residues are well conserved. On the other hand, annelids have a 3500 kDa extracellular Hb which is thought to be a homologue of vestimentiferan V1. However, annelid giant Hb has no physiological function of sulfide-binding in the case that annelids live in sulfide-free environments.

Pogonophorans and vestimentiferans are quite unique animals in their method of acquiring nutrition, and their Hbs have characteristic assembly and function of transporting sulfide. Little is known about these sulfide binding extracellular Hbs and no vascular giant Hb structure is available, whereas only a moderate resolution (5 Å) whole structure of 3500 kDa hexagonal bilayer Hb from an annelid, its partial reconstructed structure composed of 12 globins [2], and the structure of coelomic Hb (C1) of vestimentiferan *Riftia pachyptila* [3] have been reported. However, the detailed mechanism of sulfide binding is still unclear. To provide further structural insights into the sulfide-binding mechanism of these giant Hbs, especially vascular Hb, we have performed a X-ray crystal structure analysis of vascular giant Hb from pogonophoran *Oligobrachia mashikoi* (Fig. 1(a)).

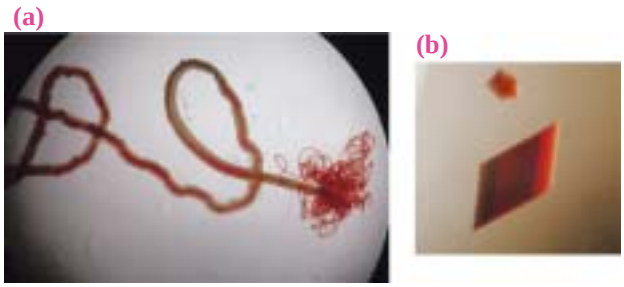

Fig. 1. **(a)** Part of body of *Oligobrachia mashikoi*, and **(b)** crystals of *Oligobrachia* Hb.

Crystals of *Oligobrachia* Hb were successfully obtained (Fig. 1(b)), and X-ray diffraction study was performed at beamlines **BL38B1**, **BL41XU**, **BL44XU**, and **BL45XU** [4,5]. The structure of *Oligobrachia* Hb is composed of 24 globin chains with six copies of each of four individual globin chains, termed A1, A2, B1, and B2. The entire structure is hollow-spherical, with outer and inner diameters of about 120 Å and 50 Å, respectively (Fig. 2). One-half of the *Oligobrachia* Hb molecule (Hb 12mer) is composed of a three-fold trimer of a tetramer. There are an intra-tetramer and an inter-tetramer disulfide bonds per tetramer. This Hb tetramer structure consists of two dimers (A1B1 dimer and A2B2 dimer in *Oligobrachia* Hb). *Oligobrachia* Hb and *Riftia* C1 show the same quaternary structure as that of 24mer and are considered to be a dimer of the 12mer. These 12mer structures are basically similar to annelid reconstructed 12mer. The dodecameric assembly of these Hbs could be a fundamental unit of Hbs from pogonophorans, vestimentiferans, and annelids, not only in 3500 kDa hexagonal bilayer Hbs but also in 400 kDa Hbs.

It has been suggested that conserved Cys residues among pogonophorans and vestimentiferans are involved in potential sulfide-binding sites. The thiol group of these Cys residues are proposed to form a persulfide group (S-sulfohemoglobin). In *Oligobrachia* Hb, both the A1 and B2 subunits possess a common conserved Cys, and the A2 subunit has another conserved Cys. There is a non-conserved Cys at a position different in the B1 subunit from those of other three subunits. Although the obtained structure is a sulfide-free form, the structure of the Hg derivative used for phasing provides significant insights into the sulfide-binding mechanism because Hg atoms specifically bind to free Cys

residues. All four of these free Cys residues are bound by the Hg compound in the Hg derivative crystal. Environments around the conserved Cys residue of the A1 and B2 subunits are revealed to be more suitable for sulfide binding. These sites surrounded by Phe residues are quite similar to each other, and are highly aromatic (Fig. 3). These Phe residues are completely conserved in pogonophorans Hb and vestimentiferan Hb. Two Phe residues come into contact with a Hg atom in the derivative structure, and this strongly suggests that in the native Hb, the sulfide bound to the Cys residue could be stabilized by aromatic-electrostatic interactions with these two Phe side chains. The environment surrounding another conserved Cys of the A2 subunit is also hydrophobic, where Leu and Ile residues contribute. A hydrophobic environment prevents bound sulfides from excessive contact with solvents to avoid undesired oxidation.

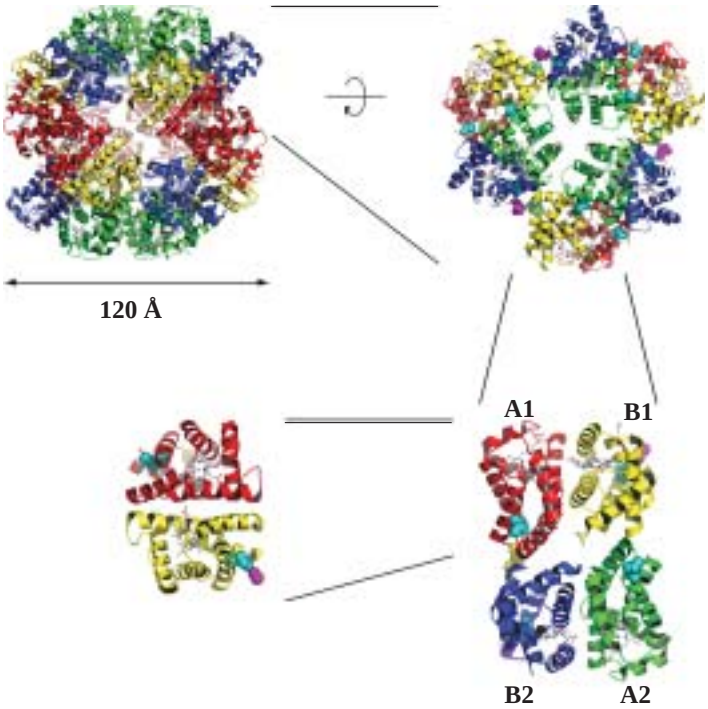

Fig. 2. Structural hierarchy in *Oligobrachia* Hb. Giant Hb is considered to be a dimer of 12mer (upper-left). The 12mer structure is composed of a three-fold trimer of a tetramer (upper-right). This tetrameric assembly has no D_2 symmetry as that in mammalian Hb (lower-right). The Hb tetramer consists of two dimers (lower-left). Space-filling models indicate disulfide bonds.

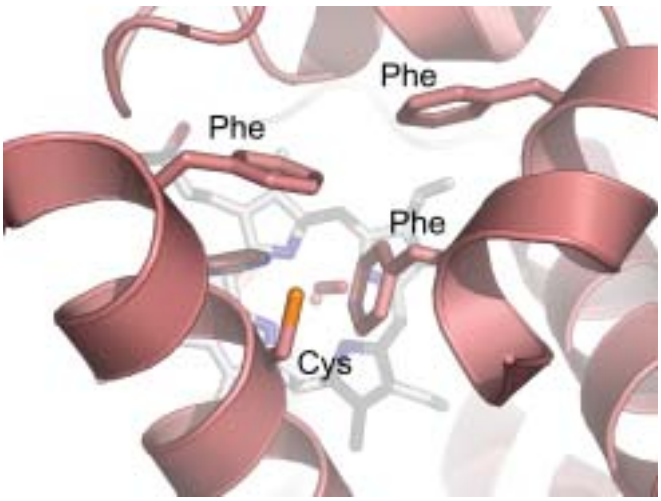

Fig. 3. Potential sulfide-binding site of A1 subunit. The environment around the conserved Cys residue is highly aromatic.

Nobutaka Numoto[a] and Kunio Miki[a,b,*]

[a] Graduate School of Science, Kyoto University
[b] SPring-8 / RIKEN

*E-mail: miki@kuchem.kyoto-u.ac.jp

References

[1] T. Nakagawa *et al.*: Zoolog. Sci. **22** (2005) 283.
[2] K. Strand *et al.*: J. Mol. Biol. **344** (2004) 119.
[3] J.F. Flores *et al.*: Proc. Natl. Acad. Sci. USA **102** (2005) 2713.
[4] N. Numoto *et al.*: Biochim. Biophys. Acta **1750** (2005) 173.
[5] *N. Numoto, T. Nakagawa, A. Kita, Y. Sasayama, Y. Fukumori and K. Miki: Proc. Natl. Acad. Sci. USA **102** (2005) 14521.*

Crystal Structure of P-protein of Glycine Cleavage System from *Thermus thermophilus* HB8

In most living organisms, the glycine cleavage system (GCS) plays a crucial role in the degradation of glycine. The GCS is a multienzyme complex composed of four different proteins (P, H, T and L) and catalyzes the oxidative cleavage of glycine in a multistep reaction (Fig. 1) [1]. In humans, a mutation in GCS genes can lead to a dramatic accumulation of glycine in blood, resulting in a severe neurological disease termed nonketotic hyperglycinemia (NKH) [2]. Accordingly, the three-dimensional structures of the GCS proteins at the atomic level are required to ultimately understand the molecular basis of NKH. From 1991 to 2004, the structures of H-, T- and L-proteins were elucidated, but only the structure of the P-protein was not reported. The P-protein structure is especially important, because more than 80% of NKH patients have a specific defect in the P-protein [2]. In this study [3], we have determined for the first time the crystal structure of the P-protein.

The P-protein is a pyridoxal 5'-phosphate (PLP)-dependent enzyme (PLP-enzyme) and catalyzes the first step of the GCS reaction (Fig. 1). The P-protein of *Thermus thermophilus* (*Tth*) HB8 forms an $\alpha_2\beta_2$ tetramer with a total molecular mass of 200 kDa. The α- and β-subunits of the *Tth* P-protein were coexpressed in *Escherichia coli*, purified and crystallized as a stable complex [4]. X-ray diffraction data were collected at the RIKEN Structural Biology beamlines **BL44B2** and **BL45XU**. The crystal structure of the P-protein in complex with PLP was determined at 2.1 Å resolution by single isomorphous replacement with anomalous scattering (Fig. 2(a)).

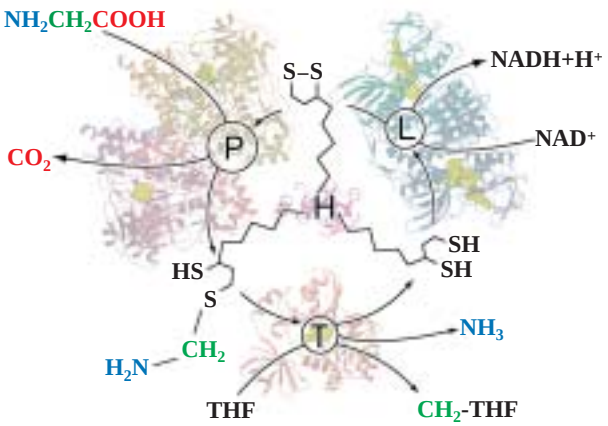

Fig. 1. Multistep reaction catalyzed by GCS.

The P-protein belongs to fold-type I of PLP-enzymes as determined on the basis of sequence similarities [5]. All other fold-type I enzymes with known structures are intimate α_2 dimers, each with an internal twofold axis, or their loose multiples (α_4, α_6 and α_{12}), where an α_2-type active dimer has two active sites at the α-α interface (corresponding to PLP molecules shown in Fig. 2(c,d)). In contrast, two intimate αβ dimers in the P-protein are related by a twofold axis to form an $(\alpha\beta)_2$ tetramer, in which each αβ-type active dimer has only one active site at the α-β interface (Fig. 2(a,b)). The α- and β-subunits show 24% sequence identity and have similar structures; therefore, the αβ dimer appears to have an approximate twofold axis (Fig. 2(b)) and to mimic $\alpha_2$dimers such as those seen in glutamate decarboxylase (Fig. 2(d)). This suggests that the αβ-type active dimer of the P-protein arose by gene duplication of a homodimeric ancestor, after which the ancestral P-protein has structurally diverged such that the protein has been specifically adapted for use as a multienzyme complex component, even though this involved the loss of one active site.

We also analyzed the crystal structures of P-proteins without PLP (i.e. apoenzyme) and in complex with PLP and an inhibitor both at 2.4 Å resolution. These structures allow us to identify functionally important residues involved in the recognition of the cofactor PLP and substrates (glycine and H-protein), and shows that most of these residues are well conserved among all living organisms. This suggests that the catalytic mechanisms should be essentially the same for both the *Tth* and human P-proteins. Shown in Fig. 3 are NKH mutations mapped on a model structure of the human P-protein built on the basis of the *Tth* P-protein. To date, eleven point mutations have been identified in NKH patients. For example, the P329T mutation causes this disease. Pro329 is fully conserved and is involved in the conformational changes upon the binding of PLP. This suggests that P329T affects the binding of the cofactor PLP and thereby leading to the loss of enzymatic activity. Likewise, for most of the other

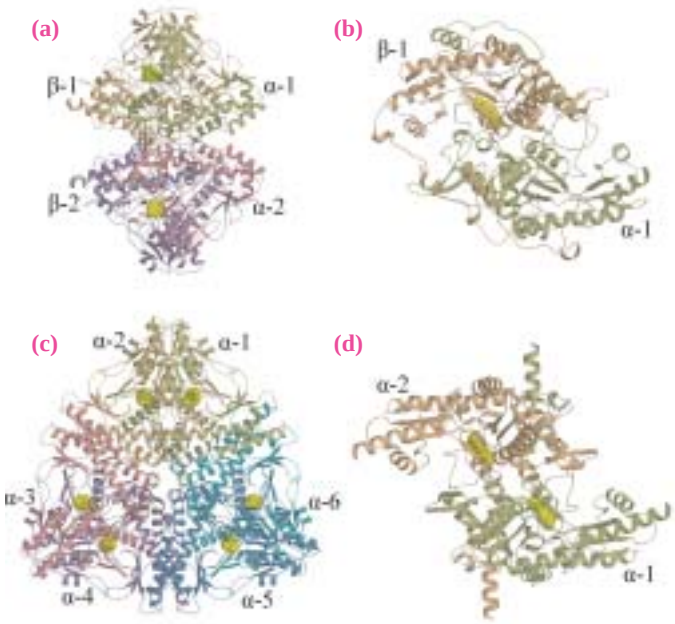

Fig. 2. Crystal structures of $(\alpha\beta)_2$ tetramer **(a)** and $\alpha\beta$ dimer **(b)** of P-protein, and (α_2) 3 hexamer **(c)** and α_2 dimer **(d)** of glutamate decarboxylase. PLP molecules are shown as yellow spheres.

NKH mutations, we have confirmed that the model structure provides a molecular basis for understanding how the mutations lead to the loss of enzymatic activity resulting in the disease [3].

In conclusion, our work on the *Tth* P-protein provides a crystal structure of the final GCS component with an unknown structure. The structural information greatly aids in understanding the molecular pathology of NKH and will be useful in interpreting other NKH mutations that may be identified in the future. Furthermore, it provides new insights into the molecular evolution of P-proteins, a structural basis for understanding catalytic mechanisms, and the architecture of the multienzyme complex, and should stimulate further structure/function studies.

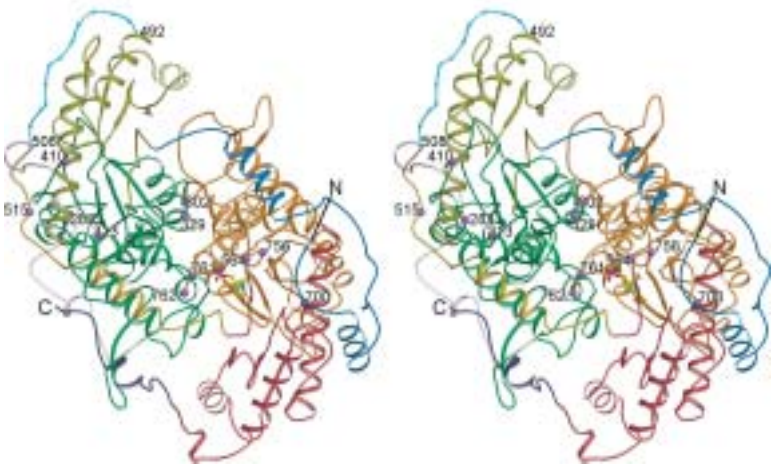

Fig. 3. NKH mutations mapped on a stereo-drawing of model structure of human P-protein.

Tadashi Nakai[a,*] and Nobuo Kamiya[a,b]

[a] SPring-8 / RIKEN
[b] Graduate School of Science, Osaka City University

*E-mail: nakaix@spring8.or.jp

References

[1] R. Douce *et al.*: Trends Plant Sci. **6** (2001) 167.
[2] K. Tada and S. Kure: J. Inherit. Metab. Dis. **16** (1993) 691.
[3] *T. Nakai, N. Nakagawa, N. Maoka, R. Masui, S. Kuramitsu and N. Kamiya: EMBO J.* ***24*** *(2005) 1523.*
[4] T. Nakai *et al.*: Acta Crystallogr. D **59** (2003) 554.
[5] N.V. Grishin *et al.*: Protein Sci. **4** (1995) 1291.

Crystal Structure of a Junction between B-DNA and Z-DNA

Z-DNA is a higher-energy form of double stranded DNA (dsDNA) with left-handed helical sense whereas most DNA is found as energetically stable B-DNA with right-handed helical sense. Z-DNA is stabilized by high salt or in the presence of positively charged molecules such as spermine *in vitro*. However, negative supercoiling is thought to be a Z-DNA stabilizing factor *in vivo*. It has been shown that negative supercoiling induced by transcription stabilizes the Z conformation behind the RNA polymerase. Several studies have suggested that the Z conformation is not only a result of transcription, but can act as a *cis*-element regulating the transcriptional status of a gene. Moreover, the identification of a family of polypeptides containing a domain specific for Z-DNA binding has supported the involvement of Z-DNA in biological processes as yet unidentified [1].

The identification of Z-DNA binding proteins and the biological evidences supporting the presence of Z-DNA *in vitro* have raised questions concerning the B-Z junction, the region linking right-handed B-DNA and left-handed Z-DNA. When a region is converted to Z-DNA within a long continuous double stranded B-DNA, two B-Z junctions will be formed flanking the region of Z-DNA. Many studies have been carried out to characterize the B-Z junction using biochemical and biophysical methods, however, the structural properties of B-Z junction have not been well studied. It is difficult to prepare a continuous hybrid B/Z DNA duplex containing both B and Z conformations in physiological conditions, which is necessary for structural analysis at high resolution. In this study, we have taken advantage of the binding of $hZ\alpha_{ADAR1}$, a Z-DNA binding domain from human ADAR1 [2], in order to stabilize the Z conformation in one-half of the DNA duplex. We designed a 15-base pair dsDNA consisting of two regions: one is CG rich and can be easily converted to Z-DNA in Z-DNA inducing conditions, and the other region is TA rich and maintains B conformation predominantly (Fig. 1). Therefore, in the presence of the $hZ\alpha_{ADAR1}$, one B-Z junction is thus formed in the middle of the DNA duplex, connecting the Z- and B-DNA. The $hZ\alpha_{ADAR1}$ domain (aa.140-202) was co-crystallized with the DNA [5'-GTCGCGCGCCATAAACC-3' and 5'-ACGGTTTATGGCGCGCG-3']. The crystal has the space group *P*61, and the structure of the complex was solved at 2.6 Å resolution using the data obtained at beamline **BL41XU** of SPring-8 (Harima, Japan) and beamline BL-6B of PLS (Pohang, Korea) (R = 23.8 %, R_{free} = 28.5 %; ref. [3]).

Overall structure of the dsDNA is composed of eight base-pair Z-DNA, six base-pair B-DNA and the B-Z junction (Figs. 1, 2). The Z-DNA is stabilized by four Z-DNA binding domains ($hZ\alpha_{ADAR1}$, Fig. 2) and shows standard base-pair step parameters of Z-DNA (Fig. 2 and Table 1). B-DNA also has standard base-pair step parameters of B-DNA (Fig. 2 and Table 1). At the B-Z junction, A and T bases are extruded from the duplex, thereby linking left-handed Z-DNA to right-

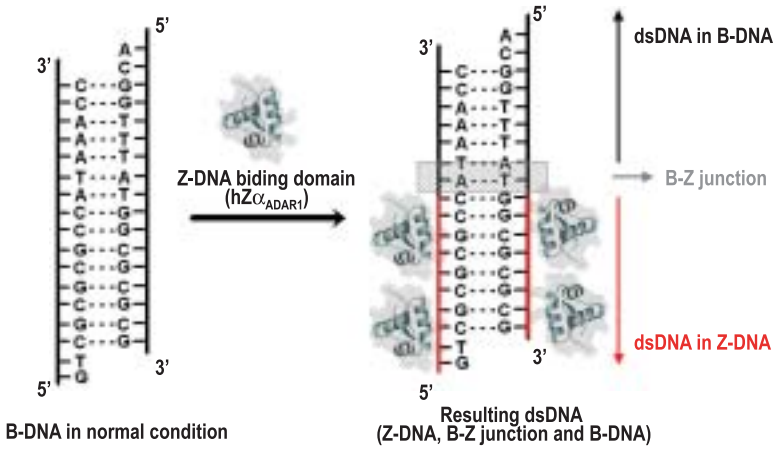

Fig. 1. The strategy of making a stable junction between B-DNA and Z-DNA. Four Z-DNA binding proteins from human ADAR1 ($hZ\alpha_{ADAR1}$) stabilize the Z-conformation in one-half of a 15 base pair dsDNA and other region remains as a junction and B-DNA.

Table 1 The base pair parameters near the junction between B-DNA and Z-DNA and the standard B- and Z- DNAs

Base step	Shift	Slide	Rise	Tilt	Roll	Twist
A3/A2	0.26	-0.20	3.49	1.82	-3.02	38.51
A2/T1	-0.26	1.46	3.37	-4.56	6.82	38.57
C-1/C-2	0.28	5.83	-4.60	8.23	4.48	-12.96
C-2/G-3	0.28	-1.34	-3.09	1.50	-8.14	-47.51
B-DNA	-0.02	0.12	3.36	-0.19	0.02	35.58
Z-DNA	-0.03	2.81	3.49	0.32	-3.14	-25.10

Each parameter was calculated using the program 3DNA. Parameters of B-DNA were calculated using crystal structure of B-DNA[4] (PDB ID: 1BNA), and those of Z-DNA were calculated using the crystal structure of Z-DNA[3] (PDB ID: 2DCG)

handed B-DNA. The base-pair step parameters of B-Z junction have 3.82 Å rise (Dz) and -16.9º twist (Fig. 2 and Table 1). Though one junctional base is extruded, base stacking is continuous from Z-DNA to B-DNA through the B-Z junction without significant impairment. Thus, base stacking is also a major stabilizing factor even at the B-Z junction as well as in B-DNA and Z-DNA regions (Fig. 2, [3-5]). It seems that extrusion of a base from each strand accommodates a reversal in the helical direction of the backbone from B- to Z conformation. It is also speculated that these extruded bases may be specific recognition sites for enzymes mediating DNA modification.

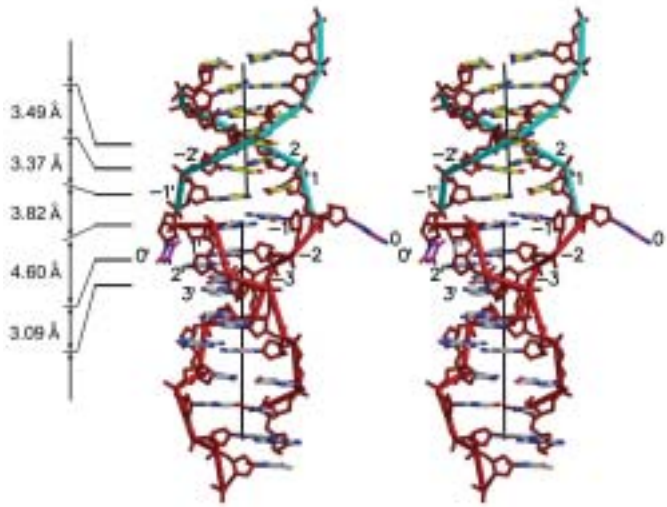

Fig. 2. Skeletal stereo views of DNA. Red and blue lines connect phosphate groups in Z-DNA and B-DNA, respectively. One strand has numbers with a prime symbol. Negative numbers start at the 5‘ end and increase toward the extruded junctional bases A0 (right) and T0′(left). The rises of base step parameters are shown.

Sung Chul Ha and Kyeong Kyu Kim*

Department of Molecular Cell Biology,
Sungkyunkwan University School of Medicine, Korea

*E-mail: kkim@med.skku.ac.kr

References

[1] A. Rich and S. Zhang: Nature Rev. Genet. **4** (2003) 566.
[2] A. Herbert *et al.*: Proc. Natl. Acad. Sci. USA **92** (1995) 7550-4.
[3] *S.C. Ha, K. Lowenhaupt, A. Rich, Y.-G. Kim and K.K. Kim: Nature **437** (2005) 1183.*
[4] H.R. Drew *et al.*: Proc. Natl. Acad. Sci. USA **78** (1981) 2179.
[5] A.H. Wang *et al.*: Nature **282** (1979) 680.

Crystal Structure of Human Flap Endonuclease-1 (FEN1) Complexed to PCNA

DNA replication in eukaryotes is a highly coordinated process involving many proteins that work cooperatively to ensure the accurate and efficient replication of DNA. In this process, flap endonuclease-1 (FEN1) plays a crucial role in the removal of RNA primers during Okazaki fragment maturation in lagging strand DNA synthesis (Fig. 1). Flap DNA removal by FEN1 is also essential during long-patch base excision repair. FEN1 appears to be a key player in maintaining genomic stability by participating in the DNA replication and repair processes.

FEN1 endonuclease activity is markedly stimulated by proliferating cell nuclear antigen (PCNA), which is well known as the 'DNA sliding clamp'. This stimulation is induced by direct binding of FEN1 to PCNA, leading to a 10- to 50-fold increase in its nuclease activity. Mutations in FEN1 that disrupt the interaction with PCNA decrease the cleavage efficiency of flap DNA at the replication fork, thus leading to the generation of unfavourably long flap DNA strands.

Recently, we successfully crystallized full-length human FEN1 complexed to PCNA [1]. A set of diffraction data was collected at SPring-8 on beamline **BL38B1** using crystals cooled to 100 K with liquid-nitrogen vapour. The phases were determined by molecular replacement method using human PCNA and archaeal FEN1 monomers as a search model. The structure was finally refined at a resolution limit of 2.9 Å.

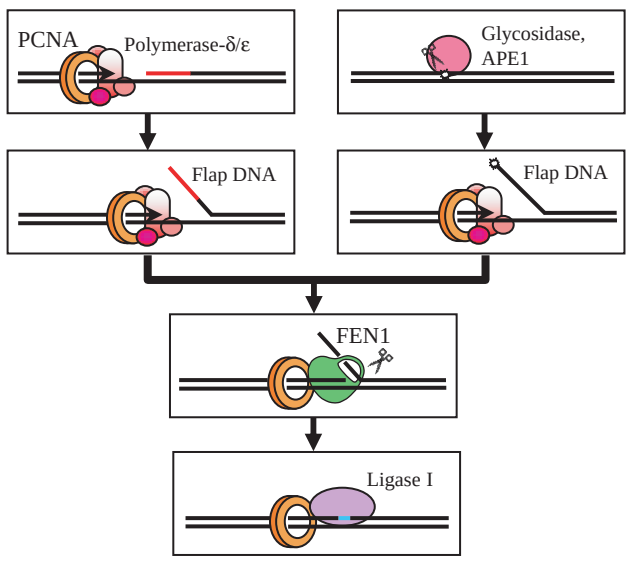

Fig. 1. FEN1 complexed to PCNA removes 5'-overhanging DNA flaps in the DNA replication (left) and repair (right) processes. RNA primer in Okazaki fragment is shown in red.

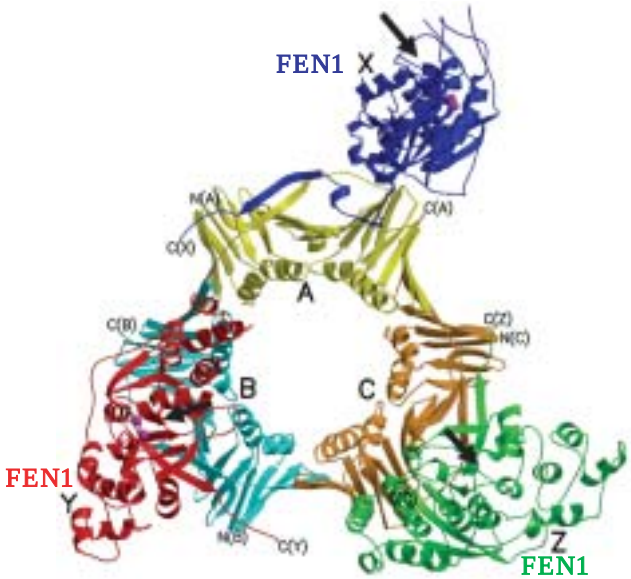

Fig. 2. Crystal structure of human FEN1-PCNA complex. Three FEN1 molecules are colored in blue (X), red (Y) and green (Z), and the three subunits of the PCNA trimer in yellow (A), cyan (B) and orange (C). The C-termini of FEN1 and PCNA are labeled. Metal ions bound to the active sites of FEN1 are shown in magenta. Proposed catalytic faces of FEN1 are indicated by arrows.

The structure revealed three FEN1 molecules (Fig. 2, molecules X, Y and Z) bound to one PCNA trimer [2]. Three PCNA subunits (subunits A, B and C) are tightly associated to form a closed ring. Each PCNA subunit binds one FEN1 molecule. The main interface involves the C-terminal tail of FEN1, which forms two β-strands connected by a short helix, the βA-αA-βB motif (Fig. 3). The FEN1 core domain is linked to this PCNA-binding tail by a short linker containing small residues. We found that this linker, ^{333}QGST^{336}, functions as a hinge which endows FEN1 with a degree of freedom to swing the core domain.

In our complexed structure, the nuclease core domains of the Z and Y FEN1 molecules swing about 90º and 100º, respectively, from that of molecule X toward the center of the PCNA ring (Fig. 4). During this swing displacement, the active site tracks on a large spherical surface with a radius of 40-50 Å. FEN1 locates its core domain in front of the PCNA, while the active site of molecules Y and Z faces toward the conceivable position occupied by the DNA substrate. The swing-in motion might be utilized in threading the flap DNA through the clamp region. Suppose that dsDNA is passing through the center of PCNA ring and that the DNA occupies a linear orientation, approximately 50º more swing-in displacement of the FEN1 core domain would be needed to place its active site on the cleavage site (the junction of dsDNA and flap-ssDNA). The most likely trigger to allow FEN1 to swing into position for cleavage would be interactions between the single-stranded flap DNA and FEN1.

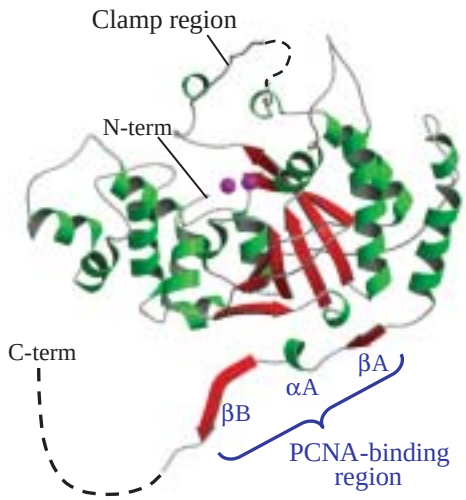

Fig. 3. Structure of human FEN1. Two metal ions in the active site are depicted in magenta. The clamp region is thought to thread along the single strand of the DNA substrate (flap DNA).

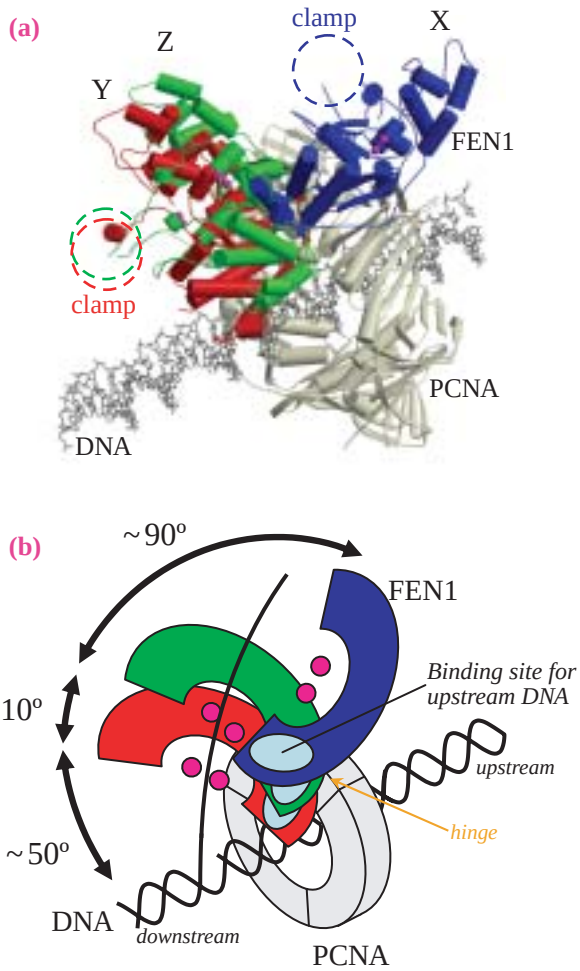

Fig. 4. The hinge flexibility of human FEN1. **(a)** Three FEN1 subunits in the crystal structure were superimposed on one site of PCNA (a gray model). The looping-out clamp regions are marked as dashed circles. The conceivable DNA model is superimposed at the center of PCNA. **(b)** Schematic model showing the orientation of the FEN1 core domains in **(a)**.

Ken Kitano[a], Shigeru Sakurai[a,b] and Toshio Hakoshima [a,c,*]

[a] Nara Institute of Science and Technology
[b] Japan Society for the Promotion of Science
[c] CREST, Japan Science and Technology Agency

*E-mail: hakosima@bs.naist.jp

References

[1] S. Sakurai *et al.*: Acta Crystallogr. D **59** (2003) 933.
[2] *S. Sakurai, K. Kitano, H. Yamaguchi, K. Okada, K. Hamada, K. Fukuda, M. Uchida, E. Ohtsuka, H. Morioka, T. Hakoshima: EMBO J.* ***24*** *(2005) 683.*

Crystal Structures of Leucyl-tRNA Synthetase Complexed with $tRNA^{Leu}$

Leucyl-tRNA synthetase (LeuRS) is one of the 20 enzymes that comprise the essential family of aminoacyl-tRNA synthetases (aaRSs). It is responsible for aminoacylating the aliphatic amino acid leucine to up to six different $tRNA^{Leu}$ isoacceptors, each with a different anticodon. Although common aaRSs strictly recognize the anticodon for cognate tRNA selection, LeuRSs do not recognize the anticodon in $tRNA^{Leu}$, possibly because the anticodons are so divergent. Instead, LeuRS strictly recognizes the adenosine residue at position 73 (A73). This tRNA position is known as the "discriminator", and is recognized by many aaRSs. In addition, the archaeal LeuRSs and most of the eukaryal LeuRSs recognize the long variable arm of $tRNA^{Leu}$, which is characteristic to $tRNA^{Leu}$. But how LeuRS recognizes the discriminator A73 and the long variable arm was unknown.

Another interesting feature of LeuRS is that it has a proofreading (editing) enzymatic activity. The aminoacylation domain mis-recognizes the near cognate amino acids, such as isoleucine and methionine, and mischarges them to the 3'-end of $tRNA^{Leu}$. If these misformed Ile-$tRNA^{Leu}$ and Met-$tRNA^{Leu}$ were delivered to the ribosome and used in protein synthesis, mutant proteins are produced. To prevent such mutant protein production, the LeuRS "editing domain" hydrolyzes the mis-formed aminoacyl-tRNA and contributes to high-fidelity aminoacylation. The previously determined crystal structure of tRNA-free archaeal *Pyrococcus horikoshii* LeuRS revealed that aminoacylation and editing sites are separated by more than 35 Å [1]. How the aminoacylated 3'-end of tRNA is delivered from the aminoacylation to editing sites was unknown.

To elucidate these mechanisms, we determined the crystal structure of *P. horikoshii* LeuRS in complex with $tRNA^{Leu}$ at 3.2 Å resolution, using the **BL26B1** and **BL41XU** beamlines (Fig. 1) [2]. The protruding C-terminal domain (light green in Fig. 1) of LeuRS reaches the tip of the long variable arm. Some residues at the C-terminal extremity recognize the tip bases of the long arm in a sequence specific manner. Thus, we clarified the recognition mechanism of the long variable arm.

The tRNA 3'-terminal adenosine is located in the aminoacylation site. Thus, our tRNA-complex structure represents the "aminoacylation complex". The editing domain swings from its tRNA-free position to avoid clashing with tRNA, and thereby lets the CCA end bend and reach the aminoacylation active site.

In the asymmetric unit of the crystal, there are two

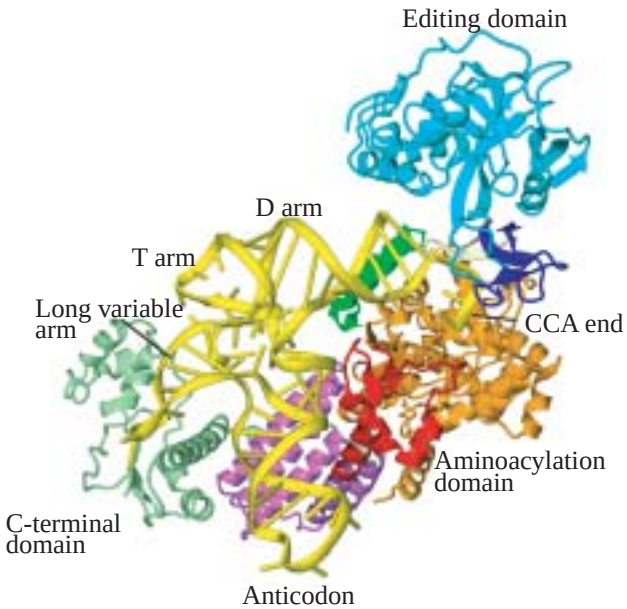

Fig. 1. Ribbon model of *P. horikoshii* LeuRS-$tRNA^{Leu}$ complex structure. $tRNA^{Leu}$ is shown in yellow. LeuRS is shown in seven colors according to the domains.

Fig. 2. Superposition of two LeuRS-$tRNA^{Leu}$ complexes (complexes A and B) in asymmetric unit. Complex A is color-coded as in Fig. 1. tRNA and the editing domain of complex B are in pink. The other parts of the LeuRS structures are almost the same between the two complexes.

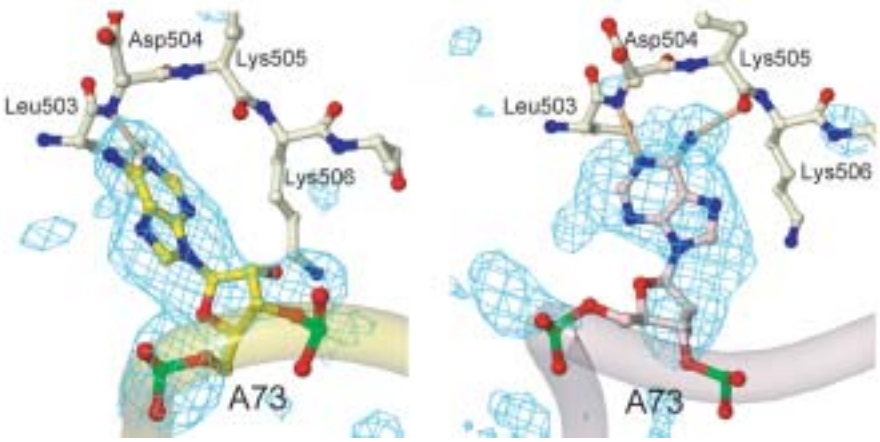

Fig. 3. Distinct conformations of A73. Omit electron density map for discriminator base A73 in complexes A **(a)** and B **(b)**.

LeuRS-tRNA^{Leu} complexes. Between the two complexes, the tRNA 3'-region assumes distinct conformations (Fig. 2) that allow A73 to be specifically recognized, but via different mechanisms (Fig. 3). One conformation (in complex A) is the canonical "aminoacylation state" (shown in yellow in Figs. 2, 3, and 4), with the tRNA 3'-region bound deeply in the aminoacylation active site. In contrast, the other conformation (in complex B) appears to be a snapshot of the "intermediate state", in which the misaminoacylated 3'-end has partially relocated to the editing domain (shown in pink in Figs. 2, 3, and 4).

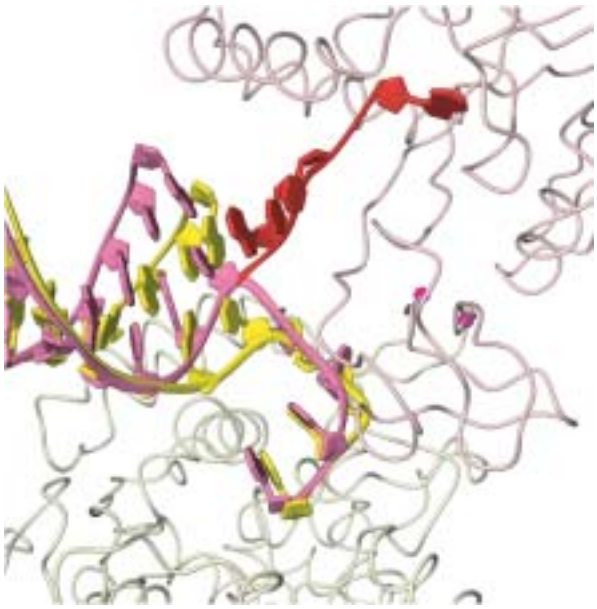

Fig. 4. Aminoacylation (complex A, yellow), intermediate (complex B, pink), and post-transfer editing (model, red) conformations. LeuRS in complex B is shown by a white line, with the editing domain in pink.

The "editing state" model, in which the 3'-end is located in the editing domain with the rest of the tRNA remains bound to the enzyme body, can be constructed on the basis of only the complex B structure, but not on the complex A structure. The discriminator base A73 is recognized via two different but switchable mechanisms (Fig. 3), indicating its important role in switching the tRNA conformation.

The structures suggest that after the aminoacylation reaction in the complex A "aminoacylation state", the conformation of the discriminator A73 is switched first. Then the tRNA 3'-end undergoes conformational change, and eventually becomes the complex B "intermediate state". After that, the 3'-end is released out of the aminoacylation site, and is bound to the editing site. The near-cognate amino acid is hydrolyzed, if present.

Ryuya Fukunaga[a,b] and Shigeyuki Yokoyama[a,b,c,*]

[a] Department of Biophysics and Biochemistry, The University of Tokyo
[b] RIKEN Genomic Sciences Center
[c] SPring-8 / RIKEN

*E-mail: yokoyama@biochem.s.u-tokyo.ac.jp

References

[1] R. Fukunaga and S. Yokoyama: J. Mol. Biology **346** (2005) 57.
[2] R. Fukunaga and S. Yokoyama: Nature Structural & Molecular Biology **12** (2005) 915.
[3] *M. Tukalo, A. Yaremchuk, R. Fukunaga, S. Yokoyama and S. Cusack: Nature Structural & Molecular Biology **12** (2005) 923.*

Structure of Phytobilin Synthesis Enzyme

Photosynthetic organisms utilize phytobilins, which are linear tetrapyrrole pigments, for photosynthesis and light sensing. Such organisms develop light-harvesting systems to accomplish efficient photosynthesis in their living environments. Red algae and cyanobacteria have giant protein-pigment complexes called phycobilisomes as a light-harvesting system, in which phycobilins (one of phytobilins) are utilized for light-harvesting pigments, whereas higher plants and green algae have light-harvesting complexes, in which chlorophylls are mainly utilized as the light-harvesting pigments [1]. Phycobilins absorb lights in the range from red to green, which are not well absorbed by chlorophylls. This characteristic of these pigments is reflected in the habitats of photosynthetic organisms; cyanobacteria and red algae can grow in deeper water rather than green algae. In addition, phytochromes, red-light sensitive photoreceptors in plants, covalently bind phytochromobilin (one of phytobilins). Phytochromes are involved in various physiological reactions such as the photoperiodic induction of flowering, the induction of germination, and leaf senescence; these reactions are initiated by the photoisomerization of phytochromobilin in phytochromes.

Phytobilins are biosynthesized from heme by heme oxygenase and ferredoxin dependent bilin reductases (FDBRs) (Fig. 1). First, the porphyrin ring of heme is oxidatively cleaved by heme oxygenase to produce BV. Then, BV is reduced by FDBRs to produce phytobilins [2]. This pathway has attracted much attention not only from the viewpoint of biological importance but also from the biotechnological aspect [3]. Phycocyanobilin:ferredoxin oxidoreductase (PcyA), one of such FDBRs, is unique in reducing BV to phycocyanobilin by two sequential steps [4]. The first step is the reduction of the vinyl group of the BV D-ring to produce 18^1, 18^2-dihydrobiliverdin IXα, and the second step is the reduction of the A-ring of 18^1, 18^2-dihydrobiliverdin IXα to produce phycocyanobilin. Each reduction step uses two electrons supplied by ferredoxin. To achieve these sequential reductions, PcyA must possess a molecular structure that allows discrimination between the A- and D-rings of BV and control of the reaction sequence.

The crystal structure of PcyA from cyanobacterium *Synechocystis* sp. PCC 6803 in complex with BV has been determined from data obtained at 1.51 Å resolution using synchrotron radiation at beamlines **BL41XU** and **BL44B2** [5]. This structure, the first determined tertiary structure of an FDBR family member, reveals how an FDBR recognizes its bilin

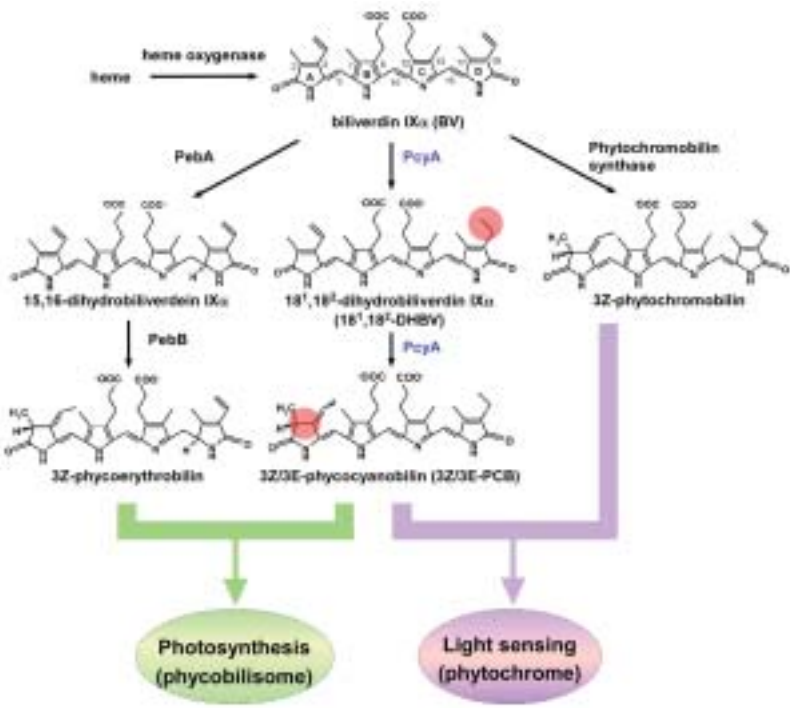

Fig. 1. Biosynthetic pathway of phytobilins by FDBRs.

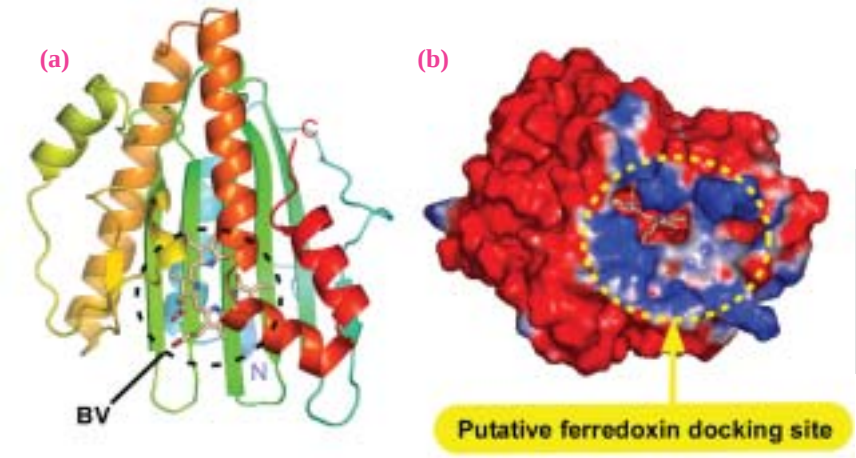

Fig. 2. Overall structure and electrostatic potential of PcyA-BV complex. **(a)** The ribbon model is displayed with the N-terminal side in blue and the C-terminal side in red. **(b)** Positive and negative surfaces are shown in blue and red, respectively. BV is shown as a stick model.

substrate and ferredoxin. PcyA is folded in a three-layer α/β/α sandwich structure, in which BV in a cyclic conformation is positioned between the β-sheet and C-terminal α-helices (Fig. 2(a)). The basic patch on the PcyA surface near the BV molecule may provide a binding site for acidic ferredoxin, allowing the direct transfer of electrons to the propionate groups of BV (Fig. 2(b)).

The electron density of BV was clearly visible, indicating that PcyA strictly recognizes the orientation of BV to reduce the BV site specifically (Fig. 3, left). On the basis of the active site structure, the conservation of amino acids in PcyAs, and the absolute configuration of the product, we propose the mechanism by which the sequential reduction of the D- and A-rings is controlled; Asp 105 located between the two reduction sites would play the central role by changing its conformation during the reaction (Fig. 3). Homology modeling on the basis of PcyA structure yielded the putative structures of other FDBRs. The model of phytochromobilin synthase fits well with the previous genetic data. Thus, the PcyA structure may provide a structural basis for understanding the common reaction mechanism of FDBRs and the specificity of the substrate-reducing site in each FDBR.

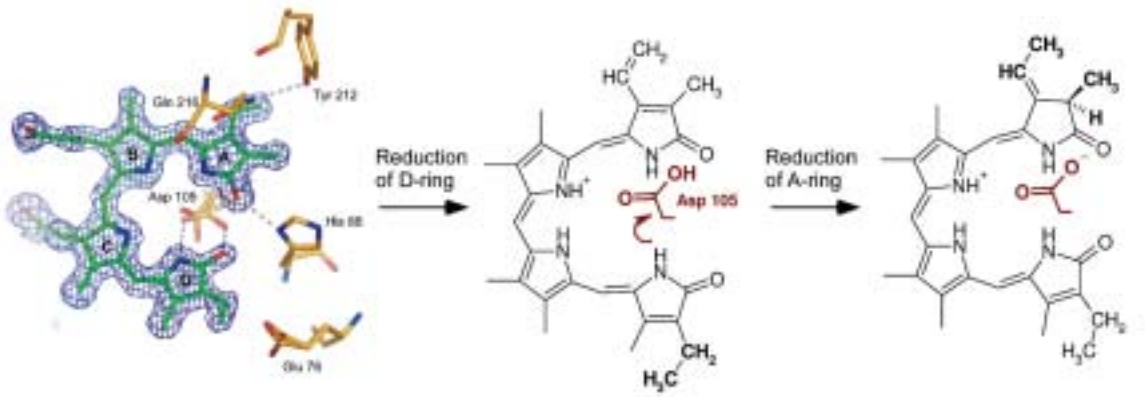

Fig. 3. Possible scheme of sequential reduction of BV catalyzed by PcyA. Electron density for BV is superimposed on the stick models of BV and candidate active residues (left). The side chains of Glu 76 and Asp 105 show multiple conformers. The essence of the sequential reduction of BV is that the side chain of Asp 105 changes its conformation after D-ring reduction allowing the stereospecific reduction of the A-ring.

Keiichi Fukuyama[a,*] and Masakazu Sugishima[b]

[a] Department of Biological Sciences, Osaka University
[b] Department of Medical Biochemistry, Kurume University School of Medicine

*E-mail: fukuyama@bio.sci.osaka-u.ac.jp

References

[1] S.I. Beale: Chem. Rev. **93** (1993) 785.
[2] N. Frankenberg *et al.*: Plant Cell **13** (2001) 965.
[3] A. Levskaya *et al.*: Nature **438** (2005) 441.
[4] N. Frankenberg *et al.*: J. Biol. Chem. **278** (2003) 9219.
[5] *Y. Hagiwara, M. Sugishima, T. Takahashi and K. Fukuyama: Proc. Natl. Acad. Sci. USA **103** (2006) 27.*

Crystal Structure of Glucooligosaccharide Oxidase from *Acremonium strictum* — A Novel Flavinylation of 6-*S*-cysteinyl, 8α-*N*1-histidyl FAD

Glucooligosaccharide oxidase (GOOX) from *Acremonium strictum* has been screened for potential applications in oligosaccharide acid production and alternative carbohydrate detection, because it catalyzes the oxidation of glucose, maltose, lactose, cellobiose and cello- and malto-oligosaccharides (Fig. 1) [1]. Here we have determined the GOOX structure in the absence, or presence of a product analog, 5-amino-5-deoxy-cellobiono-1,5-lactam (ABL) (**BL12B2**) (Fig. 2(a)) [2].

Unexpectedly, the FAD cofactor is cross-linked to the enzyme at two attachment sites (Fig. 2(b)). One is the S^{γ} atom of Cys^{130} bound to the C^{6} atom of the isoalloxazine ring, while the other is the $N^{\delta1}$ atom of His^{70} bound to the 8α-methyl group (6-*S*-cysteinyl, 8α-*N*1-histidyl FAD). Five types of covalent flavinylation have been identified up to the present and flavinylation has been shown to be an autocatalytic process [3]. The four types of flavinylation at the 8α-methyl group cross-link to His ($N^{\delta1}$ and $N^{\varepsilon2}$), Tyr (O^{η}) and Cys (S^{γ}), whereas an unusual 6-S-cysteinyl modification has been observed only in the FMN cofactor of trimethylamine dehydrogenase and its homologues. Thus, GOOX possesses a novel form of covalent flavinylation; it is the first example of 6-*S*-cysteinyl FAD and the first double covalent linkage identified to date. The His^{70} and Cys^{130} mutants suggest that the covalent attachment is able to enhance the redox potential of the flavin [1].

ABL is firmly embedded on the *si* face of the isoalloxazine ring without induction of any significant conformational change except for Glu^{247} (Fig. 3(a)). A variety of carbohydrate molecules were then modeled manually in the substrate-binding groove. D-glucose is the only monosaccharide substrate for GOOX. Simulation of the complexes shows that other hexoses and derivatives form either fewer hydrogen bonds or unfavorable contacts with the surrounding residues. GOOX possesses an open carbohydrate-binding groove, which explains why the enzyme is able to utilize oligosaccharides as good substrates (Fig. 3(b)). The substrate cellobiose was modeled into the active site, suggesting that GOOX preferentially oxidizes the β anomer with the conserved Tyr^{429} acting as a general base. As is common for flavoenzymes, the reaction mechanism of GOOX consists of two half-reactions (Fig. 1). The reductive half-reaction is involved in the oxidation of the free reducing-end β-D-glucosyl residue to glucono-1,5-lactone by hydride transfer to the N^{5} atom, probably initiated by proton abstraction from the OH^{1} group by Tyr^{429}. The lactone product is spontaneously hydrolyzed to gluconic acid. In the oxidative half-reaction, regeneration of the oxidized FAD by molecular oxygen yields hydrogen peroxide.

According to the structural fold, flavoenzymes have been classified into many superfamilies [4]. Interestingly, folding topology does not correlate with enzyme function. For example, GOOX and *Brevibacterium sterolicum* cholesterol oxidase 2 (BsCOX2) belong to the *p*-cresol methylhydroxylase (PCMH) superfamily, whereas glucose oxidase,

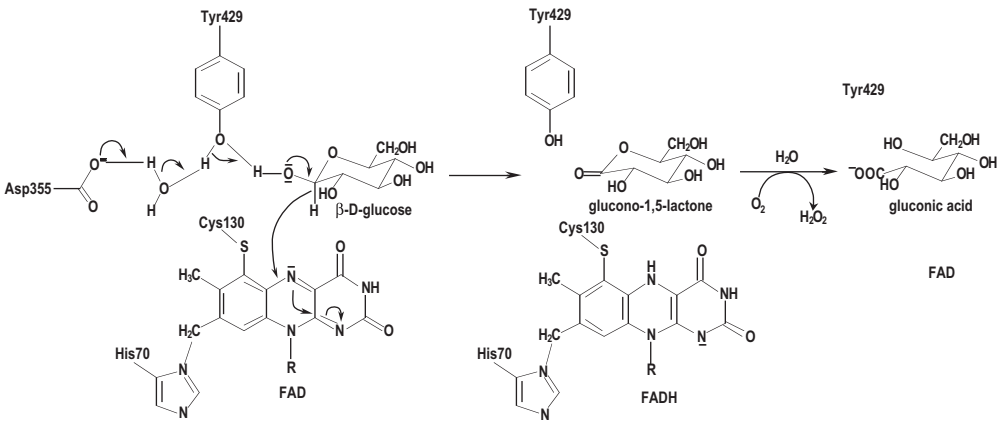

Fig. 1. The proposed catalytic mechanism for GOOX.

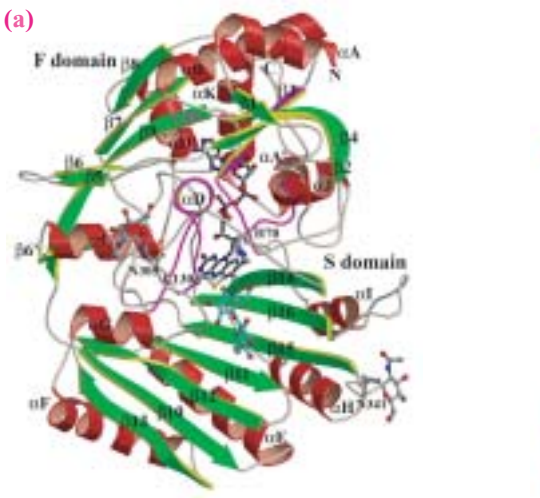

Fig. 2. (a) The GOOX structure. The protein consists of a FAD-binding (F) and a substrate-binding (S) domain, colored in *red* (helix) and *green* (strand). The intermediate analogue ABL (*cyan*), the cofactor FAD (*black*) and the linking residues His70 and Cys130, and the glycosylated Asn305 and Asn341 are displayed as *ball-and-stick* representations. The two major FAD-interacting segments are highlighted in *magenta*. **(b)** The 2Fo - Fc electron density map for the FAD cofactor and the covalently bound His70 and Cys130 contoured at 2σ level. The density map demonstrates the first known double attachment flavinylation, 6-*S*-cysteinyl, 8α-*N*1-histidyl FAD.

cellobiose dehydrogenase and BsCOX1 belong to the glutathione reductase (GR) superfamily. Location of the active center at the *re* face of the isoalloxazine ring is generally conserved within the GR superfamily, whereas that of the PCMH members is on the *si* side. Therefore, these structures provide elegant examples of convergent evolution, where starting from different ancestral folds, the same FAD-assisted glucose (or cholesterol) oxidation is achieved through opposite flavin faces within distinct substrate-binding sites. Even starting from a similar structural fold, the sugar oxidases have evolved a similar FAD-assisted oxidation mechanism but different substrate recognition, resulting in distinct binding affinities to the mono- and di-sacchardes, with *Km* values ranging from 50 μM to 30 mM.

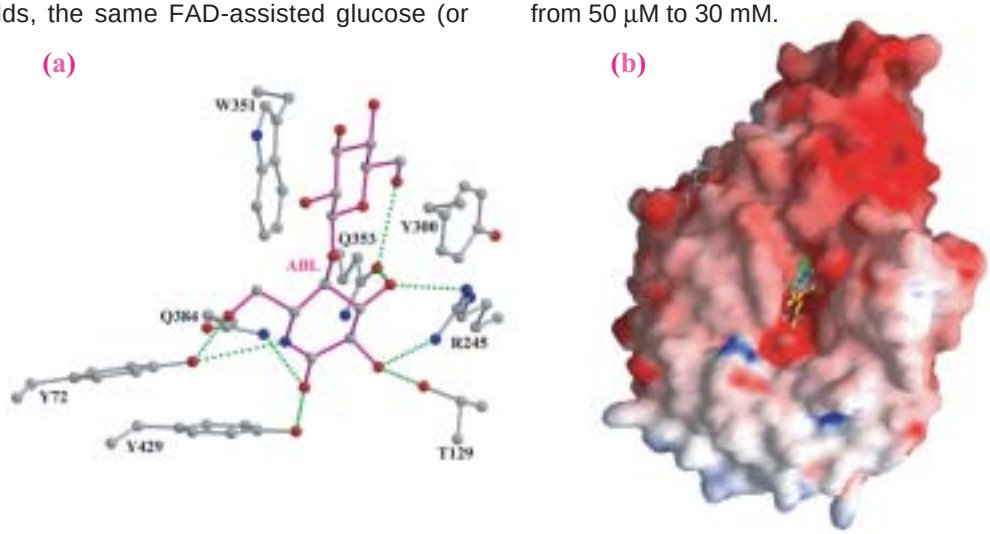

Fig. 3. **(a)** The interaction networks between ABL and GOOX. Hydrogen bonds are shown as green dashed lines. **(b)** Molecular surfaces of GOOX. The protein surface is colored for electrostatic potential from -20 k_BT (*red*) to 20 k_BT (*blue*), reflecting its pI value of 4.3-4.5. The FAD cofactor is colored in *green*, while the modeled cellobiose is in *yellow*. The open carbohydrate-binding groove explains why oligosaccharides are good substrates.

Shwu-Huey Liaw

The Structural Biology Program,
National Yang-Ming University, Taiwan

E-mail: shliaw@ym.edu.tw

References

[1] M.H. Lee *et al.*: Appl. Environ. Microbiol. **71** (2005) 8881.
[2] *C.-H. Huang, W.-L. Lai, M.-H. Lee, C.-J. Chen, A. Vasella, Y.-C. Tsai and S.-H. Liaw: J. Biol. Chem.* ***280*** *(2005) 38831.*
[3] M. Mewies *et al.*: Protein Sci. **7** (1998) 7.
[4] O. Dym & D. Eisenberg: Protein Sci. **10** (2001) 1712.

Crystal Structure of Acyl-coa Thioesterase PaaI showing 'Half-of-the-sites Reactivity'

Many proteins undergo structural changes in response to an external stimulus, and the structural changes, in turn, allow proteins to demonstrate their specific functions. The structural changes observed in crystallography and other methods are not necessarily large in scale; therefore, only proteins that undergo obvious structural changes have been the subject of research. How to analyze the subtle and complex structural changes of proteins is still one of basic propositions in structural biology. Here, such small conformational changes in an oligomeric enzyme called acyl-CoA thioesterase PaaI have been captured by applying a novel analysis method, and the oligomerization-function relationship of this protein has been explained successfully [1].

The PaaI protein is an enzyme known to be associated with the degradation of biodegradable plastics, and functions in association as a tetrameric oligomer composed of four identical subunits. To elucidate the oligomerization-function relationship of this oligomeric protein, several crystal structures of PaaI with and without coenzyme A ligands were determined on the basis of X-ray diffraction data collected at the RIKEN Structural Biology beamlines **BL44B2** and **BL45XU**. Interestingly, only two of four intersubunit active sites of the PaaI tetramer were found to be occupied by the ligands, which is a phenomenon so-called 'half-of-the-sites reactivity' (Fig. 1). This half-of-the-sites reactivity is a seemingly wasteful phenomenon observed in oligomeric enzymes where only one-half of several active parts are used, which was so far hypothesized 35 years ago [2]. Presently determined PaaI structures provide the first direct proof of half-of-the-sites reactivity in general enzymes.

To elucidate the structural basis of half-of-the-sites reactivity, a detailed structural comparison between several liganded and unliganded PaaI structures was tried. For this purpose, a novel analysis method referred to as the 'multiple superposition method' has been developed. In the multiple superposition method, the unliganded and liganded structures are precisely compared by multiple superpositions of corresponding protein atoms, where the conformational change is decomposed into following two elements: an overall rearrangement of the subunit referred to as a rigid-body shift and an intrasubunit local deformation referred to as a local shift. Applying this method allowed us to show that a subtle rigid-body rearrangement of subunits within 2º upon binding

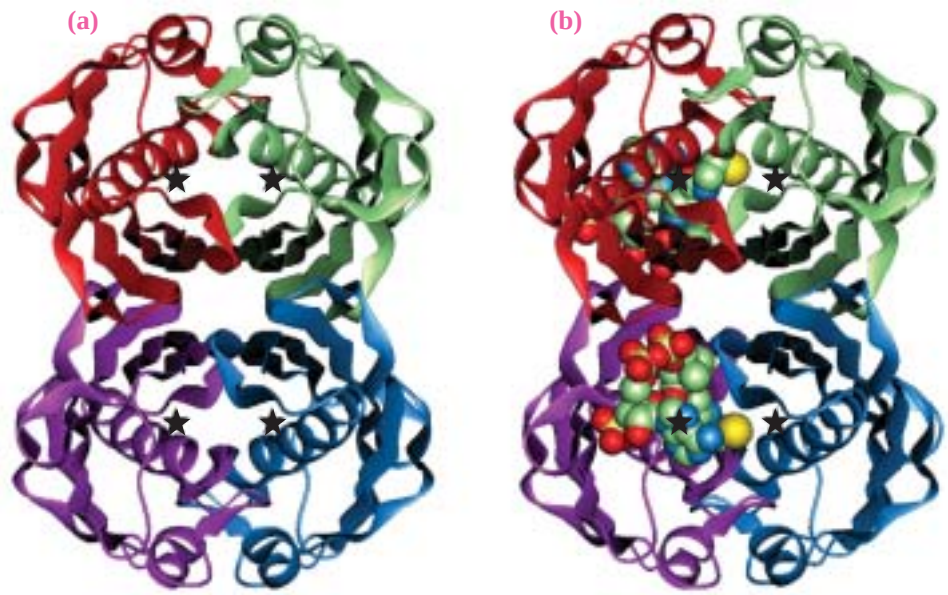

Fig. 1. Crystal structures of acyl-CoA thioesterase PaaI in **(a)** unliganded form and **(b)** coenzyme A liganded form, showing 'half-of-the-sites reactivity' of oligomeric enzyme. Four different subunits of the PaaI tetramer are distinguished by color-coding. The ligand coenzyme A molecules are depicted as space-filling models. Of four active sites indicated by asterisks, only two sites can bind ligands. Note that the structural change upon ligand binding is not obvious.

of the first two ligand molecules cooperatively induces a structural change in remaining two active sites, which may be unfavorable for further binding of ligands (Fig. 2).

Although the biological significance of half-of-the-sites reactivity has been unknown to date, the present work successfully suggests it for the first time. The molecular size of acyl-CoA, which is the substrate of PaaI, is relatively large as that of a biological ligand. The tetrameric PaaI molecule effectively accommodates the large ligand utilizing its asymmetric rigid-body rearrangement of subunits, thereby resulting in the half-of-the-sites reactivity. Therefore, the effective recognition of acyl-CoA at the first two active sites might be of advantage for PaaI even if the demerit of losing activity at remaining two is taken into account.

On the other hand, the activity regulation of this type of oligomeric enzyme through the binding of another ligand as a modulator at remaining sites may also be a pivotal role of half-of-the-sites reactivity. Human thioesterase III (hTEIII) is known as a homologue of PaaI. It was reported that hTEIII is activated by the infection of HIV that causes AIDS [3]. Therefore, the elucidation of the hTEIII activation mechanism may be useful for the structure-based drug design of AIDS therapy. Although the crystal structure of hTEIII is still unknown, half-of-the-sites reactivity can be suggested as a principle for activity regulation. In conclusion, the biological role of half-of-the-sites reactivity presented here may be one of the fundamental catalytic strategies of oligomeric enzymes.

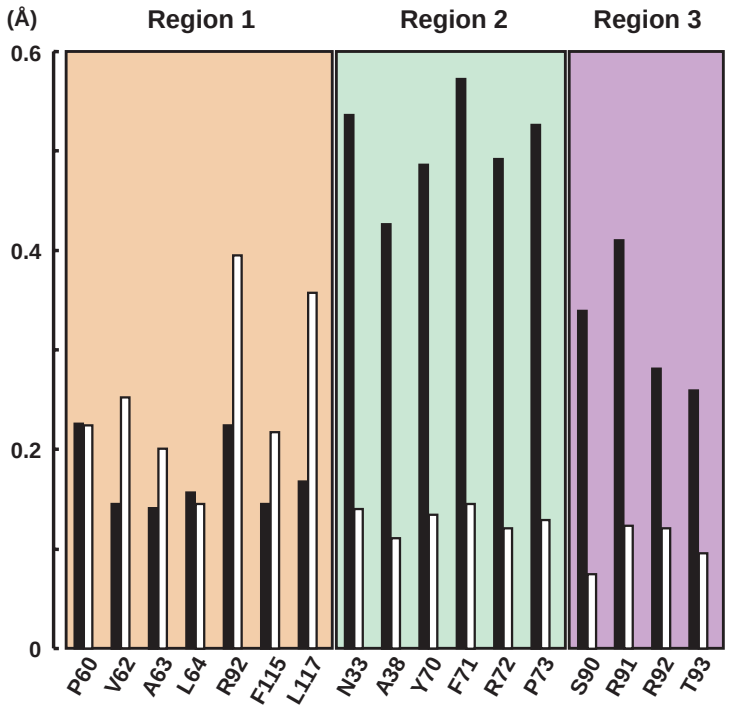

Fig. 2. Subtle structural changes of ligand recognition atoms in PaaI captured by the multiple superposition method. Rigid-body shifts of recognition atoms upon ligand binding are calculated and averaged by residue. In the PaaI tetramer, the ligand coenzyme A molecule is recognized by regions 1, 2 and 3, which are distinguished by different colors. The rigid-body shifts at occupied and vacant active sites are separately shown as closed and open bars, respectively. Different and complementary patterns of rigid-body structural changes are observed between the occupied and vacant sites, indicating a cooperativity upon ligand binding.

Naoki Kunishima

SPring-8 / RIKEN

E-mail: kunisima@spring8.or.jp

References

[1] *N. Kunishima, Y. Asada, Ma. Sugahara, J. Ishijima, Y. Nodake, Mitsu. Sugahara, M. Miyano, S. Kuramitsu, S. Yokoyama and Michi. Sugahara: J. Mol. Biol.* ***352*** *(2005) 212.*
[2] A. Levitzki *et al.*: Biochemistry **10** (1971) 3371.
[3] H. Watanabe *et al.*: Biochem. Biophys. Res. Commun. **238** (1997) 234.

Structural Analysis of Cell Membrane Complex of Hair Fiber by Micro X-ray Beam

A mammalian hair fiber consists of the medulla, cortex and cuticle from the center to the outside in this order [1]. The major mass of hair fiber is located in the cortical region, which mainly consists of keratin filaments and matrix proteins. On the outside of the cortical region, there is cuticle which has about 5 μm in thickness and consists of about 10 keratinized sheet-like-cells. There are pathways for water molecules through the cuticle into the central cortex, one of which is the cell membrane complex (CMC) in the cuticle (Fig. 1). Recently, on the cuticle surface, covalently bound lipids mainly consisting of 18-methyleicosanoic acid have been found, which contribute to the hair surface property. Therefore, it is important to obtain detailed structures of the cortex and cuticle including water molecules to understand the penetration of water. However, since the cuticle is too thin and scatters X-rays only weakly, small-angle X-ray diffraction (SAXD) had been less applicable to the cuticle than the cortex. On the basis of a pioneering SAXD experiment using a micro X-ray beam [2], we have recently developed a SAXD technique to characterize CMC and cortex structures in a mammalian hair [3].

We performed SAXD experiments using a micro-beam at beamline **BL40XU**. A high-flux X-ray beam (λ = 0.083 nm, wavelength) from a helical undulator was focused with two mirrors. In the experimental hutch, an X-ray beam of 5 μm in diameter was obtained behind two pinholes, the first 5 μm and the second 100 μm in diameter. The sample-to-detector distance was about 2.4 m. The reciprocal spacing S (= $1/d = (2/\lambda)\sin(2\theta/2)$, 2θ is the scattering angle and d is the repeat distance) was calibrated by the spacing of standard materials at room temperature.

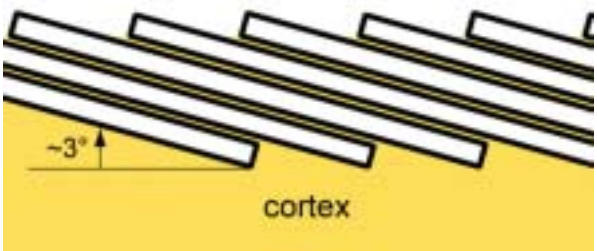

Fig. 1. Schematic cross section of mammalian hair cuticle on cortex.

From the SAXD profile of CMC (Fig. 2(a)), the equator of CMC is tilted by about 3º with respect to the equatorial direction of the fiber axis, in accordance with the structural evidence from an electron microscopic observation. Figure 2(b) is similar to the SAXD profile of the bundle of mammalian fibers. Thus, the present experiment provides structural information on CMC without interference from other structures.

CMC in the cuticle of a mammalian hair fiber is composed of three layers, which are the β, δ and β layers. It has been assumed that the electron density profile of CMC can be expressed by box-type wells. The δ and β layers are composed of proteins with flexible shapes and lipid molecules of various hydrocarbon-chain lengths, respectively. When we take into account the variation of thickness in the δ and β layers, overall features of the SAXD profile (Fig. 3) can be explained satisfactorily [3].

We focused our attention on an influence of humidity on the cortex and cuticle structures in a rat whisker. A rat whisker sample was incubated at a relative humidity (RH) between 3% and 100% which was controlled by a humidity generator (Model HUM-1, Rigaku).

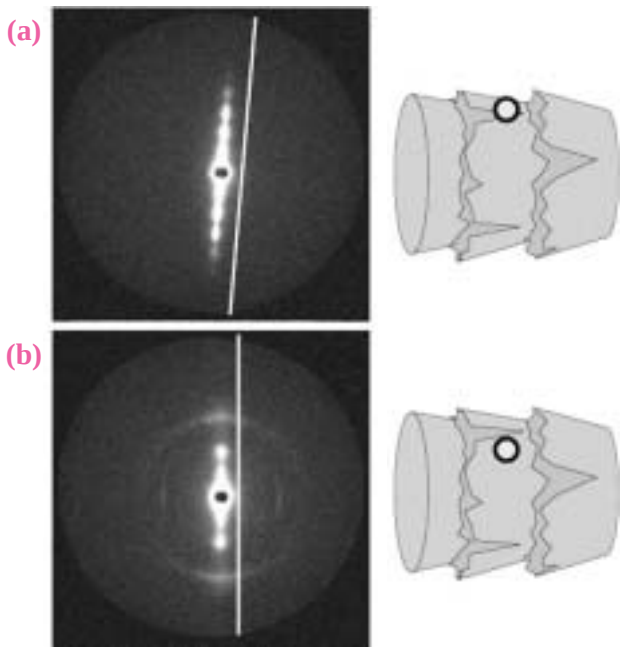

Fig. 2. SAXD patterns (left), and schematic drawing (right) of rat whisker using micro-beam X-ray, which is denoted by a circle. **(a)** cuticle, **(b)** cortex.

Whisker diameter was estimated from the distance between points on two sides of a rat whisker where the maximum intensity from the cuticle was observed. The diameter normalized by that at 3% RH is shown in Fig. 4. In addition, the first peak position was obtained in the cortex region from SAXD patterns using a micro X-ray beam. Similarly, the peak positions were normalized by that at 3% RH, which are shown in Fig. 4. It is clear that the normalized diameter corresponds to the normalized peak position over a wide humidity range. Thus, the whisker diameter is mainly characterized by the cortex structure.

CMC thickness was estimated on the basis of a CMC structural model to fit X-ray diffraction profiles of cuticle. The normalized thickness is shown in Fig. 4. As the present results indicate, the swelling property clearly differs between normalized CMC thickness and whisker diameter. CMC thickness gradually increased below 80% RH, whereas it markedly increased over the normalized whisker diameter above 80% RH. These results suggest that free water molecules penetrate into the cortex and cuticle in different manners.

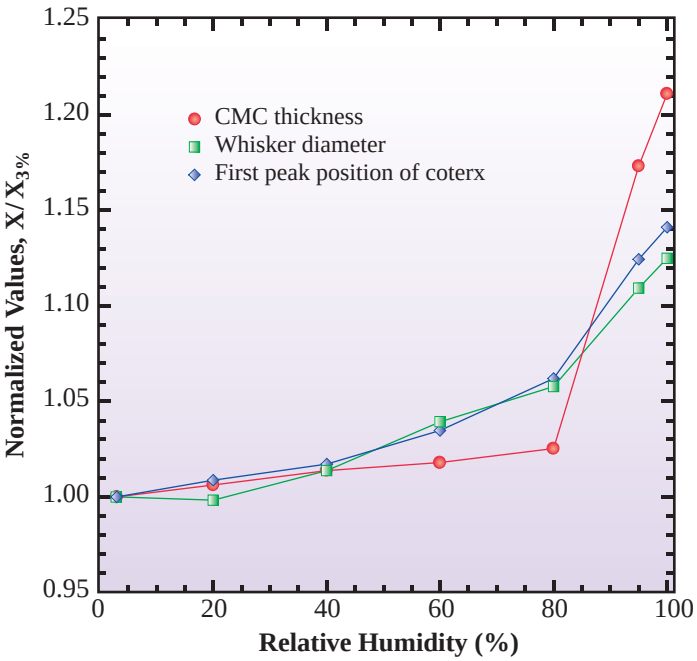

Fig. 4. CMC thickness (circle), whisker diameter (square) and first peak position of cortex (diamond), which are normalized by the value at 3% RH.

Thus, in SAXD studies using a micro-beam on the pathways of water, a rat whisker will be a promising sample for a detailed structure analysis. For cosmetic applications, we believe that our method will be useful for studying the influence of shampoo, rinse or permanent solution on the thickness of CMC, and the β and δ layers of the mammalian hair cuticle.

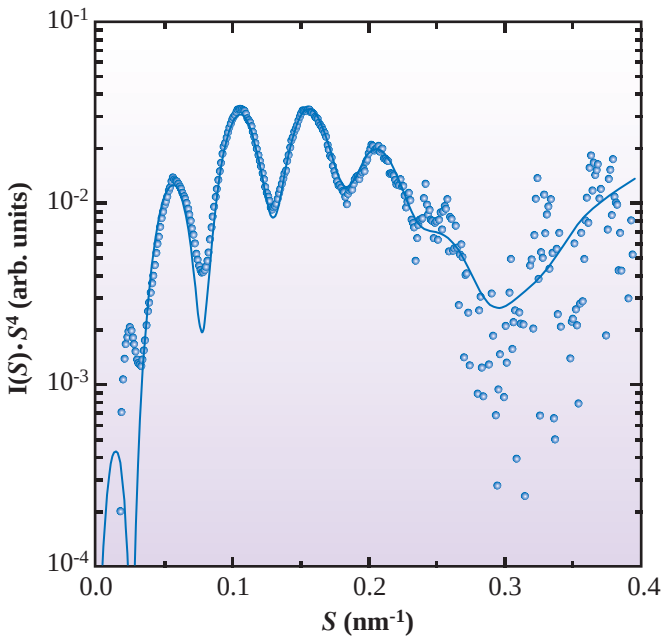

Fig. 3. SAXD profile of rat whisker and fitting result.

Noboru Ohta[a,*], Naoto Yagi[a] and Ichiro Hatta[b]

[a] SPring-8 / JASRI
[b] Department of Nuclear Engineering, Fukui University of Technology

*E-mail: noboru_o@spring8.or.jp

References

[1] C.R. Robbins: Chemical and Physical Behavior of Human Hair, 4th ed., (2001) New York, Springer.
[2] L. Kreplak *et al.*: Biochim. Biophys. Acta **1547** (2001) 268.
[3] *N. Ohta, T. Oka, K. Inoue, N. Yagi, S. Kato and I. Hatta: J. Appl. Cryst.* ***38*** *(2005) 274.*

Life Science
Medical Biology

In this brief review of achievements in "Life Science" obtained in SPring-8, I chose four research works among others because of their unique applications, i.e., (i) X-ray fluorescence microscopy for cellular mineral analysis, (ii) phase contrast X-ray imaging of fetal lungs, (iii) synchrotron radiation CT for the analysis of small-airway deformation and (iv) X-ray diffraction recording from a single sarcomere.

Ishizaka *et al.* utilized scanning X-ray fluorescence microscopy (SXFM) to detect minerals at the cellular level. They visualized platinum (Pt) with other elements in mammalian cells after treatment with an anticancer agent, *cis*-diamminedichloro platinum (II) (CDDP). They composed PC-9 cells (originally derived from a lung carcinoma) sensitive (PC/SEN) and resistive (PC/RES) to CDDP. Twelve hours after CDDP treatment, the level of Pt increased in PC/SEN cells, but it changed little in PC/RES cells, indicating that an enhanced accumulation of CDDP in the cells is responsible for the hypersensitivity of PC/SEN cells. They also found that the Zn level is high in untreated PC/RES cells with elevated intracellular glutathione level. They concluded that this method is useful for the better understanding of cancer biology.

Hooper *et al.* applied phase contrast X-ray imaging (PCXI) to evaluate the pattern of lung aeration of rabbit pups at birth. Lung images were analyzed before a breath or at fixed time intervals after birth. They found that PCXI was able to resolve terminal respiratory units, and air-filled structures gave them "speckle" appearances. The pattern of lung aeration was very dependent upon body position and was heavily influenced by respiratory activity. The increase in air volume can be calculated from the projected thickness of the lung image.

Sera *et al.* determined the localized morphometric deformation of small airways and alveoli using a synchrotron radiation CT system. Euthanized mice were mounted on the rotation stage of the CT system under quasi-static inflation to mimic respiration. They visualized the same airways of the same lung at functional residual capacity (FRC) and total lung capacity (TLC). The length (L) and diameter (D) of airway segments were measured, and the increases in L and D, i.e., ΔL and ΔD were normalized by FRC. Results showed that ΔD was larger than ΔL and both values were greater for a smaller-airway group. Thus, airways may deform differently depending on their size and tissue anisotropism.

Iwamoto *et al.* developed a technique of quick-freezing specimens of myofibrils isolated from an insect flight muscle. X-ray diffraction using microbeams was carried out to analyze the local structure. The strongest equatorial reflections (1.0 and 2.0) were observed. However, the 1.1 reflection was missing in the diffraction pattern of a myofibril, unlike in that of muscle. Because the beam diameter was ~2 μm, i.e., smaller than that of a single sarcomere, the diffraction should come from a single sarcomere within a single myofibril.

In summary, X-ray fluorescence microscopy, phase contact X-ray imaging, synchrotron radiation CT and X-ray diffraction method offer powerful tools for micro- or nano-order biological analysis.

Fumihiko Kajiya

Kawasaki Medical School
Okayama University

Element Array Analysis by Scanning X-ray Fluorescence Microscopy After *Cis*-diamminedichloro-platinum (II) Treatment

Minerals are essential for many cellular functions, and iron, magnesium, cobalt, and manganese are well characterized with respect to their roles in enzymatic catalysis. Zinc (Zn) is also a requirement for cell growth and survival, and essential for the activity of zinc-metalloenzymes that participate in cell metabolism. To clarify the biological roles of these ions it is important to characterize elements in individual cells. Highly coherent X-rays from third-generation synchrotron sources are opening up various new possibilities of nano-imaging for application in cellular biology. Although recently developed scanning X-ray fluorescence microscopy (SXFM) enable the detection of elements at cellular the level [1,2], higher resolution is still expected for imaging intracellular elements. Yamauchi *et al.* have developed a Kirkpatric-Baez (K-B)-type X-ray focusing system [3] in which, using the 1 km beamline of SPring-8, elliptically figured mirrors focus coherent X-rays to various spot sizes selectively on the demand of spatial resolution, sensitivity and time. As the first application of this method, we visualized platinum (Pt) alongside other cellular elements in mammalian cells after treatment with *cis*-diamminedichloro platinum (II) (CDDP) [4].

CDDP is an effective anti-cancer agent, but tumor cells can become resistant after CDDP-based therapy [5]. We measured intracellular elements by SXFM before and after treatment with CDDP and compared the element profiles of PC-9 cells (PC/SEN) which are originally derived from a lung carcinoma and PC-9 sublines resistant to CDDP (PC/RES). SXFM was set up at the undulator beamline **BL29XU** by combining the K-B-type X-ray focusing system [3], an xy-scanning stage for sample mounting, and an energy-dispersive X-ray detector. Monochromatic X-rays at 15 keV for Pt *L*-line excitation were focused into a 1.5 μm (H) × 0.75μm (W) spot with a measured flux of ~1 $\times 10^{11}$ photons/s. The focused X-rays simultaneously yielded the fluorescence of various chemical species in a small volume of sample cells (Fig. 1(a)). After counts were collected for 4.0-8.5 sec at each pixel of scanning, the counts were normalized with incident beam intensity. Elemental concentration per cell was also calculated from integrated elemental intensity over the entire mapping image.

Twelve hours after treatment with CDDP, the level of Pt increased in PC/SEN cells, whereas a slight increase in Pt level was observed in PC/RES cells (Fig. 1(b)). The signal intensity of Pt in PC/RES cells was 2.6-fold less than that in PC/SEN cells [4]. The

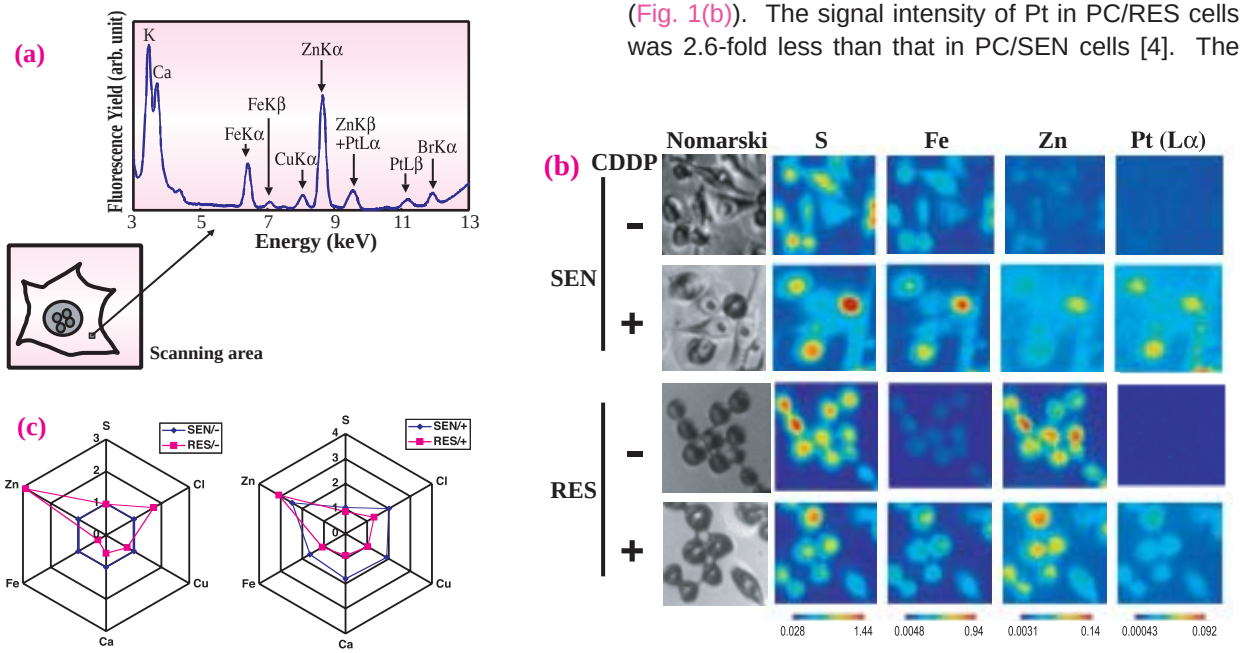

Fig. 1. Element array analysis. **(a)** Scheme of imaging cellular elements by SXFM. **(b)** SXFM analysis of original PC-9 cells (SEN) and subline cells (RES) resistant to CDDP after CDDP treatment (+) and under CDDP free condition (−). Brighter colors indicate a higher signal intensity of each element. **(c)** Element array based on SXFM analysis.

decreased accumulation of CDDP is therefore likely responsible for resistance in PC/RES cells, which is consistent with the finding that the excretion of CDDP may be one of the major factors contributing to CDDP resistance [5]. On the base of the mean signal intensity obtained by SXFM, element array analysis was carried out (Fig. 1(c)). We noted that the Zn content of untreated PC/RES cells was approximately 3-fold that of PC/SEN cells (Fig. 1(c), left panel). When CDDP was used for treatment, the high content of Zn was observed most markedly in both cell lines (Fig. 1(c), right panel).

We next focused on a zinc-related excretion system to clarify the role of Zn in a mechanism underlying resistance to CDDP. We found that the level of intracellular glutathione (GSH) was constitutively high in PC/RES cells (Fig. 2(a)), showing a significant correlation with the levels of Zn detected by both ICP-MS and SXFM (Pearson product-moment correlation coefficient r: 0.794, $P < 0.05$ and r: 0.533, $P < 0.05$, respectively) (Fig. 2(b)). Consistent with these observations, a Zn (II) chelator, N,N,N',N'-tetrakis-(2-pyridylmethl)-ethylenediamine (TPEN), decreased both cellular Zn and GSH level in PC/RES cells [4], making PC/RES cells sensitive to CDDP (Fig. 3).

In the current study, we demonstrated the use of element array analysis by SXFM for examining a mechanism of CDDP resistance. We propose that element array analysis is a powerful tool contributing to a better understanding of cancer biology as well as other fields of medical science. We expect that researchers in various life science fields would join in this promising project.

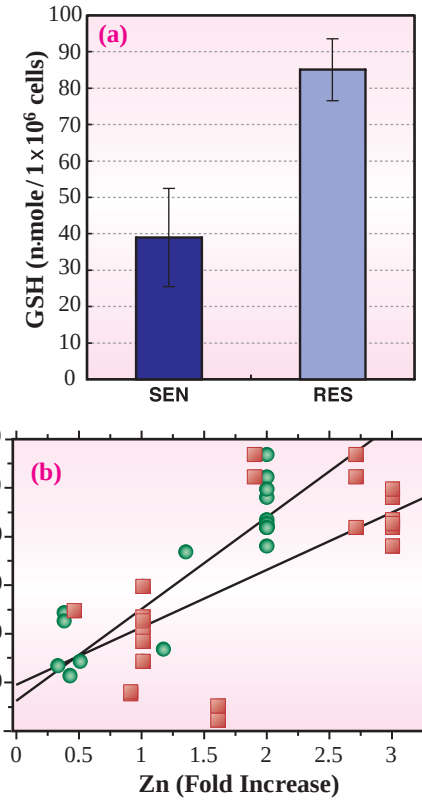

Fig. 2. **(a)** Basal level of intracellular GSH. **(b)** Correlation between Zn and intracellular GSH levels. A scatter diagram for Pearson product-moment correlation coefficient is shown. Zn level, measured by SXFM (red squares, $n = 27$) and ICP-MS (green circles, $n = 29$), was plotted against intracellular GSH level.

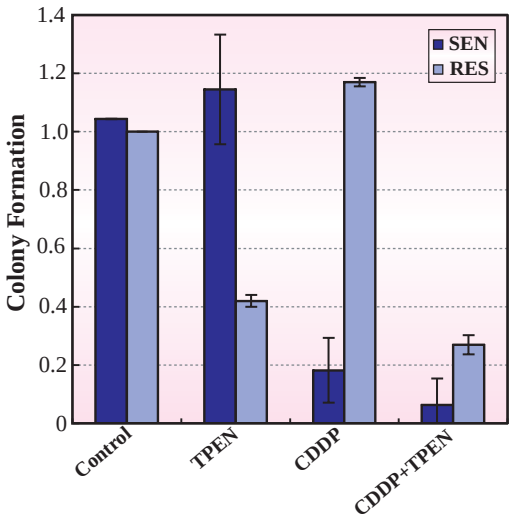

Fig. 3. Colony formation after treatment with CDDP and/or TPEN (Zn (II) chelator), which shows the effectiveness of the treatments to the cell viability. Control shows the result for treatment-free cells for comparison. Cells entitled by TPEN or CDDP + TPEN were pulse-treated for 2 h with TPEN for 5 consecutive days. The ability for colony formation, the aggregation of more than 50 cells arising from a single surviving cell, was examined.

Mari Shimura[a], Akira Saito[b] and Yukihito Ishizaka[a,*]

[a] Department of Intractable Diseases, International Medical Center of Japan
[b] Department of Material and Life Science, Osaka University

*E-mail: zakay@ri.imcj.go.jp

References

[1] P. Ilinski *et al.*: Cancer Res. **63** (2003) 1776.
[2] M.D. Hall *et al.*: J. Biol. Inorg. Chem. **8** (2003) 726.
[3]K. Yamauchi *et al.*: J. Appl. Phys. **42** (2003) 7129.
[4] *M. Shimura, A. Saito, S. Mastuyama, T. Sakuma, Y. Terui, K. Ueno, H. Yumoto, K. Yamauchi, K. Yanamura, H. Mimura, Y. Sano, M. Yabashi, K. Tsmasaku, K. Nishio, Y. Nishino, K. Endo, K. Hatake, Y. Mori, Y. Ishizaka and T. Ishikawa: Cancer Res.* ***65*** *(2005) 4998.*
[5] K. Zhang *et al.*: Mol. Pharmacology. **59** (2001) 837.

Measuring the Rate and Pattern of Lung Aeration at Birth

Survival at birth is critically dependent upon the ability of the lung to initiate air-breathing and take over the role of gas exchange. Before birth, the future airways of the lungs are liquid-filled and gas-exchange occurs across the placenta, whereas at birth the lungs must be cleared of liquid to allow the entry of air and the onset of gaseous ventilation [1]. However, a thin film of liquid remains to protect the inner surface of the lung from desiccation, leading to the formation of an air/liquid interface and the creation of surface tension within the lung for the first time. As a result the process of lung aeration markedly alters the distribution of force within lung tissue which initiates many changes in lung physiology allowing it to become the sole organ of gas exchange [2]. For instance, lung aeration and the onset of pulmonary ventilation is closely associated with a dramatic increase pulmonary blood flow (PBF) at birth and closure of vascular shunts that allow blood to by-pass the lungs during fetal life [2]. Thus, at birth, lung physiology markedly changes in order for it to assume the role gas-exchange and, therefore, it is not surprising that respiratory failure at birth is the greatest cause of morbidity and mortality in newborn infants [3].

Despite the fundamental importance of lung aeration to survival at birth, little is known about it because until recently, lung aeration could not be measured. As a result, the factors that determine the rate and pattern of lung aeration are unknown, although this information is particularly important for the resuscitation and ventilation of infants that are born preterm, as these infants often suffer from air way liquid retention. The application of phase contrast X-ray imaging has enabled us to observe and measure the rate and pattern of lung aeration at birth. Phase contrast X-ray imaging utilizes refractive index variations (phase information) in addition to conventional absorption information to greatly improve image contrast of the lung [4,5]. The air-filled lung is unique in that it is predominantly comprised of air (~80% by volume), surrounded by thin tissue structures (predominantly water), providing a marked transition in refractive index between airways and surrounding tissue structures. When X-rays pass through weakly absorbing tissues such as the lung, phase shifts are induced by the refractive index changes between air and tissue, causing a change in the direction of propagation which can be rendered visible by several methods [4]. The most simple is propagation based phase contrast imaging (PBPCI) where a gap between the object and detector allows the phase shifted wavefronts to interfere with adjacent waves producing strong edge enhancement [4]. Air-tissue interfaces contrast strongly using this technique (Fig. 2), making the air-filled structures of the lung visible [5]. As the fetal lung is liquid-filled it is not visible using phase contrast X-ray imaging, but rapidly becomes visible as the lung aerates after birth.

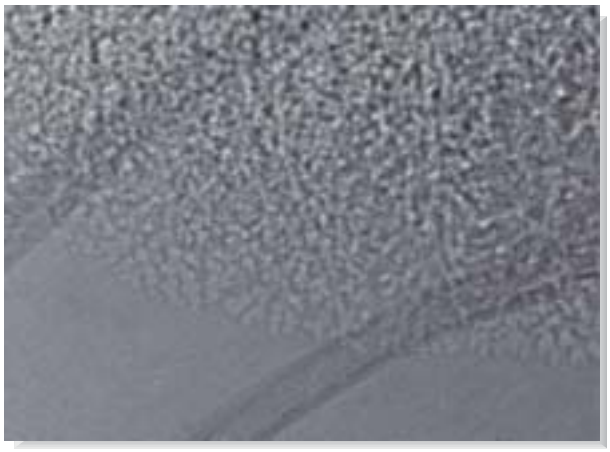

Fig. 1. Enlarged image of the peripheral margin of the lung from a newborn rabbit pup at 1 hr after birth; basal lobe of the right lung. Note that the small, terminal respiratory units are clearly visible.

Rabbit pups were delivered by Caesarian Section and were imaged either before they had taken a breath or at fixed time intervals after birth; the time points included <1 min, 3 min, 5 min, 15 min, 30 min, 1h and 2h after birth. We found that phase contrast X-ray imaging was able resolve the terminal respiratory units at the outer margins of the lungs in extraordinary detail (Fig. 1); in more medial regions, overlying air-filled structures greatly increase the complexity of the image, giving it a “speckle” appearance. In separate pups, we collected multiple images at 1-10 sec intervals for ~30 minutes after birth and measured respiratory activity from birth using a plethysmograph (Fig. 2), providing detailed information on breathing patterns after birth. Figure 3 shows the time-related changes in lung aeration that can be demonstrated using this technique. Our observations demonstrate that the pattern of lung aeration is very

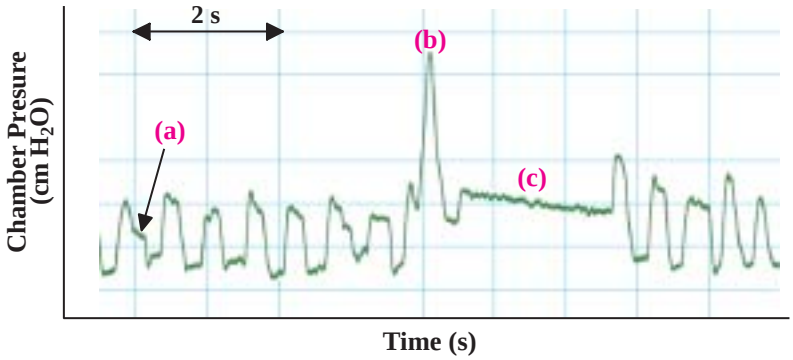

Fig. 2. Physiological recording of a newborn rabbit pup at 1 hour of age using a water-based plethysmograph. Note that expiratory braking **(a)**, deep inspiratory efforts **(b)** and breath holds **(c)** are a common feature of neonatal breathing. It is likely that significant lung aeration occurs in response to respiratory activities depicted, for example by **(b)**.

dependent upon body position and is heavily influenced by respiratory activity. Using suitable phase retrieval algorithms, we can calculate the projected thickness of the lungs from a single image allowing us to calculate the increase in air volume with time; plethysmograph recordings will be used to valid these calculations.

In conclusion, the techniques we have developed allows us to simultaneously measure respiratory activity while imaging lung aeration from birth. In future experiments we will determine the factors that determine the rate and pattern of lung aeration.

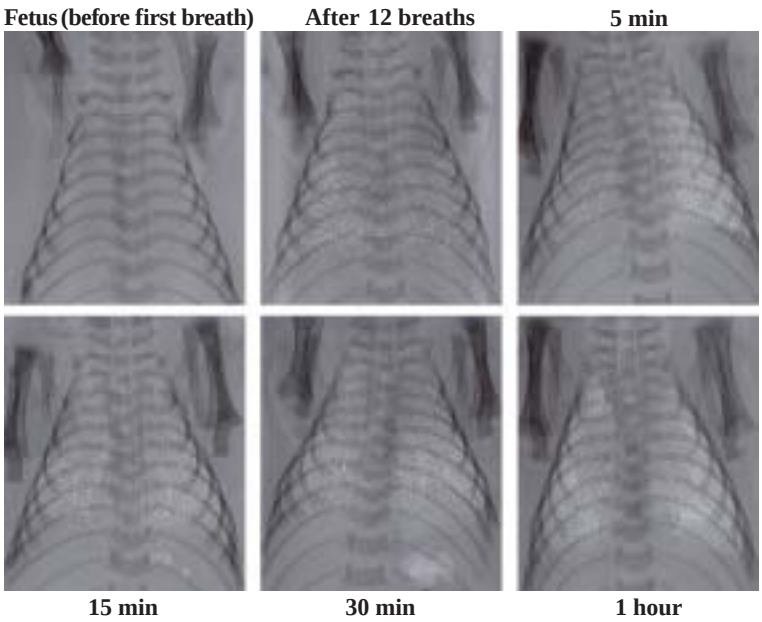

Fig. 3. Phase contrast X-ray images of rabbit pup lungs at selected times after birth.

Stuart B. Hooper [a,*], Robert Lewis[b] and Naoto Yagi[c]

[a] Department of Physiology, Monash University, Australia
[b] Centre for Synchrotron Science, Monash University, Australia
[c] SPring-8 / JASRI

*E-mail: Stuart.Hooper@med.monash.edu.au

References

[1] S.B. Hooper and R. Harding: Clin. Exp. Pharmacol. Physiol. **22** (1995) 235.
[2] *S.B. Hooper and R. Harding: Current Resp. Med. Rev.* ***1*** *(2005) 185.*
[3] R.H. Clark *et al.*: J. Pediatr. **139** (2001) 478.
[4] M.J. Kitchen *et al.*: Brit. J. Radiol. **78** (2005) 1018.
[5] *R.A. Lewis, N. Yagi, M.J. Kitchen, M.J. Morgan, D. Pagani, K.K.W. Siu, K. Pavlov, I. Williams, K. Uesugi, M.J. Wallace, C.J. Hall, J. Whitley and S.B. Hooper: Phys. Med. Biol.* ***50*** *(2005) 5031.*

Small Airway Deformation of Healthy Mice during Quasi-static Lung Inflation

Airway consists of a number of various compliant tubes from the trachea to alveoli, and the airway geometry deforms markedly during respiration. Respiratory diseases occur most frequently at small airways and alveoli, and the condition of small airways and alveoli has important physiological and clinical implications [1]. In many respiratory diseases, significant compliance abnormalities mainly occur in localized regions of bronchi and bronchioles, and thus localized or microscopic conditions of small airways must be identified by high resolution observations. Localized deformations reflect restricted regions in which small airways are embedded into the parenchyma and thorax (Fig. 1). In this study, to determine localized morphometric deformations (diameter (D) and length (L)) in microscopic regions of airways, such as small airways and alveoli, during respiration, we visualized the same airways of the same lung at functional residual capacity (FRC) and total lung capacity (TLC) during quasi-static inflation process [2].

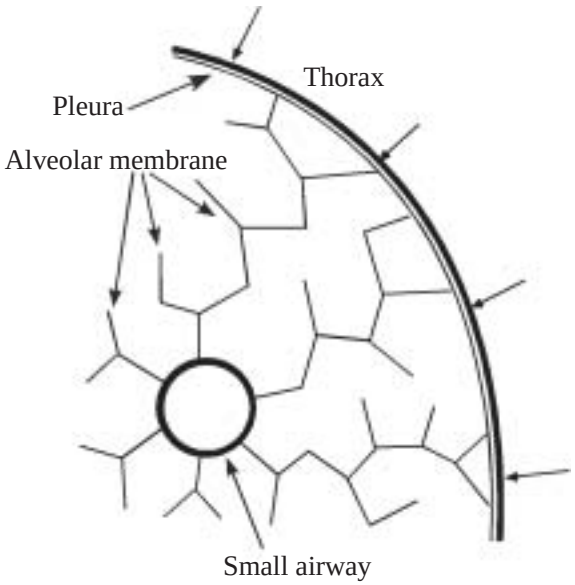

Fig. 1. Schematic model of small airways and alveoli in thorax.

The synchrotron radiation CT system was constructed at beamline **BL20B2**. The X-ray energy was 20 keV. To reconstruct CT images by the convolution back projection method, a series of projections were acquired at 1500 rotational positions around 180º in 7 ~ 15 min. The pixel size was 11.8 μm and the slice pitch was equal to the pixel size. A euthanized healthy mouse (C3H/HeJ, 9 weeks) was mounted on the rotation stage. To analyze the morphometric deformation of the same airway networks, the same branching networks were visualized at FRC and TLC during quasi-static inflation. FRC was defined as the lung volume at euthanasia, and lung volume could be externally regulated using a syringe connected to the trachea. The volume of TLC was defined as the sum of FRC + 800 μL [3]. We approximated the airway as a cylinder network, and the length (L) and diameter (D) of airway segments were determined by 3D thinning algorithm [2]. The fractions of increases in L and D (δ_L and δ_D) were normalized by FRC.

Figure 2 shows representative CT images and 3D volumes at FRC and TLC. At TLC, the airspace clearly increased and the airway geometry deformed markedly. δ_D and δ_L were presented as functions of the original diameter at FRC (Fig. 3). As the diameter at FRC decreased, δ_D increased. On the other hand, δ_L was not affected by the diameter at FRC. Then, the airway segments of all animals were classified into four groups using a diameter-based technique [4]: diameter ranges were FRC < 200 μm, 200 ~ 300 μm, 300 ~ 400 μm, and > 400 μm. δ_D and δ_L were 0.688 ± 0.026 and 0.295 ± 0.023 (average ± S.E.) for the smaller airways group (D at FRC < 200 μm), and 0.452 ± 0.017 and 0.229 ± 0.034 for the larger airways group (D at FRC > 400 μm), respectively. δ_D was larger than δ_L for all groups. Previously, Wang *et al.* [5] reported that the membrane was stiffer in the longitudinal than in the circumferential direction of the airway. To explain these differences, they histopathologically analyzed the morphometric structures of airway fibers and reported that the elastic fibers were mainly in the longitudinal direction, in agreement with the present results.

In conclusion, our study is the first to evaluate the localized morphometric deformation of small airways.

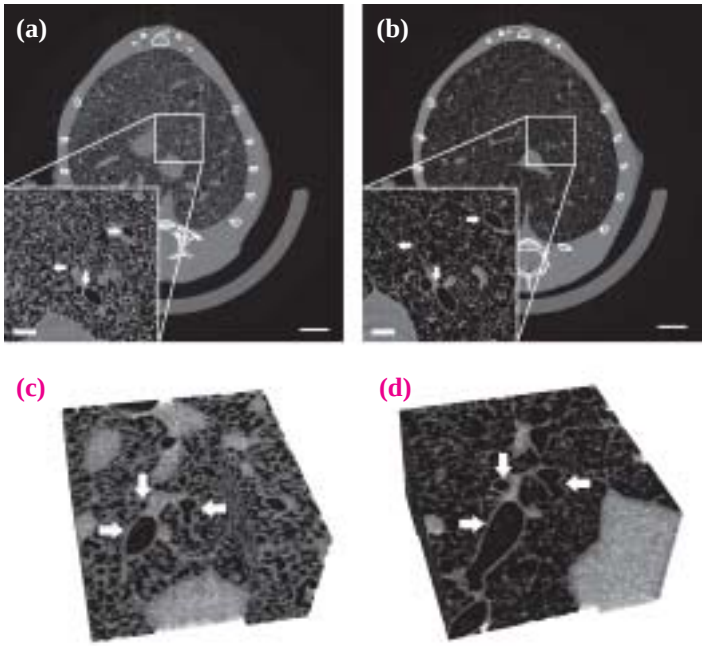

The airway diameter and the length of smaller airways (D < 200 μm) were respectively 68.8 % and 29.5 % larger at TLC than at FRC; in particular, the diameter was higher for smaller airways. Our results show that not all airways deform in the same manner.

Fig. 2. Representative CT images and 3D volumes at FRC (**a** and **c**) and TLC (**b** and **d**). Bars in normal images are 2 cm and those in zoomed images are 500 μm. Arrows with the same directions (**a** and **b**) and (**c** and **d**) indicate the same airways.

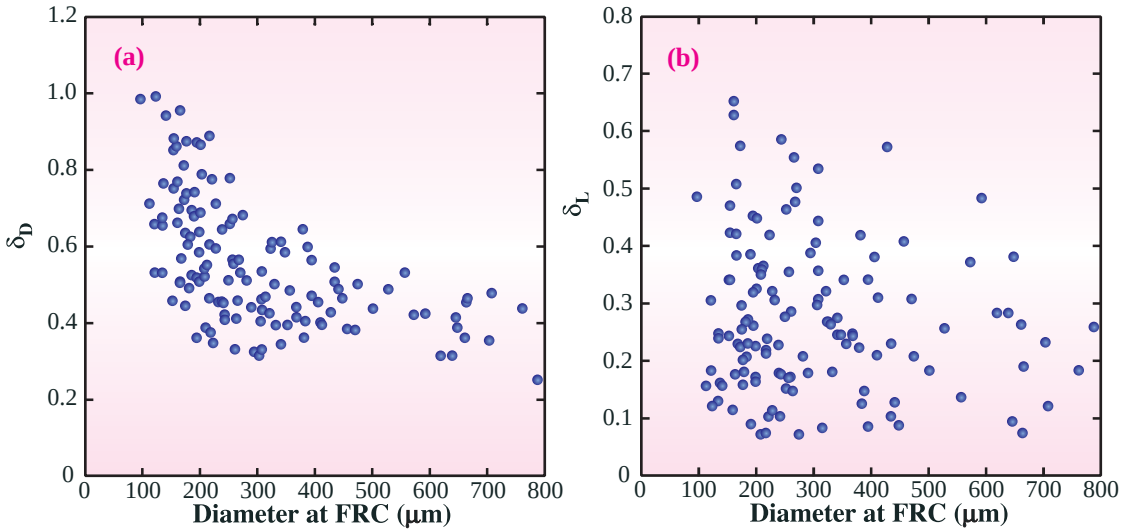

Fig. 3. Morphometric deformations ((**a**)δ_D and (**b**) δ_L) as functions of diameter at FRC.

Toshihiro Sera†

SPring-8 / JASRI

E-mail: sera@riken.jp

†Present address: Computational Biomechanics Unit, RIKEN, Wako

References

[1] P.T. Macklem: Am. J. Respir. Crit. Care Med. **157** (1998) S181.
[2] *T. Sera, K. Uesugi and N. Yagi: Resp Physiol. Neurobi.* ***147*** *(2005) 51.*
[3] H. Schulz *et al.*: Acta. Physiol. Scand. **174** (2002) 367.
[4] C.G. Phillips and S.R. Kaye: Respir. Physiol. **102** (1995) 303.
[5] L. Wang *et al.*: J. Appl. Physiol. **88** (2000) 1022.

X-ray Diffraction Recordings from Single Sarcomere within Isolated Myofibril

The third-generation synchrotron radiation sources can focus their intense X-ray beams (10^{13}~10^{15} photons/sec) in a small area of ~0.01 mm^2, and a practical level of X-ray intensity remains even after the beam diameter is decreased to a micrometer-size. Such very thin X-ray beams, or X-ray microbeams, now have a wide range of applications including diffraction, element analysis and X-ray microscopy.

X-ray diffraction using microbeams (microdiffraction) has been used for analyzing local structures of synthetic and biopolymers, and hard dried tissues such as hair and feather. This technique is also potentially applicable to hydrated biological specimens, and is expected to be particularly effective for analyzing minute structures inside living cells (organelles). The first example of microdiffraction recording from hydrated biological specimens is that from single myofibrils of insect flight muscle, revealing that the entire myofibril (diameter, ~3 μm; length, ~3 mm) has common crystal lattice planes and therefore can be regarded as a single giant protein crystal [1]. The estimated volume of the specimen in the beam was ~10,000 μm^3.

However, most organelles of interest are usually much smaller than this, requiring longer exposure times with increased risks of radiation damage; hydrated biological specimens are much more vulnerable to radiation damage than dry biopolymers. To overcome this problem, we have developed a technique of quick-freezing hydrated biological specimens and recording microdiffraction patterns while the specimens are kept frozen [2]. It is known that the radiation damage can be greatly reduced by lowering the temperature, and the fine structure of the specimens can be preserved if they are frozen properly.

Figure 2 shows a series of microdiffraction patterns recorded, at **BL40XU** beamline, from quick-frozen single myofibrils isolated from an insect flight muscle. The orientation of the incident microbeam was made perpendicular to the myofibrillar axis, and this configuration generates a number of “equatorial” reflections arising from the hexagonal array of myofilaments (Fig. 1). In Fig. 2, the strongest equatorial reflections (1,0 and 2,0 reflections) are observed.

The series of diffraction patterns shown in Fig. 2 were obtained by scanning the specimen with respect to the microbeam. From the change in the intensity of reflection, one can estimate the size of the diffracting object. Figure 3(a) shows the change in 1,0 reflection intensity as the specimen is scanned across its long axis. The analysis indicates that there are two objects next to each other, one diffracting more strongly than the other. After corrections for microbeam diameter, the diameter of both objects was estimated to be ~3 μm, i.e., the diameter of a myofibril.

Generally, only a limited number of reflections are observed at the same time in a diffraction pattern from a crystal. This is because of the “Bragg condition”, which requires that the incident beam make a specific angle with respect to a lattice plane to generate reflections. For example, when the condition is met for the 1,0 and 2,0 reflections, the 1,1 reflection should

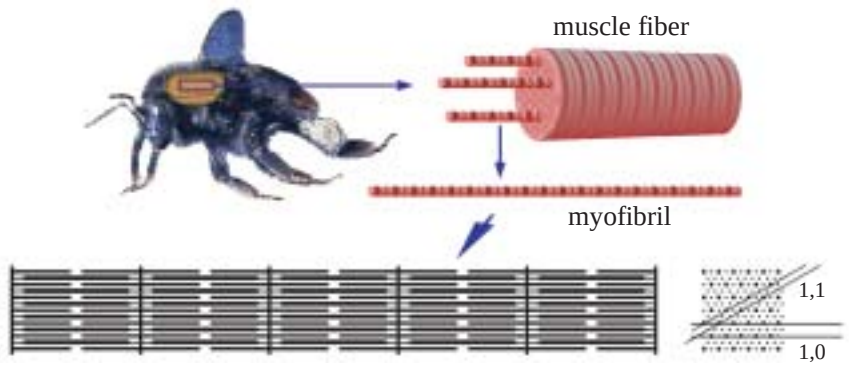

Fig. 1. Structure of myofibril from insect flight muscle, consisting of sarcomeres (minimal functional unit of muscle, ~3 mm in length) connected in series. In each sarcomere, the myofilaments are packed into a hexagonal array (lower right). Two lattice planes (1,0 and 1,1) are indicated.

not be observed. In the textbook diffraction patterns from muscle, however, the three reflections are always observed at the same time (dashed pale-green curve in Fig. 3(b)). This is because the specimen in usual settings (muscle cell or whole muscle) contains a large number of myofibrils with random lattice orientations. On the other hand, the 1,1 reflection is completely missing from the diffraction pattern from a myofibril (solid dark-green curve in Fig. 3(b)). This is what is expected for a single crystal, and therefore, another piece of evidence that the specimens were indeed single myofibrils.

Because the beam diameter was ~2 μm, i.e., shorter than a single sarcomere, it is considered that the diffraction patterns shown in Fig. 2 came from a single sarcomere within a single myofibril. The volume of specimen in the beam is estimated to be ~10 μm^3, i.e., 1/1,000 of the previous record [1]. This makes the similarly sized organelles realistic targets for structural analyses by X-ray microdiffraction.

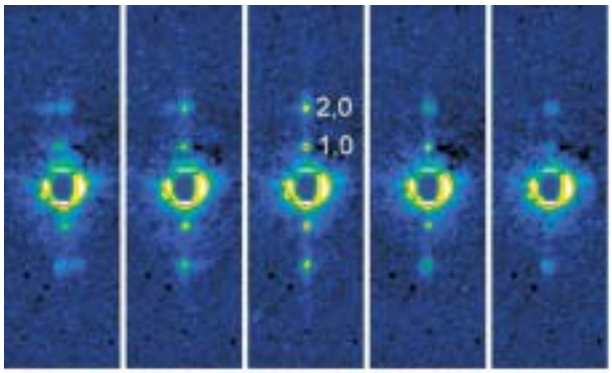

Fig. 2. Series of diffraction patterns from two quick-frozen single myofibrils (or single split myofibril) recorded by scanning the specimen by 0.87 μm steps.

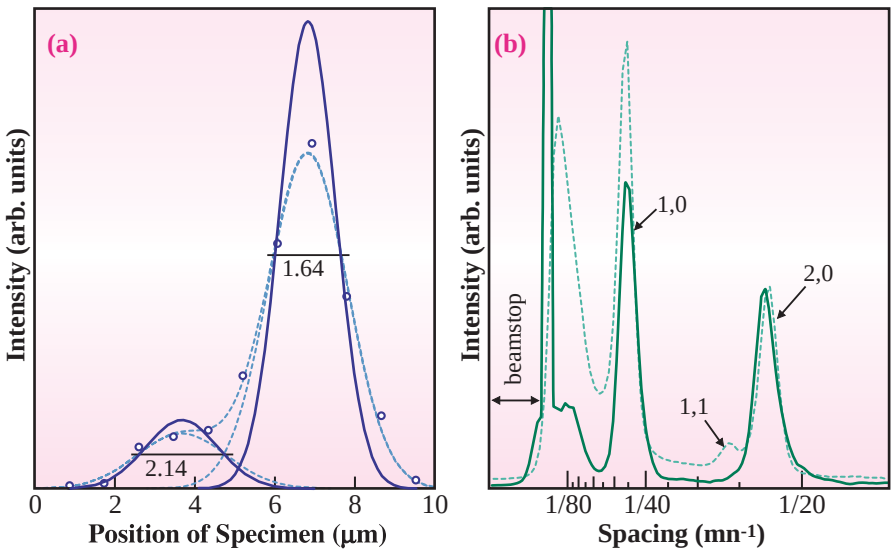

Fig. 3. **(a)** Intensity of 1,0 reflection as a function of the specimen position with respect to the beam. This provides information about the size of the specimen. The numbers indicate the full widths at half maximum of the two myofibrils. Dashed and solid curves represent the best-fit Gaussian distributions before and after correction for beam size, respectively. **(b)** Intensity profile of one of the diffraction patterns in Fig. 2 (solid dark-green curve), which lacks 1,1 reflection observed in the diffraction from bulkier muscle cell (dashed pale-green curve). All the figures except for the upper drawings shown in Fig. 1 are reproduced from [2] with permission from IUCR.

Hiroyuki Iwamoto

SPring-8/JASRI

E-mail: iwamoto@spring8.or.jp

References

[1] H. Iwamoto *et al.*: Biophys. J. **83** (2002) 1074.
[2] *H. Iwamoto, K. Inoue, T. Fujisawa and N. Yagi: J. Synchrotron Rad.* ***12*** *(2005) 479.*

Materials Science
Structure

Materials Science is one of the most active fields in synchrotron researches and covers nearly 45 percent of all applications proposed to SPring-8 during the 2005A period. Synchrotron radiation is extremely powerful and is used for studying the structure of advanced materials, where the atomic and electronic structures of a large variety of crystals and fluids are determined to make a connection with the physical and chemical properties in bulk, surface and interface states. Most of structure-related research programs are being carried out by X-ray diffraction, scattering and imaging techniques. Examples of such experiments are compiled in this volume.

At SPring-8, ten public beamlines mainly serve the experiments of structure-related materials science, having various purposes such as structure analyses by single-crystal X-ray diffraction (BL02B1), structure analyses by powder X-ray diffraction (BL02B2), amorphous and liquid researches with high-energy X-rays (BL04B2), structure analyses of surface and interface (BL13XU), X-ray imaging (BL20B2, BL20XU), inelastic scattering (BL08W, BL35XU), white X-ray topography (BL28B2), magnetic scattering (BL39XU), and R&D and diffraction (BL46XU). The experiments corresponding to the following topics have been also performed at JAERI (BL14B1, BL22XU), RIKEN (BL19LXU) and Hyogo Prefecture (BL24XU) Beamlines. Each of the above beamlines provides the requisite number of photons, sufficient energy, and spatial resolutions and polarization.

Nine topics are selected here out of a considerable number of structure-related studies in materials science. In this volume, scientific interest is focused on (1) charge ordering, spin-density wave and magnetic-field-induced phase transition, (2) liquid structures of D_2O and Se, (3) surface structures, chemical state and strain distribution, and (4) phase tomography and time-resolved X-ray imaging. The works under these topics are advancing the frontiers of synchrotron researches.

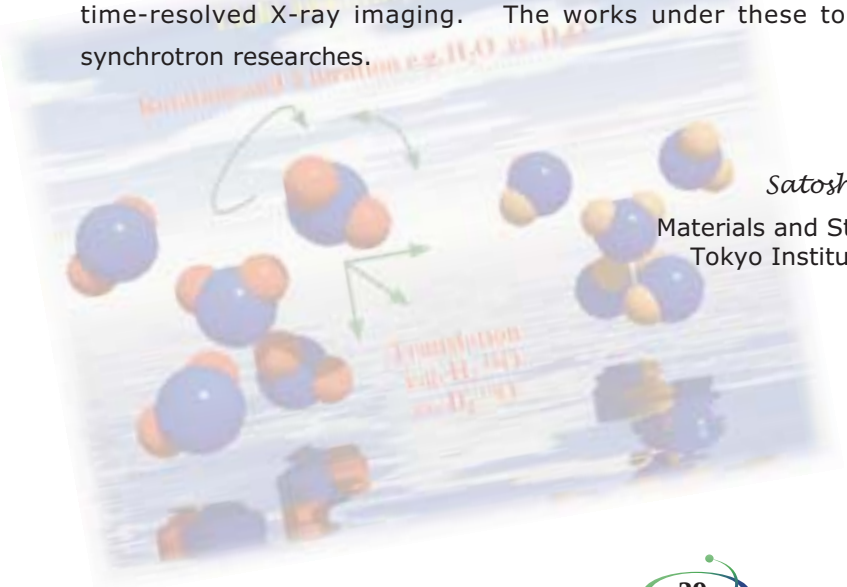

Satoshi Sasaki

Materials and Structure Laboratory
Tokyo Institute of Technology

Discovery of the Ferroelectricity Originated from Electron-electron Interaction

Ferroelectric material is ubiquitous. You can find it in any electrical devices such as handy phones, music players, computers, cars, microwave ovens and even in the magnetic hard disks. This is because a ferroelectric can store electric charges and has an enormously large dielectric permittivity. Thus, it can shrink down the size of an electric condenser in any electrical devices.

It is known that the ferroelectricity (that is, the name for the character of ferroelectric material) occurs from the coherent arrangement of electric dipoles in the material. The electric dipole had been believed to arise from the spontaneous displacement of an anion and a cation forming a polar symmetry. Such a situation is schematically modeled in Fig. 1, which provides a typical explanation of Perovskite ferroelectrics where the center of a negative charge (anion, oxygen ion) and the center of a positive charge (cation, B-site ion) do not coincide. The occurrence of the off-centering of the anion and cation is explained by the slowing down and freezing processes of an optical phonon.

Such motion of an anion and a cation is called "displacement." The concept of the displacement of ions had been a central paradigm on the origin of ferroelectricity in the last half century. An example is seen in the recent research achievement in SPring-8, where the covalent bonding between the anion and cation has the central role in the formation of such displaced ions [1].

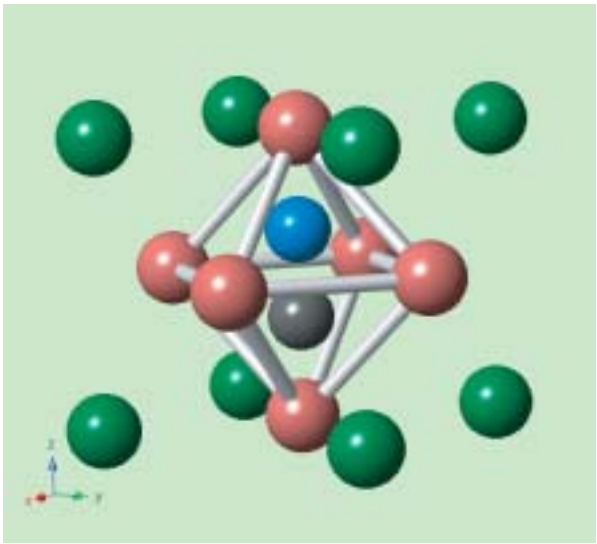

Fig. 1. Schematic drawing for origin of displacement-type ferroelectrics; for perovskite. The center of an anion (oxygen; red) and the position of a B site cation do not coincide. The B site cation has two stable positions drawn in blue and gray.

On one hand, we found a new ferroelectric mechanism in triangular mixed valence material RFe_2O_4 behaving as a ferroelectric [2]. A possible new ferroelectricity had suggested in the formation of the charge superstructure in this material. With the appearance of the electric polarization the superstructure appears as an order parameter. If this superstructure is confirmed to be the charge superstructure it would be a new ferroelectricity.

In order to clarify the origin of the superstructure, we performed a resonant X-ray scattering (RXS) experiment, which is the most sensitive technique for detecting the charge superstructure. The experiment on single-crystal $LuFe_2O_4$ was performed with a four-circle diffractometer at beamlines **BL02B1** and **BL22XU**. A crystal sample grown by the floating zone melting method was cut to orient the *c*-axis normal to the sample surface. The intensity of a superlattice spot ($n/3\ n/3\ m$+0.5) where n and m are integers was recorded as a function of the X-ray energy near the *K*-absorption edge of iron. The sample was cooled in a refrigerator down to 18 K, which is far below the ferroelectric transition temperature.

A typical result of the RXS experiment is shown in Fig. 2. In the spectrum, a maximum and a minimum at around 7.113 keV and 7.120 keV, respectively, and a background independent of X-ray energy were found. The maxima at 7.113 keV and 7.120 keV arise from the in-phase component of the anomalous atomic scattering factor of Fe^{2+} and Fe^{3+}, respectively. The corresponding *K*-absorption edges for both ions were confirmed by the X-ray absorption near-edge structure measurements for $LuCoFeO_4$ and $LuFeGaO_4$, which are isostructural to RFe_2O_4 but contain only Fe^{3+} and Fe^{2+}, respectively.

This result clearly indicates that the structure factor of this superlattice point is contributed by the positive atomic scattering factor of Fe^{3+} and the negative factor of Fe^{2+}. Therefore, we can conclude that the structure factor at this Bragg point arises from the 'difference' in atomic scattering factor for Fe^{2+} and Fe^{3+}. This is the evidence for the formation of the long-range ordering of Fe^{2+} and Fe^{3+} with the $\sqrt{3} \times \sqrt{3}$ structure as shown in Fig. 3.

This structure is consistent with the proposed charge-ordering model for Fe^{2+} and Fe^{3+} in RFe_2O_4 [3,4], which had been derived from the consideration on the competitive Coulomb interaction between electrons on a triangular lattice. Interestingly, the charge structure allows the presence of a local electrical polarization, since the centers of Fe^{2+} (excess electron) and Fe^{3+} (electron deficiency) do not coincide in the cell of the superstructure. This indicates the ferroelectricity originating from the electron density modulation without a dipole of a cation and anion pair.

Therefore, we concluded that RFe_2O_4 is a novel ferroelectric material, reflecting the correlated nature of the electrons. This conclusion is consistent with the previously reported dielectric properties of this material. For example a large dielectric dispersion found in this material was explained with the electron fluctuation proceeding the ferroelectric domain boundary motion [5,6].

This ferroelectricity by the electron correlation offers great potential when designing future ferroelectric devices to be coupled or controlled with the degrees of freedom of the electron: charge, spin and orbital. Such properties may lead to a new multiferroic material. Also, the low activation energy of electron motion of this material, which suggests less coupling between polarization switching and the lattice distortion, may enable the development of a fatigue-free solid charge capacitor. These possibilities of new ferroelectric materials will be examined in future studies.

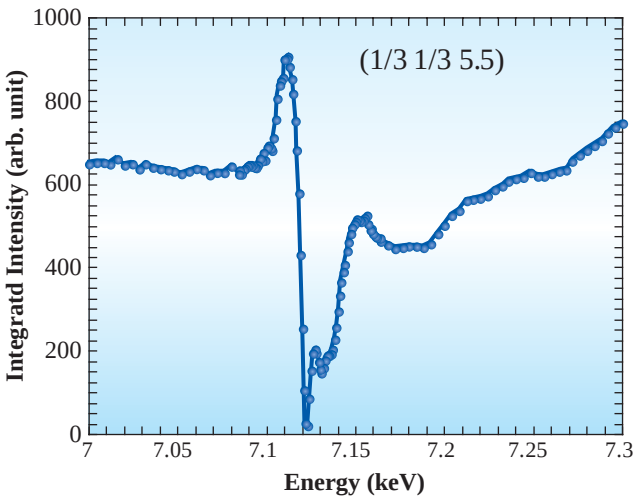

Fig. 2. X-ray energy dependence of superlattice reflection (1/3, 1/3, 5.5) for $LuFe_2O_4$. The peak and minimum arise from the in-phase component of the anomalous atomic scattering factor for Fe^{2+} and Fe^{3+}, respectively.

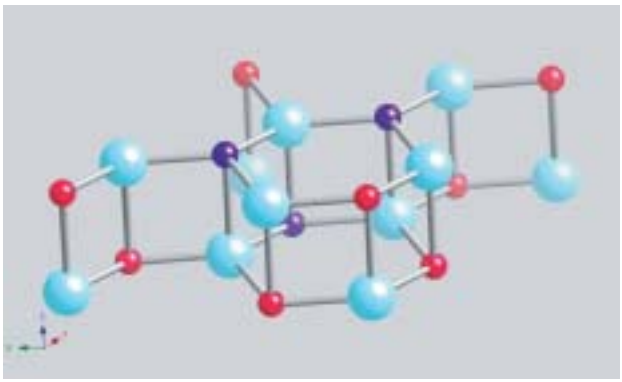

Fig. 3. Charge-ordering model of iron double layer in charge superstructure for RFe_2O_4. Fe^{2+} (negative charge) and Fe^{3+} (positive charge) are represented with red and light blue balls. The negative ions (oxygen atoms, light blue balls) do not have the role in the formation of the polarization in this model.

Naoshi Ikeda†

SPring-8 / JASRI

E-mail: ikedan@science.okayama-u.ac.jp

†Present address: Department of Physics, Okayama University

References

[1] Y. Kuroiwa *et al.*: Phys. Rev. Lett. **87** (2001) 217601.
[2] *N. Ikeda, H. Ohsumi, K. Ohwada, K. Ishii, T. Inami, K. Kakurai, Y. Murakami, K. Yoshii, S. Mori, Y. Horibe and H. Kitô: Nature* ***436*** *(2005) 1136.*
[3] Y. Yamada *et al.*: J. Phys. Soc. Jpn. **66**(1997) 3733.
[4] K. Siratori *et al.*: Proc. 6th Int. Conf. on Ferrites Tokyo and Kyoto, The Japan Society of Powder and Powder Metallurgy (1992) p.703 .
[5] N. Ikeda *et al.*: J. Phys. Soc. Jpn. **63** (1994) 4556.
[6] N. Ikeda: J. Phys. Soc. Jpn. **69** (2000) 1526.

Investigation of SDW/CDW State in UCu_2Si_2 using Non-resonant X-ray Scattering

Actinides attract strong interests in the field of condensed matter physics from the rich variety of unusual properties in magnetism, multipole ordering and unconventional superconductivity, among others. Actinide has unfilled 5*f* electrons in the outermost shell. The 5*f* electron has a magnetism dominated by its orbital contribution and multipolar degree of freedom due to LS coupling. On the other hand, the 5*f* wave function is expanded due to the large relativistic effect, which leads to hybridization with the valence states of neighboring atoms. The itinerant 5*f* electron appears in valence and conduction bands, which plays an important role in bringing about the unusual properties. The strongly correlated many body *f* electron system is realized only in a light actinides 5*f* system. Therefore, there is an open field for investigating actinides in the area of condensed matter physics.

Recently, we have determined the magnetic structure of UCu_2Si_2 by neutron scattering as shown in Fig. 1(a) [1]. This compound shows the longitudinal amplitude modulation of the magnetic moment with a long periodicity Λ = 85.7 Å corresponding to ~17 uranium layers along the tetragonal *c*-axis. The opening gap accompanied by the spin density wave (SDW) state indicated by the BCS-type magnetic order parameter [1] reminds us of the nesting origin of the itinerant magnetism in 3*d* transition metals such as chromium [2], in which the charge density wave (CDW) state coexists with SDW.

We succeeded in revealing the SDW/CDW state of an itinerant 5*f* electron system for the first time in UCu_2Si_2 by performing a non-resonant X-ray scattering (NRXS) experiment at beamline **BL46XU**. Figure 2 shows the observed CDW peak at the second-order satellite, whose intensity is in the order of 10^{-7} of the (0 0 8) fundamental reflection.

The charge origin was unambiguously confirmed by the polarization analysis, where we utilized the variable scattering plane method [3]. Also, the inclination angle dependence of the signal intensities of fundamental reflection and that of satellite reflection is well explained in terms of the charge origin peak as denoted by a solid line in Fig. 3, whereas an almost flat dependence is expected for the SDW origin peak as shown by a dashed line. The polarization analysis of such a subtle reflection is the great advantage of the six-circle diffractometer installed at BL46XU.

Figure 1(b) shows schematic pictures of the charge density modulation. The NRXS intensity of the observed satellite comes from the lattice strain in the order of 10^{-4} Å. This is consistent with the contraction of the lattice parameter of the *c*-axis around the magnetic transition. Thus, we suppose that the lattice spacing around the node of the CDW is slightly larger than the loop where a large U moment appears in the modulation. Besides the strain wave, we expect charge modulation of the 5*f* component in connection with exchange splitting. This charge modulation could be directly observed by resonant X-ray scattering, which is now under consideration.

A similar but rather short periodicity incommensurate modulation has been reported in UPd_2Si_2 and UNi_2Si_2. The magnetic structures were

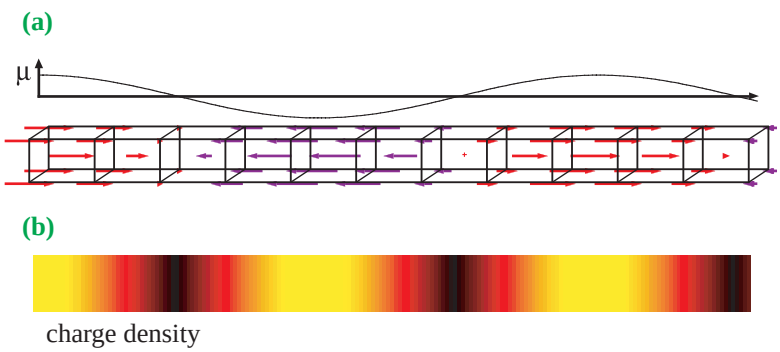

Fig. 1. **(a)** Antiferromagnetic structure of UCu_2Si_2 and magnetic amplitude modulation. **(b)** Charge density distribution in UCu_2Si_2.

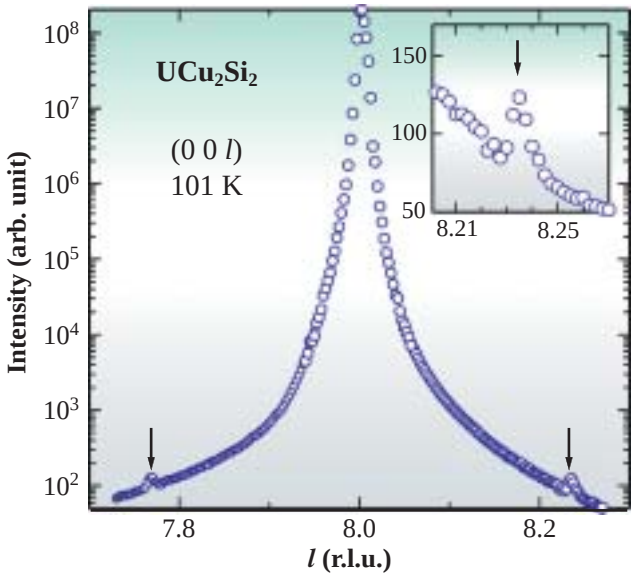

Fig. 2. Line scan along (0 0 8) at 101 K measured by non-resonant X-ray scattering.

interpreted with an axial next nearest neighbor ising (ANNNI)-type model based on a frustrated short-range interaction between localized 5*f* electrons [4]. There is no way to explain such a long sinusoidal modulation in UCu_2Si_2 with the ANNNI model unless the long-range interactions for up to the ~9th nearest neighbors are taken into account. Since the electronic properties of these three compounds are similar, we suggest the strong intinerant character of 5*f* electrons in these compounds as the origin of the SDW state.

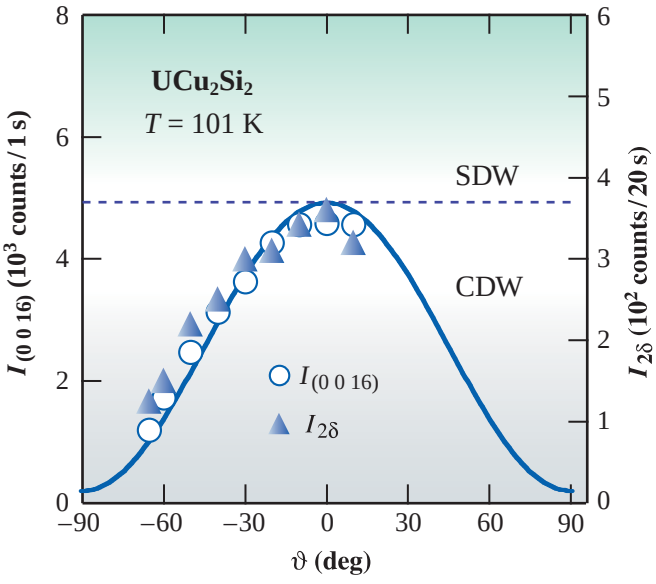

Fig. 3. Scattering intensity as a function of inclination angle, ϑ. The open circles and closed triangles are the observed data at the (0 0 16) fundamental and satellite reflections, respectively. The solid and dashed lines indicate the calculated results for charge and magnetic peak.

F. Honda[a,*], N. Metoki[a,b] and H. Ohsumi[c]

[a] Advanced Science Research Center, JAEA (Tokai)
[b] Department of Physics, Tohoku University
[c] SPring-8 / JASRI

*E-mail: honda.fuminori@jaea.go.jp

References

[1] *F. Honda, N. Metoki, T.D. Matsuda, Y. Haga and Y. Onuki: J. Phys. Condens. Matter* ***18*** *(2006) 479.*
[2] Y. Tsunoda *et al.*: Solid State Commun. **14** (1974) 287.
[3] H. Ohsumi: SPring-8 Research Frontiers 2003, p.121.
[4] V. Sechovsky and L. Havela: Handbook of Magnetic Materials, ed. K.H.J. Buschow (Amsterdam: Elsevier Science B.V.) **11** (1998) 1; and references therein.

Synchrotron Radiation Experiments under Very Strong Magnetic Fields

A strong magnetic field is indispensable for studying the physical properties of strongly correlated electron systems. A variety of novel phenomena, such as metamagnetism, insulator-metal transition and structural transition, are induced by a strong magnetic field. On the other hand, performing an X-ray experiment using synchrotron radiation is a powerful means of investigating the structural, electronic and magnetic properties of solids. Hence, a combination of strong magnetic fields and synchrotron radiation is one of the most promising experimental techniques for opening up a new area for both synchrotron radiation materials science and high magnetic field physics.

The key to realizing a synchrotron radiation experiment in strong magnetic fields is how to develop a magnetic field generator in or near a synchrotron radiation facility. Although a strong magnetic field of up to 20 T is available with a commercial superconducting magnet at the present, it cannot be used for the X-ray experiment as it is because of its narrow sample space, the small aperture for the access to the sample and other factors. In fact, the world's strongest DC magnet for X-ray diffraction is the 15-T split-pair type magnet installed on beamline **BL19LXU** [1].

Since various kinds of phase transitions or peculiar phenomena were discovered in strong magnetic fields exceeding 20 T, the development of the technique for the synchrotron X-ray experiment under stronger fields is urgently required. A pulsed magnet can generate much stronger magnetic fields than a DC magnet because of its short pulse duration time and hence small heat production. However, the construction of a conventional-type pulsed field generator in a synchrotron radiation facility is still not easy because the generation of strong fields exceeding 30 T requires large electric power, large space and special skills.

Fig. 1. Photograph of miniature split-pair type magnet for X-ray diffraction.

In order to overcome this problem, we have recently developed a very small pulse magnetic field generator for the synchrotron X-ray experiment. It consists of a portable size capacitor bank (~2 kJ) and a miniature pulsed magnet (3 mm inner diameter) [2,3]. A photograph of the magnet is shown in Fig. 1. The capacitor bank only weighs 100 kg and can be readily installed into a synchrotron X-ray facility from the outside. The magnet is small enough to be set in a standard cryostat and cooled together with a sample. The energy of the capacitor bank and the volume of the magnet are roughly two orders of magnitude smaller than those of a conventional pulsed magnet.

We applied this technique to the X-ray diffraction study on a field-induced valence transition of $YbInCu_4$. $YbInCu_4$ is known to show a first-order valence transition at 42 K. At low temperatures the local magnetic moment of the Yb ion is compensated and a Fermi liquid state is realized due to the strong *c-f* hybridization. The valence of the Yb ion becomes fluctuating (v = 2.8+ ~ 2.9+) from an integer valence state (v ~ 3+) with decreasing temperature; the lattice volume increases by 0.45% at the transition, while maintaining C15b cubic structure.

The first-order valence transition is also induced by a strong magnetic field at low temperatures. According to previous papers, the valence fluctuating state (v = 2.8+ ~ 2.9+) is transformed into the integer valence state (v ~ 3+) by a magnetic field of around 30 T at 4.2 K [4]. The distinct metamagnetic transition is observed.

The experiment was performed on undulator beamline **BL22XU**. A split-pair type miniature magnet that can generate 36 T at 1.3 kJ was used. We made a time-resolved measurement using an avalanche photodiode (APD) and a multichannel scalar (MCS). A single crystal of $YbInCu_4$ grown from In-Cu flux was used. The available lowest temperature is 3 K at present.

Figure 2 shows the time dependence of the (220) Bragg reflection peak intensity in $YbInCu_4$ and that of the magnetic field. We see that the (220) reflection intensity suddenly decreases and recovers at the time corresponding to around 30 T. This field dependent behavior of the reflection intensity indicates that the structural transition occurs due to the field induced valence change [3,5].

The (220) reflection peak profiles in magnetic fields are obtained by repeating the measurements at different reflection angles. The field dependence of the (220) reflection profile is shown in Fig. 3. It is found that the new reflection peak denoted as peak A appears at around 26 T and its intensity increases as the field increases. Correspondingly, the reflection peak B from the low-field phase disappears with increasing magnetic fields higher than 26 T. This phenomenon is attributed to the lattice contraction due to the field-induced valence transition. It is worth noting that peak B dose not successively translate to peak A. Hence, it is apparent that the valence state transition of $YbInCu_4$ is of first order.

We carefully analyzed the field dependence of the integrated reflection intensities and the peak positions of peaks A and B. It is found that the intensity of peak B (low-field phase) is nearly scaled with the magnetization. On the other hand, peak A (high-field phase) appears at slightly higher fields than expected from the magnetization. This is most probably because the domain size of the high-field phase at the early stage of the transition is too small to be observed as a well-defined X-ray diffraction peak [5]. Moreover, we found that both peaks (peaks A and B) show a small continuous shift in the vicinity of the transition field (25 T~ 28 T) where the two phases coexist. This may suggest that the lattice is slightly deformed by a kind of internal stress due to the interaction between two domains of different valence states [5].

As shown above, X-ray diffraction in a strong magnetic field is considered to be one of the most interesting means of investigating the field induced phase transitions of strongly correlated electron systems. Our experimental technique can also be applied for other kinds of experiments such as those based on X-ray absorption spectroscopy (XAS) and X-ray magnetic circular dichroism (XMCD). The development of the technique for XAS under strong magnetic fields is now in progress and the preliminary experiment has been conducted at BL22XU up to 51 T using a solenoid-type mini-magnet.

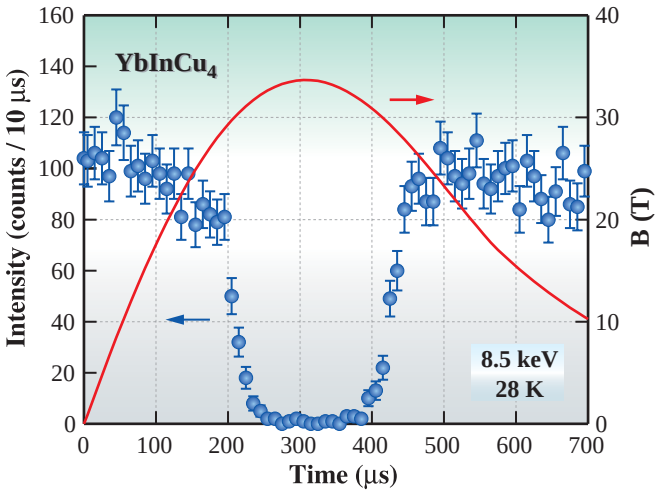

Fig. 2. Time dependences of (220) Bragg reflection peak intensity and magnetic field.

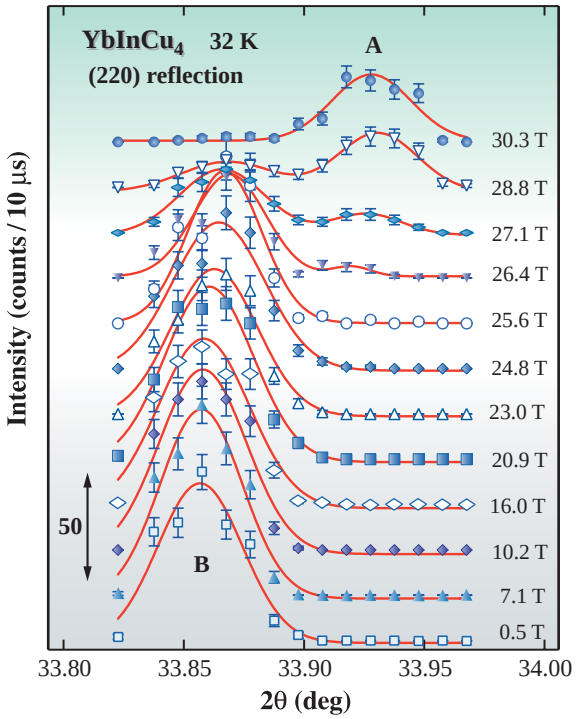

Fig. 3. (220) Bragg reflection peak profiles in magnetic fields. The solid curves are the results of the curve fitting.

Yasuhiro H. Matsuda[a,*,†] and Toshiya Inami[b]

[a] Graduate School of Natural Science and Technology, Okayama University
[b] SPring-8 / JAEA

*E-mail: matsuda@imr.tohoku.ac.jp

[†]Present address: Institute for Materials Research, Tohoku University

References

[1] K. Katsumata: Physica B **345** (2004) 49.
[2] Y.H. Matsuda *et al.*: Physica B **346-347** (2004) 519.
[3] *T. Inami, K. Ohwada, Y. H. Matsuda, Y. Ueda, H. Nojiri, Y. Murakami, T. Arima, H. Ohta, W. Zhang and K. Yoshimura: Nucl. Instrum. Meth. B **238** (2005) 233.*
[4] K. Yoshimura *et al.*: Phys. Rev. Lett. **60** (1988) 851.
[5] *Y.H. Matsuda, T. Inami, K. Ohwada, Y. Murata, H. Nojiri, Y. Murakami, H. Ohta, W. Zhang, K. Yoshimura: J. Phys. Soc. Jpn. **75** (2006) 024710.*

Isotopic Quantum Effects in Water

Quantum mechanics plays an important role in describing the properties of water and intermolecular hydrogen bonding interactions in aqueous solutions. The most commonly recognized “quantum effect” is the freezing point of heavy water, D_2O, at 4ºC [1] yet these effects also have implications for many biological processes, as high levels of D_2O are known to be toxic. From a chemical physics perspective, standard classical simulations on water using any simple potential will predict identical structural and thermodynamic properties for both H_2O and D_2O. The zero point motions of light and heavy water molecules therefore need to be included to provide an accurate description of the structure of liquid water. These motions are governed by quantum mechanical vibrations, rotations and translations.

Heavy water is closer to the classical approximation whereas light water exhibits larger degree of motion [2]. Quantum effects appear as small differences in the X-ray structure factor for different isotopic enrichments of water.

High energy diffraction technique experiments on H_2O and D_2O provide a direct insight into the quantum mechanical part of the hydrogen bond in water, information which is not accessible using neutron diffraction. At beamline **BL04B2** the effects of substituting the hydrogen for deuterium as well as the oxygen isotope ^{16}O for ^{18}O have been measured. The total mass change from $H_2{}^{16}O$ to $H_2{}^{18}O$ is the same as $H_2{}^{16}O$ to $D_2{}^{16}O$ but the mass distribution is different. Since the oxygen atom is nearly at the center of mass of the molecule, the effect of substitution at the proton sites (D for H) is dominated by rotational and vibrational molecular motions, while hindered translational motions may be expected to be the most prevalent effect in $^{16}O/^{18}O$ substitution. The structural isotope difference for the $^{16}O/^{18}O$ substitution is found to be approximately one quarter of the magnitude of the observed H *versus* D effect [3]. The experiment shows that the $^{16}O/^{18}O$ substitution effect is small and limited to the first coordination shell, while a simulation has predicted larger structural rearrangements in both the first and second coordination shells [4].

At 26ºC it has been found that H_2O may be considered to have the same structure as D_2O at ~32ºC [5]. This difference increases dramatically at lower temperatures due to quantum mechanical tunneling [1]. Quantum molecular dynamics simulations [2] have show that water is essentially tetrahedral with an additional loosely bound fifth molecule, and as the quantum effects increase the average distances of the tetrahedra increase. Our experiments have shown that the total structural isotope effect increases by a factor of 3.5 as the temperature is decreased from 45ºC to -5ºC [3].

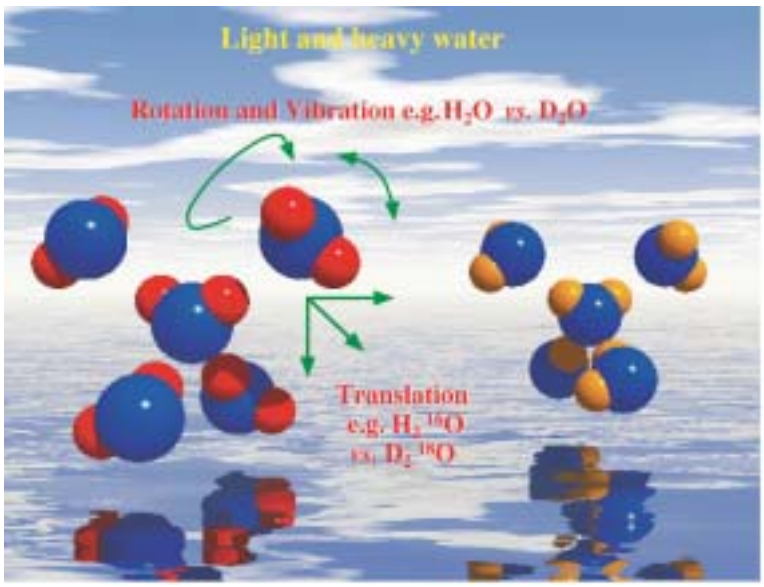

Fig. 1. Representation of the local structure and motion of water molecules.

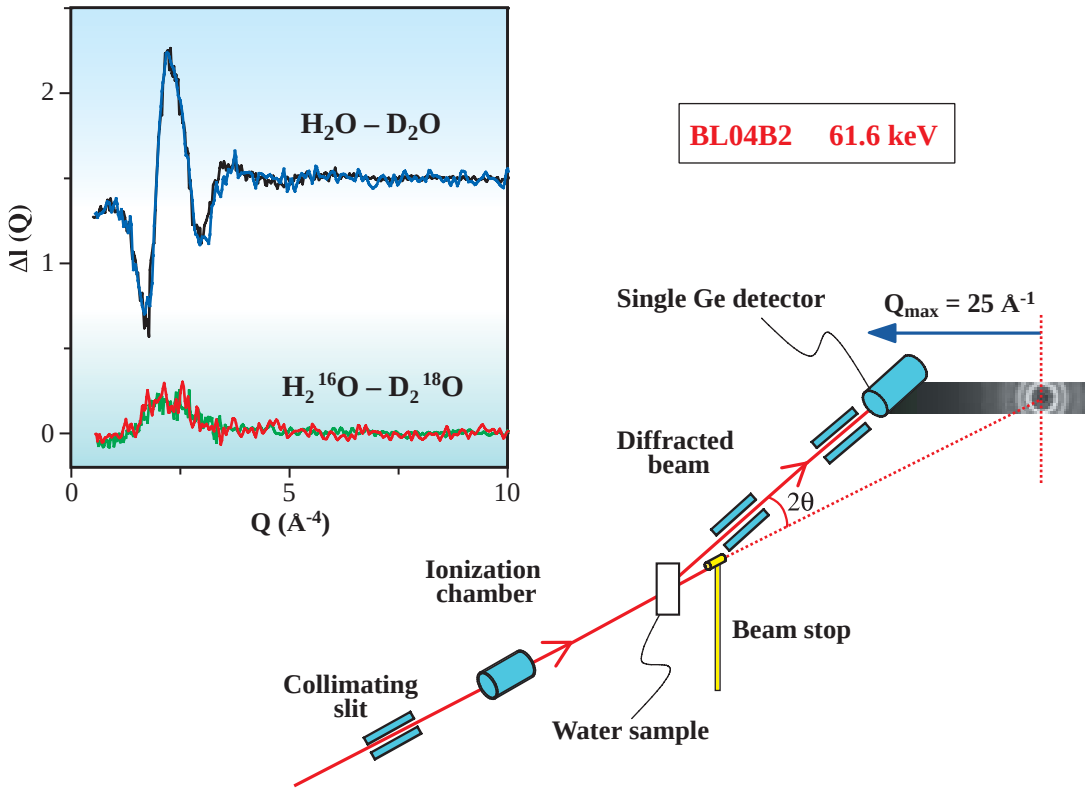

Fig. 2. Schematic diagram of high energy diffraction set-up and isotopic differences for H/D and $^{18}O/^{16}O$ substitutions.

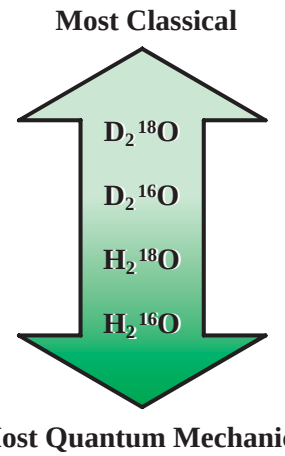

Fig. 3. Variations in quantum mechanical behavior of different isotopes of water.

C. J. Benmore[a,*], J. Neuefeind[b] and S. Kohara[c]

[a] Intense Pulsed Neutron Source and Advanced Photon Source, Argonne National Laboratory, USA
[b] Spallation Neutron Source, Oak Ridge National Laboratory, USA
[c] SPring-8 / JASRI

*E-mail: Benmore@anl.gov

References

[1] L.H. de la Peña and P.G. Kusalik: J. Am. Chem. Soc. **127** (2005) 5246.
[2] B. Guillot and Y. Guissani: Fluid Phase Equilib. **150** (1998) 19.
[3] *R.T. Hart, C.J. Benmore, J. Neuefeind, S. Kohara, B. Tomberli and P. A. Egelstaff: Phys. Rev. Lett. **94** (2005) 047801.*
[4] R.A. Kuharski and P.J. Rossky: J. Chem. Phys. **82** (1985) 5164.
[5] B. Tomberli *et al.*: J. Phys. Condens. Matter. **12** (2000) 2597.

Anomalous Dynamical Narrowing in Liquid Se

We have observed strong narrowing in the inelastic X-ray scattering (IXS) spectra of liquid (l-) Se at the momentum transfer Q between 12 and 15 nm^{-1} [1]. Typically, in simple monatomic liquids, narrowing is observed at the first structure factor maximum, in this case, about 19 nm^{-1}. However, we see it at a somewhat lower Q. This is probably related to the covalent nature of the liquid. Se forms two-fold coordinated linear chain molecules, where atoms are covalently bonded. Crystalline Se with a trigonal form is stable at ambient conditions and it consists of helical chains, while metastable monoclinic forms consist of Se_8 ring molecules. When Se is melted, its two-fold coordinated chain structure is largely preserved and l-Se consists of disordered long chains where segments with a helical chain-like configuration (a) and ring-like one (b) are randomly distributed (see Fig. 1).

We measured the dynamic structure factor $S(Q,E)$, where E is the energy transfer, using a high-resolution IXS spectrometer at beamline **BL35XU**. The energy of the incident beam was 21.747 keV and the spectrometer resolution depending on the analyzer crystals was 1.5 - 1.8 meV in the present experimental setup. The Se sample of 99.999 % purity and 0.04 mm in thickness was mounted in a single-crystal sapphire cell. IXS spectra of l-Se at 523 K were measured from 1.8 to 42 nm^{-1} over 40 meV.

Figure 2 shows the overall features of the $S(Q,E)$ of l-Se at 523 K. The energy integrals of $S(Q,E)$ become the static structure factor $S(Q)$, which agrees

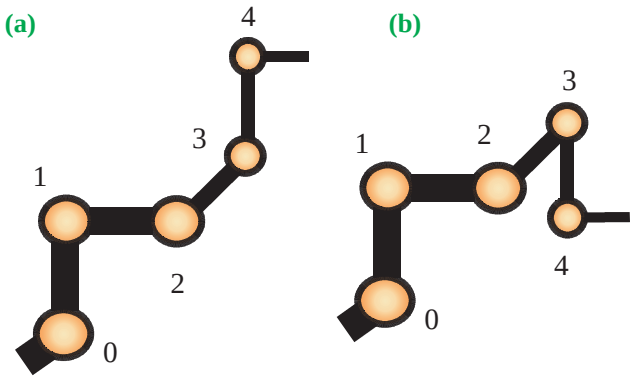

Fig. 1. Schematic illustration of helical chain-like **(a)** and ring-like **(b)** segments along a disordered chain.

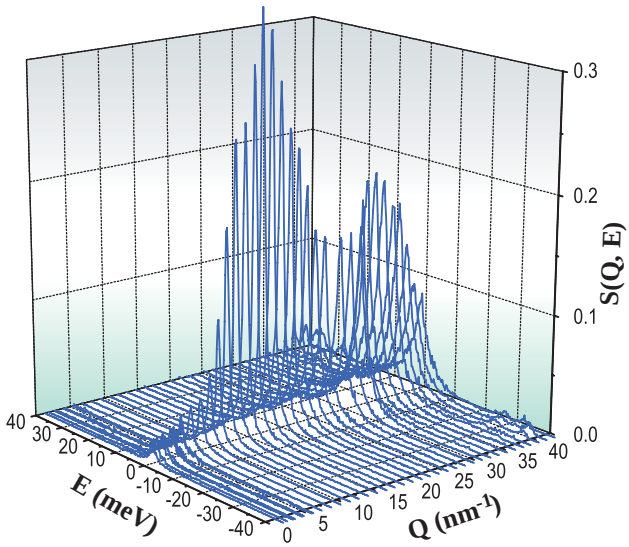

Fig. 2. Three-dimensional plots of $S(Q,E)$ of liquid Se at 523 K.

well with that obtained from neutron scattering (NS) [2] as shown in Fig. 3(a). $S(Q,0)$, shown in Fig. 2, has a sharp first peak at 15 nm^{-1}, which is a little smaller than the first $S(Q)$ maximum. That is, the $S(Q,E)$ observed is very narrow at around 15 nm^{-1}.

The spectra were analyzed using a model function consisting of several Gaussians to deconvolute $S(Q,E)$ from the spectrometer resolution. Then we calculated the normalized second frequency moment of $S(Q,E)$, $\omega_0(Q)$, from the deconvoluted model function. Figure 3(b) shows the E-Q dispersion relation of $\omega_0(Q)$ deduced from $S(Q,E)$ (triangles). The triangles reasonably follow the solid line in Fig. 3(b) that is calculated using the sum rule, $\omega_0^2(Q) = k_B T Q^2 / (mS(Q))$, where m is a particle mass and $S(Q)$ is obtained from NS [2]. More exactly, however, the triangles deviate below the solid line at the Q between 12 and 15 nm^{-1}. This discrepancy can be explained if we assume the Q dependence of m. Figure 3(c) shows the effective mass deduced from $\omega_0(Q)$. The mass as large as 2 - 3 atoms just pinpoints the Q where the strong narrowing occurs. The distance corresponding to the Q is close to the fourth-nearest-neighbor distance, and it is crucial to distinguish between helical chain-like and ring-like segments in

the disordered chain as shown in Fig. 1. Thus, the large effective mass hints that the segments cooperatively move like a rigid molecule under the propagation of longitudinal waves with the corresponding Q. This must be the origin of the present narrowing.

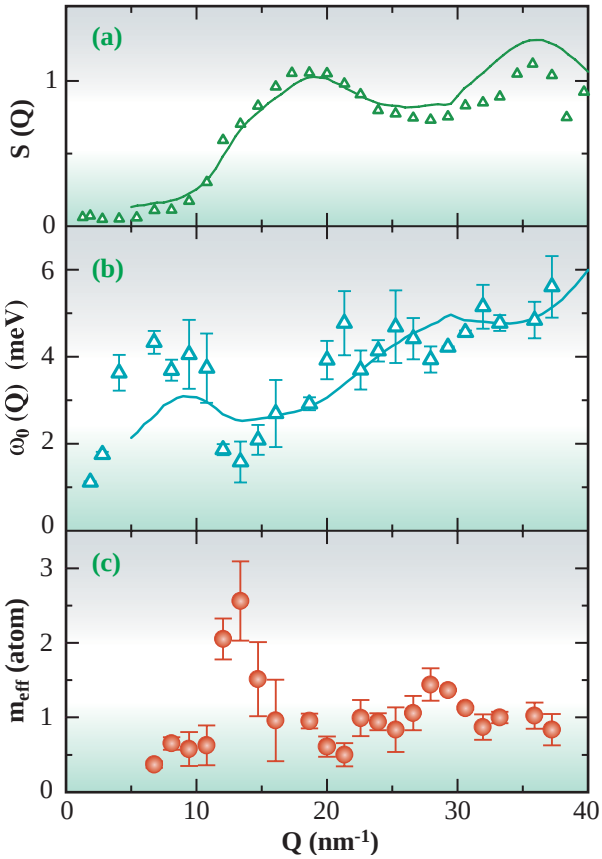

Fig. 3. **(a)** The energy integral of $S(Q,E)$ (open triangles) is plotted after being properly normalized. Also shown is the $S(Q)$ obtained from neutron scattering (solid line). **(b)** E-Q dispersion relation of ω_0 (Q) obtained from $S(Q,E)$ (open triangles) and sum rule (solid line). **(c)** Q dependence of effective mass.

M. Inui*, S. Hosokawa and K. Matsuda

Faculty of Integrated Arts and Sciences,
Hiroshima University

*E-mail: inui@mls.ias.hiroshima-u.ac.jp

References

[1] *M. Inui, S. Hosokawa, K. Matsuda, S. Tsutsui and A.Q.R. Baron - in preparation.*
[2] K. Maruyama *et al.*: J. Phys. Soc. Jpn. **74** (2005) 3213.

Structural Verification of Bi Nanolines in Si using Obvious-at-a-glance X-ray Diffraction Method

Most nanoscaled structures that have so far been created have single-unit or independent structures. A multiple-layer structure fabricated by the combination of such single-unit structures is required for practical nanodevice application and is called a nanoarchitecture. Miki's (a coauthor of this article) research group has succeeded in developing a new processing method for encapsulating Bi nanolines in silicon by epitaxial growth of Si. This success has been the first step toward the fabrication of nanoscale interconnections in epitaxial silicon; eventually, this method would allow us to form nanoarchitectures. During growth using the conventional process, a nanostructure is fragile or destroyed because a surface segregation phenomenon occurs. To use a Bi surfactant to avoid the destruction is a key point of the processing method that the research group developed; consequently, it has been possible to embed the Bi-nanoline structures in silicon.

It is in general difficult to nondesructively observe such a nanostructure embedded in a crystal from its surface. This is because the standard surface-structural-analysis tools such as scanning probe microscopy and electron diffraction are not available for direct observation of the embedded nanostructure. There could be a possibility to observe the nanostructure with a transmission electron microscope; however, the structure would be unintentionally destroyed during sample preparation before the observation. On the other hand, any synchrotron-based diffraction technique is nondestructive but had not revealed the Bi-nanoline structure.

Sakata (the first author of this article) applied the "obvious-at-a-glance" X-ray diffraction method based on reciprocal-lattice space imaging to quick observation and characterization of one-dimensional (1D) nanostructures. It disclosed the structural information such as a crystalline-domain size across ultrathin NiO nanowires and their crystal system successfully [1]. The basic idea behind the method is that Bragg conditions of such 1D structures are sheet shapes and are fulfilled more easily than those of 2D and 3D structures. Figure 1 depicts a typical geometry of reciprocal-lattice space imaging. The diffraction conditions or scattering patterns (the Fourier transform) of a 1D crystal are sheets, which are perpendicular to the 1D, located at Bragg positions of the corresponding bulk crystal of the 1D in the reciprocal-lattice space. For example, the segmented streaks would simultaneously arise from the intersection of the sheet-shape structures with the Ewald sphere.

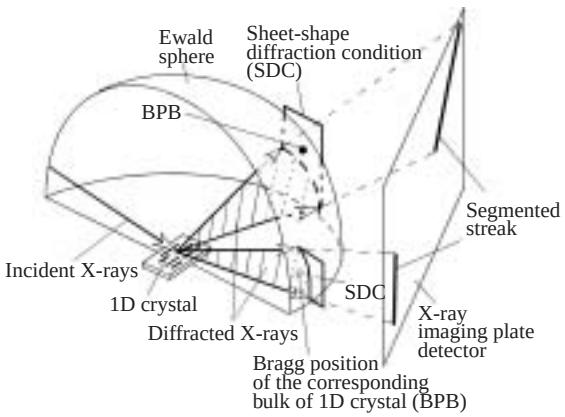

Fig. 1. Geometry of reciprocal-lattice space imaging for 1D crystal perpendicular to incident X-rays.

A principal objective of this research was to elucidate whether the Bi-nanoline structure remains after encapsulation. We used the "obvious-at-a-glance" X-ray diffraction method with possibly high-energy monochromatic X-rays for incidence to excite as many segments as possible and a 2D detector for straightforward analysis. Sample preparation, X-ray experimental conditions, results, and its atomic-scale structural model were already reported in [2].

Bi nanolines were grown on a Si(001) surface by molecular beam epitaxy in ultrahigh vacuum following the established recipe [3]. By scanning tunneling microscopy observation, the lines were 1.5 nm in width and more than 400 nm in length. The surface was at about 1/8 monolayer Bi coverage. Then an 11-nm-thick Si(001) epitaxial layer was grown epitaxially on the substrate at a temperature of *ca.* 400 ºC for about 2 min. We also prepared a second sample capped with an 11-nm-thick Si amorphous layer at room temperature. A more explicit procedure for sample preparation was described in [2].

X-ray measurements were performed in air at the undulator beamline **BL13XU** for surface and interface structure determination. A special purpose camera was used, including a pair of slits to limit the beam size to 0.1 mm × 0.1 mm, a sample, a direct-beam stopper, and a cylindrical X-ray imaging-plate (IP) detector to record diffraction. The distance of the sample to the IP detector camera length was 133 mm. The X-ray exposure time was typically 2 min. An X-ray beam with a photon energy of 25.3 keV was incident on the sample at an angle of 0.1º, giving a

penetration depth of 2.7 μm; it is clear that the X-rays reached the Bi lines under the cap layers.

We recorded X-ray patterns diffracted from the samples at different azimuthal angles around the surface normal. The right pattern in Fig. 2 shows a typical one for the incident X-rays perpendicular to the Bi nanolines. A 1D structure in a crystal gives rise to diffraction sheets perpendicular to itself; these are imaged as segmented streaks because of the intersection of the sheets with the Ewald sphere (see Fig.1 again). The magnified pattern (the left of Fig. 2) has segmented streaks.

The average length of the buried 1D lines was about 100 nm, which was estimated from the width of the k = 0 streak, where we use standard notation of h k l to indicate a point in reciprocal space that is defined by the surface unit cell. It should be noted that such streaks or circular arcs were not observed in the case of a Si(001) sample where no Bi nanolines were buried.

Magnifying the pattern (the left image in Fig. 2) gives more information on the 1D structures. Three streaks from the diffraction sheets appeared around the reciprocal lattice points of 0 -1/2 1, 0 0 1, and 0 1/2 1, which correspond to diffraction sheets of k = -1/2, k = 0, and k = 1/2, respectively. This shows that the buried 1D structure has a superstructure along the line, the periodicity of which is two times as large as the length of the primitive vector of the Si(001) surface. In additional to the epitaxial Si cap, we also used a cap of amorphous Si. In this case, the k = 0 streak was barely detectable, and no fractional-order streaks were observed around the direct-beam position, implying a complete loss of the Bi nanoline structure. Our X-ray results indicate that while Si amorphous

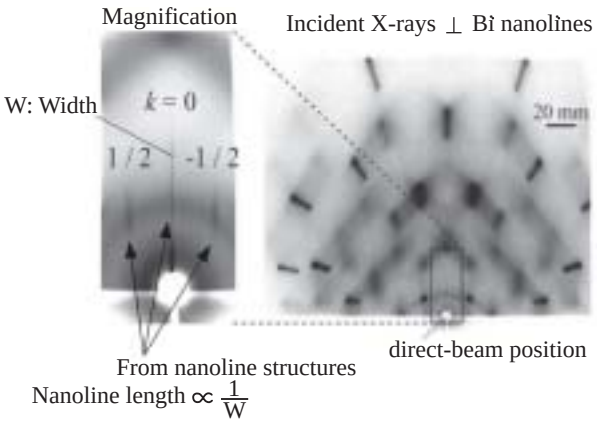

Fig. 2. X-ray patterns diffracted from Si epilayer cap/Bi lines/Si(001) sample. Whole pattern (right figure) recorded on imaging-plate detector and magnified pattern (left figure) around direct-beam position for incident X-rays perpendicular to Bi atomic lines. The surface unit vectors [1 0 0]*S* and [0 1 0]*S* having lengths of 3.84 and 3.84 Å are parallel to the bulk vectors [1 -1 0]*B* and [1 1 0]*B*, respectively.

growth seriously disturbed the atomic lines, Si epitaxial growth with a Bi overlayer confined the 1D atomic lines to the interface, while retaining the two-by periodicity along their length.

On the basis of the structural information obtained from these experiment results, we modeled the optimum atomic structure (Fig. 3) using tight binding and density-functional-theory (DFT) calculations. The starting structure was the “haiku” structure [4] for Bi nanolines on the Si(001) surface.

In summary, Bi nanolines embedded in a Si crystal were found to remain by observation of X-ray sheet-like diffraction for the first time. Sharp images appeared in the X-ray diffraction patterns obtained from the nanolines covered with only the Si epitaxial layer. The nanolines with the epitaxial cap were found to have a 2 × n superstructure having their Bi-dimer bonds parallel to themselves. The atomic-scale structural model for the embedded Bi nanolines has been proposed using tight binding and DFT calculations.

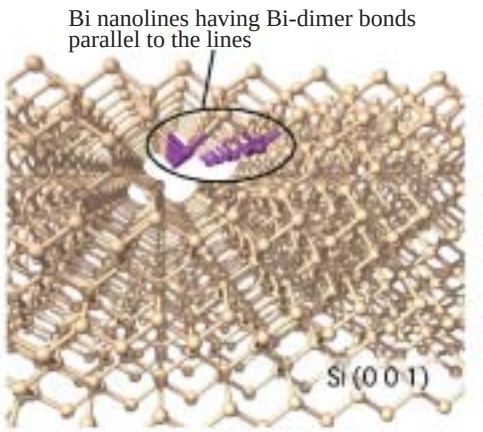

Fig. 3. Perspective view of our proposed model for buried Bi lines, showing their one-dimensional nature.

Osami Sakata[a,*], Kazushi Miki[b] and David Bowler[c]

[a] SPring-8 / JASRI
[b] Nanomaterials Laboratory (NML), National Institute for Materials Science (NIMS)
[c] International Center for Young Scientists and NML, NIMS

*E-mail: o-sakata@spring8.or.jp

References

[[1] O. Sakata *et al.*: Appl. Phys. Lett. **84** (2004) 4239.
[2] *O. Sakata, W. Yashiro, D.R. Bowler, A. Kitano, K. Sakamoto and K. Miki: Phys. Rev. B **72** (2005) 121407(R).*
[3] K. Miki *et al.*: Surf. Sci. **421** (1999) 397.
[4] J.H.G. Owen *et al.*: Phys. Rev. Lett. **88** (2002) 226104.

Sb on In/Si(111) Processes with Dynamically Observable LEEM, Selected Area LEED and Chemically Analyzed SR-XPEEM

The formation of the hetero-interface of semiconductors is of importance not merely as industrial requirement but also in the fundamental research aspect. To understand such growth behavior, the knowledge of spatially resolved local properties, such as the structure and chemical state, is required. Low energy electron microscopy (LEEM) and photoemission electron microscopy (PEEM) are quite suitable for this purpose. Low energy electron diffraction (LEED) patterns from the selected local area whose size is on the order of 0.1-1 μm, can be observed using the same LEEM optics to get local structure information. By combining with intense synchrotron radiation (SR), local chemical state analysis is possible using PEEM [1]. Experiments were carried out using a spectroscopic photoemission and low energy electron microscope (SPELEEM) installed in the soft X-ray beamline **BL27SU** [3].

Figure 1(a) shows a bright-field LEEM image of the prepared In/Si(111) surface. The bright area is the $\sqrt{31}\times\sqrt{31}$ region and the dark area the $\sqrt{3}\times\sqrt{3}$ region. The narrower terraces completely show the $\sqrt{31}\times\sqrt{31}$ structure, and the $\sqrt{3}\times\sqrt{3}$ terraces are observed centrally with the decoration by the $\sqrt{31}\times\sqrt{31}$ structure at the step edges. Figures 1(b)-1(d) show the bright-field LEEM images during Sb growth on it. The contrast becomes uniform in the initial stage of adsorption, and the first contrast reversal can be observed in Fig. 1(b).

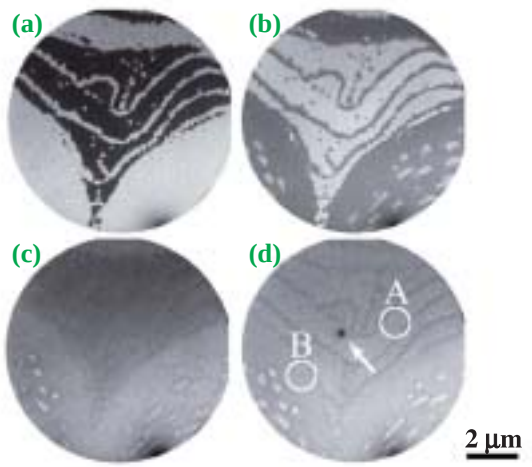

Fig. 1. Series of bright-field LEEM images during Sb adsorption on In/Si(111) surface at around 300 ºC. The electron energy was 10.4 eV and the field-of-view was 10 μm. **(a)** Original In/Si(111) $\sqrt{3}\times\sqrt{3}$ (dark) and $\sqrt{31}\times\sqrt{31}$ (bright) surfaces. The Sb coverages are approximately **(b)** 0.42 ML, **(c)** 0.7 ML and **(d)** 0.75 ML.

Two-dimensional islands with the same contrast as that in the initial $\sqrt{3}\times\sqrt{3}$ surface also forms on the initial $\sqrt{3}\times\sqrt{3}$ surface. By increasing further the amount of Sb deposition, the contrast becomes uniform again, and the second contrast reversal takes place as shown in Fig. 1(c). Such contrast change in bright-field LEEM images is due to the change of the surface structure by Sb adsorption on the $\sqrt{3}\times\sqrt{3}$ and $\sqrt{31}\times\sqrt{31}$ structures. After the second contrast reversal, the contrast becomes uniform again and the black dot, which is indicated by the arrow, appears as shown in Fig. 1(d). The deposition of Sb was ended here and this surface was investigated using selected area LEED, SR-XPEEM and selected area XPS.

Figures 2(a) and 2(b) show the SR-XPEEM images taken for In 3*d* and Sb 3*d* photoelectrons, respectively. The energy resolution corresponds to 0.6 eV energy width. The photon energy was 530 eV for In 3*d* and 580 eV for Sb 3*d*, then the kinetic energy of the photoelectrons imaged was 83.2 eV for In 3*d* and 49.3 eV for Sb 3*d*. Duplicated images exposed for 1200 s were simply added to minimize the image blur by sample drift and to get sufficient signal-to-noise ratio. Figure 2(c) shows the bright-field LEEM image taken at an electron energy of 49.3 eV as the reference. The contrast observed in Figs. 2(a) and 2(b) is reversed. The dark region in Fig. 2(c), where the In/Si(111) $\sqrt{3}\times\sqrt{3}$ surface was initially located, shows much higher In 3*d* intensity than the bright region, and vice versa for Sb 3*d* photoelectrons. The bright region in Fig. 2(c) was initially the In/Si(111) $\sqrt{31}\times\sqrt{31}$ surface, in which the coverage of In is larger than that in the In/Si(111) $\sqrt{3}\times\sqrt{3}$ surface. The In 3d intensity distribution in SR-XPEEM image is opposite to the initial In/Si(111) surface.

The difference in the amounts of In and Sb in the dark and bright areas could simply explain the contrast of the SR-XPEEM images. In this case, the removal of In atoms by Sb exposure is required. That is, the In-Si bond is broken and the Sb-Si bond is newly formed. The In-Si bond breaking followed by the formation of the Sb-Si bond occurred. In the present study, the black dot appeared in the LEEM image as shown in Fig. 1(d). The intensity of In 3*d* photoelectrons around the black dot in the SR-XPEEM image (Fig. 2(a)) is higher than that in the surrounding region. Moreover, the Sb 3*d* intensity around the black dot in Fig. 2(b) is low. Therefore, the black dot that appeared

in Fig. 1(d) is considered to be the In island, although it is not known whether the island is a pure In metal one or not. At higher Sb coverage, the formation of a lot of In islands was observed and the surface showed no distinct In 3*d* peaks in the XPS spectrum. Therefore, the formation of an Sb-terminated Si(111) surface by the replacement of In atoms is the most plausible scenario in the present experimental condition.

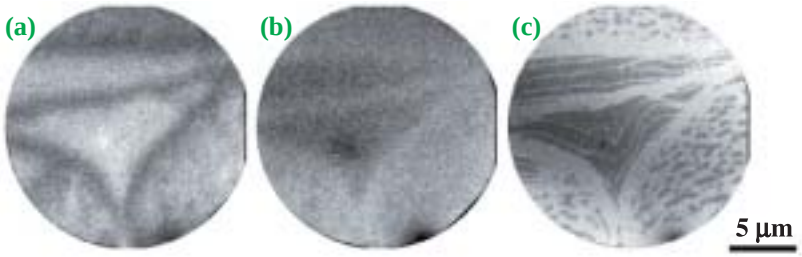

Fig. 2. **(a)** and **(b)** show SR-XPEEM images for In 3*d* and Sb 3*d* photoelectrons, respectively. The photon energy was 530 eV for In 3*d* and 580 eV for Sb 3*d*. The field-of-view was 20 μm. **(c)** Bright-field LEEM image of the same region as reference. The electron energy was 49.3 eV.

According to the above mentioned scenario, the chemical interaction of In and Sb atoms with Si might be modified. Then, it is quite interesting to get the local chemical information on the surface. The selected area XPS spectra were investigated for the purpose. Figures 3(a) and 3(b) show the selected area In 3*d* and Sb 3*d* XPS spectra, respectively. The probed areas are indicated by circles in Fig. 1(d). The solid lines show the selected area XPS spectra obtained at the area labeled as A, and the dotted lines at the area labeled as B. The intensity of In 3*d* photoelectrons from area A is larger than that from area B, and vice versa for the Sb 3*d* signal. The difference in intensity here denotes the quantitative contrast difference in the SR-XPEEM images shown in Fig. 3. The chemical shift, however, is hardly observed in both In 3*d* and Sb 3*d* spectra. Although the $\sqrt{3}\times\sqrt{3}$ and $\sqrt{31}\times\sqrt{31}$ surfaces exist on the initial In/Si(111) surface, the chemical environment is almost the same in both surfaces, which has been confirmed by the combined study of selected area XPS using LEEM. The replacement of In atoms by Sb adsorption would result in the simple intensity reduction in In 3*d* signal on both surfaces without any chemical shift. Once the replacement takes place, the chemical interaction of Sb with Si is uniquely determined. Then, the chemical shift for Sb spectra would not be expected as well in the initial stage.

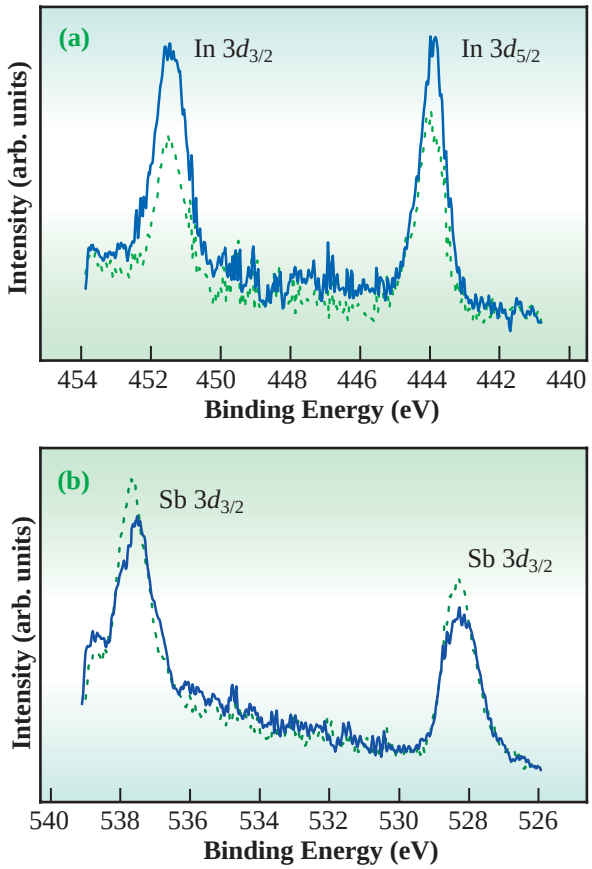

Fig. 3. Selected area **(a)** In 3*d* and **(b)** Sb 3*d* XPS spectra obtained in circles shown in Fig. 1**(d)**. The solid lines show XPS spectra taken in A, and the dotted line those in B. The photon energy was 530 eV for In 3*d* and 580 eV for Sb 3*d*.

The In coverage in the In/Si(111) $\sqrt{31}\times\sqrt{31}$ surfaces is larger than that in the In/Si(111) $\sqrt{3}\times\sqrt{3}$ surface. After Sb exposure, In 3*d* intensity in the initial $\sqrt{31}\times\sqrt{31}$ surface becomes smaller than that in the initial $\sqrt{3}\times\sqrt{3}$ surface. This indicates that the exchange rate between In and Sb depends on the surface structure. The exchange in the $\sqrt{31}\times\sqrt{31}$ surface proceeds faster than that in the $\sqrt{3}\times\sqrt{3}$ surface as the experimental finding. The reason for the different exchange rates, however, is not well understood at present.

T. Koshikawa[a,*], F.-Z. Guo[b] and T. Yasue[a]

[a] Fundamental Electronics Res. Inst. & Academic Frontier, Osaka Electro-Communication University
[b] SPring-8 / JASRI

*E-mail: kosikawa@isc.osakac.ac.jp

References

[1] T.H. Schmidt *et al.*: Surf. Rev. Lett. **5** (1998) 1287.
[2] H. Hirayama *et al.*: Appl. Surf. Sci. **33-34** (1988) 193.
[3] *F.-Z. Guo, T. Wakita, H. Shimizu, T. Matsushita, T. Yasue, T. Koshikawa, E. Bauer, K. Kobayashi: J. Phys. Condens. Matter* ***17*** *(2005) S1363.*

Strain Distribution in Surface Region of Thin Silicon Overlayers on Insulator

High-quality thin silicon overlayers (SOLs) in silicon-on-insulator (SOI) wafers have attracted much interest in recent years [1]. This is because thin, nanometer-thick SOLs (SNOLs) are expected to exhibit a clear quantum confinement effect at low temperatures and because they have a great potential as advanced Si substrates. To obtain a SNOL less than 50 nm thick, thermal oxidation of a SOL with a thickness of several hundred namometers on SOI wafers is usually employed. During the thermal oxidation, the thickness of the SOL decreases as the oxide thickness increases. In this way, cyclically thinning by thermal oxidation of a thick (>100 nm) SOL and by HF etching of the top silicon oxide (TOX) layers, one can produce thin (<50 nm) SNOLs on top of a buried silicon oxide (BOX).

It is well known, however, that strain exist in SOI wafers, originating from the difference in specific volume and thermal expansion coefficients between the Si and SiO_2 at the SiO_2/Si interface. The strain usually induces defects at the interface and inside the SNOL. This degrades the electronic and optical properties of the final structures.

In this work, we characterized the lattice strain and strain distribution in a 47-nm-thick SNOL on a SIMOX wafer using grazing incidence X-ray diffraction (GIXD) near the critical angle of total reflection using synchrotron radiation.

GIXD experiments were performed using the z-axis goniometer at beamline **BL24XU** [2]. The 0.124 nm X-ray wavelength was used at incident angle α varying from 0.01 to 0.4º. This is schematically shown in the inset of Fig. 1. We used <001>-oriented SIMOX wafers with a diameter of 15 mm. After etching a wafer in HF dilute solution, the wafer was oxidized at 1200 ºC in a 0.2% O_2/Ar mixture to form a silicon oxide layer on top of the SOL and promote an internal thermal oxide layer on the bottom of the SNOL. Then, the thermal oxide on the SNOL was removed in a HF bath and X-ray diffraction was measured from the 47-nm thick SNOL on top of the SIMOX wafer.

Figure 1 shows the (220) Bragg diffraction curves collected from the 47-nm-thick SNOL at different grazing angles from 0.01 to 0.2º. The strong peak at the center (θ=0) comes from bulk Si(220). Additional oscillating subpeaks (denoted as 0th, 1st, 2nd in Fig. 1) appear at the lower and higher sides of the

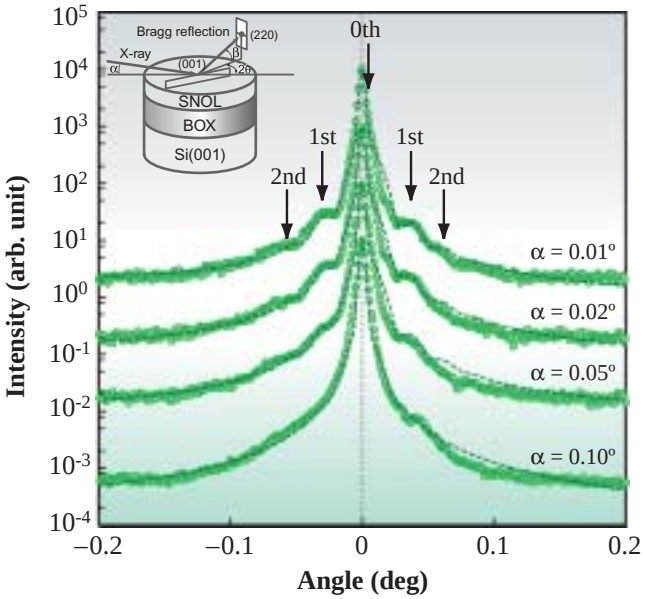

Fig. 1. Grazing incident X-ray diffraction curves of SIMOX wafer at different grazing angles. The broken lines are the kinematical calculations based on the structural model mentioned in the text. The inset shows a schematic diagram of grazing incident X-ray diffraction from the SIMOX wafer, where α, β, and 2θ represent the X-ray incident angle with respect to the sample surface, the angle between Bragg reflected beam and the sample surface, and the angle between the incident X-ray and the (220) plane.

Si(220) reflection, they are clearly observed for the grazing angles between 0.01º and 0.1º. However, for increasing grazing angle, the peaks merge and become unclear at the shoulder of the main peak. This suggests that they originate from the surface region of the sample. In addition, it can be seen that the oscillating peaks are asymmetric with respect to the center of the Si(220) peak. The asymmetric feature also becomes clear when decreasing the grazing angle from 0.1 to 0.01º. These findings indicate that the origin of the peak oscillation is independent of the strong peak related to the Si(220) reflection, suggesting the existence of finite domains at the SNOL surface.

The additional oscillating curves at the side of the main Si(220) peak can be explained in the framework of the kinematical scattering theory [3,4]. To reproduce the experimental curves, we constructed a structural model for the SNOL on the insulator, assuming that the SNOL is composed of two layers (surface region and underlying layers) with two different strain levels. Moreover, the surface region is composed of finite domains with less in-plane strain ε than the underlying SNOL. We also assume that the distribution of domain size is a Gaussian function, with average size D and standard deviation σ. The broken lines in Fig. 1 are the results of the kinematical calculations based on the two-layer model for different angles. The simulation reproduces well the experimental data. The GIXD shows that the difference in in-plane strain between the surface region of the SNOL and the remaining one is a few 10^{-4}. The size of the strain domain D on the surface region is about 500 nm with a deviation s of 70 nm.

To assess the thermal stability of the SNOL, we annealed the sample at 1000ºC and measured GIXD at the grazing angle of 0.01º. Figure 2 shows the GIXD curves obtained during the annealing at 1000ºC and at room temperature (RT) after the annealing. At 1000ºC, as seen in Fig. 2, the additional peaks completely disappear at the shoulder of the Si(220) (compare Fig. 1 and Fig. 2), which makes the peak symmetric with respect to θ=0. After the annealing, it is evident that the main peak becomes sharper while there are no additional peaks at the shoulder of the main peak. The broken lines in Fig. 2 are the simulation results obtained using the fitting parameters. These results clearly show that the post-annealing treatment is effective in improving the spatial inhomogeneous strain distribution in the SNOL.

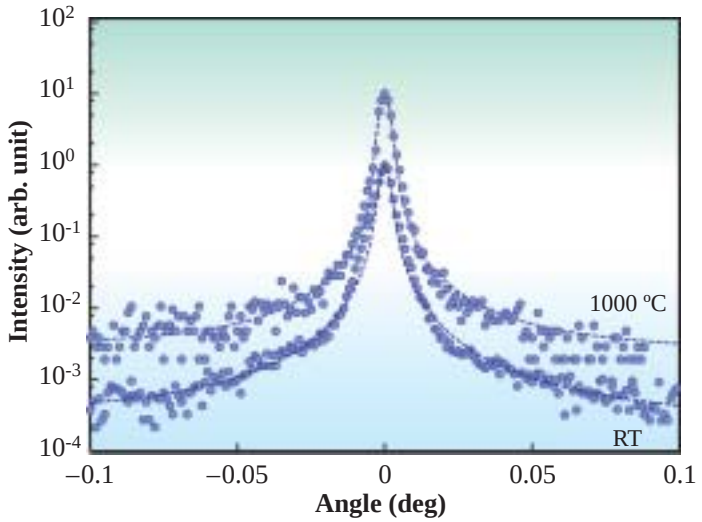

Fig. 2. Grazing incident X-ray diffraction curves of SIMOX wafer obtained at different temperatures. The broken lines are the kinematical calculations.

Hiroo Omi* and Tomoaki Kawamura

NTT Basic Research Laboratories, NTT Corporation

*E-mail: homi@will.brl.ntt.co.jp

References

[1] J. Camassel *et al.*: Phys. Rev. B **63** (2000) 035309.
[2] *H. Omi, T. Kawamura, S. Fujikawa, Y. Tsusaka, Y. Kagoshima and J. Matsui: Appl. Phys. Lett.* ***86*** *(2005) 263112.*
[3] V.S. Speriosu: J. Appl. Phys. **52** (1981) 6094.
[4] T. Baumbach *et al.*: J. Appl. Phys. **87** (2000) 3744.

Depicting Phase Separation in Polymer Blends by X-ray Phase Tomography

X-ray phase tomography using a crystal X-ray interferometer has been developed at beamline **BL20XU** [1]. This technique is attractive in the observation of weakly absorbing materials, and biological imaging results have been reported [2]. X-ray phase tomography reveals the distribution of the refractive index difference, which is approximately proportional to the mass density. The detection limit of the density deviation was evaluated to be a few mg/cm^3. This sensitivity is also attractive for the observation of polymer blend systems.

Blending polymers is commonly tried because the properties of plastic materials can be tailored to meet various demands, which is not possible with a single polymer. Many combinations of polymers are immiscible, and phase separation occurs in their blends and plays a significant role in determining their properties. Although phase-separated structures have been studied two-dimensionally for technical convenience, important quantities in three-dimensional space, such as the volume fractions of phases, the interfacial areas between coexisting phases, and interfacial curvatures, cannot be evaluated. It is clear that three-dimensional observation and analysis should be performed for the complete understanding of polymer blend morphologies.

X-ray phase tomography meets the demand, and we started research preliminarily with a test blend of polystyrene (PS) and poly(methyl methacrylate) (PMMA). A benzene solution containing 50 vol% PS and 50 vol% PMMA was freeze-dried. The resulting freeze-dried powder was annealed at 180 ºC in cylindrical holes (2 mm in diameter) made on a copper plate sandwiched in a melt-press machine.

Figure 1 shows the experimental setup for X-ray phase tomography. 17.7-keV X-rays were introduced into the X-ray interferometer, which was monolithically cut out of a silicon single-crystal ingot. Three crystal lamellae were formed, and one of those was characteristically thinned down to 40 μm to avoid spatial-resolution degradation [1]. A polymer blend sample was fixed on a rotation rod and immersed in water poured into a sample cell. X-ray interference patterns were recorded with a CCD-based X-ray image detector, whose effective pixel size was 3.14 μm.

Figure 2 shows a tomogram and a three-dimensional rendering view of the reconstructed data of the PS/PMMA blend [3]. Two phases in the blend were clearly depicted, and bicontinuous phase-separated structures were revealed. The volume ratio of the two phases was evaluated to be 52 : 48, in agreement with the blend composition. The bright and dark areas in Fig. 2(a) correspond to PMMA- and PS-rich phases, which were confirmed from the histogram of the reconstructed values shown in Fig. 3. The arrows indicate the values calculated for pure PS and PMMA. The peaks of the histogram appeared slightly inside the arrows, indicating that the PS-rich phase contained a small amount of PMMA and *vice versa*. This result quantitatively suggests that X-ray phase tomography can be used not only to depict structures but also to measure the composition of each phase, thereby allowing the determination of a phase diagram.

X-ray phase tomography is thus demonstrated to be an attractive technique for the three-dimensional observation of a polymer blend as is. Since no

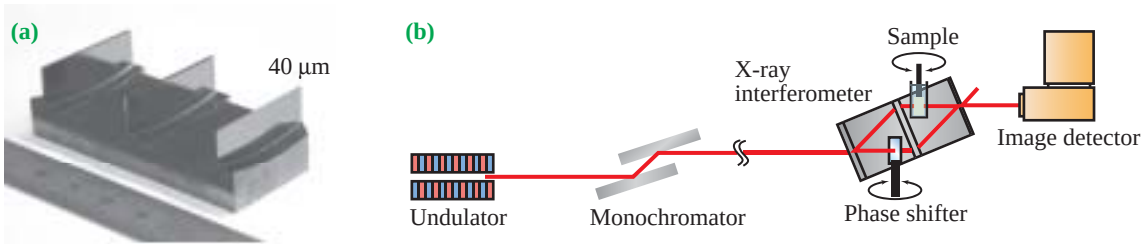

Fig. 1. X-ray interferometer having 40-μm lamella **(a)** and experimental setup for phase-contrast X-ray tomography **(b)**.

treatment is required for contrast enhancement, some intriguing experiments, such as the *in situ* three-dimensional tracing of phase separation and the observation of structural changes under mechanical stress, would be feasible. In addition, X-ray phase tomography can contribute to the observation of not only binary blends but also ternary and more complex blends.

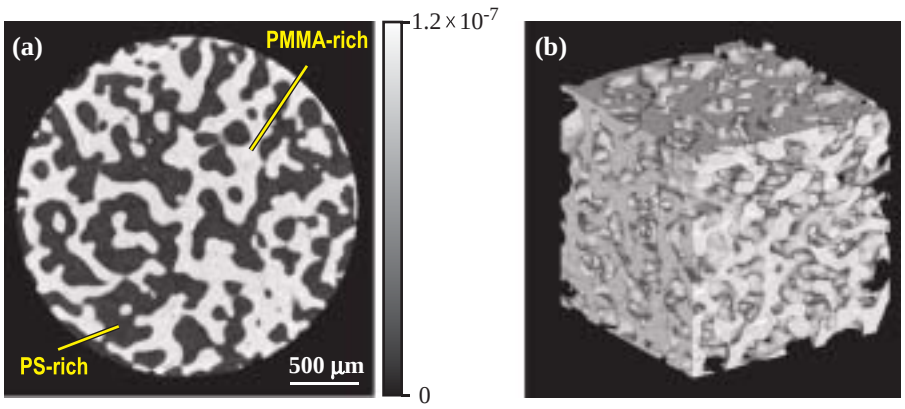

Fig. 2. Image of PS/PMMA blend reconstructed by X-ray phase tomography: **(a)** phase tomogram and **(b)** volume rendering view of reconstructed three-dimensional data, where PS-rich region has been made transparent.

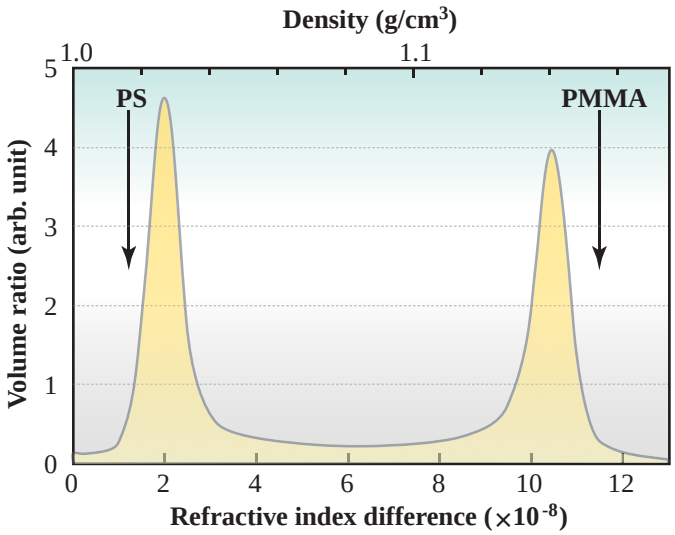

Fig. 3. Histogram of refractive index difference between sample and water. The refractive index differences of pure PS and PMMA are indicated by arrows.

Atsushi Momose[a,*] and Hiroshi Jinnai[b]

[a] Graduate School of Frontier Sciences, The University of Tokyo
[b] Department of Polymer Science and Engineering, Kyoto Institute of Technology

*E-mail: momoe@exp.t.u-tokyo.ac.jp

References

[1] A. Momose *et al.*: AIP Proc. **705** (2004) 1259.
[2] A. Momose: Jpn. J. Appl. Phys. **44** (2005) 6355.
[3] *A. Momose, A. Fujii, H. Kadowaki and H. Jinnai: Macromolecules **38** (2005) 7197.*

Time-resolved X-ray Imaging of Solidification Phenomena of Metallic Alloys

Observation is the first step for understanding various phenomena. In the field of crystal growth, solidification and casting processes of metallic alloys, it is an important issue to avoid some defects, which are introduced during the processes, to reduce segregation, which is the inhomogeneous distribution of constituent elements, and consequently to improve the quality of products. There are still ambiguities in understanding the mechanisms, since we cannot see what really happens inside the products using conventional microscope systems.

The third generation synchrotron radiation facilities such as SPring-8 enable us to use monochromatized hard X-ray that is attractive for observing the microstructure of various materials. Recently, time-resolved X-ray imaging was successfully performed to observe the crystal growth and solidification of Sn-based and Al-based alloys [1-3]. The observations improve our understanding of the solidification mechanism and help us develop numerical simulation techniques with high reliability.

In our research projects at SPring-8, we focus on the fragmentation of dendrite arms during the solidification of metallic alloys. One of the major defects is the stray crystals that have undesirable crystal orientations. There are two possible mechanisms for the formation of the stray crystals. One is nucleation ahead of the advancing dendrites, and the other is the detachment of fragmented dendrites from the mushy zone. Until now, it is uncertain whether the fragmentation is an origin of the stray crystals or not.

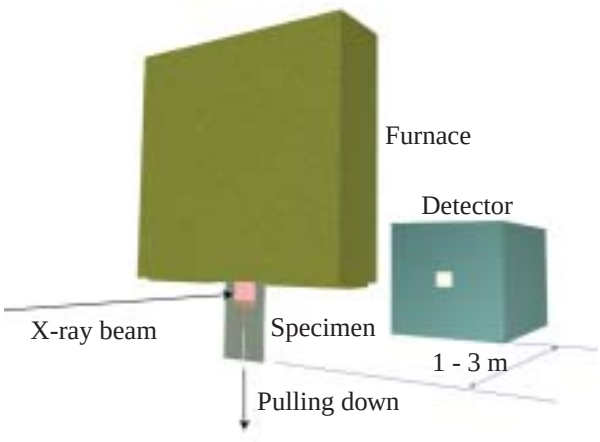

Fig. 1. Configuration of specimen, furnace and X-ray detector for observing solidification of Sn-Bi alloys and Al-Cu alloys.

The experiments were performed at beamline **BL20B2**. A large beam size at the experimental hutch (approximately 300 mm in the horizontal direction and 20 mm in the vertical direction) has an advantage for observing rather macroscopic phenomena at a high spatial resolution. Figure 1 shows a schematic illustration of the observation systems. An image detector consisting of an X-ray direct-sensing pickup tube SATICON was used (10 or 4 μm/pixel, 1024 pixels × 1024 pixels and 10-bit resolution). The sample-to-detector distance was 2.5-3.0 m, which gave rise to the phase contrast along with the absorption contrast. The specimen was melted in the furnace and unidirectional solidification was performed by pulling the specimen at a given rate.

It is of interest to investigate the detachment of dendrite arms when the dendrites grow in the enlarged region after passing the re-entrant corner, since the stray crystals were often observed in the enlarged region for turbine blades. Figure 2 shows a sequence of the obtained images (Sn-21mass%Bi alloy, 100 μm in thickness) after the dendrite passed the re-entrant corner. The dendrites immediately covered the enlarged region after passing around the corner (t = 16 s). The detachment of a fragmented dendrite arm was seen at the position indicated by an arrow (33.07 s). The detached crystals grew ahead of the advancing front and consequently the stray crystal was formed (138.67 s). The observations showed that the deceleration of the growth rate significantly enhanced the fragmentation and detachment. The observation proved that the detachment of the segmented crystals provided seeds of the stray crystals.

The direct observation was also performed for Al-Cu alloys. Figure 3 shows a sequence of the solidification of the Al-15mass%Cu alloy at a pulling rate of 10 μm/s. The Al dendrites are rapidly developed in the undercooled region and then grew in the vertical direction. The fragmentation frequently occurred and the detached crystals became stray crystals ahead of the advancing dendrites from the

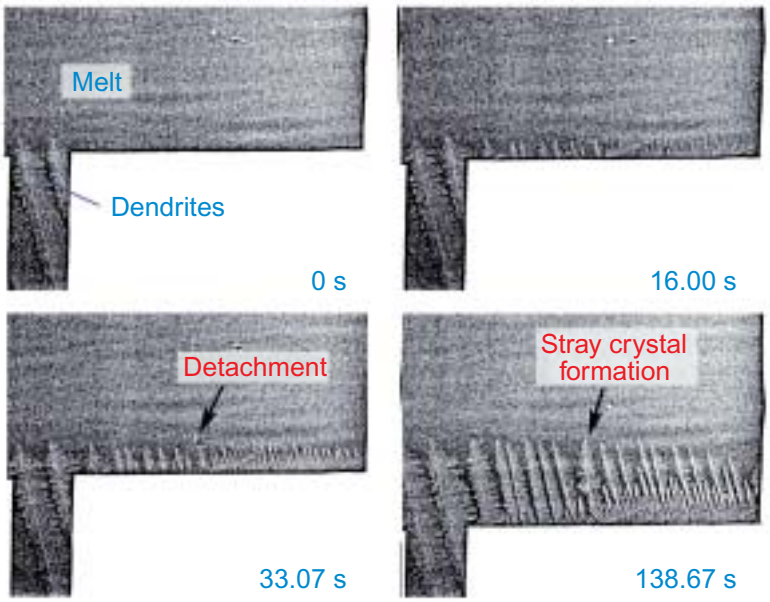

Fig. 2. Sequential photographs of microstructure after dendrites pass re-entrant corner during unidirectional solidification of Sn-21mass%Bi alloy at growth rate of 10 μm/s. The X-ray energy was 29 keV, which is just below the Sn edge.

bottom. In this case, the equiaxed grain structure, which consisted of fine grains with isotropic shape, was produced due to the frequent fragmentation. The observations show that the fragmentation dominantly contributes to the formation of the stray crystals and equiaxed grains, comparing the nucleation in the melt.

The time-resolved imaging using synchrotron radiation is the best technique for observing solidification phenomena of metallic alloys. The development of X-ray imaging techniques is expected to improve understanding of various phenomena.

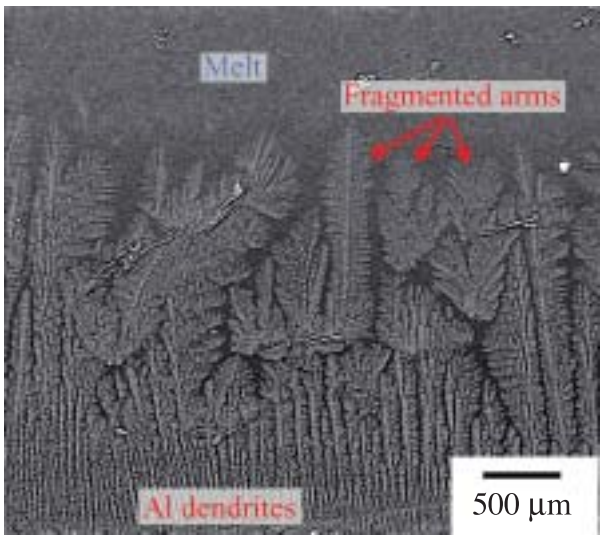

Fig. 3. Sequence of solidification for Al-15mass%Cu alloy at pulling rate of 10 μm/s. The X-ray energy was 29 keV.

Hideyuki Yasuda

Department of Adaptive Machine Systems,
Osaka University

E-mail: yasuda@ams.eng.osaka-u.ac.jp

References

[1] R.H. Mathiesen *et al.*: Phys. Rev. Lett. **83** (1999) 5062.
[2] R.H. Mathiesen *et al.*: Metall. Mater. Trans. B **33** (2002) 613.
[3] *H. Yasuda, I. Ohnaka, K. Kawasaki, A. Sugiyama, T. Ohmichi, J. Iwane and K. Umetani: J. Crystal Growth **262** (2004) 645.*
[4] B. Li *et al.*: Phys. Rev. E **70** (2004) 062602.

Materials Science
Electronic & Magnetic Properties

Materials science, in particular, to investigate the electronic and/or magnetic properties of novel materials, has been markedly in progress these years in SPring-8 because of the improvement and development of new beamlines dedicated to these researches. The high brilliance of SPring-8 is a strong merit to revealing the precise and detailed electronic and magnetic structures of materials by high-resolution and high-quality measurements. Representative experimental techniques used here include high-resolution X-ray scattering, high-resolution X-ray photoemission spectroscopy, high-resolution Compton scattering. A variety of novel materials such as strongly correlated *d*-electron oxides, low-dimensional organic salts, superconducting diamond, and novel uranium compounds are intensively studied by use of the above-mentioned high-resolution spectroscopies. Furthermore, not only bulk materials but also thin films and nanoparticles have become a target of intensive researches because of the recent enhancement of the close relationship between basic and industrial researches. Kubota *et al.* have observed an interesting ferro-type orbital ordering in $Ca_{2-x}Sr_xRuO_4$ by resonant X-ray scattering and interpreted it in terms of two-dimensional crystal field and superexchange interaction. High-resolution X-ray scattering by Terasaki *et al.* has revealed the basic mechanism of charge ordering/melting in an "organic thyristor." Both occupied and unoccupied band structures of high-T_c superconductors have been studied by resonant inelastic X-ray scattering (report by Ishii *et al.*). Recently discovered superconducting diamond has been investigated X-ray photoemission spectroscopy (report by Yokoya *et al.*), which has revealed the electron dispersion essential to the superconductivity. A variety of peculiar properties of nanoparticles such as nanomagnetism and nonlinear optics have been studied by spin-polarized Compton scattering (report by Duffy *et al.*) and high-energy X-ray spectroscopy (report by Yoshikawa *et al.*). Compton scattering has been also applied on Ni-Al shape-memory alloy by Dugdate *et al.* to study the Fermi surface topology. The phonon density of states of PtFe alloy films has been studied by nuclear resonant inelastic scattering for application to perpendicular magnetic recording (report by Hideshima *et al.*). A beautiful Fermi surface of $UFeGa_5$ has been obtained by bulk-sensitive high-resolution X-ray angle resolved photoemission spectroscopy (report by Fujimori *et al.*). Research activity in Materials Science at SPring-8 is now rapidly expanding in both methods and materials. New proposals and challenges are welcome.

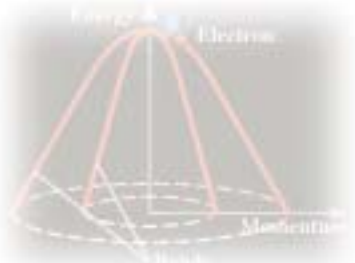

Takashi Takahashi
Department of Physics
Tohoku University

Ferro-type Orbital State in Mott Transition System $Ca_{2-x}Sr_xRuO_4$ Revealed by Resonant X-ray Scattering Interference Technique

Among 4*d* electron systems, $Ca_{2-x}Sr_xRuO_4$ has especially attracted attention because of its rich and novel ground states such as in Mott transition [1-3]. Since $Ca_{2-x}Sr_xRuO_4$ has four 4*d* electrons in the t_{2g} orbitals, the significance of orbital degree of freedom is invoked. Nevertheless, few works have been carried out on orbital ordering in 4*d* electron system so far.

The anisotropic tensor of an X-ray susceptibility signal is enhanced near an absorption edge. However, conventional resonant X-ray scattering (RXS) measurement is not useful for the observation of a *ferro-type* orbital state, in which charges are distributed with the same local symmetry at each Ru ion site. This is because it is difficult to extract the signal for a ferro-type orbital state at Γ points, which is accompanied with large magnitude of a fundamental reflection by Thomson scattering. However, the RXS interference technique can offer unique access to observing the *ferro-type* orbital state, in which the signal of the ferro-type orbital state is magnified by the interference with a fundamental signal. In the present study, it is revealed that the observation of orbital states by a resonant X-ray scattering interference technique is significant for understanding the rich phase diagram of $Ca_{2-x}Sr_xRuO_4$ [4].

Figure 1(a) shows the resonant X-ray scattering configuration at beamline **BL46XU**. ψ is an azimuthal angle, which is the angle around scattering vector *Q*, while φ_A indicates the detector angle. The X-ray absorption of Ru is observed around 22.15 keV in Fig. 1(b). Figure 1(c) shows the energy profiles at *Q* = (0 2 6) with polarization angles of φ_A = 98° (dotted thick line) and 82° (thin line) at ψ = 270° at 305 K.

The *interference term* for ferro-type orbital ordering is obtained by subtracting the intensity at φ_A = 82° from that at φ_A = 98°: for φ_A = 90° ± Δφ (Δφ = 8°), $I(90° + \Delta\varphi) - I(90° - \Delta\varphi) \propto 2Re\,[F_{\sigma\sigma}\ F_{\sigma\pi}]\ \sin^2 2\theta_A \sin 2\Delta\varphi$, in which $F_{\sigma\sigma}$ and $F_{\sigma\pi}$ denote the scattering factors for the $\sigma \rightarrow \sigma$ and $\sigma \rightarrow \pi$ scattering processes, respectively, and $2\theta_A$ is the scattering angle in the analyzer crystal.

$F_{\sigma\pi}$ has information on the asphericity of 4*d* charge distribution, while $F_{\sigma\sigma}$ corresponds to a fundamental signal. Noticeable point is that $F_{\sigma\pi}$ is enhanced by $F_{\sigma\sigma}$. Therefore, a small signal for a ferro-type ordering is detectable. The resonant signal for ferro-type orbital ordering in Fig. 1(c) appears near the *K* absorption edge. Near the *K* absorption edge, an atomic scattering factor is represented by a tensor and the RXS signal has an azimuthal angle dependence.

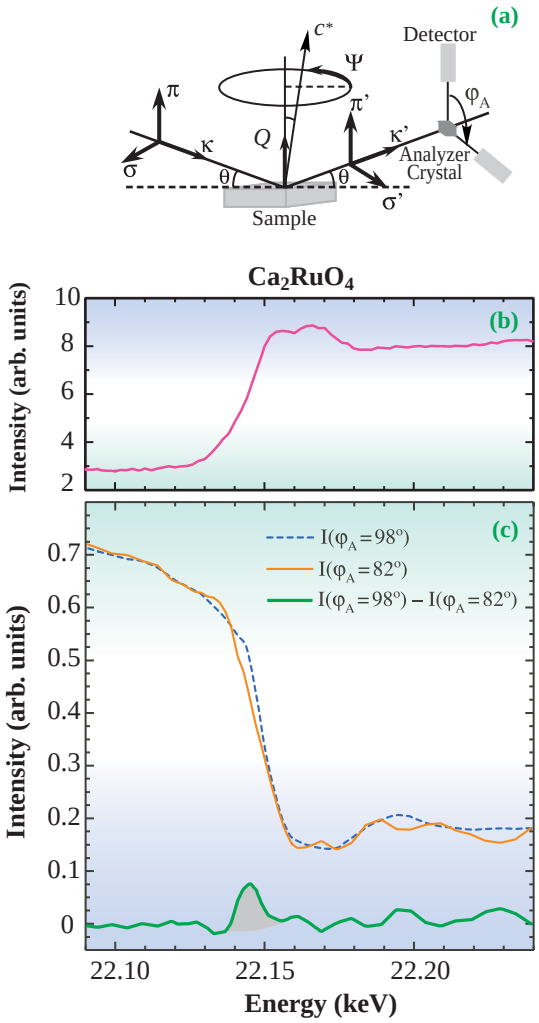

Fig. 1. **(a)** Schematic picture of resonant X-ray scattering configuration. **(b)** Incident energy dependence of X-ray fluorescence in Ca_2RuO_4. **(c)** Energy scans at 305 K for φ_A = 98° (dotted thick line) and φ_A = 82° (thin line) at azimuthal angle ψ = 270° at *Q* = (0 2 6). The bottom thick line is obtained by subtracting the energy spectrum at φ_A = 82° from that at φ_A = 98°, which corresponds to the interference term.

In order to further verify that the observed resonant signal corresponds to the orbital ordering in Ca_2RuO_4, the azimuthal angle dependence has been observed. The magnitude of the signal at the main edge peak at 305 K exhibits the characteristic oscillation with the 360º period (Fig. 2). $F_{\sigma\pi}$ mainly contributes to the ψ dependence of the interference signal.

The observed ψ dependence shows the minimum and maximum at around ψ = 90º and 270º, respectively, while the intensity approaches zero at ψ = 0º and 180º. These features are well explained by the analysis for a ferro-type d_{xy} ordering, as shown in Fig. 2. In addition, we analyzed the ψ-dependence of the resonant signal at Q = (0 2 14), which is also consistent with the behavior of the d_{xy} orbital.

Figure 3 shows the temperature dependence of the RXS signal. Above 200 K, the magnitude gradually decreases and then disappears near a metal-insulator transition (T_{MI} ~ 357 K). Note that the RXS signal is observed at room temperature. Braden *et al.* showed that at around 300 K, the apical bond length RuO(2) is almost equal to the averaged equatorial bond length RuO(1) [5]. Therefore, the Jahn-Teller distortion is unreasonable for the main origin of the orbital ordering in Ca_2RuO_4. As discussed in ref. [6], it is possible that a two-dimensional crystal field as well as a superexchange interaction play a significant role in stabilizing the ferro-type orbital ordering, in addition to the Jahn-Teller effect of a RuO_6 octahedron.

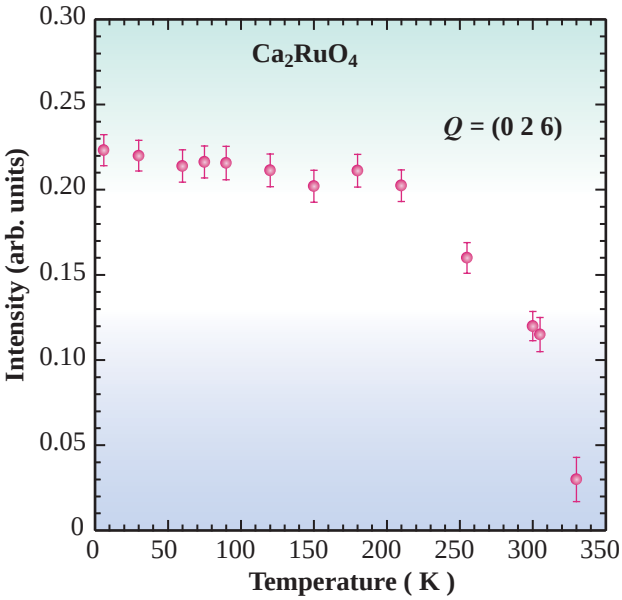

Fig. 3. Temperature dependence of *interference term* at Q = (0 2 6) with ψ = 270º in Ca_2RuO_4.

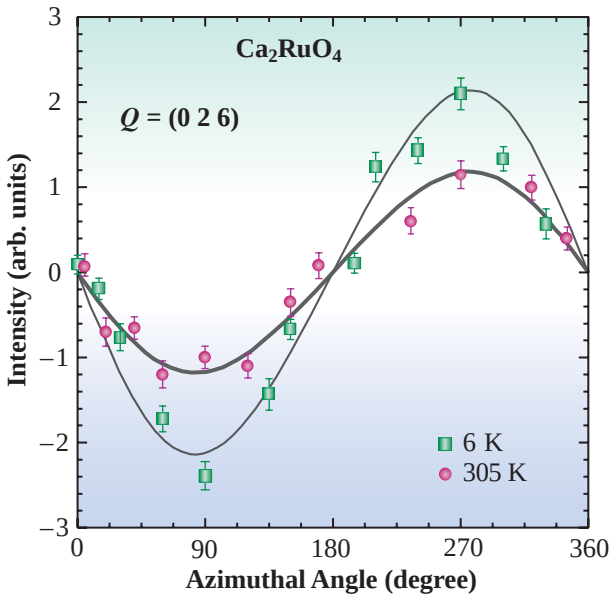

Fig. 2. Azimuthal angle dependences of *interference term* for main edge peak at 305 K and 6 K at Q = (0 2 6).

M. Kubota[a,*], Y. Murakami[b,c] and M. Mizumaki[c]

[a] Photon Factory, IMSS, KEK
[b] Department of Physics, Tohoku University
[c] SPring-8 / JASRI

*E-mail: masato.kubota@kek.jp

References

[1] Y. Maeno *et al.*: Nature **372** (1994) 532.
[2] S. Nakatsuji *et al.*: J. Phys. Soc. Jpn. **66** (1997) 1868.
[3] S. Nakatsuji and Y. Maeno: Phys. Rev. Lett. **84** (2000) 2666.
[4] *M. Kubota, Y. Murakami, M. Mizumaki, H. Ohsumi, N. Ikeda, S. Nakatsuji, H. Fukazawa and Y. Maeno: Phys. Rev. Lett.* ***95*** *(2005) 026401.*
[5] M. Braden *et al.*: Phys. Rev. B **58** (1998) 847.
[6] Fang *et al.*: Phys. Rev. B **69** (2004) 045116.

Organic Thyristor

Recently, "intrinsically inhomogeneous" states have attracted a keen interest in strongly correlated electron systems. A prime example is high-temperature superconductors, in which nano-size domains of the superconducting-gap and pseudo-gap phases coexist in the CuO_2 plane. Another example is perovskite manganites, in which percolation paths of the ferromagnetic metal phase in the charge-ordered insulator phase give rise to colossal magneto-resistance effects. These nano-scale inhomogeneities are driven by the interaction between coexisting/competing phases, not by imperfections of the crystal, hence the name "intrinsic inhomogeneity" [1].

We have discovered giant nonlinear conduction in the organic salt θ-$(BEDT\text{-}TTF)_2CsM(SCN)_4$ (M=Co and Zn), which is a brand new function in intrinsically inhomogeneous states [2,3]. This salt is a layered material composed of conducting BEDT-TTF layers and insulating $CsM(SCN)_4$ layers alternately stacked along the *b*-axis, as shown in Fig. 1(a). The Greek letter θ specifies a packing pattern of BEDT-TTF molecules in the conducting layer, representing a "triangular lattice". Because of charge frustration on the triangular lattice, two kinds of charge order compete at low temperatures [4]. They are eventually frozen as nano-size domains without long-range order, forming an intrinsically inhomogeneous charge-order phase.

Figure 1(b) shows the voltage-current (*V*-*I*) characteristics of the θ-salt. The current is applied along the *b*-axis direction (perpendicular to the conducting BEDT-TTF plane). The voltage is highly nonlinear with respect to current, and negative derivative resistance is clearly seen from 10^{-5} to 10^{-4} A. Since the voltage-current curve is essentially identical to that of a thyristor device, we call the θ-salt an organic thyristor.

A high-intensity X-ray from beamline **BL02B1** has revealed that the data in Fig. 1 stems from the melting of the charge order domains by an external current. Figure 2 shows the DC current dependence of the two diffuse peaks at $\mathbf{q}_1$=(2/3 *k* 1/3) and $\mathbf{q}_2$=(0 *k* 1/2) at 12 K, which correspond to competing charge order domains. Clearly, the $\mathbf{q}_2$ peak loses its intensity with increasing current, while the $\mathbf{q}_1$ peak remains nearly intact. This is a non-equilibrium thermodynamic phenomenon in which ordered phase domains are melted by an external steady flow. On a cold wintry

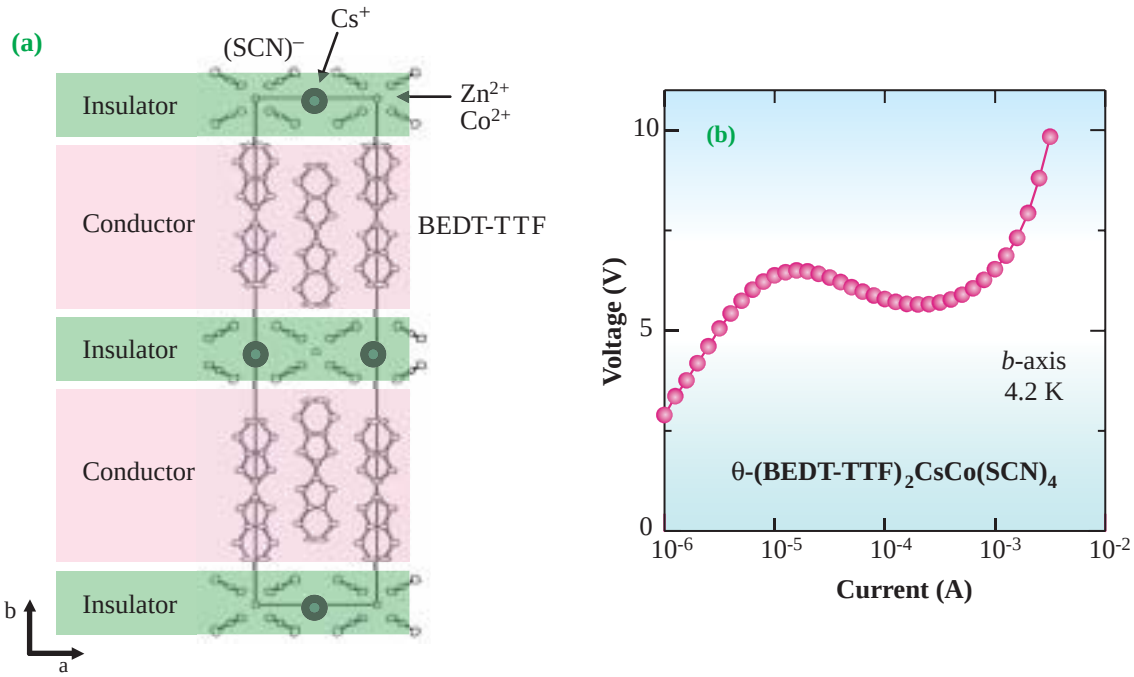

Fig. 1. **(a)** Crystal structure of θ-$(BEDT\text{-}TTF)_2CsM(SCN)_4$ (M=Co and Zn). **(b)** Voltage-current characteristics for M=Co at 4.2 K. The current was applied along the *b*-axis direction.

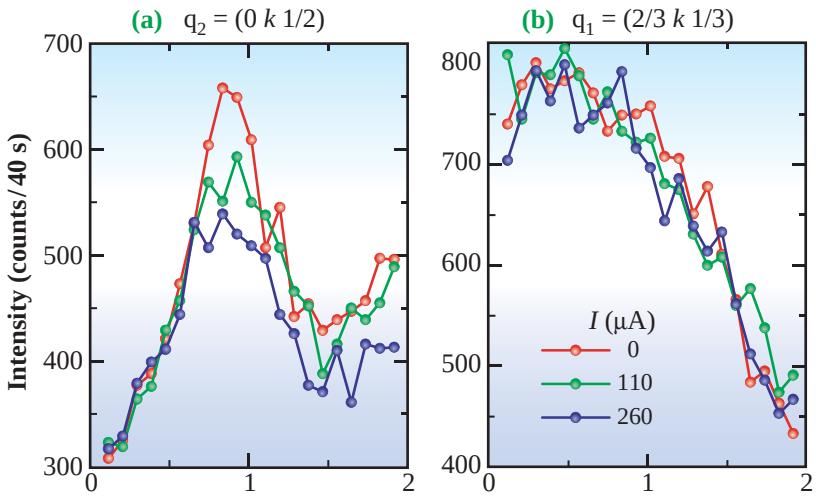

Fig. 2. Diffuse peaks for competing charge ordered domains for various external currents. **(a)** $\mathbf{q}_2$ = (0 *k* 1/2) and **(b)** $\mathbf{q}_1$=(2/3 *k* 1/3). Only the $\mathbf{q}_2$ peak loses its intensity with increasing current.

day, we often see ice on a pond and water flowing in a river. The present result is a manifestation of such phenomena in a sea of conduction electrons.

Since a thyristor is an essential component in an inverter (DC-to-AC converter), the organic thyristor is expected to work as a "nature-made" inverter. In fact, we have succeeded in observing DC-to-AC conversion in this organic salt. We measured the ac voltage component across a standard resistor connected to the sample in series for various DC bias voltages at 4.2 K. As shown in Figs. 3(a) and 3(b), the nonlinear resistance shows an abrupt jump between 6.2 and 6.5 V, at which a large AC signal of 40 Hz suddenly appears. The observed oscillation is nearly sinusoidal, as shown in the fast Fourier transform (FFT) spectra in Fig. 3(c). The results shown here suggest a new way to design electronic devices using intrinsically inhomogeneous states.

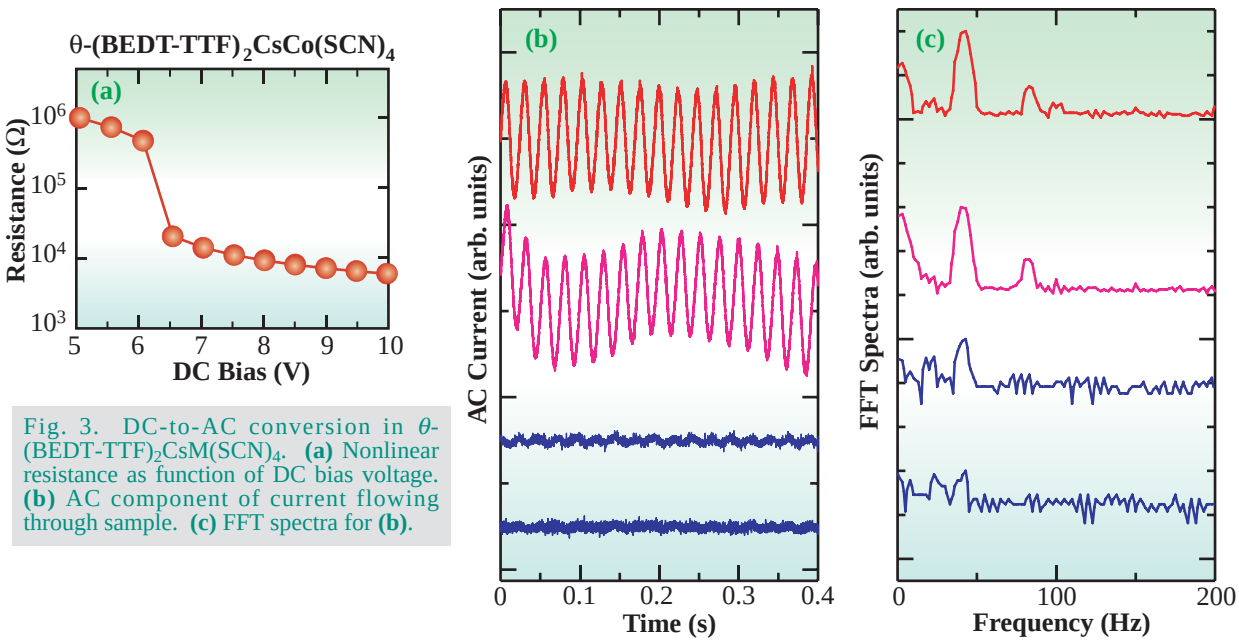

Fig. 3. DC-to-AC conversion in *θ*-(BEDT-TTF)$_2$CsM(SCN)$_4$. **(a)** Nonlinear resistance as function of DC bias voltage. **(b)** AC component of current flowing through sample. **(c)** FFT spectra for **(b)**.

Ichiro Terasaki

Department of Applied Physics, Waseda University

E-mail: terra@waseda.jp

References

[1] J. Burgy *et al.*: Phys. Rev. Lett. **87** (2001) 277202.
[2] K. Inagaki *et al.*: J. Phys. Soc. Jpn. **73** (2004) 3364.
[3] *F. Sawano, I. Terasaki, H. Mori, T. Mori, M. Watanabe, N. Ikeda, Y. Nogami and Y. Noda: Nature **437** (2005) 522.*
[4] M. Watanabe *et al.*: J. Phys. Soc. Jpn. **68** (1999) 2654.

Resonant Inelastic X-ray Scattering of High-T_c Superconducting Cuprates

Recently, resonant inelastic X-ray scattering (RIXS) has been developed as a new spectroscopic technique to measure the electronic structure of materials utilizing intense synchrotron radiation X-rays [1]. Especially, RIXS in the hard X-ray regime has the great advantage that the momentum dependence of the excitations can be measured unlike conventional optical methods. While angle-resolved photoemission spectroscopy, which also gives momentum-resolved spectra, essentially yields the one-particle spectra for the occupied states below the Fermi energy, RIXS yields two-particle (electron-hole pair) excitation from which both occupied and unoccupied states are elucidated. We have applied the RIXS technique to strongly correlated electron systems, such as manganites and cuprates, in order to understand the electronic structure and underlying correlation effects. Here, we show two RIXS studies at the Cu *K*-edge on high-T_c superconducting cuprates, $YBa_2Cu_3O_{6.93}$ (YBCO, T_c = 93 K) and $Nd_{1.85}Ce_{0.15}CuO_4$ (NCCO, T_c = 25 K). The carrier concentration of both compounds is at the optimal condition for the superconducting transition temperature.

The RIXS experiments were carried out at beamline **BL11XU**. A Si(400) channel-cut monochromator and a Ge (733) analyzer were used. The total energy resolution estimated from the FWHM of the elastic scattering is about 400 meV. The energy of the incident X-ray was tuned near the Cu *K*-edge (~ 8990 eV) where the excitation across the Mott gap is resonantly enhanced. More precisely, the Mott gap in the cuprates is the charge-transfer gap between the Zhang-Rice singlet band and the upper Hubbard band.

YBCO has a unique crystal structure and two crystallographically inequivalent Cu sites exist in the unit cell as shown in Fig. 1. One (dark blue) is in the CuO_2 plane, which is a common unit in the most superconducting cuprates. The other (light blue) forms a CuO chain running along the ***b***-axis. Substantial anisotropic character in both normal and superconducting states indicates that the CuO chain also contributes to the bulk electronic properties. A separate measurement of the electronic structure between the CuO chain and the CuO_2 plane is necessary to understand the role of the chain and we could succeed in determining it from the momentum dependence of a twin-free crystal. Figure 2 shows the RIXS spectra of YBCO in the *ab* plane and two characteristic excitations can be seen. One is an excitation at 2 eV, which is prominent at the zone boundary of the ***b****-direction; that is, the intensity is enhanced near (0,π) and (π,π). The other is a broad excitation at 1.5-3.5 eV, which is observed at all the momenta. Clear momentum dependence along the ***b****-direction is direct evidence that the peak at 2 eV is the excitation across the Mott gap of the chain because the excitation along the ***b****-axis should be equivalent to that along the ***a****-axis in the plane. On the other hand, the momentum-independent broad feature corresponds to the excitation in the CuO_2 plane. These characters are well reproduced by a theoretical calculation based on the one-dimensional Hubbard model for the chain and the two-dimensional one for the plane when different values of the on-site Coulomb energy are assumed. This means that the Mott gap of the chain is found to be smaller than that of the plane [2].

While the carrier in the most superconducting cuprates is a hole, superconductivity in $Nd_{2-x}Ce_xCuO_4$ occurs by electron-doping. Therefore $Nd_{2-x}Ce_xCuO_4$ is an important material to study the asymmetry

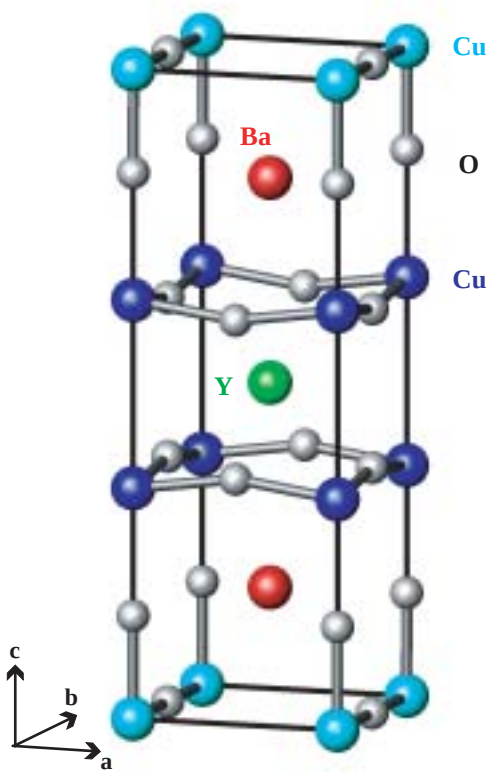

Fig. 1. Crystal structure of $YBa_2Cu_3O_7$. Two crystallographically inequivalent Cu sites exist in the unit cell. One (dark blue) is in the CuO_2 plane and the other (light blue) forms a CuO chain running along the ***b***-axis.

of hole- and electron-doping. In general, an interband excitation across the Mott gap and an intraband excitation by doped carriers are observed when carriers are introduced in the Mott insulators. The intraband excitation in hole-doped $La_{2-x}Sr_xCuO_4$ appears as a continuous spectral weight below the Mott gap [3]. In contrast, intraband excitation in electron-doped $Nd_{2-x}Ce_xCuO_4$ is more prominent and shows a clear dispersion relation. Figure 3 shows the RIXS spectra of NCCO. The spectral shape near the Brillouin zone center is insensitive to the carrier concentration (x), and the 2 eV peak at (0,0) is the interband excitation across the Mott gap. Another excitation in the spectra is broad but dispersive. As a function of the momentum transfer, the excitation shifts to higher energy up to 2-2.5 eV at the Brillouin zone boundary accompanied by an increase in spectral width. Because its intensity is roughly proportional to x, it can be identified as the intraband excitation by the doped electrons. It is noted that the larger resonance of the intraband excitation in NCCO comes from the difference in resonance process; namely, the intraband excitation in the electron-doped system is fairly enhanced when a core hole is screened by a doped electron in the intermediate state of the resonant scattering, and this process is absent in the hole-doped systems. These experimental results are consistent with a theoretical calculation. Furthermore, we found that the intraband excitation in the RIXS spectra is quantitatively similar to the dynamical charge correlation function of the doped carrier in the CuO_2 plane [4].

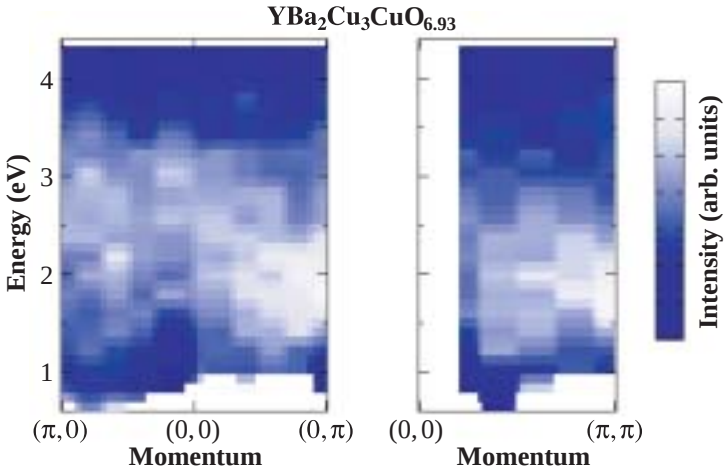

Fig. 2. RIXS spectra of $YBa_2Cu_3O_{6.93}$. The tail of the quasielastic scattering and the excitations at higher energy are subtracted. The excitation across the Mott gap of the CuO chain is enhanced at 2 eV at (0,π) and (π,π), while that of the CuO_2 plane is broad at 1.5-3.5 eV and almost independent of the momentum transfer.

In summary, our results on YBCO and NCCO demonstrate that the excitation across the Mott gap persists even in the carrier-doped metallic state. This is an important character of strongly correlated metals. We also observed the dispersion relation of the intraband excitations in NCCO by taking advantage of the resonant process of the electron-doped system.

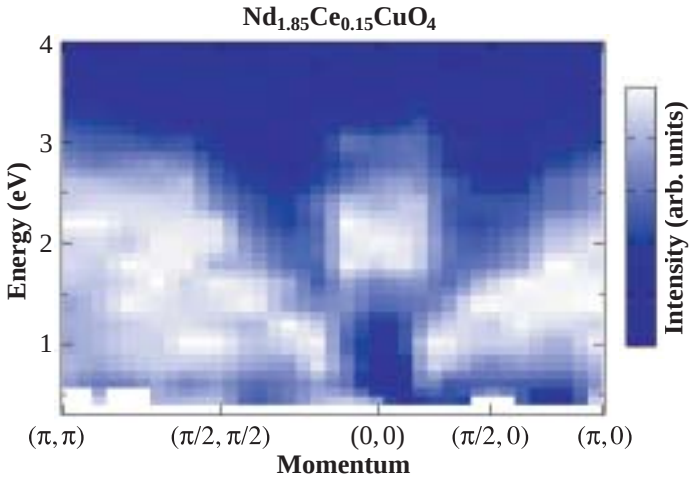

Fig. 3. RIXS spectra of $Nd_{1.85}Ce_{0.15}CuO_4$. The tail of the quasielastic scattering and the excitations at higher energy are subtracted. The peak at 2 eV at the Brillouin zone center is the interband excitation across the Mott gap, and the dispersive excitation with momentum-dependent width is the intraband excitation in the upper Hubbard band.

Kenji Ishii

SPring-8 / JAEA

E-mail: kenji@spring8.or.jp

References

[1] A. Kotani and S. Shin: Rev. Mod. Phys. **73** (2001) 203.
[2] *K. Ishii, K. Tsutsui, Y. Endoh, T. Tohyama, K. Kuzushita, T. Inami, K. Ohwada, S. Maekawa, T. Masui, S. Tajima, Y. Murakami and J. Mizuki: Phys. Rev. Lett.* ***94*** *(2005) 187002.*
[3] Y.-J. Kim *et al.*: Phys. Rev. B **70** (2004) 094524.
[4] *K. Ishii, K. Tsutsui, Y. Endoh, T. Tohyama, S. Maekawa, M. Hoesch, K. Kuzushita, M. Tsubota, T. Inami, J. Mizuki, Y. Murakami, and K. Yamada: Phys. Rev. Lett.* ***94*** *(2005) 207003.*

Electronic Structures of Superconducting Diamond Films

Diamond, known as a jewel, exhibits outstanding physical properties, e.g., hardness, high thermo-conductivity, a wide band gap, and so on. Slightly doped diamond is a semiconductor and is often called a next generation semiconductor due to these properties that exceed those of other semiconductors [1]. In 2004, a Russian group reported superconductivity in a heavily boron-doped diamond [2]. The observation of the new property in diamond may promote application research for inventing new devices that utilize both the semiconducting and superconducting properties. Even fundamentally, superconductivity in diamond has stimulated a discussion on the origin of the metallic states responsible for the superconductivity [3]. This is because, even though the electric properties of lightly doped semiconductors are understood very well, those in highly doped semiconductors have not been fully understood.

In order to study the electronic structure of heavily boron-doped diamond, we have performed soft X-ray angle-resolved photoemission spectroscopy (SXARPES) for homoepitaxially grown heavily boron-doped (111) diamond films made by a microwave plasma assisted chemical vapor deposition method [4]. SXARPES is a unique experimental method that allows us to determine bulk-sensitive momentum(k)-resolved electronic states, namely electronic bands, of solids, by detecting the kinetic energy and direction of a photoelectron that is emitted from a sample being irradiated with a soft X-ray (Fig. 1). The measurements have been performed at beamline **BL25SU**, using an 825 eV photon energy with energy and angular resolutions of ~250 meV and ±0.1°.

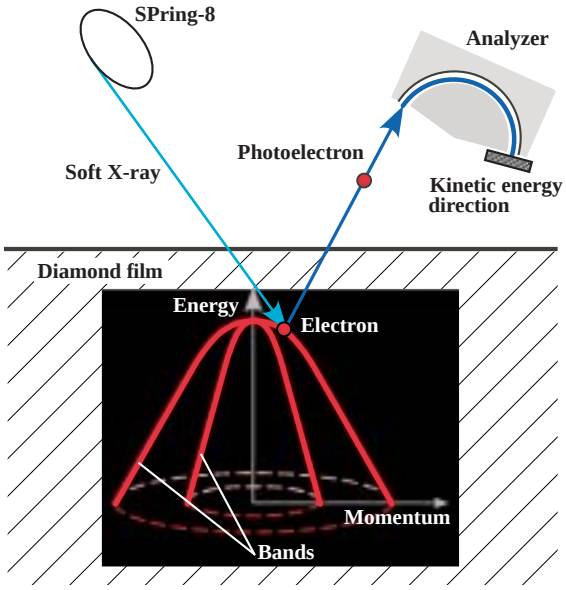

Fig. 1. Schematic illustration of SXARPES measurements.

Some of the physical parameters of three heavily boron-doped diamond films (BDD1, 2 and 3) are listed in Table 1. Figure 2(a) shows a valence band SXARPES intensity map from BDD2 measured along a blue curve in the Brillouin zone (Fig. 2(b)). In the map, higher intensity regions forming several curves correspond to experimentally determined bands. The shape of band dispersions is unique to a particular material (like a fingerprint of a person). Thus, from a comparison with calculated bands for pure diamond, one can find that the electronic structures of diamond retains with heavy boron doping [5].

It is known that the conducting properties of solids are determined by the electronic structures near the Fermi level (E_F), which is the highest occupied energy level. Boron doping dependent SXARPES intensity maps in the vicinity of E_F are shown in Figs. 3(a), 3(b), and 3(c). For BDD1, we clearly see three bands near E_F (1, 2, and 3) and find two bands 1 and 2 that form a parabolic-like dispersion having energy and intensity maxima at k = 0. As the boron concentration increases, the intensity of the top of the parabolic-like

Table 1. Transition temperatures, and boron and carrier concentrations of measured samples. $T_{c,mag.}$, onset of superconducting transition from magnetization measurement, $T_{c,res.}$, onset of superconducting transition from resistivity measurement. $n_{B,SIMS}$, boron concentration determined from secondary ion mass spectroscopy (SIMS). n_{PES}, carrier concentration estimated from present PES studies.

	BDD1	BDD2	BDD3
T	Nonsuperconducting (T > 1.7 K)	$T_{c,res.}$ ~ 2.5 K	$T_{c,mag.}$ ~ 7.0 K
n_{SIMS} m	2.88×10^{20}	1.18×10^{21}	8.37×10^{21}
n_{S} m		6.6×10^{20}	1.9×10^{21}

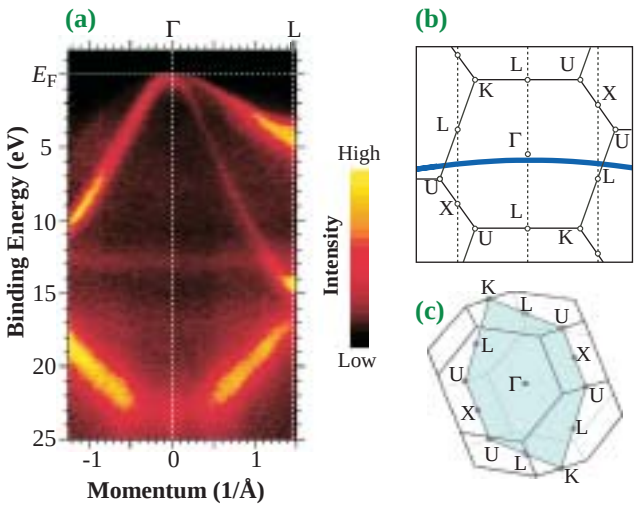

Fig. 2. **(a)** Valence band SXARPES intensity map of heavily boron-doped diamond film measured along a blue curve in two-dimensional Brillouin zone of diamond **(b)**, which is a slice (sky blue plane) of three-dimensional Brillouin zone **(c)**.

band decreases and, consequently, the intensity maps of BDD2 and 3 show local minima at k = 0 near E_F. For BDD3, the top of the parabolic-like band appears to be terminated, which is indicative of introducing holes into the top of the valence band. From comparisons with calculated band dispersions, the locations of E_F with respect to the top of the valence band were estimated to be 0.2 ± 0.1 eV for BDD2 and 0.4 ± 0.2 eV for BDD3 [5]. The systematic shift of E_F indicates increasing carrier numbers as a function of boron concentration. From a simple analysis of the observed data, the concentration of carriers can be also estimated (n_{PES}, in Table 1).

The doping-dependent SXARPES has shown that occupied electronic structures are consistent with the diamond bands and E_F shifts systematic with respect to the valence band. These results indicate that holes in the diamond bands play an essential role for the metallic properties of the heavily boron-doped diamond superconductor, and also provide a foundation for the possible development of diamond-based devices. Moreover, the present study demonstrates the usefulness and reliability of SXARPES for studying electronic structures of new materials. We hope that this study promotes further SXARPES works on various types of materials at SPring-8 in the near future.

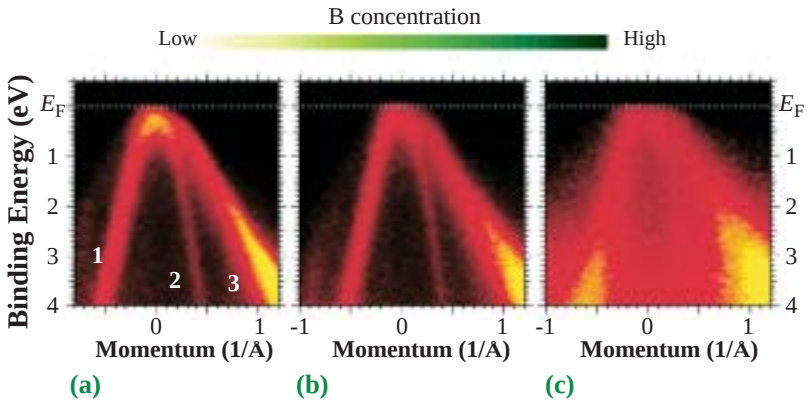

Fig. 3. **(a)-(c)** Near $_F$ SXARPES intensity maps of heavily boron-doped diamond fims with different boron concentrations.

Takayoshi Yokoya

The Graduate School of Natural Science and Technology, Okayama University

E-mail: yokoya@cc.okayama-u.ac.jp

References

[1] C. E. Nebel and J. Ristein: Thin-film diamond II, Elsevier B.V., Amsterdam (2004).
[2] E. A. Ekimov *et al.*: Nature **428** (2004) 542.
[3] G. Baskaran: cond-mat/0404286; For example, L. Boeri *et al.*: Phys. Rev. Lett. **93** (2004) 237002.
[4] Y. Takano *et al.*: Appl. Phys. Lett. **85** (2004) 2851.
[5] *T. Yokoya, T. Nakamura, T. Matsushita, T. Muro, Y. Takano, M. Nagao, T. Takenouchi, H. Kawarada and T. Oguchi: Nature **438** (2005) 647.*

Size-enhanced Spin Moment in NiO Nanoparticles

Nanomagnetism promises much, given the scope of proposed applications and associated phenomena. These include the targeted delivery of drugs to tumors, magnetic storage with nanomagnetic particles, improved battery lifetimes and also quantum computing. For much of this exploitation, there is a pressing need to study directly the microscopic spin-polarized electronic properties.

In the experiment reported here, spin-polarized Compton scattering was used on the **BL08W** beamline to study NiO nanoparticles. Compton scattering measures a one-dimensional projection of the electron momentum density in the sample. In the spin-polarized technique, as used here, one can obtain the momentum density distribution of just those electrons that contribute to the net *spin* magnetic moment (the orbital moment is not measured). The Compton profile is obtained from the spectrum of inelastically scattered high energy photons with the use of the known scattering cross-section. The sample is maintained in a magnetic field, which is reversed regularly so that profiles can be obtained for both field directions. Use of circularly polarized photons results in a difference between these profiles, and upon subtraction, the charge scattering cancels out, but the spin scattering does not. A schematic of the experimental set-up is shown in Fig. 1. The total area under the spin-polarized Compton profile gives the total *spin* moment.

In this experiment, nanoparticles of NiO were investigated. Three samples were synthesized by heat treatment of NiOH powder [1,2], and characterized using powder X-ray diffraction and SQUID magnetometry. The estimated mean particle diameters of the samples under study were 6±1 nm, 8±1 nm and 13±1 nm. Bulk NiO is an antiferromagnet, with T_N = 522K. In bulk NiO, there is a 17% orbital contribution to the total magnetic moment [3]. NiO nanoparticles, however, exhibit ferromagnetism, with moments of around 0.05 μB per formula unit in the smallest particles. The contribution of the orbital moment in the nanoparticles is not known. In Fig. 2 the hysteresis loops for the three different particle size are plotted. The magnetic moment is observed to increase with decreasing particle size. It is thought that the ferromagnetic component is confined to the near-surface region, so that the spin moment increases with smaller particle sizes because the surface to volume ratio is larger.

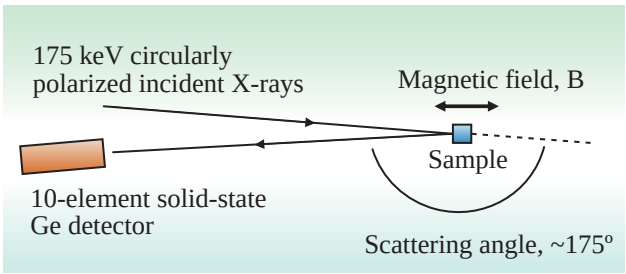

Fig. 1. A schematic of the experimental configuration used to measure spin-polarized Compton profiles on BL08W.

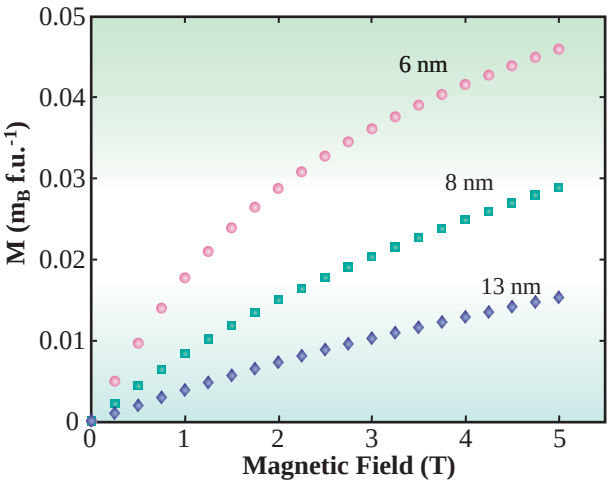

Fig. 2. The total moment, measured with SQUID magnetometry, as a function of applied magnetic field for the three particle sizes under study measured at 10 K.

In Fig. 3 we plot the magnetic Compton profile for the smallest NiO nanoparticle sample measured in a magnetic field of 2.5 T and a temperature of 10 K. The data are compared to a spin-polarized Compton profile of bulk ferromagnetic nickel. At large momenta (p_z > 2.5 a.u., say) the profile of bulk nickel is dominated by the 3*d* spin moment [4]. The fact that the two profiles are identical in this region shows that the 6±1nm nanoparticles also exhibit this 3*d*-like moment. However, at low momenta the two profiles are distinctly different. This is likely to be due to the insulating nature of NiO and its different electronic band structure. For a fuller discussion electronic

structure calculations will need to be performed and compared to the data.

The spin magnetic moment was found for our samples by integrating the magnetic Compton profiles. The 8±1 nm and 13±1 nm NiO samples have a spin moment that are comparable to the total moment. However, the smallest of the samples has a spin moment that appears to be significantly larger than the total magnetic moment. This is the most surprising result; it suggests that there is an appreciable orbital moment, and that there is an *antiparallel* arrangement of the spin and orbital moments.

In summary we have used magnetic Compton scattering to study the effect of reducing the diameter of NiO nanoparticles on the spin moment. The spin moment increases as the nanoparticle diameter decreases. It appears that an enhanced orbital moment is exhibited by the smallest particles, and further studies are planned to investigate this.

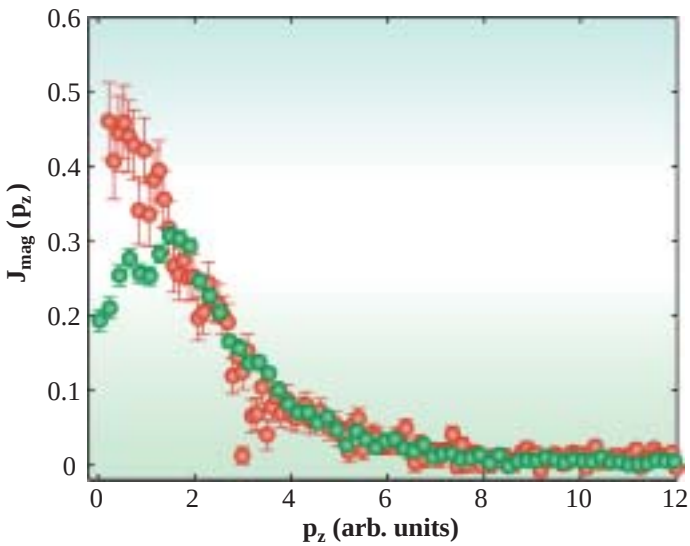

Fig. 3. Magnetic Compton profile of NiO nanoparticles with a mean particle size of 6±1 nm (red circles) and of bulk nickel (green circles).

Chris Steer, Caroline Shenton-Taylor and Jon Duffy*

Department of Physics, University of Warwick, U.K.

*E-mail: j.a.duffy@warwick.ac.uk

References

[1] S.A. Makhlouf *et al.*: J. Appl. Phys. **81** (1997) 5561.
[2] S.D. Tiwari and K. P. Rajeev: Phys. Rev. B. **72** (2005) 1004433.
[3] V. Fernandez *et al.*: Phys. Rev. B **57** (1998) 7870.
[4] M.A.G. Dixon, J.A. Duffy, S. Gardelis, J.E. McCarthy, M.J. Cooper, S.B. Dugdale, T. Jarlborg and D.N. Timms: J. Phys. Condens. Matter **10** (1998) 2759.

High Energy XPS and XANES Analysis of Ag-Diacetylene Hybrid Nanoparticles Related to Plasmon Damping

It is well known that electric field enrichment by surface plasmon excitation on a metal is useful for enhancing nonlinear optical properties. A nanometer-sized metal particle is the most suitable material for realizing nonlinear optical properties owing to its large surface area and quantum confinement effect. Neeves and Birnboim have suggested that hybrid nanocrystals constructed of a core-sphere and spherical-shell have an attractive nonlinear optical susceptibility [1].

Masuhara *et al.* succeeded in synthesizing core-shell type hybridized nanocrystals using the co-reprecipitation procedure [2]. They used diacetylene monomers which were composed of 1,6-di(N-carbazolyl)-2,4-hexadiyne (DCHD), and covered Ag nanoparticles. They found that the surface plasmon in these hybridized Ag/diacetylene nanoparticles was damped by the polymerization of diacetylene after ultraviolet (UV) light irradiation. Figure 1 shows the transmission electron microscope (TEM) image for Ag-diacetylene hybridized nanocrystals and the visible absorption spectral change of hybridized nanocrystals with UV irradiation [3]. It was clearly observed that the absorbance peak of the surface plasmon (marked with LSP in Fig. 1(b)) of the Ag core was damped while that of an exciton (marked with EA in Fig. 1(b)) of the polydiacetylene shell increased. The surface plasmon peak eventually disappeared after 10 minutes of UV irradiation.

Neeves and Birnboim [1] showed theoretically that the simple coupling between the optical properties of metal and polystyrene decreases the intensity of the surface plasmon peak in some cases. However, according to their calculation, the surface plasmon remains as a consequence of coupling and the decrease in the surface plasmon peak coincides with the drastic energy shift of the plasmon. It should be noted that the experimental result in Fig. 1(b), which showed plasmon annihilation and no energy shift of the surface plasmon during plasmon damping, is significantly different from Neeves and Birnboim's theoretical analysis results. This peculiar phenomenon leads us to consider other mechanism of plasmon damping.

In this work, we have focused attention on the core Ag structure before/after diacetylene polymerization. For this, we have measured the high energy XPS spectra of these nanocrystals to evaluate the electronic structure of hybrid nanocrystal, especially core Ag particles on which a surface plasmon exists. Ag-diacetylene nanocrystals were dispersed on a Si wafer. The detailed process of synthesizing nanocrystals is described in ref. [2]. The high energy XPS experiment was performed at beamline **BL15XU**. The photon energy was set to be 4750 eV (the maximum analyzing energy is 4800 eV for the XPS machine at BL15XU). Figure 2 shows the valence band XPS spectra of the Ag core of hybridized nanocrystals before/after UV irradiation. The valence band XPS spectrum of Ag metal is also indicated as a reference. In Fig. 2, it can be concluded that we observed no difference between the valence band XPS spectra of the Ag core covered with monomer-diacetylene and the Ag core covered with polydiacetylene. However, there is a difference in valence band XPS spectra between the hybrid nanocrystal and the Ag metal. These results can be summarized as follows: "4*d* band narrowing", "5*s* band enrichment", "broadening of Fermi edge", and "Fermi edge shift to higher binding energy." Usually, these types of phenomena are explained on the basis of two models. One is a chemical reaction of core Ag with other elements (such as carbon and oxygen). The other is a cluster size effect. The cluster size effect has been well investigated for simple metal clusters on a substrate. For example, Roulet *et al.*

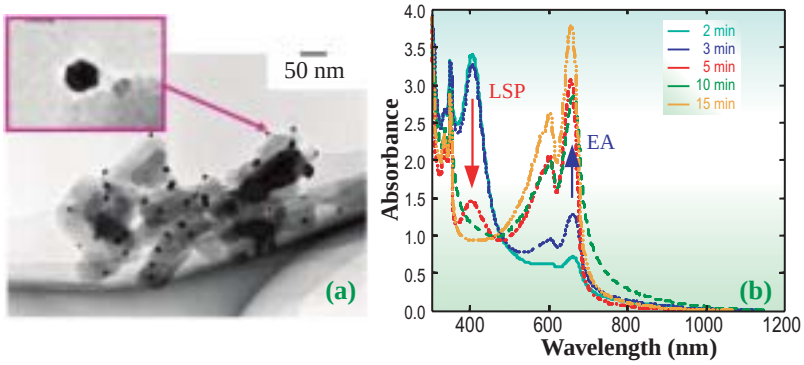

Fig. 1. TEM image of Ag-diacetylene hybridized nanocrystals **(a)** and its absorption spectral change during solid-state polymerization of diacetylene by UV irradiation **(b)** [3]. The inset of Fig. 1**(b)** indicates the irradiation time of UV.

discussed that the *d* valence-band width of XPS spectra for Au clusters on a NaCl(100) substrate becomes narrower with decreasing cluster size, and the critical size for band narrowing is 4 nm (about 10^3 atoms in a cluster). Tanaka *et al.* pointed that a 3.8 nm Ag cluster on HOPG substrate has a broad Fermi edge of UPS spectra [4].

In Fig. 2, we could not identify which model mentioned above is the actual one. We have, therefore, performed Ag-element-specific spectroscopy for checking a chemical reaction of Ag. Usually, one measures a chemical shift of XPS inner-shell peaks for checking the chemical reaction, but a sharp Ag 3*d* XPS peak is not sensitive to the chemical reaction. Therefore, we have measured the X-ray absorption near edge structure (XANES) spectra at the Ag L_3 edge by detecting Ag L_3MM Auger peaks, since the XANES spectra of Ag are very sensitive to a chemical reaction [5]. Figure 3 shows the XANES spectra of the Ag L_3 edge for hybridized nanocrystals before/after sufficient UV irradiation. The XANES spectrum of Ag metal [5] is also indicated in Fig. 3 as a reference. These data led us to recognize that the Ag core of hybridized nanocrystals was metallic and stable before/after UV irradiation.

Since XANES spectra clarified that the overall Ag core was metallic, we can conclude that the XPS valence band of the Ag core shown in Fig. 2 is caused by the cluster size effect. It should be noted that this cluster size effect is visible under the condition that the cluster size is smaller than about 4 nm as mentioned above. However, TEM data (e.g. in Fig. 1) showed that the average size of the overall Ag core was roughly estimated to be 15 nm. We considered with much interest that the Ag core is a lump of clusters smaller than 4 nm from the viewpoint of electronic structure.

It is well known that a plasmon comes from a collective oscillation of conduction electrons, and its intensity is dependent on the electron mean free path of conduction electrons. Muvlaney stated that conduction electrons are largely scattered by the surface with decreasing size of the metal cluster, and a smaller mean free path dependent on the cluster size results in the stronger plasmon damping [6]. This means that the shortening of electron mean free path on the Ag core's surface of hybridized nanocrystals results in the stronger damping of the surface plasmon when Ag core size is unchanged. It should be noted that this type of plasmon damping phenomenon, which shows a vanishingly small plasmon peak shift and enables plasmon annihilation as a consequence, is consistent with the experimental result in Fig. 1. According to Muvlaney's s study, a cluster size less than 4 nm is small enough for us to take account of plasmon damping. Since the overall Ag core of hybridized nanocrystals remained metallic after UV irradiation, we had better consider a part of the Ag core surface which cuts off surface plasmon oscillation spreading over the small cluster surface. We explained as a hypothesis that the surface plasmon damping of hybridized nanocrystals after UV irradiation is caused by the generation of spots, where the interface of the Ag core and diacetylene is non-metallic, on the Ag core surface by the UV irradiation. These spots might be coming from a local chemical reaction or a local optical-property-mixing at part of the interface of the Ag core and the diacetylene shell.

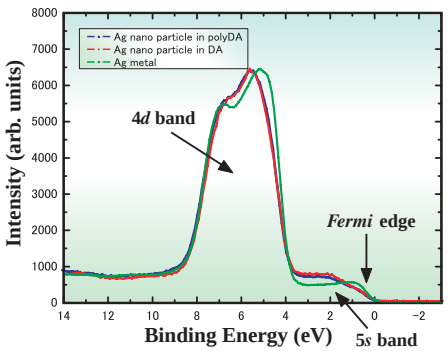

Fig. 2. Valence band XPS spectra of core Ag of hybridized nanocrystals before/after UV irradiation [3]. The valence band XPS spectrum of bulk Ag metal is also indicated as a reference. The X-ray energy was 4750 eV.

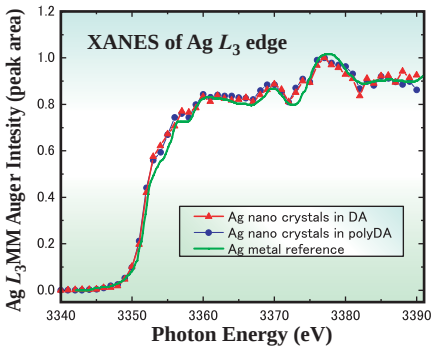

Fig. 3. XANES spectra of Ag L_3 edge for hybridized nanocrystals before/after UV irradiation. The XANES spectrum of Ag metal [5] is also indicated as a reference.

Hideki Yoshikawa[a,*] and Hidetoshi Oikawa[b]

[a] National Institute for Materials Science
[b] Institute of Multidisciplinary Research for Advanced Materials, Tohoku University

*E-mail: hyoshi@spring8.or.jp

References

[1] A.E. Neeves and M.H. Birnboim: J. Opt. Soc. Am. B **6** (1989) 787.
[2] A. Masuhara *et al.*: Jpn. J. Appl. Phys. **40** (2001) L1129.
[3] *H. Oikawa, A. M. Vlaicu, M. Kimura, H. Yoshikawa, S. Tanuma, A. Masuhara, H. Kasai and H. Nakanishi: Nonlinear Optics, Quantum Optics* ***34*** *(2005) 275.*
[4] A. Tanaka *et al.*: Surface Science **532-535** (2003) 281.
[5] M.T. Czyyk *et al.*: Phys. Rev. B **39** (1989) 9831.
[6] P. Mulvaney: Langmuir **12** (1996) 788.

Observation of a Strongly Nested Fermi Surface in the Shape-Memory Alloy $Ni_{0.62}Al_{0.38}$

Smart alloys which exhibit shape-memory and super-elastic phenomena have been deployed in a wide variety of applications ranging from actuators in aircraft wings to surgical instruments. However, an atomic-scale understanding of the origin of the martensitic transformation, the structural transformation at the heart of these phenomena, is still lacking. It has been hypothesized that lattice vibrations are the key, an idea supported by first-principles calculations indicating that strong coupling of certain phonons to the electrons (phonon softening), due to particular features in the Fermi surface, plays a crucial role [1]. It is well-known that when parallel pieces of Fermi surface exist in a metal, there will be a strong electronic response at the wavevector which translates, or nests, one parallel piece onto the other. This role of the Fermi surface in influencing the electron-phonon coupling was extensively investigated during the last two decades where premartensitic phenomena [2] were explained in terms of Fermi surface nesting.

In order to make a direct comparison with the Fermi surface predicted by band theory, we performed *ab initio* electronic structure calculations to reproduce the earlier work of Stocks *et al.* [3] for the disordered $Ni_{0.62}Al_{0.38}$ alloy (Fig. 1). We employed the fully relativistic Koringa-Kohn-Rostoker (KKR) method within the atomic sphere approximation, and the disorder was taken into account by the coherent potential approximation.

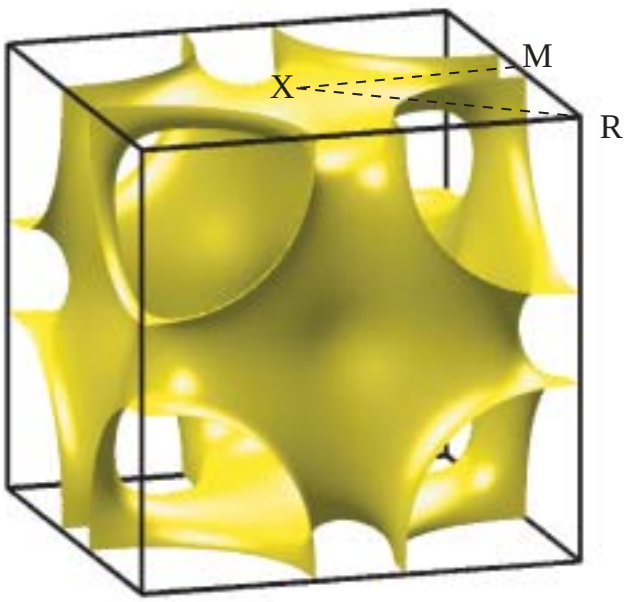

Fig. 1. Calculation of the Fermi surface using the KKR-CPA method. The Γ point is at the centre of the cubic Brillouin zone, and some other symmetry points are labelled.

Our single crystal sample was cut by spark erosion from a single grain of a large ingot of $Ni_{0.62}Al_{0.38}$ grown using the Bridgman method. A total of twenty-four Compton profiles along different crystallographic directions were measured at room temperature on the high-resolution Compton spectrometer of beamline **BL08W** [4]. This spectrometer is of the Cauchois type, consisting of a crystal analyzer and a position-sensitive detector, with a resolution FWHM at the Compton peak of ~0.16 atomic units. Compton scattering is a robust technique insensitive to defects or disorder, providing a one-dimensional projection (double integral) of the underlying bulk electron momentum distribution. For each Compton profile approximately 300,000 counts in the peak data channel were accumulated. A three-dimensional momentum density was reconstructed from this set of 24 profiles and then folded back into the first Brillouin zone to obtain the occupation density. The experimental Fermi surface (shown in Fig. 2) was extracted by contouring this density at a level fixed by an extremum in the first derivative along a direction where our calculations indicated the Fermi surface was likely to be well-defined.

A plane-by-plane inspection of the Fermi surface throughout the Brillouin zone revealed that a vector ~ 0.18 [1,1,0] ($2\pi/a$) connects a large area in the manner predicted in [1]. The plane through the BZ at k_z = 0.48 (π/a) is shown in Fig. 3, with the nesting vector indicated.

Clearly, the general shape of the experimental Fermi surface (Fig. 2) agrees well with the calculation (Fig. 1). As discussed above, the regions of Fermi surface responsible for the nesting are observed experimentally to be relatively flat. This, in conjunction with the large density of states (predicted by the calculations) spanning these wavevectors, provides a large propensity for nesting. There is, however, some noteworthy discrepancy between the calculated and experimental Fermi surfaces.

Experimentally, a neck is observed to open around the X-point of the Brillouin zone whereas according to the calculations this sheet remains closed. The calculated bandstructure reveals flat (almost dispersionless) bands along X-M and M-R, lying just below the Fermi level, leading to a van Hove singularity in the density of states at that energy. The opening up of a Fermi surface neck along Γ-X implies that the Fermi level has crossed below this van Hove singularity and may be indicative of the impending lattice instability at the martensitic transformation (where the Fermi surface would undergo more substantial rearrangement).

In conclusion, we have presented the experimental Fermi surface of the disordered alloy $Ni_{0.62}Al_{0.38}$ from the results of Compton scattering experiments, providing evidence in support of the intimate link between the electronic structure and the observed phonon softening.

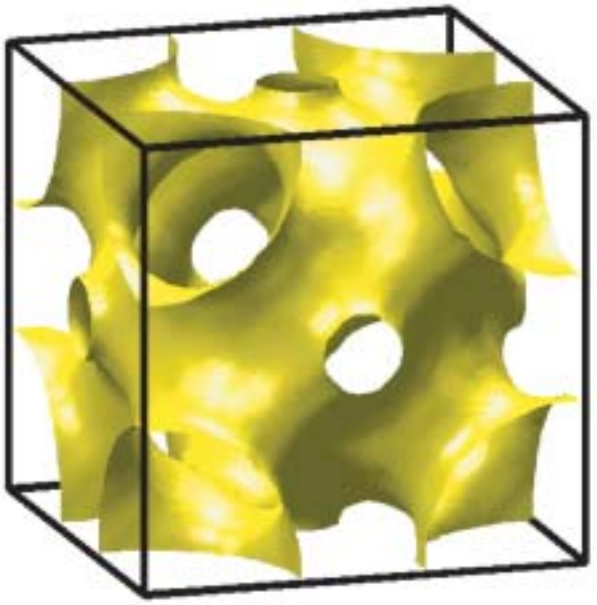

Fig. 2. Reconstruction of Fermi surface from 24 measured directional Compton profiles.

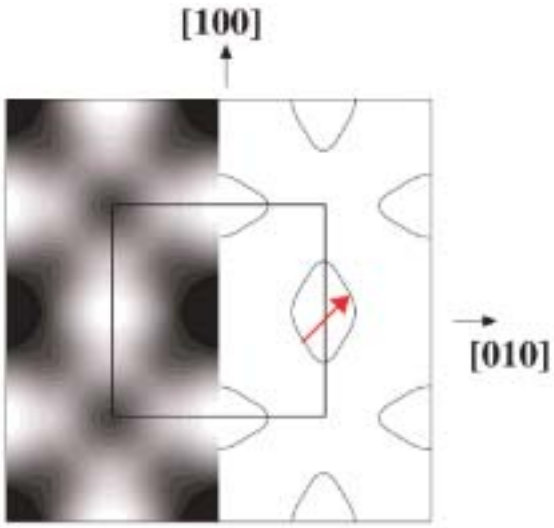

Fig. 3. A slice through the $k_z = 0.48(\pi/a)$ plane of the experimental data, for comparison with Fig 1. Shown on the left is the occupation density through this slice, where brighter shades represent a larger occupation. On the right is the experimentally determined Fermi surface, with the nesting vector shown in red.

Stephen Dugdale

H. H. Wills Physics Laboratory,
University of Bristol, U.K.

E-mail: s.b.dugdale@bristol.ac.uk

References

[1] G.L. Zhao and B.N. Harmon: Phys. Rev. B **45** (1992) 2818.
[2] S.M. Shapiro *et al.*: Phys. Rev. B **44** (1991) 9301.
[3] G.M. Stocks *et al.*: in "Ordered Intermetallics - Physical Metallurgy and Mechanical Behaviour", edited by C.T. Liu *et al.* (1992) p. 15.
[4] Y. Sakurai and M. Itou: J. Phys. Chem. Solids **65** (2004) 2061.
[5] *S.B. Dugdale, R.J. Watts, J. Laverock, Zs. Major, M.A. Alam, M. Samsel-Czekala, G. Kontrym-Sznajd, Y. Sakurai, M. Itou and D. Fort: Phys. Rev. Lett.* ***96*** *(2006) 046406.*

Phonons in PtFe Thin Films as High-density Magnetic Recording Media

Since an $L1_0$ (CuAu I) type PtFe alloy has a large uniaxial magnetocrystalline anisotropy energy of 7×10^7 erg/cm^3 [1], saturated magnetization and good chemical stability, this alloy is considered to be an excellent candidate for future ultrahigh density perpendicular magnetic recording media. Moreover, the alloy is expected as a thin film magnet which applies microscopic magnetic fields to an integrated circuit. PtFe alloy undergoes a chemical ordering transition from the disordered-fcc phase to the ordered-fct phase at about 1300 ºC. The ordered crystal has an uniaxial anisotropy along the [001] direction. Recently, one of the present authors found that the tetragonal lattice distortion (1-c/a) of PtFe alloy increases with increasing temperature up to 750K [2]. Since the magnetic anisotropy energy is strongly related to the tetragonality of the lattice, it is important to understand the origin of the increasing tetragonality at high temperature. To investigate the increasing tetragonality of the lattice, we tried to look into the phonon density of states (PDOS) in PtFe alloy. In particular, we take notice of information for thin film as an application material.

The PDOS of ^{57}Fe atoms in the PtFe alloy was investigated using the nuclear resonant inelastic scattering (NRIS) method. The NRIS experiments were performed at beamline **BL11XU** [3,4]. The incident beam energy of the synchrotron radiation was varied around the first nuclear resonant energy of ^{57}Fe (14.413 keV). The incident beam intensity was monitored with an ionization chamber and a beam flux monitor. A Si-avalanche photodiode (APD) detector was used to observe the delayed photons in the nuclear resonant scattering from ^{57}Fe in the PtFe alloy.

The PtFe thin film sample was deposited on a MgO single crystal substrate and piled up to 25 PtFe layers. This sample was prepared in Takanashi Laboratory at the Institute for Materials Research, Tohoku University. To investigate the special feature of thin film, bulk crystal and powder samples were also prepared and the results were compared. Fe atoms enriched by the ^{57}Fe isotope were used in these samples. The bulk crystal was prepared in a furnace with a carbon electrode in Ar gas atmosphere. The powder sample was prepared by filing down the bulk crystal with a diamond file. From X-ray diffraction, it is confirmed that the bulk sample is chemically ordered and the powder sample is disordered.

Figure 1 shows raw energy spectra obtained at room temperature for the bulk crystal, powder sample and thin film. Figure 2 shows the PDOS of bulk, powder and thin film samples derived from the observed energy spectra after correcting the multiphonon process. The greater part of PDOS is in the high energy side. In the NRIS method, phonons

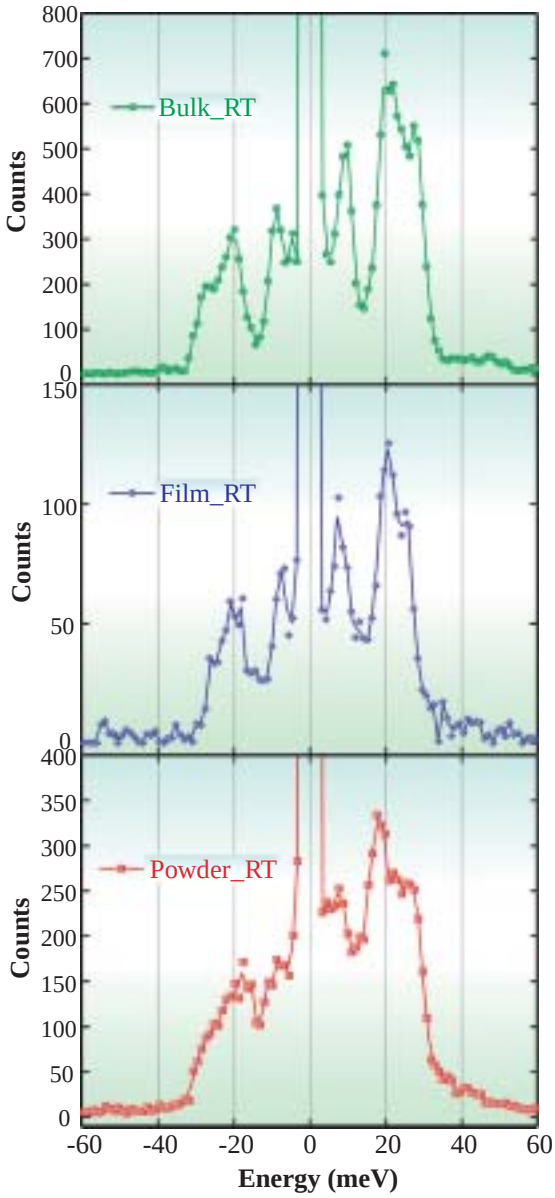

Fig. 1. Energy spectra at room temperature for bulk crystal, powder sample and thin film.

of resonant nuclei (^{57}Fe) are observable. Since an Fe atom is far lighter than a Pt atom, Fe's contribution to the acoustic phonon is small. On the other hand, the optical phonons are mainly determined by the vibrations of Fe atoms. There is a phonon band gap around 13 meV due to the large difference between the atomic masses of Fe and Pt. Comparing the PDOS in Fig. 2, the bulk crystal shows a well-defined band gap, while for the powder sample and thin film, the band gap is buried under the tails of the acoustic and optical phonons. This is already seen in the raw data at around 13 meV (Fig. 1). Considering that the powder sample is chemically disordered, the loss of the band gap in the thin film is caused by the chemical disorder, indicating that the atomic order parameter of the thin film sample is smaller than that of the bulk sample. The optical phonon band width of the thin film is narrower than those of the bulk crystal and powder sample. Although the bulk crystal and powder sample have a multidomain, the thin film surface is oriented to the [001] axis. Thus, the phonons on the (001) plane were predominantly observed for the thin film specimen. Figure 3 shows the temperature variation of the thin film PDOS. At any temperature, the phonon gap around 13 meV is ill defined. The PtFe thin film is a very important material as magnetic recording media. In order to improve its performance, raising the degree of atomic order would be important.

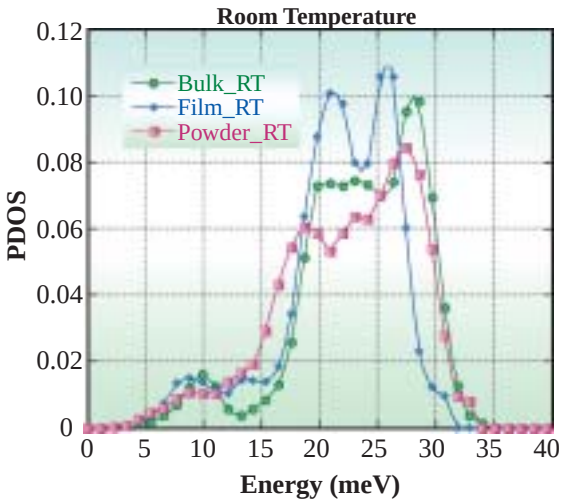

Fig. 2. PDOS at room temperature for bulk crystal, powder sample and thin film.

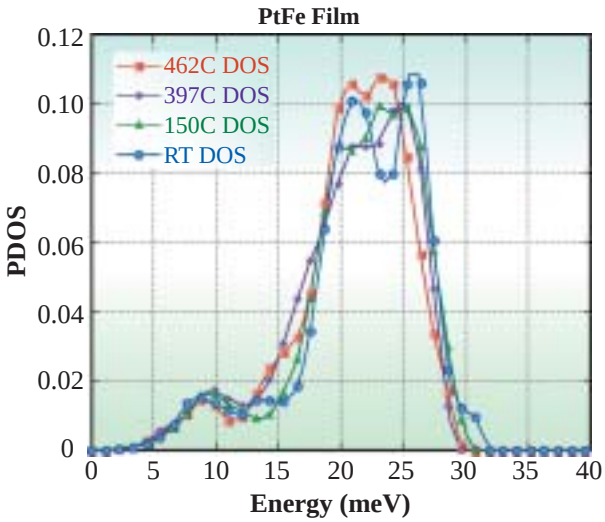

Fig. 3. PDOS for thin film at various temperatures.

Mabune Hideshima

Department of Applied Physics, Waseda University

E-mail: mabune-h@fuji.waseda.jp

References

[1] O.A. Ivanov *et al.*: Phys. Met. Metallogr. **35** (1973) 92.
[2] Y. Tsunoda and H. Kobayashi: Proc. Int. Conf. on Magnetism (ICN'03 Rome Italy, 2003)
[3] M. Seto *et al.*: Phys. Rev. Lett. **74** (1995) 3828.
[4] T. Mitsui *et al.*: Nucl. Instrum. Meth. Phys. Res. Sect. A **467-468** (2001) 1105.

Electronic Structure of Uranium Compounds Revealed by Angle Resolved Photoemission Spectroscopy

Actinide compounds exhibit a rich variety of electrical and magnetic properties such as heavy Fermion behaviors, a variety of superconductivity and magnetic ordering. Recently, "high-T_c" superconductivity at T_c =18 K was found in $PuCoGa_5$ [1], indicating that there remains an unexplored class of exotic materials in actinide compounds. In these compounds, the 5*f* electrons in actinide atoms are responsible for these properties. They have both atomic-like "localized" and band-like "itinerant" properties, and are difficult to treat theoretically. The most fundamental question is how the 5*f* states are involved in their band structure and Fermi surfaces (FSs), and what kind of theoretical treatment is appropriate for their description. To address this question, we have performed angle-resolved photoemission experiments on uranium compounds using the soft X-rays from beamline **BL23SU**. Angle-resolved photoemission spectroscopy (ARPES) is one of the most powerful experimental methods of determining the band structures and FSs of solids experimentally. By performing ARPES experiments in the soft X-ray region (SX-ARPES) [2], bulk-sensitive and 5*f*-dominant band structures and FSs are obtained, and they can be directly compared with theoretical calculations. The present target material is the layered uranium compound $UFeGa_5$. $UFeGa_5$ is a paramagnetic uranium compound which has the same crystal structure as $PuCoGa_5$. Among the series of compounds with the same crystal structure, this compound is know as the "itinerant" U 5*f* compound.

Figures 1(a) and 1(b) show the experimental band structures of $UFeGa_5$ for the Z-R and Z-A directions of the Brillouin zone derived from SX-ARPES spectra measured at $h\nu$= 500 eV. The bright part in the image plot corresponds to the position of the band structure. In these plots, the contributions from U 5*f* states and Fe 3*d* states are dominant. For both directions, we could successfully observe the energy dispersion of the U 5*f* states. We compare these results with the energy band structure calculation, treating U 5*f* electrons as being itinerant states. Figures 1(c) and 1(d) show the results of the calculation for the Z-R and Z-A directions to be compared with Figs. 1(a) and 1(b), respectively. Contributions from the U 5*f* and Fe 3*d* states, which have large contributions in the spectra, are indicated on the color scale in each band. Although the overall agreement between experiment and calculation is not so complete, some calculated bands have a correspondence to the experimental bands. For the Z-R direction, there exist two or three bands around the Z point in the experimental band structure. In the band structure calculation, there are few bands in this energy region, and bands 1-3 seem to correspond to the experimental bands among them. Around the R point, the parabolic

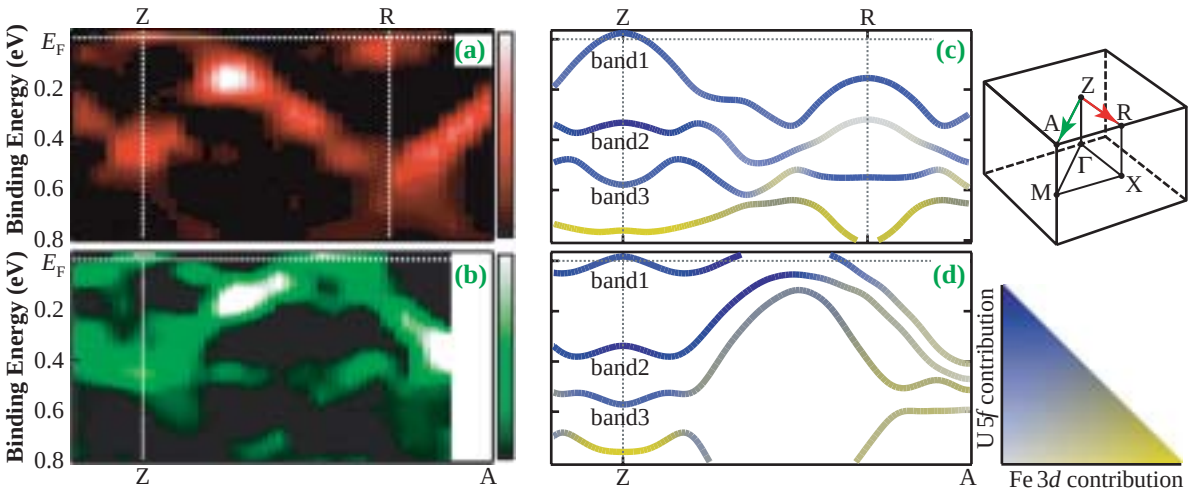

Fig. 1. Band structure of $UFeGa_5$ measured along **(a)** Z-R and **(b)** Z-A directions. Calculated energy band dispersions to be compared with the experiment along **(c)** Z-R and **(d)** Z-A directions are shown.

band dispersion was observed in the experiment, but it does not exist in the calculation. Instead, there exist bands 1-3 in the calculation, and the experimental band seems to correspond to the trace of these calculated bands. For the Z-A direction, while the positions of E_F-crossing are different between the calculation and experiment, the experimental band near E_F shows a good correspondence to the calculations. At the Z point, a hole-like FS is observed in both the experiment and calculation. In addition, the hole-pocket, which is observed in the middle of the Z-A line, also exists in the calculated energy band dispersion.

To obtain more information about the FSs, we have made a 2D mapping of the photoemission intensity at EF. Figure 2(a) shows the mapping as a function of k_x and k_y. A bright part corresponds to higher intensity and a dark part to lower intensity. The most prominent feature in this image is the large round-shaped high intensity part centered at the point A. Its inner and outer boundaries correspond to the hole-like and electron-like FS centered at the point A, respectively. The calculated FSs of $UFeGa_5$ for the Z-R-A plane are also shown in Fig. 2(b). In the band structure calculation, there exist two large quasi-2D cylindrical FSs centered at the A-M line as indicated in Fig. 2(c). These cylindrical FSs have large contributions from the U 5*f* states. The comparison of the experimental FSs with those of the calculation shows that although their sizes and shapes are different between the experiment and the calculation, these FSs exist in the experiment also. Hence, we have obtained a qualitative agreement between experimental FS and the result of the band structure calculation. Meanwhile, an important point to note is that the high intensity part persists from the outer hole-like FS to the inner electron FS as indicated in Fig. 2(b). This indicates the renormalization of bands around E_F. This result shows an existence of the electron correlation effect in this compound.

Accordingly, we conclude that although the agreement between the calculation and the experiment is not complete, the essential band structure and morphology of FS of $UFeGa_5$ are explained by the band structure calculation. At the same time, we have observed that the bands near E_F are renormalized, suggesting the importance of electron correlation effects even in itinerant uranium compounds.

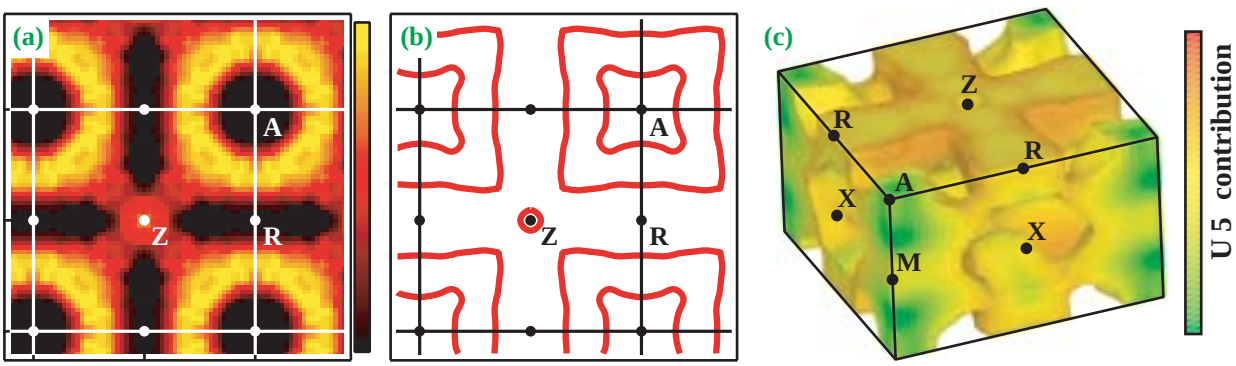

Fig. 2. **(a)** Experimental Fermi surface of $UFeGa_5$ **(b)** Calculated Fermi surface of $UFeGa_5$ in Z-R-A plane. **(c)** Calculated three-dimensional Fermi surface of $UFeGa_5$.

Shin-ichi Fujimori

SPring-8 / JAEA

E-mail: fujimori@spring8.or.jp

References

[1] J.L. Sarrao *et al.*: Nature **420** (2002) 297.
[2] A. Sekiyama *et al.*: Phys. Rev. B **70** (2004) 060506(R).
[3] *S. Fujimori, K. Terai, Y. Takeda, T. Okane, Y. Saitoh, Y. Muramatsu, A. Fujimori, H. Yamagami, Y. Tokiwa, S. Ikeda, T. Matsuda, Y. Haga, E. Yamamoto and Y. Ōnuki: Phys. Rev. B* ***73*** *(2006) 125109.*

Chemical Science

Chemical Science involves various studies including soft matter for devices, nanoparticles, reaction mechanisms, and properties of atoms, molecules and clusters. Soft matter is often composed of organic molecules with a large molecular weight which are bound together through van der Waals interaction. It can be characterized by flexibility, lightness and diversity. Poly[(R)-3-hydroxybutyrate] fibers are bio-based and biodegradable structure plastics. Micro-beam X-ray diffraction at BL47XU revealed that these fibers have a core-sheath structure. The application of soft matter to electronic and magnetic devices draws much attention because it can replace heavy and rigid inorganic semiconductors. The structure of the single component molecular metal, [Au(tmdt)$_2$], which has unique electronic and magnetic properties, has been determined by a powder X-ray diffraction method at BL02B2. The color of the dye in crystal and aggregate is not determined only by molecular structure but by intermolecular interaction. The structure of J-aggregates at the air/water interface has been determined by grazing incidence X-ray diffraction at BL46XU. The origin of the change in the color of J-aggregates comes from the interaction of both TDS (transition dipole moment) and EDM (electric dipole moment). Metal-organic hybrid compounds are another interesting material. They often form a pore structure. Cu(II) *trans*-1,4-cyclohexanedicarboxylate (Cuchd) was studied using powder X-ray diffraction method at BL02B2, and showed that anomalous structural phase transition and toluene adsorption suppress phase transition. [$Cu_2(pzdc)_2(pyz)$] can adsorb C_2H_2 selectively and can separate it from coexisting CO_2. The powder diffraction revealed that the hydrogen bonding of C_2H_2 with free oxygen atoms fixed C_2H_2 molecules in the pore in 1D channels. Fundamental studies of atoms, molecules and clusters are important in nanoscience. Symmetry resolved high-resolution photoelectron spectra of CO and N_2 were measured at BL27SU and the fine structures in the satellite were found to arise from vibrational modes in excited molecules. Another interesting paper from BL27SU is that on the electronic structure of hydrogen-bonding clusters which must be the base for understanding of solvation and protonation in liquid chemistry. Bimetallic nanoparticles are important in catalysts and optical materials. A new means of classifying the inner structure of bimetallic nanoparticles by EXAFS at BL12B2 has been proposed and the structure of PtRu has been determined. Last but not least, important progress has been made from IR beamline BL43IR, which showed pseudo gap formation in CdSb under multiple extreme conditions (i.e., high temperature, high pressure and high magnetic field).

Kiyotaka Asakura

Catalysis Research Center
Hokkaido University

New Core-sheath Structure of Poly[(*R*)-3-hydroxybutyrate] Fibers Revealed by Micro-beam X-ray Diffraction

Plastic products have gained universal use not only in food, clothing and shelter, but also in the transportation, construction, medical and leisure industries. There is a growing demand for bio-based and biodegradable polymers as a solution to problems concerning energy resources, the global environment and solid waste management. Research on bio-based and biodegradable plastics and polymers has been carried out worldwide with the aim of achieving a balance between human activities and the natural environment.

A wide variety of bacteria synthesize an optically active polymer of (*R*)-3-hydroxybutyric acid and accumulate it as intracellular carbon and energy storage material. Poly[(*R*)-3-hydroxybutyrate] (P(3HB)) isolated from bacteria is extensively studied as biodegradable and biocompatible thermoplastic with a melting temperature of ~180ºC (Fig. 1). P(3HB) was discovered by Maurice Lemoignei of Institute Pasteur, France, in the 1920s, and until now many researchers have been investigating its physical properties, crystal structure, and biosynthesis and biodegradation mechanisms among others. P(3HB) was initially produced by Imperial Chemical Industries by using an industrial-scale fermentation process in the 1980s. In 1995, the process and related patents were bought by Monsanto and subsequently acquired by Metabolix. Recently, Lenz and Marchessault have reported a historical review of the chemical, biochemical and microbial highlights of P(3HB) covering a discovery time span of 75 years [1].

Recently, we have succeeded in processing P(3HB) fibers with a high tensile strength and acceptable mechanical properties by a method combining cold-drawing and two-step-drawing procedures [2,3]. We present, herein, highly ordered structures in monofilaments revealed by micro-beam X-ray diffractions using synchrotron radiation.

Until now, three research groups have succeeded in obtaining melt-spun fibers with tensile strengths of 190 ~ 420 MPa from P(3HB) (weight-average-molecular-weight (M_w) of 0.3 ~ 0.8 × 10^6) produced by wild-type bacteria. However, the strength of such fibers is not sufficient for industrial and medical applications as fishing line and suture among others. Furthermore, it is well known that the mechanical properties of P(3HB) fibers and films markedly deteriorate by a process of secondary crystallization.

We have developed several new drawing techniques for obtaining strong P(3HB) fibers. Amorphous fibers were obtained by quenching melt-spun fibers of ultra-high-molecular-weight P(3HB) (UHMW-P(3HB)) with M_w = 5.3 × 10^6 in ice water. The cold-drawing of amorphous fibers of UHMW-P(3HB) was achieved easily and reproducibly at a temperature below but near the glass transition temperature of 4ºC in ice water with two sets of rolls. The cold-drawn amorphous fibers were kept at room temperature for several minutes to generate the crystal nucleus, and then two-step drawing was applied using a stretching machine at room temperature to further increase the degree of chain orientation. The cold-drawn fibers were easily drawn at a very low stress by more than 1000%, but elastic recovery occurred on release from the stretching machine. Accordingly, annealing procedure is required to fix the extended polymer chains. Figure 2 shows the two-step drawn fibers processed from UHMW-P(3HB).

The tensile strength of two-step-drawn and annealed fibers linearly increased with the ratio of two-step drawing. When the total drawn ratio reached 60 times (cold-drawn for 6 times and two-step-drawn for 10 times), the tensile strength increased to 1320 MPa. This value is higher than those of poly(ethylene), poly(propylene), poly(ethylene

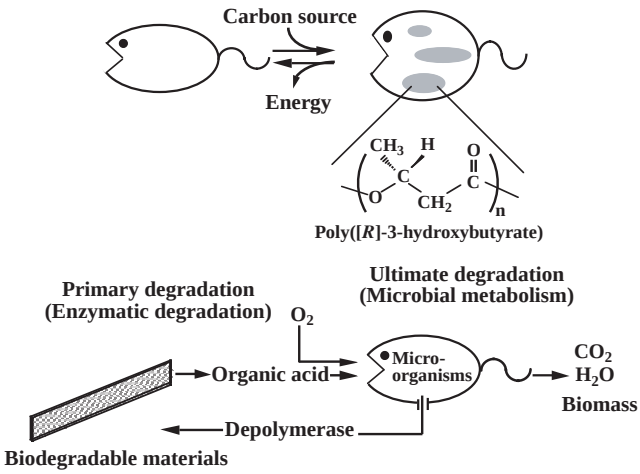

Fig. 1. Biosynthesis and biodegradation processes of P(3HB) and its copolymers.

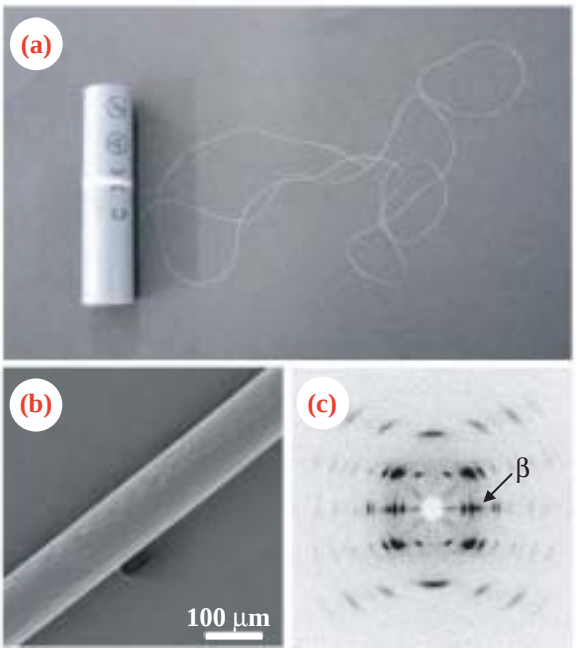

Fig. 2. **(a)** UHMW-P(3HB) fiber processed by cold-drawing (6 times) in ice water and two-step-drawing (10 times) at room temperature, and subsequently annealed at 50°C. **(b)** Scanning electron micrograph and **(c)** X-ray fiber pattern of UHMW-P(3HB) fiber.

terephtalate), and poly(vinyl alcohol) of industrial grade, and poly(glycolic acid) used as suture. Thus, it was revealed that the P(3HB) homopolymer becomes a much attractive material from the viewpoint of mechanical properties.

An X-ray fiber pattern for a bundle of ten pieces of P(3HB) fibers obtained using the laboratory X-ray source (beam size: 300 μm) is shown in Fig. 2(c). This pattern includes reflections from both the α-form (2_1 helix conformation) [4] and β-form (planar zigzag conformation) [5] of P(3HB) simultaneously. It is well known that P(3HB) crystallizes as an orthorhombic crystal system with a space group of $P2_12_12_1$ (α-form), and that β-form is introduced from the orientation of free chains in amorphous regions between α-form lamellar crystals. Thus, the generation of β-form seems to introduce the increase in tensile strength.

To reveal the detailed fiber structure and the distribution of the two types of molecular conformation in mono-filaments, the micro-beam X-ray diffraction was performed using synchrotron radiation at beamline **BL47XU**. The beam size was focused onto 0.5 μm spot with a Fresnel zone plate and a mono-filament was linearly scanned perpendicular to the fiber axis in 2 μm steps [2,3].

Figure 3 shows micro-beam X-ray diffraction patterns of a two-step-drawn P(3HB) mono-filament obtained from three marked points in the microscope image. In the micro-beam X-ray fiber pattern of No. 1 (edge part), all the reflections were indexed by only the α-form crystal system with a 2_1 helix conformation. However, in the patterns of No. 2 and 3 (center part), the other reflection indexed by the β-form (planar zigzag conformation) was observed, together with α-form crystal system with 2_1 helix conformation.

These results indicate that a strong two-step-drawn UHMW-P(3HB) fiber has a core-sheath structure with only a 2_1 helix conformation (α-form) in the sheath region and with both a planar zigzag conformation (β-form) and a 2_1 helix conformation (α-form) in the core region.

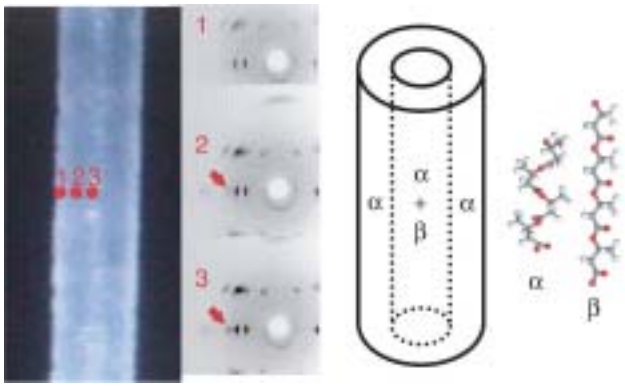

Fig. 3. Micro-beam X-ray fiber pattern of cold-drawn and two-step-drawn UHMW-P(3HB) mono-filament recorded from three marked points in microscope image, and a schematic display of core-sheath structure with two kinds of molecular structures revealed by micro-beam X-ray diffractions. The arrows indicate the reflection derived from the β-form.

Tadahisa Iwata* and Toshihisa Tanaka

Polymer Chemistry Laboratory, RIKEN Institute, Wako

*E-mail address: tiwata@riken.jp

References

[1] R.W. Lenz & R.H. Marchessault: Biomacromolecules **6** (2005) 1.
[2] T. Iwata: Macromol. Biosci. **5** (2005) 689.
[3] *T. Iwata, Y. Aoyagi, M. Fujita, H. Yamane, Y. Doi, Y. Suzuki, A. Takeuchi and K. Uesugi: Macromol. Rapid Commun.* ***25*** *(2004) 1100.*
[4] M. Yokouchi *et al.*: Polymer **14** (1973) 267.
[5] W.J. Orts *et al.*: Macromolecules **23** (1990) 5368.

Structure Determination of Single-componentMolecular Metals by X-ray Powder Diffraction

The realization of a molecular metal based on single-component molecules had been one of the important targets in the field of molecular conductors. The difficulty in designing a single-component molecular metal is naturally related to the facts that the highest occupied molecular orbital (HOMO) is doubly occupied. However, we have noticed that even in electronic bands constructed from single-component molecules, the bottom energy level of the lowest unoccupied molecular orbital (LUMO) band can be lower than the top energy level of the HOMO band and the free carriers might be generated by the electron transfer between HOMO and LUMO bands when the molecule has sufficiently large intermolecular interactions and an unprecedented small HOMO-LUMO gap. By adopting metal complexes with extended tetrathiafulvalene (TTF) dithiolate ligands, we have realized the first example of the single-component molecular metal, $[Ni(tmdt)_2]$ (tmdt = trimethylenetetrathiafulvalenedithiolate) [1,2]. Recently, direct experimental evidence of the existence of three-dimensional electron and hole Fermi surfaces was obtained by the observation of de Haas-van Alphen effect [2,3].

The neutral bis(dithiolato)gold complex has an odd number of total electrons, which makes the electromagnetic properties very attractive [2]. $[Au(tmdt)_2]$ was obtained electrochemically on a platinum electrode as microcrystals. High-resolution synchrotron X-ray powder diffraction data were collected using an imaging plate detector and a Large Debye-Scherrer camera at beamline **BL02B2**. The X-ray powder pattern showed that the crystal structure of $[Au(tmdt)_2]$ to be isostructural to that of $[Ni(tmdt)_2]$. The lattice constants of $[Au(tmdt)_2]$ were determined as a = 6.4129(1), b = 7.5514(2), c = 12.1543(3) Å, α = 90.473(3), β = 96.698(2), γ = 103.008(3)°, V = 569.21(2) Å^3. Structure analysis was performed by the MEM/Rietveld method [4], resulting that the final R factors for 3751 points (2θ range for analysis is 2.5 – 40.0°) were R_{wp} = 0.028 and R_I = 0.073. Figure 1 shows the unit cell and MEM electron density of $[Au(tmdt)_2]$. The molecule has an almost planar structure. The gold atom has a square planar coordination with an average Au-S distance of 2.296(2) Å and a S-Au-S angle of 89.9(1)°. A comparison of electron densities around the central metal atoms of $[M(tmdt)_2]$ (M = Ni, Au) revealed a

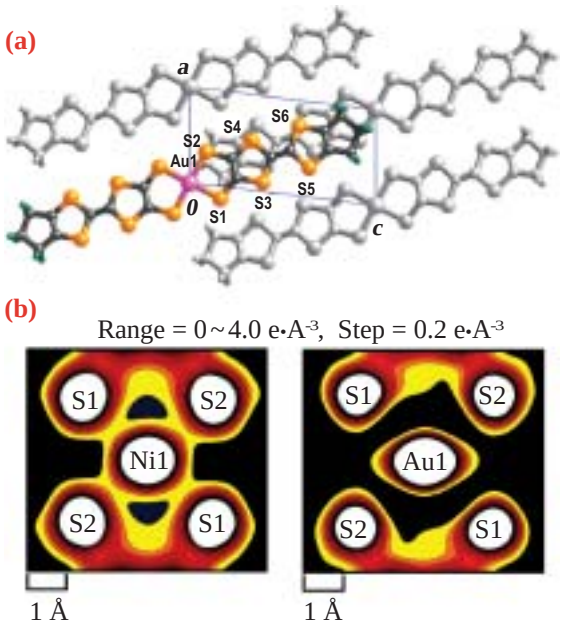

Fig. 1. **(a)** Simple structure of $[Au(tmdt)_2]$. **(b)** Comparison of electron densities around central metal atoms of $[M(tmdt)_2]$ (M = Ni, Au).

relatively small bonding electron density on Au-S bonds, which depends on the difference in the distribution of *d* electrons of the central metal atoms.

Figure 2 indicates the physical properties of $[Au(tmdt)_2]$. The spin susceptibilities χ_{spin} increased gradually down to *ca.* 130 K and decreased abruptly at *ca.* 110 K. For a magnetic field above 40 kOe and below 5 kOe, the static magnetic susceptibilities χ_{SQUID} were nearly constant above 50 K. These results suggest that the anomaly at *ca*. 110 K is an antiferromagnetic transition with the critical magnetic field of spin flipping transition between 10 and 30 kOe. The first-principle band structure calculation suggested the possibility of the nesting of warped Fermi surfaces of $[Au(tmdt)_2]$ [5]. At the same time, the expected imperfect nesting seems to be consistent with the highly conducting properties below 110 K. ^{1}H NMR studies of $[Au(tmdt)_2]$ by Kanoda *et al.* also suggested the antiferromagnetic transition at *ca*. 110 K. To the best of our knowledge, $[Au(tmdt)_2]$ is the first molecular conductor exhibiting magnetic transition above liquid nitrogen temperature without loss of its high conductivity.

We have recently succeeded in the preparation of the first "single-component alloy" $[Ni_{1-x}Au_x(tmdt)_2]$. The diffraction peaks of $[Ni_{1-x}Au_x(tmdt)_2]$ shifted systemically to the lower angle with an increase in Au content (x), and no extra peak attributable to other phases was observed, showing that the alloys $[Ni_{1-x}Au_x(tmdt)_2]$ with arbitrary mixing ratio could be synthesized. Single-component molecular conducting systems will provide various new materials with unprecedented electronic properties.

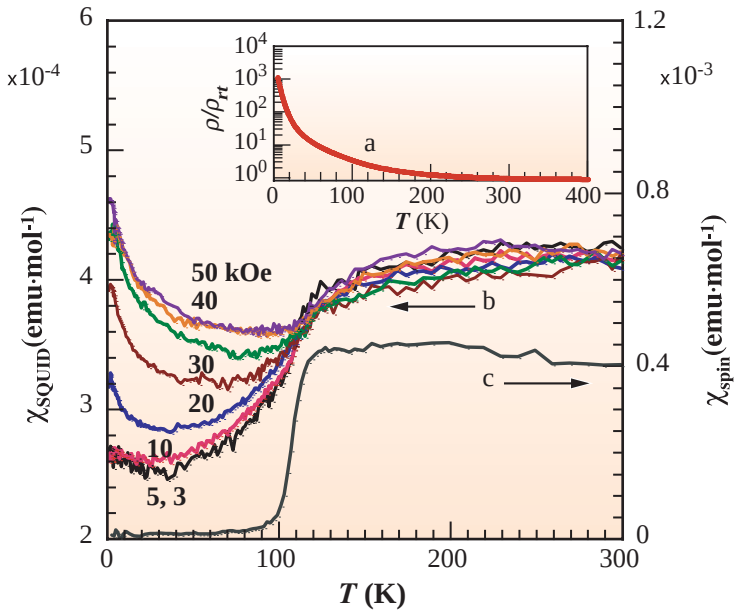

Fig. 2. Resistivities and susceptibilities of $[Au(tmdt)_2]$: **(a)** Resistivity of a compaction pellet (ρ_{rt} = 0.02Ω·cm) **(b)** Magnetic susceptibilities by SQUID at 3, 5, 10 , 20, 30, 40 and 50 kOe. **(c)** Spin susceptibility by ESR of polycrystalline sample ($\chi_{spin\ rt}$ = 3.8 (10^{-4} emu·mol^{-1}).

Akiko Kobayashi[a,*,†], Emiko Fujiwara[a] and Eiji Nishibori[b]

[a] Research Centre for Spectrochemistry, The University of Tokyo
[b] Department of Applied Physics, Nagoya University

*E-mail: akoba@chs.nihon-u.ac.jp

[†] Present address: Department of Chemistry, Nihon University

References

[1] H. Tanaka *et al.*: Science **291** (2001) 285.
[2] A. Kobayashi *et al.*: Chem. Rev. **104** (2004) 5243.
[3] H. Tanaka *et al.*: J. Am. Chem. Soc. **126** (2004) 10518.
[4] M. Takata *et al.*: Nature **377** (1995) 46.
[5] *S. Ishibashi, H. Tanaka, M. Kohyama, M. Tokumoto, A. Kobayashi, H. Kobayashi and K. Terakura: J. Phys. Soc. Jpn.* ***74*** *(2005) 843.*

Molecular Arrangement in Organic Dye Monolayer at Air-water Interface and Its Visible Absorption Band

When organic dye molecules form a crystal or an aggregate, their color becomes different from that of isolated molecules. Due to the close packing in a crystal, the interaction of optical transition dipole moments (TDM[#]) among molecules splits the degenerated state of the ensemble of the molecules and induces a splitting of the molecular energy levels into energy bands. The energy levels in the energy bands, where optically allowed transitions from the ground state take place, are often different from those of an isolated molecule, resulting in a shift of the visible absorption band upon crystallization or aggregation (E_{Shift}). This is a usual interpretation of E_{Shift}. However, in dye aggregates, we have found that not only TDM interaction but also electric dipole moment (EDM[##]) interaction plays an important role in E_{Shift} [1,2].

When the energy levels, where optically allowed transitions from the ground state take place, are localized at the bottom edge of the first energy band, the aggregates are classified into J-aggregates [3]. Amphiphilic merocyanine dye (MD) molecules (Fig. 1(a)) form J-aggregates at the air-water interface. Figure 1(a) indicates the visible absorption spectra of the monomer and J-aggregate states of the MD monolayer at the air-water interface. Since the former has an absorption band at 524 nm (2.366 eV) and the latter at 618 nm (2.006 eV), MD J-aggregates exhibit E_{Shift} = − 0.36 eV and their colors differ as shown in Fig. 1(b). To evaluate the contribution of TDM and EDM interaction energies to E_{Shift} quantitatively, a structural analysis of MD J-aggregates was carried out and E_{Shift} calculations, where the TDM and EDM interaction energies were rigorously accounted for, were performed on the determined structure [1,2].

For structural determination, the grazing incidence X-ray diffraction of the MD monolayer was observed at beamline **BL46XU**. Figure 2 shows the optical setup. A 12 keV X-ray beam was irradiated on the monolayer at the air-water interface. Using Si mirrors, θ_{in} was set at 0.09º, which was below the critical angle of the total reflection for the water surface. The DS2 and DS3 slits were 1 mm wide and 0.15 mm high. Incidence intensity was monitored using an ion chamber to normalize detected intensity. A trough for the monolayer was mounted on an 8-axis diffractometer and θ_{out} was also set at 0.09º. The RS1 and RS2 slits were 4 mm wide and 10 mm high. A $2\theta_z$ scan was performed to obtain an in-plane diffraction pattern of the monolayer, and the Soller slit ensured a $2\theta_z$ resolution better than 0.2º. Since the monolayer consisted of randomly oriented J-aggregate crystallites, the observed diffraction corresponds to the two-dimensional powder diffraction.

Figure 3 shows the obtained diffraction pattern, where the Lorentz factor and the background were corrected. Red solid lines are fitting curves for the diffraction peaks. The Miller indices were based on the unit cell in Fig. 3. Structure analysis was carried out by calculating the R-factor. For simplicity, the Debye-Waller factor and water molecules were neglected and the molecular structure obtained by an *ab initio* calculation was used. By changing the molecular orientation while keeping the plane of the planar dye group normal to the lattice plane, and by

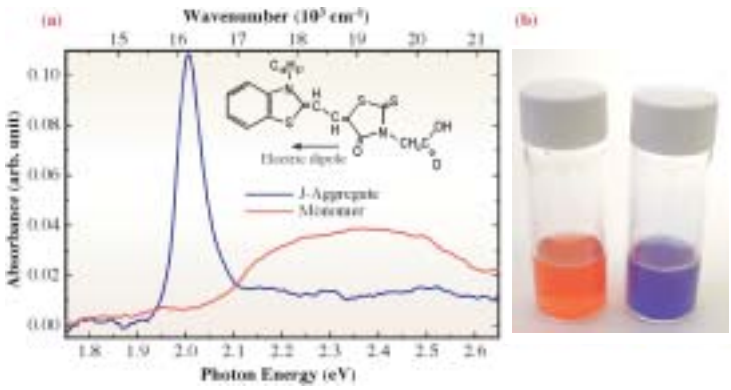

Fig. 1. **(a)** Chemical structure of amphiphilic merocyanine dye (MD) and visible absorption spectra of MD monolayer in monomer (isolated) and J-aggregate states. **(b)** Photograph of aqueous dispersions of monomers (left) and J-aggregates (right) prepared with lipids.

[#] A charge distribution in a molecule changes on a transition from its initial to final states. The TDM is related to an overlap between the charge distributions of the initial and final states. The square of the absolute value of the TDM is proportional to the transition probability.

[##] The EDM is related to an asymmetry of the charge distribution in a molecule. Polar molecules have finite EDMs.

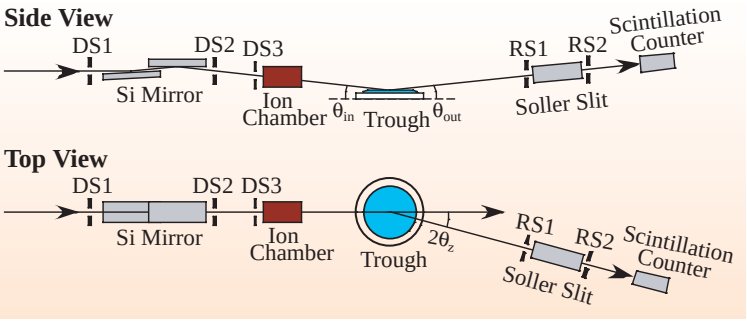

Fig. 2. Optical setup of grazing incidence X-ray diffraction measurements.

rotating the alkyl chain around the N-C bond on the benzothiazole group, the R-factor was investigated. The minimum R-factor (13%) was achieved using the arrangement in Fig. 4. Since the long axis of the dye group, where π electrons are delocalized, is almost parallel to the *b*-axis, the TDM and EDM are reasonably considered to be parallel to the *b*-axis.

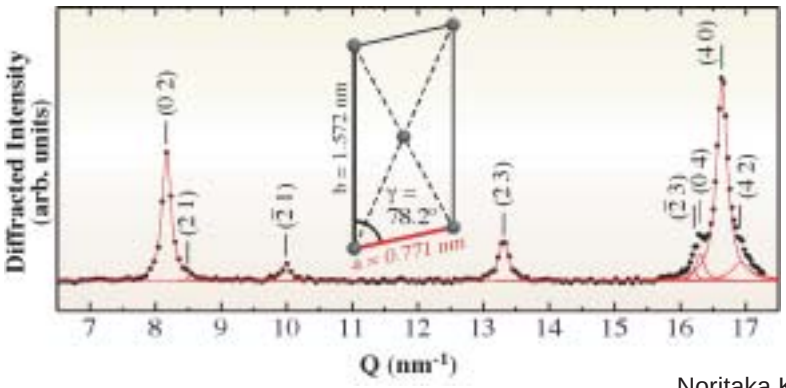

Fig. 3. Diffraction pattern of MD J-aggregate monolayer at air-water interface ($Q = 4\pi \sin\theta_z / \lambda$ with $\lambda = 0.103$ nm) and two-dimensional unit cell.

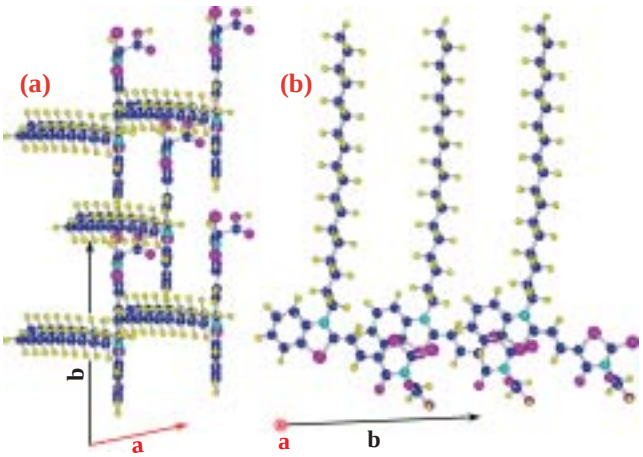

Fig. 4. Molecular arrangement illustrated in direction normal to lattice plane **(a)** and in the direction along the *a*-axis of unit cell **(b)**. Due to overlaps, two molecules are hidden in **(b)**.

Taking into account the electrostatic interaction among the molecules in a perturbative way, the eigenvalue equation of E_{Shift} for an infinitely large aggregate was driven [4]. The selection rule for the optical transition permits the aggregate to be optically excited to only one of the eigenstates in the present case, and the eigenvalue is calculated by $E_{Shift} = J + K$, where J and K represent the TDM and EDM interaction energies, respectively. The latter originates from the difference between the EDMs in the ground and excited states of the molecule. According to the determined arrangement (Fig. 4), all the dipole moments were set to be parallel to the *b*-axis, and J and K were calculated using formulas simplified by extended dipole approximation. It was clearly shown that J could not explain the observed E_{Shift} solely. Our quantitative analysis revealed that J and K contributed to 44% and 56% of E_{Shift}, respectively, indicating the importance of EDM interaction.

The determination of the aggregate structure led to a deeper understanding of the physics of color change upon dye crystallization, and clarified the contribution of EDM interaction to E_{Shift}, which has not duly been discussed so far, can be significant when the aggregate is formed by polar dye molecules.

Noritaka Kato*,†, Kazuya Yuasa†† and Yoshiaki Uesu

Department of Physics, Waseda University

*E-mail: nkato@kurenai.waseda.jp

Present address: † Department of Electronics & Communications, Meiji University

†† Research Center for Information Security, National Institute of Advanced Industrial Science and Technology (AIST)

References

[1] *N. Kato, K. Yuasa, T. Araki, I. Hirosawa, M. Sato, N. Ikeda, K. Iimura and Y. Uesu: Phys. Rev. Lett.* ***94*** *(2005) 136404.*

[2] *N. Kato, K. Yuasa and Y. Uesu: J. Surf. Sci. Soc. Jpn.* ***27*** *(2006) 258.*

[3] "J-Aggregates" ed. by T. Kobayashi (World Scientific, Singapore, 1996).

[4] A.S. Davydov: "Theory of Molecular Excitons" (McGraw-Hill, New York, 1962).

Structural Phase Transition in Absorbed and Non-absorbed Copper(II) *Trans*-1,4-Cyclohexanedicarboxylate

Nano-porous materials attract much attention because of their potential technological applications in gas storage, molecular sieves and catalysts among others. A series of copper dicarboxylate compounds such as copper(II) *trans*-1,4-cyclohexanedicarboxylate have recently been synthesized, and it has been found that they show a peculiar absorption/desorption of large amount of molecules. Here, we report our recent studies on the structural phase transition of copper(II) *trans*-1,4-cyclohexanedicarboxylate (Cuchd), which is strongly influenced by absorption of molecules.

Figure 1 shows the molar heat capacity of toluene-free and toluene-absorbed samples of Cuchd measured using a homemade adiabatic calorimeter between 13 and 300 K [1]. An anomaly with a maximum at about 160 K was found for the empty host compound of Cuchd. The shape of the anomaly is very broad, but it is clearly assigned to first-order phase transition, which is confirmed by the observation of super-cooling of the high temperature phase. The enthalpy and entropy of transition are determined to be 413.4 J mol^{-1} and 2.66 J K-$1mol^{-1}$, respectively. The partially absorbed sample (11 % toluene) exhibits a smaller anomaly at higher temperatures than the toluene-free sample. No anomaly is observed for the 65 % toluene-absorbed sample, which means that no phase transition takes place. Lattice distortion caused by the absorption of guest molecules may hinder phase transition and increase phase transition temperature. Thus, the fully absorbed sample should have the structure of the low temperature phase of the host compound even at room temperature.

Phase transition has also been studied by powder X-ray diffractometry with high-energy synchrotron radiation (λ = 0.8007 Å) at beamline **BL02B2** [2]. The sample Cuchd was put in a Pyrex glass capillary (0.3 mm inside diameter), connected to a vacuum line, evacuated, and sealed using a hand-torch after adding a small amount of helium gas. To prepare a fully toluene-absorbed sample, the evacuated host compound was exposed to saturated toluene vapor at room temperature. Powder X-rays diffraction patterns of the empty Cuchd were obtained in the heating direction from 100 to 300 K. A significant change is observed at around 200 K, and the lattice parameter

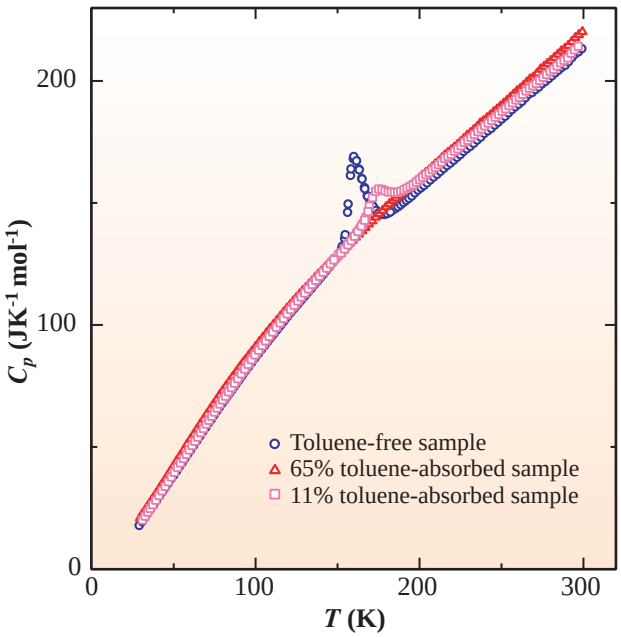

Fig. 1. Measured molar heat capacities of toluene-free and toluene-absorbed copper(II) *trans*-1,4-cyclohexane dicarboxylate.

change is large in the *c*-axis compared with those in the *a*- and *b*-axes. Such anisotropic nature should be caused by the difference between two binding forces: van deer Waals force in the *c*-direction and a strong covalent bond in the *a*- and *b*-directions. Using the obtained lattice parameters at 100 K, the stable structure of the empty Cuchd was estimated using molecular dynamics simulation with Cerius2. Rietveld refinement was carried out using the stable structure estimated by simulation as the initial structure. The program RIETAN-2000 was used for the analysis. In the process of the refinement, ten hydrogen atoms were excluded. The refinement yielded a final R_{wp} of 8.51 % (R_p = 6.37 %), and the refined structure is shown in Fig. 2, where nanopores are clearly seen. The structure of high temperature phase could not be refined completely because of some disorders in the structure and thermal motion: The position and isotropic displacement parameters of copper atoms were refined, but the positions of the oxygen atoms and the carbon atoms could not be determined. On the other hand, no structural change was observed between 100 and 300 K in the fully toluene-absorbed sample. Furthermore, the structure was similar to that of the low temperature phase of the toluene-free sample. The shrinkage of the crystal lattice due to the toluene absorbed was also observed. These results are in good agreement with the results of calorimetry. Thus, the host compound of copper(II) *trans*-1,4-cyclohexane dicarboxylate has a structural phase transition at about 160 K, and the fully toluene-absorbed sample has no phase transition and its crystal structure is fixed to the low temperature phase of the host compound by a strong host-guest interaction. Similar phenomena in structural phase transition were observed in the samples absorbing other guest molecules [3].

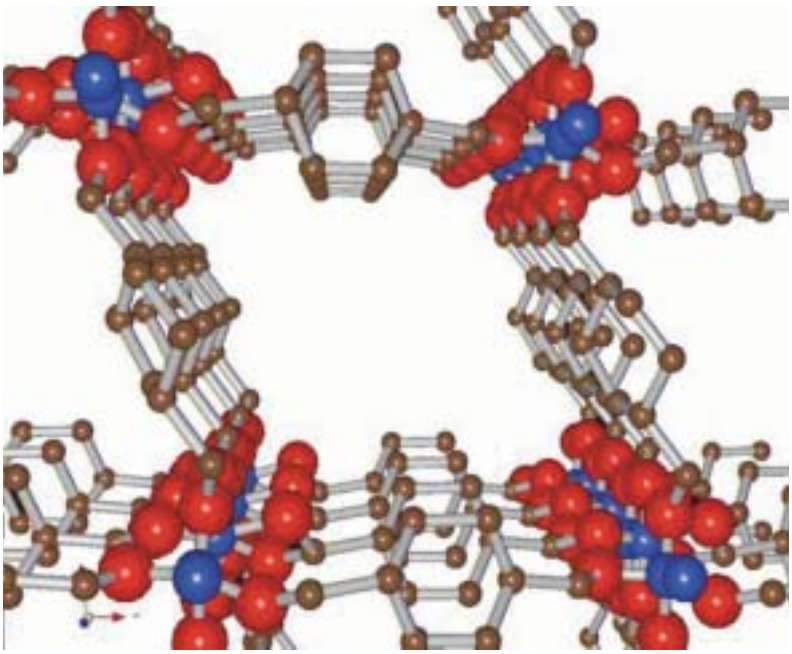

Fig. 2. Structure of low temperature phase (at 100 K) of copper(II) *trans*-1,4-cyclohexane dicarboxylate obtained by Rietveld analysis.

Hitoshi Kawaji*, Mikako Inoue and Tooru Atake

Materials and Structures Laboratory,
Tokyo Institute of Technology

*E-mail: kawaji@msl.titech.ac.jp

References

[1] M. Inoue *et al.*: Chem. Phys. Lett. **365** (2002) 509.
[2] M. Inoue *et al.*: Solid State Commun. **134** (2005) 303.
[3] *M. Inoue, T. Atake, H. Kawaji and T. Tojo: submitted to Thermochim. Acta.*

Highly Dense & Selective Acetylene Accommodation in Metal-Organic Microporous Material

The recent advent of metal(organic microporous materials (MOMs), as new functional microporous adsorbents has attracted the attention of chemists [1,2] owing to scientific interest in the creation of unprecedented regular nano-sized spaces and in the finding of novel phenomena, as well as commercial interest in their application for storage, separation and heterogeneous catalysis. One of the advantages of MOMs, over other microporous materials such as activated carbons, is designability, which provides a variety of surface properties. This prominent feature leads us to expect that MOMs will show a high adsorption capability for specific molecules. However, few useful concepts and strategies for the specific adsorption of smaller molecules have been established to date. Here, we have found superb sorption of acetylene molecules on the functionalized surface of an MOM and show an enhanced "confinement effect," which can be achieved by precisely and regularly arranged double hydrogen bonding sites in a nano-sized pore wall, applicable to a highly stable, selective adsorption system [3].

Acetylene (C_2H_2) is one of the key molecules as a starting material for many chemical and electric materials. In order to obtain highly pure C_2H_2 for the preparation of these materials, the separation of C_2H_2 from a mixture gas containing carbon dioxide (CO_2) impurities without a large expenditure of energy is an important subject. However the separation is considerably difficult because these molecules are quite similar to one another in equilibrium sorption parameters, related physico-chemical properties, and molecular size and shape (Fig. 1). In addition, acetylene is well known as a highly reactive molecule and, therefore, it cannot be compressed above 0.2 MPa; otherwise, it explodes without oxygen, even at room temperature. With this background, more feasible and safe materials for C_2H_2 separation are required.

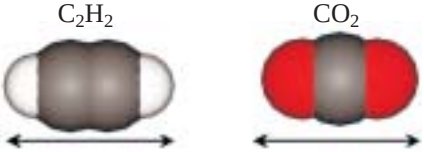

	C_2H_2	CO_2
Molecular Size	5.5 Å	5.3 Å
Critical Temperature	308.2 K	304.2 K
Standard Boiling Point	189.2 K	194.7 K

Fig. 1. Molecular size and thermodynamic properties of C_2H_2 and CO_2.

The complex **1** $[Cu_2(pzdc)_2(pyz)]$ (pzdc = pyrazine-2,3-dicarboxylate, pyz = pyrazine) is a suitable adsorbate for the adsorption of C_2H_2 and CO_2 molecules due to their permanent one-dimensional channel, with a cross section of 4×6 Å. In addition, **1** has oxygen atoms in its pore surface, which act as basic adsorption sites for guest molecules. Accordingly, it is expected that 1 would exert an effective sorption ability for C_2H_2 molecules because C_2H_2 molecules have a linear form with acidic hydrogen atoms at both ends (pK_a = 25). The adsorption isotherms of C_2H_2 and CO_2 at 270, 300 and 310 K were measured on anhydrous **1** (Fig. 2). A marked difference between C_2H_2 and CO_2 adsorption isotherms was observed. The adsorption isotherms of C_2H_2 show a steep rise in the very low-pressure region and reach saturation, whereas those of CO_2 indicate gradual adsorption. The saturation-adsorbed amount of C_2H_2 corresponds to just one molecule per unit pore. The maximum ratio of the amount adsorbed of C_2H_2 relative to that of CO_2 absorbed is 26.0 (at 1.1 kPa) at 270 K, indicating that 1 adsorbed C_2H_2 more preferentially than CO_2.

To elucidate the mechanism of the high adsorption ability for C_2H_2 molecules in **1**, we determined the structure and electron density of **1** with adsorbed C_2H_2 molecules by the MEM (maximum entropy method)/Rietveld analysis using synchrotron X-ray powder diffraction (XRPD) data of **1** with C_2H_2 at 10 kPa at 170 K (Fig. 3), beamline **BL02B2**. Only one C_2H_2 molecule locates in the middle of the channels. Surprisingly, the density of adsorbed C_2H_2 in the pore is equivalent to the value of an imaginary state of acetylene at 41 MPa at room temperature and is 200 times larger than the value of the compression limit for the safe use of C_2H_2 at room temperature, 0.20 MPa.

In the channels, C_2H_2 molecules align along the *a*-axis, and each end of the C_2H_2 molecule is oriented to two non-coordinated oxygen atoms on the pore wall. We can recognize a few electrons (0.21 $eÅ^{-3}$) between the hydrogen atom of C_2H_2 and the free oxygen atom, indicating that O---H–C hydrogen bonds exist. These interactions strongly fix the C_2H_2 molecule in a periodic unit pore and isolate the C_2H_2 in the 1D-channel, which enhances the "confinement effect" and enables stable accommodation.

The specific sorption ability of **1** for C_2H_2 is ascribed to the binding of the acetylene molecule in two basic oxygen atom sites, which are ideally arranged on a regular micropore surface. Usually, small molecules such as CO_2 are adsorbed in the micropore only by the deep van der Waals type potential energy well. However, these functional sites of flexible MOMs attain optimal chemical bonding with specific adsorbates and significantly enhance the "confinement effect." According to the results, when the multiple specific interaction-sites are located at suitable positions on a regular micropore, a specific adsorption system to the target molecule can be realized. This new guideline for the specific adsorption system on microporous materials will be applicable to a wide range of target molecules.

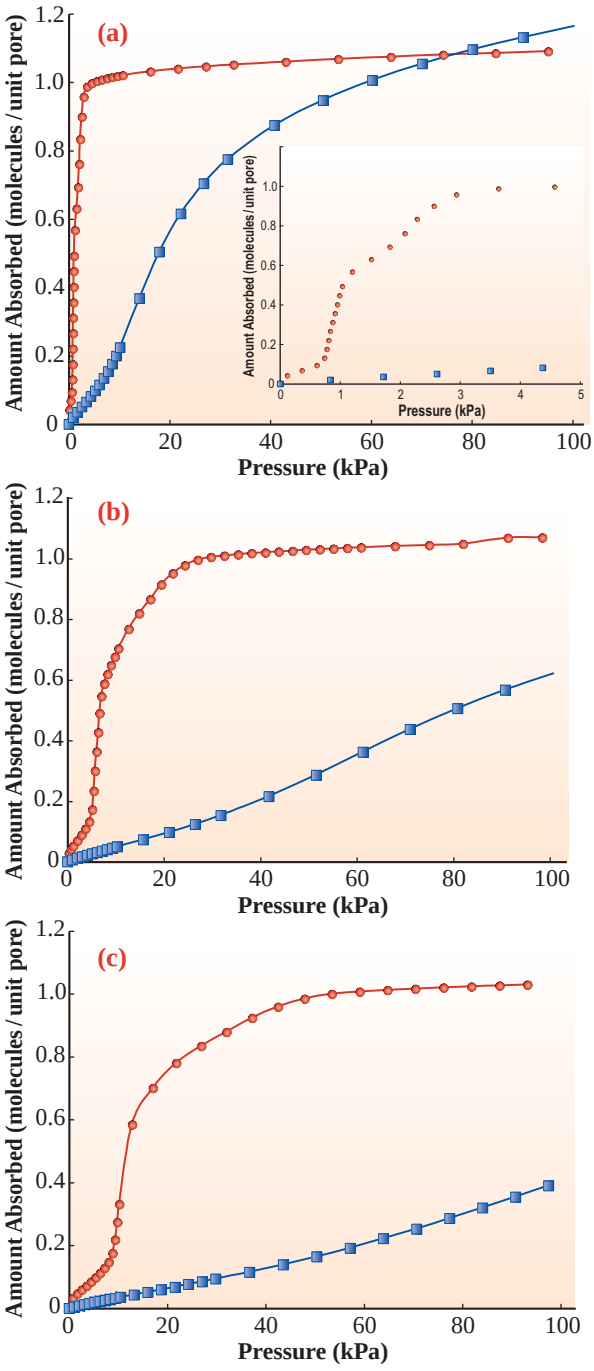

Fig. 2. Adsorption isotherms for C_2H_2 (red circles) and CO_2 (blue squares) on **1**. The pressure range is from 10^{-4} to 100 kPa and the temperatures is 270 K (inset shows a lower pressure region) **(a)**, 300 K **(b)** and 310 K **(c)**.

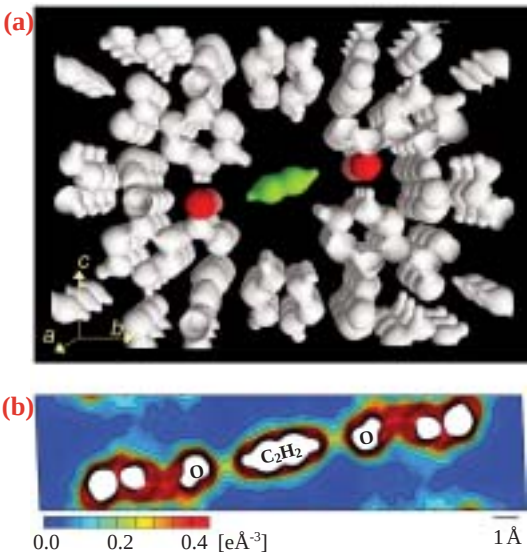

Fig. 3. MEM electron density views. **(a)** MEM electron densities of C_2H_2 adsorbed **1** at 170 K as equal-density contour surface along *a*-axis. The equicontour level is 1.0 eÅ^{-3}. The central C_2H_2 molecule and oxygen atoms are in yellow-green and red, respectively. Other atoms are in white. **(b)** MEM electron density distribution views on two-dimensional section along molecular axis of C_2H_2 molecule down the *a*-axis.

Ryotaro Matsuda[a,*], Susumu Kitagawa[a] and Masaki Takata[b,c]

[a] Department of Synthetic Chemistry and Biological Chemistry, Kyoto University
[b] SPring-8 / JASRI
[c] CREST, Japan Science and Technology Agency

*E-mail: ryotato@sbchem.kyoto-u.ac.jp

References

[1] S. Kitagawa *et al.*: Angew. Chem. Int. Ed. **43** (2004) 2334.
[2] R. Matsuda *et al.*: J. Am. Chem. Soc. **43** (2004) 14063.
[3] *R. Matsuda, R. Kitaura, S. Kitagawa, Y. Kubota, R. V. Belosludov, T. C. Kobayashi, H. Sakamoto, M. Takata and Y. Kawazoe: Nature* ***436*** *(2005) 238.*

Symmetry-dependent Vibrational Excitation in Core-level Photoionization of Small Molecules: Experiment and Theory

Electronically excited states often have individual stable geometries that are different from the ground state. Photoexcitation causes a sudden redistribution of electric charges. Nuclei cannot adapt to this on the same time scale and are considered stationary during electronic transition. As a consequence, the final state is often left vibrationally excited. One can obtain information on the stable geometry of the electronically excited state by analyzing the distribution of the population of vibrational components on the basis of the Franck-Condon (FC) principle [1].

A high photon flux at very narrow photon bandwidths available using high-resolution soft X-ray monochromators installed at high-brilliance third generation synchrotron radiation light sources has stimulated renewed interest in core-level photoelectron spectroscopy [2,3]: one can observe vibrational structures in the core-level photoelectron mainline spectra of various molecules and thereby discuss the stable geometries of core-hole states [3,4]. In the present work, we demonstrate that one can observe vibrational structures even in the core-level photoelectron satellite spectra and thereby can discuss potential energy surfaces of the shake-up satellite states based on the FC principle [5,6].

Photoelectron satellites are classified into two groups, direct shake-up and conjugate shake-up. The conjugate shake-up contribution is significant near the ionization threshold and decreases rapidly with increasing energy. At high energies, the direct shake-up contribution becomes dominant and the asymmetry parameter approaches two. Thus, recording photoelectron satellite spectrum as a function of photon energy, in the direction both parallel and perpendicular to the polarization axis, one can separate the direct and conjugate shake-up contributions and therefore the symmetries of the shake-up satellite states.

Symmetry-resolved C 1*s* photoelectron satellite spectra of CO were obtained by angle-resolved photoelectron spectroscopy carried out on the c-branch of the soft X-ray photochemistry beamline **BL27SU**. The results are compared in Fig. 1 with those of *ab initio* calculations employing symmetry-adapted cluster-expansion configuration-interaction (SAC-CI) general-*R* methods, where vibrational intensity ratios were determined by FC factors [5]. Very reasonable agreements of the vibrational distributions between the experimental and theoretical spectra confirm not only the assignments of these satellite states to $2\sigma^{-1}1\pi^{-1}2\pi^{*}\ ^{2}\Sigma^{+}$ dominated by the direct shake-up and $2\sigma^{-1}5\sigma^{-1}2\pi^{*}\ ^{2}\Pi$ attributed to the conjugate shake-up, but also the validity of the present *ab initio* potential curves of these shake-up satellite states. The activation of the high vibrational states in the $^{2}\Sigma^{+}$ band is due to the large relaxation with

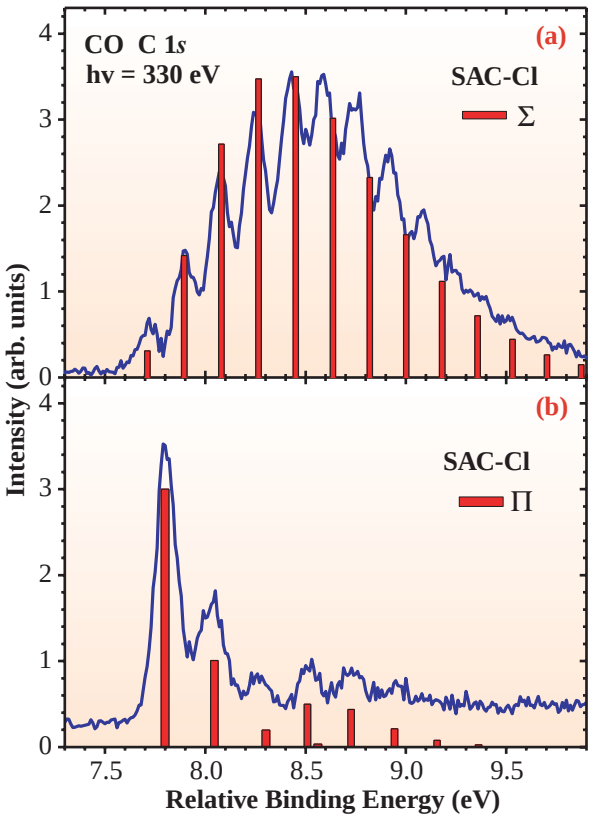

Fig. 1. C 1s satellite bands of CO for transitions to $2\sigma^{-1}1\pi^{-1}2\pi^{*}\ ^{2}\Sigma^{+}$ **(a)** and $2\sigma^{-1}5\sigma^{-1}2\pi^{*}\ ^{2}\Pi$ **(b)**: comparison between experimental (blue solid line) and theoretical (red vertical bars) results. The binding energy scale is relative to the C 1*s* binding energy.

elongation of the bond length by 0.17 Å relative to the neutral ground state. The spectra for both $^2\Pi$ bands have a maximum intensity at v = 0 as a result of the small relaxation with bond elongation of less than 0.1 Å.

The work has been extended to N_2 [6]. Compared with CO, N_2 has an additional complication: each of its mainline and satellite states splits into closely-separated gerade (g) and ungerade (u) states. FC analysis of the g and u individual mainlines, whose separation is ~100 meV, indicates that bond length shrinks by 0.018 and 0.023 Å for the g and u core-hole states, respectively. SAC-CI calculations for the potential energy curves successfully confirmed the observed difference in stable geometry between the g and u core-hole states. The g-u separations for the satellite states estimated by the SAC-CI calculations are ~40 meV, much smaller than the lifetime width of ~120 meV, and thus cannot be resolved experimentally. As shown in Fig. 2, SAC-CI satellite spectra agree well with experimental ones, confirming the assignments to $1\sigma_u^{-1}1\pi_u^{-1}1\pi_g^{1}\ ^2\Sigma_g^+$, $1\sigma_g^{-1}1\pi_u^{-1}1\pi_g^{1}\ ^2\Sigma_u^+$, $1\sigma_u^{-1}3\sigma_g^{-1}1\pi_g^{1}\ ^2\Pi_u$, and $1\sigma_g^{-1}3\sigma_g^{-1}1\pi_g^{1}\ ^2\Pi_g$. SAC-CI calculations predict large elongation of the bond length by 0.164 Å for the $^2\Sigma_{g,u}^+$ states and 0.062-0.091 Å for the $^2\Pi_{g,u}$ states. This explains that the high vibrational states are activated in the $^2\Sigma_{g,u}^+$ band and that the vibrational states are less excited in the $^2\Pi_{g,u}$ band.

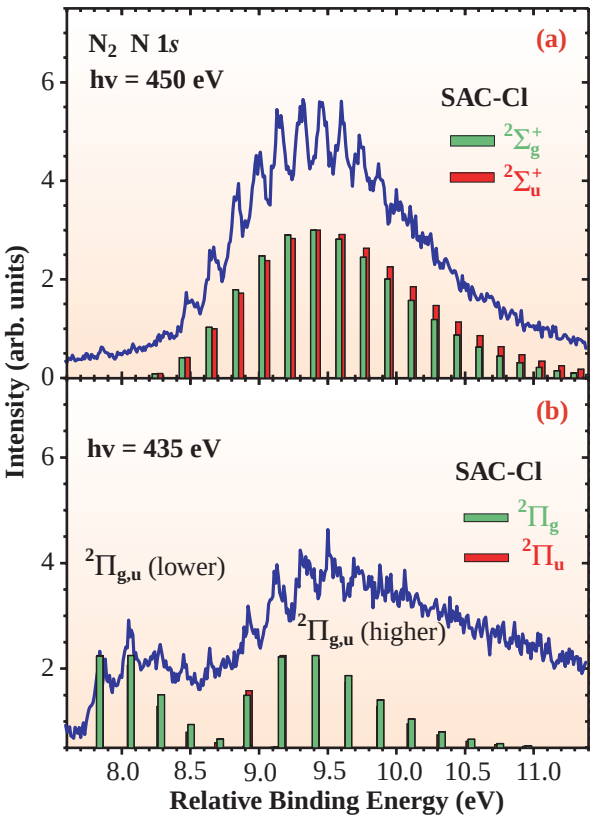

Fig. 2. N 1*s* satellite bands of N_2 for the transitions to $1\sigma_u^{-1}1\pi_u^{-1}1\pi_g^{1}\ ^2\Sigma_g^+$ and $1\sigma_g^{-1}1\pi_u^{-1}1\pi_g^{1}\ ^2\Sigma_u^+$ **(a)** and $1\sigma_u^{-1}3\sigma_g^{-1}1\pi_g^{1}\ ^2\Pi_u$ and $1\sigma_g^{-1}3\sigma_g^{-1}1\pi_g^{1}\ ^2\Pi_g$ **(b)**: comparison between experimental (blue solid line) and theoretical (green and red vertical bars for g and u, respectively) results. The binding energy scale is relative to the N 1*s* $1\sigma_g$ binding energy.

Kiyoshi Ueda[a,*], Masahiro Ehara[b] and Hiroshi Nakatsuji[b]

[a] Institute of Multidisciplinary Research for Advanced Materials, Tohoku University
[b] Department of Synthetic Chemistry and Biological Chemistry, Kyoto University

*E-mail: ueda@tagen.tohoku.ac.jp

References

[1] G. Herzberg: Molecular Spectra and Molecular Structure 1, Spectra of Diatomic Molecules (D. Van Nostrand, London, 1967).
[2] K. Ueda: J. Phys. B, At. Mol. Opt. Phys. **36** (2003) R1.
[3] U. Hergenhahn: J. Phys. B: At. Mol. Opt. Phys. **37** (2004) R89.
[4] *M. Matsumoto, K. Ueda, E. Kukk, H. Yoshida, T. Tanaka, M. Kitajima, H. Tanaka, Y. Tamenori, K. Kuramoto, M. Ehara and H. Nakatsuji: Chem. Phys. Lett.* ***417*** *(2006) 89.*
[5] *K. Ueda, M. Hoshino, T. Tanaka, M. Kitajima, H. Tanaka, A. De Fanis, Y. Tamenori, M. Ehara, F. Oyagi, K. Kuramoto and H. Nakatsuji: Phys. Rev. Lett.* ***94*** *(2005) 243004.*
[6] *M. Ehara, H. Nakatsuji, M. Matsumoto, T. Hatamoto, X.-J. Liu, T. Lischke, G. Prümper, T. Tanaka, C. Makochekanwa, M. Hoshino, H. Tanaka, J.R. Harries, Y. Tamenori and K. Ueda: J. Chem. Phys.* ***124*** *(2006) 124311.*

Probing of Local Electronic Structure in Small Hydrogen Bonding Clusters using Soft X-ray Photoabsorption Spectroscopy

Unlike valence orbitals, inner-shell orbitals are highly localized around an atom to which electrons originally belong. Inner-shell photoabsorption spectroscopy is therefore sensitive to the chemical environment of each atom and enables us to investigate the local geometric and electronic structures of matter [1]. This is applied not only to atoms and molecules in the gas phase but to those adsorbed on surfaces.

Inner-shell photoabsorption spectroscopy has also been applied to the analysis of gas phase clusters, which bridge a gap between an isolated molecule and a molecule in the condensed phase [2]. An inner-shell photoabsorption study of clusters is expected to become a useful probe for research on the local properties of electronic structures in small clusters, because higher unoccupied orbitals have further spatial extension and are strongly perturbed by surrounding molecules. From this viewpoint, inner-shell excitation spectra of small clusters have been extensively measured in recent years [2]. However, only few studies of the inner-shell excitation of hydrogen-bonding (HB) clusters have been reported. The purpose of our investigation is to elucidate the change in electronic structure by HB interaction at the cluster level [3].

Experiments were carried out at the soft X-ray photochemistry beamline **BL27SU**. The experimental setup is shown in Fig. 1. Ethanol clusters were produced by a seeded beam method. Helium at a pressure of 4 atm was bubbled through a sample reservoir containing room temperature ethanol, and the mixture was expanded through a nozzle of 30 μm diameter. A supersonic beam was collimated by a skimmer and led to the main chamber. In the main chamber, it was crossed with a soft X-ray beam in the ionization region of a double-field type time-of-flight (TOF) mass spectrometer. Ions and electrons formed by the soft X-ray absorption were extracted toward opposite directions in the ionization region. The electrons were detected by a micro-sphere-plate (MSP) and the ions were detected by another MSP after the flight through the TOF tube. Electron signals were fed into the start pulse input of a multi-stop time-to-digital converter and ion signals were fed into the stop pulse input to obtain electron-ion coincidence signals.

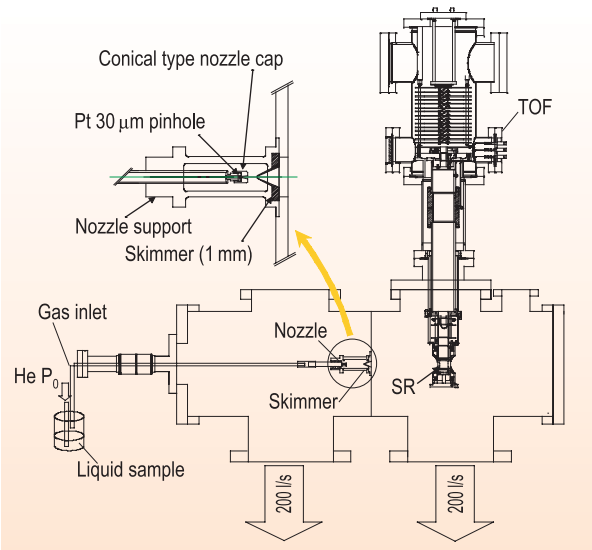

Fig. 1. Schematic layout of experimental chamber.

Figure 2 shows TOF mass spectra of ethanol measured under (a) seeded supersonic beam (He 4 atm) and (b) effusive beam conditions. Under the effusive beam condition, no ions larger than m/z=45 were found in the TOF mass spectrum. Because the effusive beam consists of only ethanol monomers, these ions are formed from the fragmentation of ethanol molecules. On the other hand, under the seeded supersonic beam condition, several ions larger than m/z=45 appear. Prominent peaks are assigned to protonated ethanol cluster ions, $H(C_2H_5OH)_n^+$ (n=1-6). Owing to an intracluster ion-molecular reaction that proceeds rapidly during cluster fragmentation, the protonated cluster ions $H(C_2H_5OH)_n^+$ become predominant products.

Inner-shell excitation spectra of ethanol clusters were obtained using the partial-ion-yield (PIY) method. The PIY spectra were obtained from the area of the peaks in the TOF spectra measured across the O *K*-edge. Soft X-ray photoabsorption spectra (XAS) of ethanol molecules and PIY spectra of $H(C_2H_5OH)^+$ are shown in Fig. 3. A salient feature is that the PIY of $H(C_2H_5OH)^+$ is very different from that of XAS of ethanol molecules. The PIY of $H(C_2H_5OH)^+$ does not show any enhancement at 534.7 eV which is assigned to the transition

O(1s-σ*(OH)). A similar result, i.e., the loss of a pre-edge feature, has been observed by Nilsson *et al.* [4]. They observed that resonance pre-edge structures in the XAS of liquid water and ice are different from that of water molecules and ascribed this difference to the occurrence of the HB. They suggested that the OH group donating the hydrogen atom does not show the feature in the pre-edge region. The resonance pre-edge feature in the XAS comes from the free OH group that does not donate the hydrogen atom. Unoccupied molecular orbitals responsible for the resonance feature in the XAS of water molecules lose their p-character by participating HB. The present result suggests that a similar change in electronic structure occurs in ethanol clusters. In the case of ethanol clusters, the small clusters are expected to gather via the (H-O...H-O) network. Unlike water, ethanol molecule has only one OH; thus, no free OH remains in the HB clusters. This interaction leads to a drastic reduction in the intensity of σ*(OH) excitation in PIY spectra.

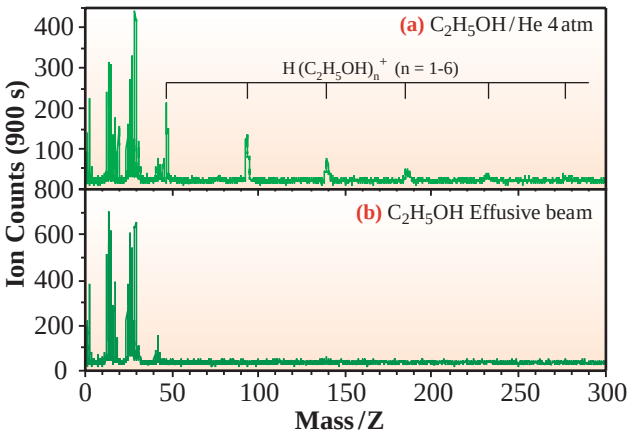

Fig. 2. Comparison of TOF mass spectra of ethanol measured under **(a)** seeded supersonic beam (He 4 atm) and **(b)** effusive beam conditions. The spectra were taken at a photon energy of 545.0 eV, which is higher than the O 1*s* ionization threshold of ethanol.

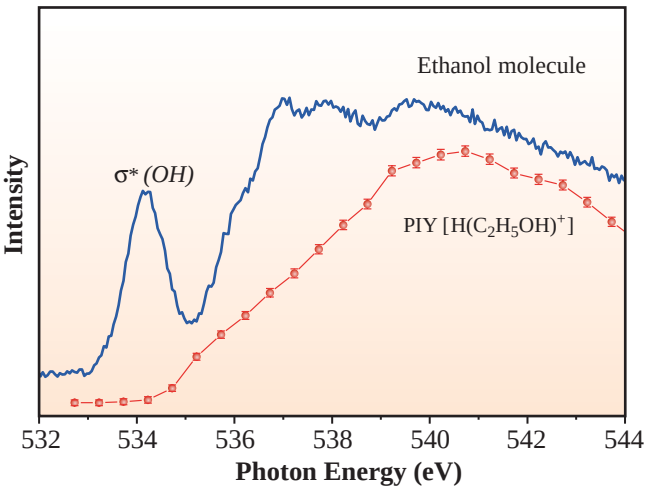

Fig. 3. Comparison of experimental soft X-ray absorption spectra of ethanol cluster (red) and molecule (blue).

Yusuke Tamenori

SPring-8 / JASRI

E-mail: tamenori@spring8.or.jp

References

[1] J. Stöhr: NEXAFS Spectroscopy (Springer-Verlag, 1992).
[2] A.A. Pavlychev and E. Rühl: J. Electron Spectrosc. Relat. Phenom. **207-210** (2000) 106.
[3] *Y. Tamenori, T. Yamaguchi, K. Okada, K. Tabayashi, T. Gejo and K. Honma: J. Electron Spectrosc. Relat. Phenom.* ***144-147*** *(2005) 235; Y. Tamenori, T. Yamaguchi, K. Okada, K. Tabayashi, T. Gejo and K. Honma: submitted to J. Chem. Phys.*
[4] Ph. Wernet *et al.*: Science **304** (2004) 995.

Structural Models of Bimetallic Nanoparticles The Importance of Alloying Extent as Studied By X-Ray Absorption Spectroscopy

Studies of bimetallic nanoparticles (NPs) received great attention from both a scientific and technological communities because most of the nanoparticles catalytic activity depends on their structural aspects [1]. Among the various structural aspects it is of most important to control the homogeneity, dispersion, and alloying extent as they have profound influence on the surface properties which affect the catalytic activity and stability of the bimetallic NPs. Hence methods to get more insights into structural aspects are highly needed. Even though alloying is a well-known phenomenon, detailed studies on quantitative assessment of alloying extent in bimetallic NPs have been lacking so far. By deriving the structural parameters from X-ray absorption spectroscopy (XAS) analysis we proposed a general methodology to estimate the alloying extent or atomic distribution in bimetallic NPs and demonstrated the results on two commercially available carbon-supported Pt-Ru NPs [2].

The XAS spectra were recorded in the transmission mode on two commercial Pt-Ru/C catalysts (*ca.* 2-3 nm, 20% Pt/10% Ru with a Pt/Ru atomic ratio of 1:1) at beamline **BL12B2**. By estimating the ratio of the coordination number (CN) of A around B and also the CN of B around A to the total CNs, we have deduced the alloying extent of A (J_A) and B (J_B) in A-B bimetallic NPs. The parameters that are needed to derive the extent of alloying are represented as $P_{observed}$, $R_{observed}$, P_{random}, and R_{random}. The parameter $P_{observed}$ can be defined as a ratio of the scattering atoms 'B' CN around absorbing 'A' atoms (N_{A-B}) to the total CN of absorbing atoms (ΣN_{A-i}), ($P_{observed} = N_{A-B}/\Sigma N_{A-i}$). Similarly, $R_{observed}$ can be defined as a ratio of the scattering atoms 'A' CN around absorbing 'B' atoms (N_{B-A}) to the total CNs of absorbing atoms (ΣN_{B-i}), ($R_{observed} = N_{B-A}/\Sigma N_{B-i}$). Whereas, P_{random} and R_{random} can be taken as 0.5 for perfect alloyed bimetallic NPs if the atomic ratio of 'A'and 'B' is 1:1. The J_A and J_B for 1:1 A-B bimetallic NPs can then be estimated by using the equations (1) and (2) respectively.

$$J_A = (P_{observed}/P_{random})\_100\% \quad (1)$$
$$J_B = (R_{observed}/R_{random})\_100\% \quad (2)$$

Based on the ΣN_{A-i}, ΣN_{B-i}, J_A and J_B it is possible to predict the structural models of NPs. Seven possible cases were discussed and schematics of the corresponding models are shown in Fig. 1. In case if $\Sigma N_{A-i} > \Sigma N_{B-i}$ there appears core is rich in 'A' atoms

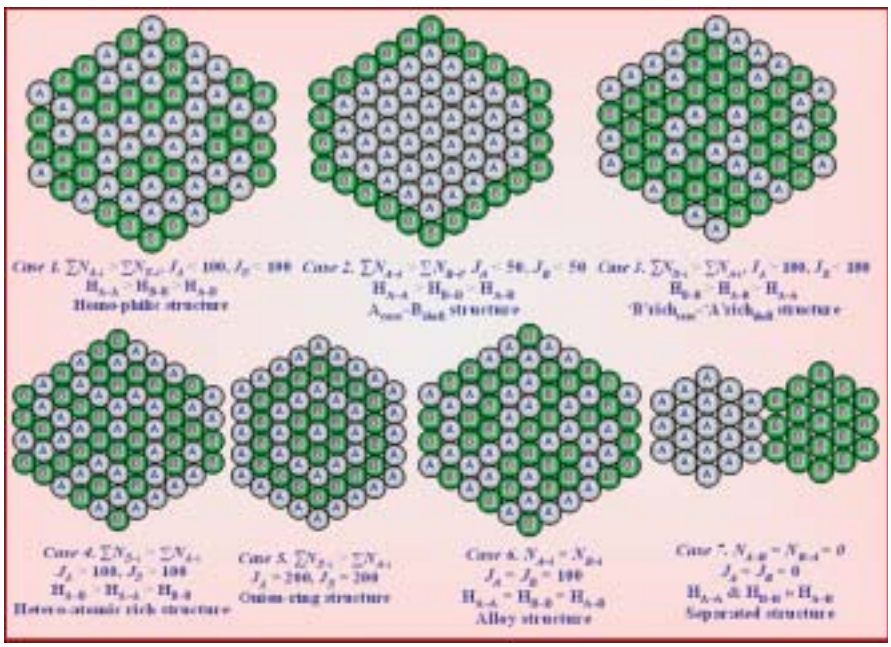

Fig. 1. Schematics of bimetallic nanoparticles at various degrees of alloying.

and shell is rich in 'B' atoms. In this case if both J_A & J_B < 100% then the extent of homo-atomic interactions will become more ($H_{A-A} > H_{B-B} > H_{A-B}$) and results in a homo-philic structure (case 1, Fig. 1). However if J_A & J_B < 50% with a coordination number relationship of $\Sigma N_{A-i} > \Sigma N_{B-i}$ then bimetallic NPs structure is close to A_{core}-B_{shell} (case 2, Fig. 1). In another case, if $\Sigma N_{B-i} > \Sigma N_{A-i}$ then the resultant structure is similar to 'B' rich in core-'A' rich in shell (case 3, Fig. 1). Here if J_A > 100% & J_B < 100% it indicates that 'B' atoms prefers 'B' atoms rather than 'A' and 'A' atoms prefer 'B' atoms rather than 'A' atoms, as a result atomic distribution of 'A' atoms is better than 'B' atoms. In other words we can say that the segregation of 'A' atoms are less pronounced than 'B' atoms with the order of interactions $H_{B-B} > H_{A-B} > H_{A-A}$. However if both J_A and J_B > 100 then the atomic distribution of both 'A' and 'B' atoms are improved with more hetero-atomic interactions than the homo-atomic interactions and bimetallic NPs adopt hetero-atomic rich structure ($H_{A-B} > H_{A-A}$ and H_{B-B}, see case. 4 of Fig. 1). In case 5, if J_A = 200% & J_B = 200% indicates that 'A' atoms always prefer 'B'atoms and vice-versa and the resulting structure look like an onion ring (case 5, Fig. 1). In case 6, if $\Sigma N_{A-i} = \Sigma N_{B-i}$ and $J_A = J_B$ = 100% then bimetallic NPs adopt an alloy structure (case 6, Fig. 1). However if $J_A = J_B = 0$ results in a separated structure (case 7, Fig. 1).

The alloying extent of Pt (J_{Pt}) and Ru (J_{Ru}) for commercial catalysts viz JM 30 and E-TEK 30 Pt-Ru/C catalysts can be obtained from the expression (1) and (2), respectively. The J_{Pt} and J_{Ru} values are calculated as 40 and 78% respectively for JM 30 Pt-Ru/C with $P_{observed}$ and $R_{observed}$ as 0.20 and 0.39 respectively. For E-TEK 30 catalyst the structural parameters $P_{observed}$ and $R_{observed}$ are calculated as 0.13 and 0.24 respectively and the J_{Pt} and J_{Ru} values are 26 and 48% respectively. For both the catalysts it was found that $\Sigma N_{Pt-i} > \Sigma N_{Ru-i}$ and $J_{Ru} > J_{Pt}$ and it indicates that the catalysts adopt a Pt rich in core and Ru rich in shell structure (Fig. 2).

From the quantitative extent of alloying values we infer that in both the catalysts considerable amount of Ru is segregated on the shell layer but its extent is higher in E-TEK 30 when compared to the JM 30. The increased value of J_{Ru} in JM 30 catalyst indicated that most of the Ru is involved in alloying and hence less segregation of Ru in the shell whereas in the case of ETEK 30 catalyst lesser extent of Ru is involved in the alloying and considerable extent of segregation of Ru can be expected in the shell region.

The higher segregation of Ru in the case of ETEK 30 in part may be responsible for its lower methanol oxidation activity compared to JM 30. Increase in J_{Pt} and J_{Ru} values in JM 30 compared to E-TEK 30 indicates that the atomic distribution of Pt and Ru atoms are much facilitated. Increase in atomic distribution can be taken as a measure for enhanced homogeneity.

The alloying extent in bimetallic NPs can easily be estimated by the proposed XAS methodology. From this approach it is possible to provide a quantitative index measuring the changes in atomic distribution in bimetallic NPs which have strong influence on physico-chemical properties of NPs. This methodology can also convenient to extend to other multi-metallic NPs.

JM 30 Pt-Ru/C catalyst E-TEK 30 Pt-Ru/C catalyst

Fig. 2. Structural models deduced for JM 30 **(a)** and E-TEK 30 Pt-Ru/C catalysts **(b)** based on XAS parameters.

Bing-Joe Hwang [a,b,*], Jyh-Fu Lee [b] and Mau-Tsu Tang [b]

[a] Nanoelectrochemistry Laboratory, National Taiwan University of Science and Technology, Taiwan ROC
[b] National Synchrotron Radiation Research Center, Taiwan ROC

*E-mail: bjh@mail.ntust.edu.tw

References

[1] N. Toshima and T. Yonezawa: New J. Chem. **22** (1998) 1179.
[2] *B.-J. Hwang, L.S. Sarma, J.-M. Chen, C.-H. Chen, S.-C. Shih, G.-R. Wang, D.-G. Liu, J.-F. Lee, M.-T. Tang: J. Amer. Chem. Soc.* ***127*** *(2005) 11140.*

Infrared Spectroscopy under Multiextreme Conditions: Direct Observation of Pseudogap Formation and Collapse in CeSb

Cerium monoantimonide (CeSb) has many magnetic phases with complex magnetic structures at low temperatures, high pressures and high magnetic fields [1]. The magnetic structure affects the transport property through the hybridization between Ce 4*f* and Sb 5*p* orbitals, referred to as *pf* mixing [2]. One of the characteristic properties is that at pressures (*P*) of several GPa [3] the electrical resistivity at a temperature (*T*) of around 30 K increases by one full order over that at ambient pressure. Then, we investigated the origin of this enhancement of the electric resistivity using the infrared spectroscopy under multiextreme conditions of low temperatures, high pressures and high magnetic fields.

The experiment was performed at the infrared magneto-optical imaging beamline **BL43IR**. To perform infrared spectroscopy under multiextreme conditions, a diamond anvil pressure cell with a sample was set at the sample position located at the center of a superconducting magnet. The sample conditions were $T \geq 4$ K, $P = 4$ GPa and magnetic fields of $B \leq 14$T.

The temperature dependence of the optical conductivity [σ(ω)] spectrum derived from the Kramers-Kronig analysis of the reflectivity spectrum at P = 4 GPa and B = 0 T is shown in Fig. 1. Below $T = 30$ K and above 60 K, the spectra are typically metallic because σ(ω) increases with decreasing photon energy. At intermediate temperatures, the σ(ω) spectrum displays a strong temperature dependence. At 30 K, the spectrum changes drastically. In particular, σ(ω) below 0.1 eV decreases with decreasing photon energy. This means that the metallic character is suppressed at intermediate temperatures. The σ(ω) spectrum at 35 K has a peak with a center energy of 65 meV. The peak structure indicates the pseudogap appears under the given condition.

The pseudogap collapses not only by increasing temperature but also by applying magnetic field higher than 6.5±0.5 T. The magnetic field - temperature (*B*-*T*) phase diagram at 4 GPa resulting from changes in the σ(ω) spectrum is shown in Fig. 2. In the phase named AF-1, an antiferromagnetic spin aligns directly along the magnetic field. The Sb 5*p*

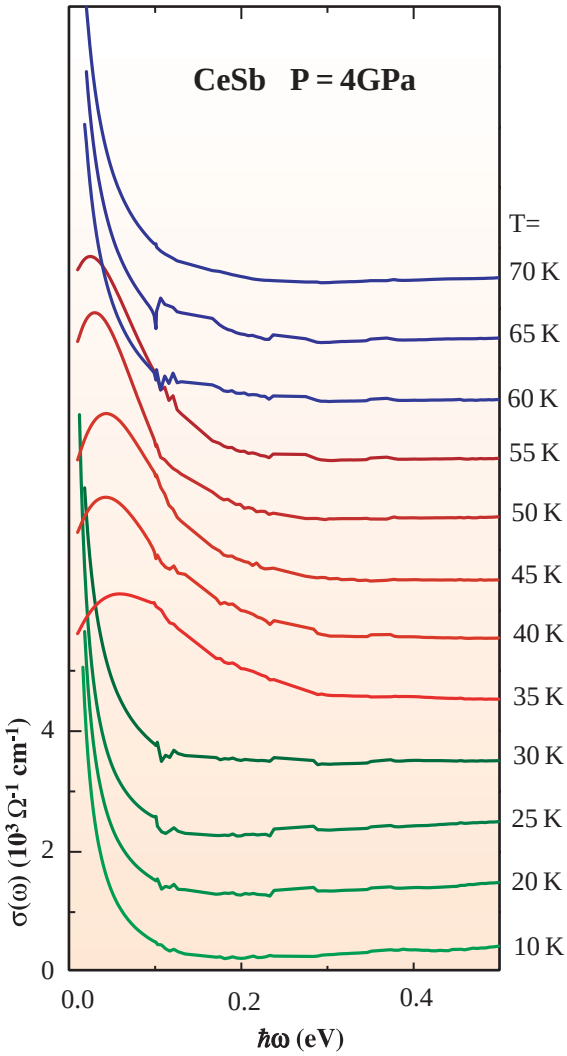

Fig. 1. Temperature dependence of optical conductivity (σ(ω)) spectrum of CeSb at $P = 4$ GPa and $B = 0$ T. Successive curves are offset by 10^3 for clarity. Same phases are shown by the same colors.

band is modulated by the magnetic structure and then the energy gap opens at the Fermi level. In the figure, two phase diagrams of *P*-*T* at B = 0 T [1] and *B*-*T* at ambient pressure [4] are also plotted. The phase diagram at 4 GPa is simpler than that at ambient pressure. In particular, the complex magnetic structure at ambient pressure disappears at 4 GPa. At ambient pressure, since the *pf* mixing competes with other magnetic interactions and crystal field splitting, such complex magnetic phases and structures appear. With increasing pressure, the *pf* mixing is enhanced and then predominates among these interactions. The enhancement of *pf* mixing also results in a simpler magnetic phase diagram at 4 GPa. This is the plausible result of the *pf* mixing enhancement due to applied pressure. This is the first optical observation of the magnetic field induced nonmetal-metal phase transition at high pressures [5].

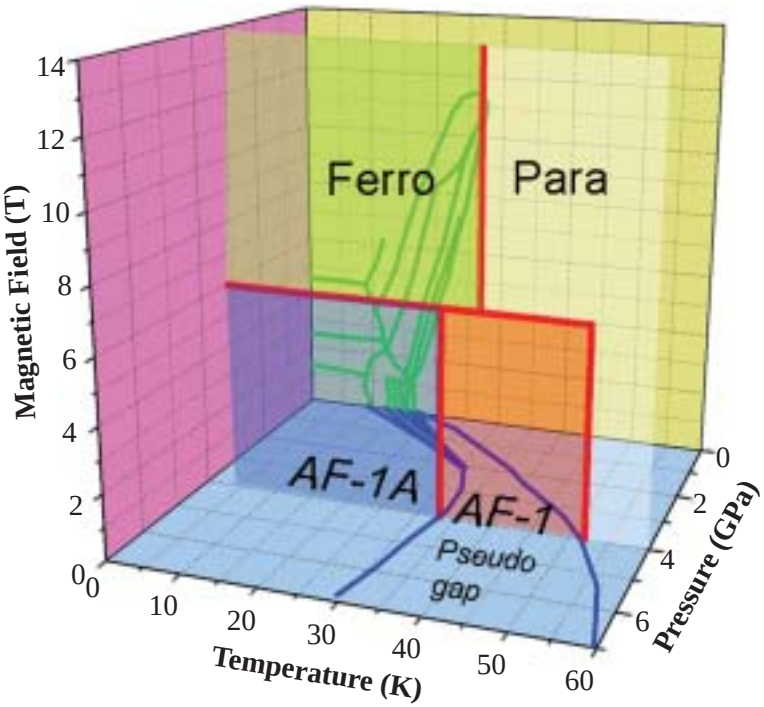

Fig. 2. Magnetic field - temperature (*B*-*T*) phase diagram of CeSb at *P* = 4 GPa derived from σ(ω) spectra under multiextreme conditions. The phase diagrams of *P*-*T* at 0 T (blue lines) [1] and *B*-*T* at ambient pressure (green lines) [5] are also plotted for reference. AF-1 and AF-1A are the names of the phases. Only AF-1 phase has a pseudogap structure.

Shin-ichi Kimura

UVSOR Facility, Institute for Molecular Science

E-mail: kimura@ims.ac.jp

References

[1] T. Osakabe *et al.*: Acta Phys. Pol. **34** (2003) 1469.
[2] H. Takahashi and T. Kasuya: J. Phys. C: Solid State Phys. **18** (1985) 2697; *ibid* 2709; *ibid* 2721; *ibid* 2731; *ibid* 2745; *ibid* 2755.
[3] N. Môri *et al.*: JJAP Series 8 (1993) 182.
[4] S. Kimura *et al.*: J. Phys. Soc. Jpn. **71** (2002) 2299.
[5] *T. Nishi, S. Kimura, T. Takahashi, Y. Mori, Y.S. Kwon, H.J. Im and H. Kitazawa: Phys. Rev. B* ***71*** *(2005) 220401(R).*

Earth & Planetary Science

High-pressure and high-temperature *in-situ* X-ray observation using synchrotron radiation has become an indispensable technique for Earth and planetary sciences. Pressure and temperature conditions available in the laboratory using a laser-heated diamond anvil have been extended considerably at SPring-8 and have reached to the condition corresponding to the center of the Earth. The first paper by Kuwayama *et al.* is a work of this category and is no doubt frontier research in this field. One of the unique features of SPring-8 is that there are many multi-anvil type high-pressure and high-temperature apparatus combined with synchrotron radiation. Although the pressure range attainable by this type of apparatus is limited compared with that attainable by a diamond anvil, many unique studies have been carried out using the merit of a much larger sample space available in multi-anvil apparatus. Higo *et al.*'s work provides direct information on the elastic wave velocity of minerals in the Earth's deep interior. Many arguments can be made on the mantle structure by comparing these data with the results obtained from seismic observations. The kinetics of the phase transformation of silicates are an important factor for the discussions of dynamics in the Earth, and Kubo *et al.* have succeeded in obtaining high-quality data in this field. Molten silicates play very important roles in many processes in the Earth, but because of technical difficulties, only very limited knowledge of its physical properties has been so far obtained. Urakawa *et al.* have succeeded in developing a new technique for determining the density of silicate melts under mantle conditions. This will provide fruitful information on the evolution and dynamics of magma in the mantle. These four papers provide new frontier research information in the fields of Earth and Planetary Science.

Takehiko Yagi

Institute for Solid State Physics
University of Tokyo

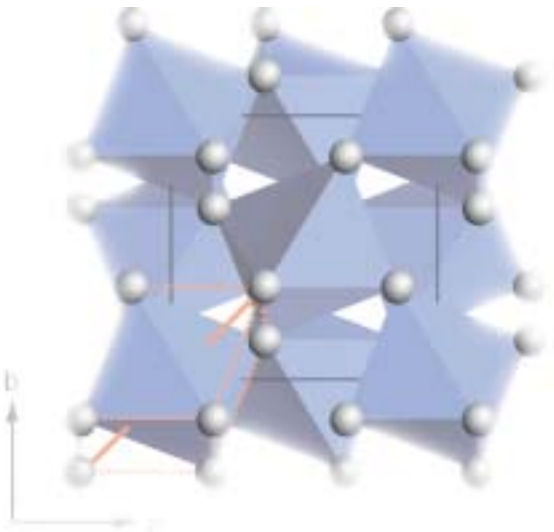

New High-pressure form of Pyrite-type Silica under Multimegabar Pressure

Silica (SiO_2) is one of the most important compounds across a range of sciences, along with water and hydrogen and it is the most abundant component of the Earth's crust and mantle. Therefore, the high-pressure behavior of silica has long been of great interest owing to its wide range of implications in geophysics, materials science, and solid-state physics. At relatively low pressures, Si is tetrahedrally coordinated by O in silica polymorphs. Since the discovery of stishovite (a rutile-type polymorph of silica with octahedrally coordinated silicon which is stable above ~10 GPa), there has been significant interest in the possibility of denser phases at high pressures. Previous experimental studies have shown that stishovite undergoes a second-order structural phase transition to a $CaCl_2$-type phase at around 70 GPa and 1600 K and further transforms to an α-PbO_2-type phase above 121 GPa and 2400 K without change in the coordination number of Si, in excellent agreement with the first-principles predictions. Since the theoretical calculations of Park *et al.* in 1988 [1] indicated that cubic silica should be stable at a higher pressure, a number of subsequent theoretical studies have demonstrated the phase transition from the α-PbO_2-type to a pyrite-type (modified fluorite-type) structure at around 200 GPa [2-4]. However, no experimental studies of silica have been carried out at such multimegabar pressures due to significant difficulties in compression as well as heating. Here, we report the first experimental data on the crystal structure and stability of pyrite-type silica.

We performed *in situ* X-ray observations of silica at high pressure and temperature of up to 300 GPa and 2000 K [5]. Angle-dispersive X-ray diffraction spectra were collected at beamline **BL10XU**. The high pressure and temperature conditions were generated in a laser-heated diamond anvil cell (LHDAC). Temperature was measured by the spectroradiometric method. Pressure was determined from the unit-cell volume of platinum mixed with the sample using the *P-V-T* equation of state.

The results demonstrate that the α-PbO_2-type silica is stable up to 260 GPa and 2000 K (Fig. 1). Above 268 GPa and 1800 K, eight new peaks were observed in the X-ray diffraction pattern (Fig. 2). These new peaks can be indexed by a cubic cell with lattice parameter a = 3.9299(2) Å at 271 GPa and 300 K and assigned to a pyrite-type structure (space group $Pa\bar{3}$). To determine the crystal structure, profile fitting was performed by the Rietveld method. The crystal structure of pyrite-type silica is illustrated in Fig. 3. The pyrite structure has an unusual 6 + 2 cation coordination. Rietveld analysis showed that pyrite-type silica has six Si-O bonds with a distance of 1.608 Å and two additional interpolyhedral Si-O bonds with a distance of 2.372 Å. Such interpolyhedral Si-O distance in the pyrite-type structure is considerably shorter than that in the α-PbO_2-type structure (2.726 Å when the average Si-O distance in SiO_6-octahedra is 1.649 Å) in which Si is six-coordinated. The increase in the coordination number of Si from 6 to 6 + 2 results in a large increase in density. The density of pyrite-type silica is 6.576(1) g/cm^3 at 271 GPa and

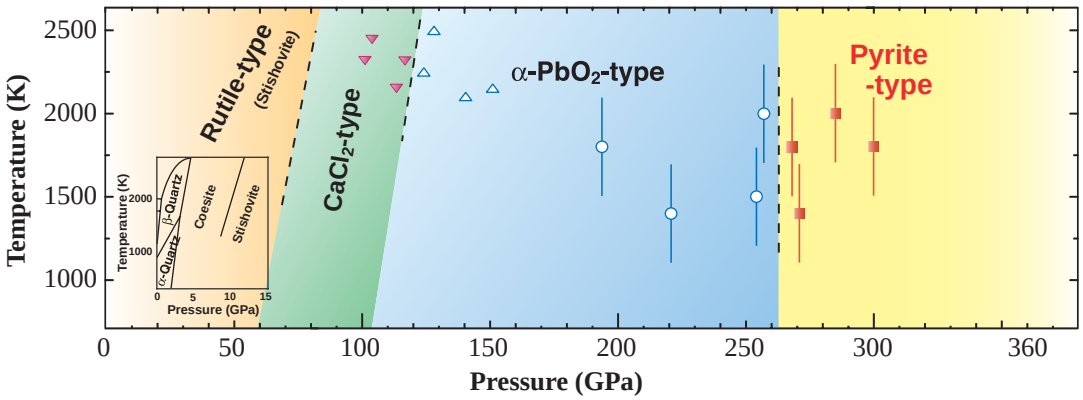

Fig. 1. Phase diagram of SiO_2. Open circles and solid squares indicate the stabilities of α-PbO_2-type and pyrite-type phases, respectively.

300 K. It is larger by 4.7% when compared with that of the α-PbO_2-type phase at equivalent pressure. FeS_2 pyrite has relatively short S-S covalent bonds and is the cause of its metallic nature. If O-O bonds exist in pyrite-type silica, it possibly indicates a pressure-induced metallization of SiO_2. However, the Rietveld analysis showed that the shortest O-O distance in pyrite-type silica is 2.063(6) Å, which is considerably longer than the typical distance of a single covalent O-O bond (~1.5 Å). These experimental data support the argument that there are no O-O covalent bonds in pyrite-type silica [4].

Silica is the most abundant oxide component of the Earth's crust and mantle; however, the pressure required for the formation of pyrite-type silica is greater than that found in the Earth's mantle. Nevertheless, silica is also one of the most important oxide components of other planets in our solar system. The theoretical modelling of the interiors of ice giant planets suggests that both Uranus and Neptune may have a rocky core at pressures of around 800 GPa and below, and therefore, pyrite-type silica might be an important constituent of these planets. Moreover, because silicates are important oxide components in extrasolar systems and in the formation of terrestrial planets where pressures may exceed 260 GPa, the pyrite-type silica phase may be included.

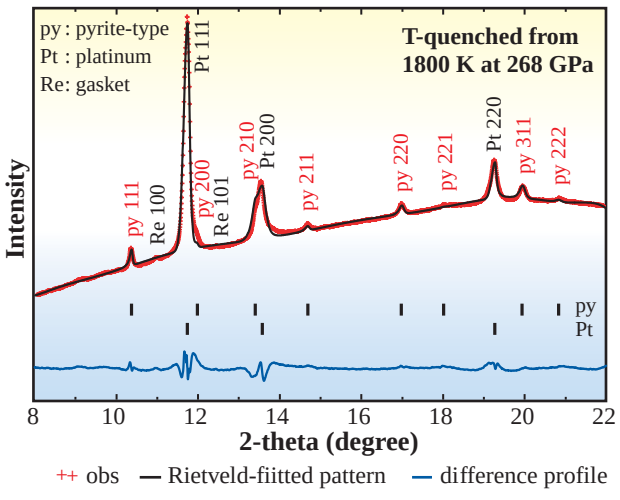

Fig. 2. XRD pattern of pyrite-type silica at 271 GPa and 300 K after heating for 1 hr at 268-271 GPa and 1400-1800 K.

The pressure and temperature conditions at the center of the Earth are 364 GPa and above ~5000 K. A study of the mineralogy at such high pressure and temperature conditions is a prerequisite for understanding the physical properties of the Earth's core; however, such extreme conditions could not be created. Our recent developments with regard to ultra-high pressure and temperature experiments will guide us toward better understanding the deep planetary interiors.

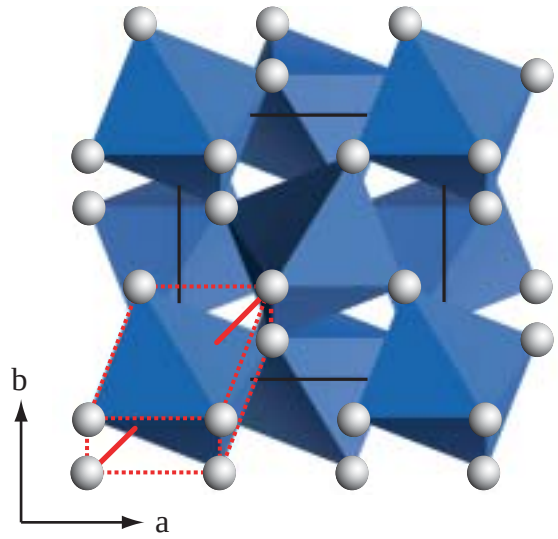

Fig. 3. Crystal structure of pyrite-type silica. The coordination polyhedra of O atoms around Si atoms are shown as octahedra. O atoms are represented by spheres. The black line indicates the unit cell, and the bold red lines indicate the interpolyhedral Si-O bonds.

Yasuhiro Kuwayama* and Kei Hirose

Department of Earth and Planetary Sciences,
Tokyo Institute of Technology

*E-mail: ykuwayam@geo.titech.ac.jp

References

[1] K.T. Park *et al.*: Nature **336** (1988) 670.
[2] B.B. Karki *et al.*: Phys. Rev. B **55** (1997) 3465.
[3] D.M. Teter *et al.*: Phys. Rev. Lett. **80** (1998) 2145.
[4] A.R. Oganov *et al.*: Phys. Rev. B **71** (2005) 064104.
[5] *Y. Kuwayama, K. Hirose, N. Sata and Y. Ohishi: Science **309** (2005) 923.*

Precise Measurement of Seismic Wave Velocities under Deep Mantle Conditions

Variations in seismic wave velocities (Vp and Vs) as a function of depth are the most fundamental information to assess the materials in the Earth's deep interior. The elastic wave velocities of minerals have been measured by various methods, such as ultrasonic interferometry, Brillouin scattering, and ultrasonic resonance, but none of these methods have achieved measurements under the conditions of the mantle transition region (P = ~13-24 GPa, T = ~1700-2000 K). We have developed techniques of combined ultrasonic and *in situ* X-ray observations to precisely measure elastic wave velocities in sintered aggregates of high-pressure phases at simultaneous high pressure and high temperature. As a result, we succeeded in such measurements for representative mantle minerals at pressures up to ~19 GPa and temperatures up to ~1700K, equivalent to the P-T conditions of the middle part of the mantle transition region.

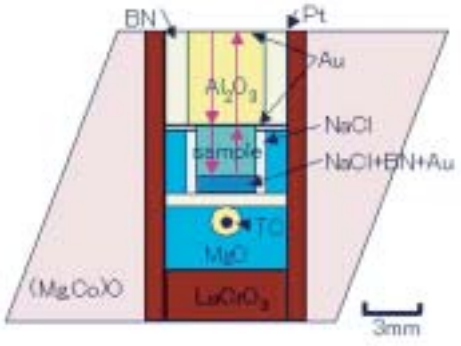

Fig.1. Cross section of cell assemblage used for present ultrasonic/X-ray diffraction measurement at high pressure and high temperature.

We first synthesized the sintered bodies of $(Mg_{0.9}Fe_{0.1})_2SiO_4$ ringwoodite and majorite with a complex chemical composition [1], which are supposed to be the major high-pressure phases in the mantle transition region, using a large (3000-ton) Kawai-type multianvil apparatus (ORANGE-3000) at Geodynamics Research Center, Ehime University. The top and bottom surfaces of the sintered rod samples with dimensions of ~2 mm both in diameter and length were carefully polished, and transferred to the cell assemblage for ultrasonic measurement, as illustrated in Fig. 1. Platinum tube heater was used, and temperature was measured using a W-Re thermocouple, while pressure was measured by the volume change in NaCl using an appropriate equation of state.

Combined *in situ* X-ray and ultrasonic measurements under high pressure and high temperature were conducted at **BL04B1**, using a 1500-ton multianvil press (SPEED-1500). A schematic illustration of the experimental setup and the X-ray optics used is shown in Fig. 2. Travel times for both P- and S-waves passing through the sample were measured by ultrasonic interferometry developed by [2], while the sample length under pressure and temperature was determined from the X-ray image of the sample using a high-resolution CCD camera. At the same time, X-ray diffraction data both from the sample and the pressure marker were acquired, and the produced pressure and the phases present were monitored throughout the run. An example of the ultrasonic echoes observed at almost the highest pressure and temperature is shown in Fig. 3.

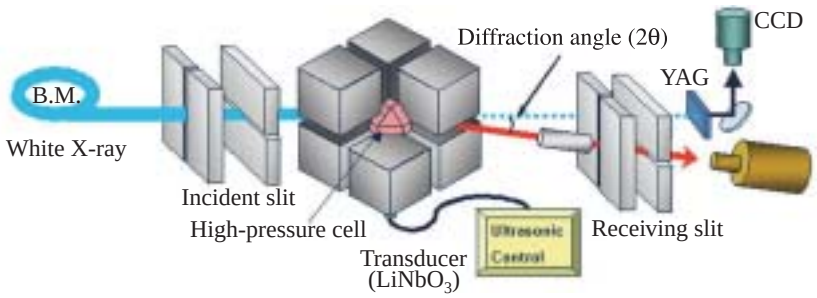

Fig. 2. Schematic illustration of experimental setup for combined ultrasonic and X-ray observations.

As velocity is basically defined by sample length divided by travel time, we can determine Vp and Vs as functions of pressure and temperature from the observed data sets. Figure 4 shows an example of such variations for the ringwoodite sample, which shows that both of these velocities increase with pressure but significantly decrease with increasing temperature. From these data, we are able to derive elastic moduli and their pressure/temperature derivatives quite precisely, which can be used to tightly constrain the mineralogy and chemistry of the mantle transition region, which have been controversial for many years (e.g., ref. [3]). Further extension of the pressure and temperature conditions toward those of the lower mantle is currently being pursued, which should yield comprehensive understanding of the constitution of the whole mantle.

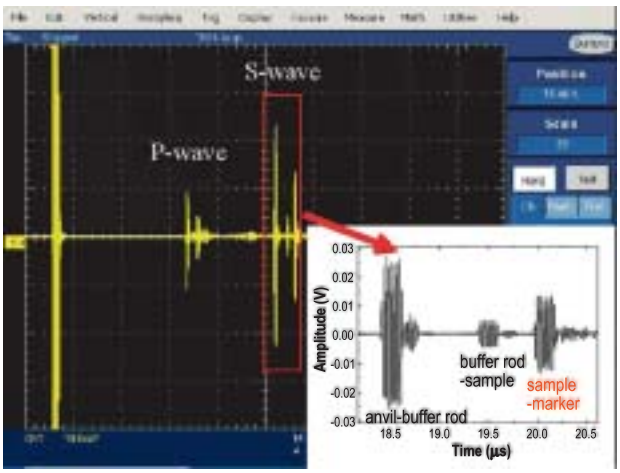

Fig. 3. Example of observed ultrasonic echoes at high pressure and high temperature.

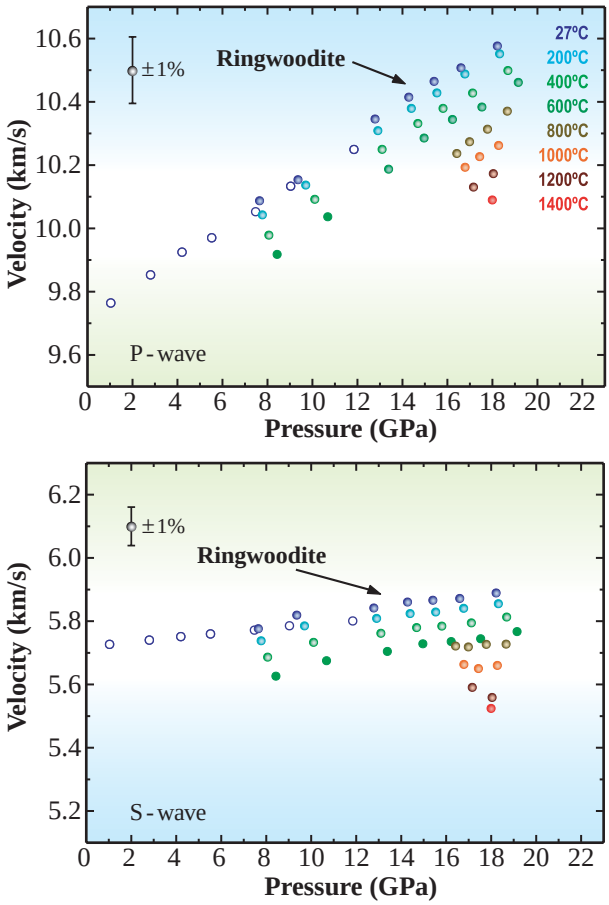

Fig. 4. Example of variations in Vp and Vs in sintered ringwoodite sample with pressure and temperature.

Yuji Higo*, Toru Inoue and Tetsuo Irifune

Geodynamics Research Center, Ehime University

*E-mail: higo@sci.ehime-u.ac.jp

References

[1] T. Irifune: Phys. Earth Planet. Inter. **45** (1987) 324.
[2] B. Li *et al.*: Phys. Earth Planet. Inter. **143** (2004) 599.
[3] D.L. Anderson and J.D. Bass: Nature **320** (1986) 321.

Kinetics of Olivine-Wadsleyite Transformation and Presence of Metastable Olivine in Cold Subducting Oceanic Plates

As the oceanic plate descends into the Earth's mantle, the major constituent mineral olivine $(Mg,Fe)_2SiO_4$ transforms to wadsleyite and ringwoodite at around 400-500 km depths. It has been suggested that these transformations are kinetically inhibited due to low temperatures in the plate and olivine exists beyond the equilibrium boundary as a metastable low-pressure phase producing buoyancy force against subduction [1,2] (Fig. 1). Because the density increase of ~10% caused by these transformations is much larger than the thermal density difference between the plate and the surrounding mantle, kinetics possibly affects the style of the mantle convection by determining whether cold plates (~600-1200ºC) sink into the hot mantle (~1600ºC). The presence of the metastable olivine also changes the stress state in subducting plates and is a possible candidate for the origin of deep earthquakes. Thus, to understand the dynamics of the cold current of mantle convection, it is indispensable to examine the kinetics of olivine transformations. The purpose of our study is to estimate the fields of metastable olivine in subducting oceanic plates on the basis of experimentally determined quantitative kinetic data.

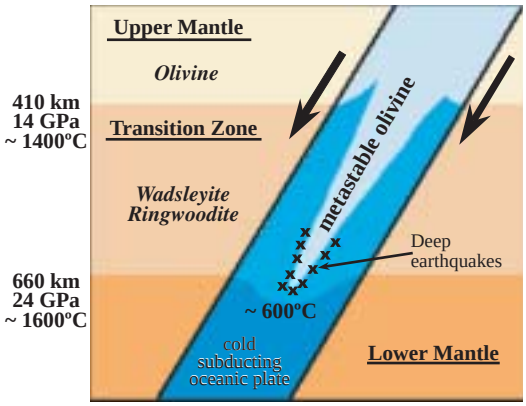

Fig. 1. Schematic illustration showing metastable model of olivine transformation in cold subducting oceanic plate into hot Earth's mantle.

It is known that water greatly enhances the rate of olivine transformation [3] and some amounts of water are contained in the Earth's mantle. Therefore, it is needed to determine pressure, temperature and water content dependence on the transformation rate to discuss the transformation rate in the interior of the Earth. We have developed the experimental technique and directly measured the rate of the olivine-wadsleyite transformation at various pressures, temperatures, and water content conditions [4,5]. High-pressure *in situ* X-ray diffraction experiments have been carried out using the Kawai-type high-pressure apparatus "SPEED-1500" installed in beamline **BL04B1**. The kinetics of the olivine-wadsleyite transformation was observed at 15 different points of 13.4 - 15.8 GPa, 730 - 1100ºC, and 660 - 4400 wt·ppm H_2O by time-resolved X-ray diffraction measurements for every 10 - 300 seconds by the energy-dispersive method using a solid-state detector. The concentration of the hydroxyl of the samples was estimated using infrared spectroscopy.

We estimated transformed volume fraction assuming that the relative integrated intensities of the diffraction peak are proportional to the weight fraction of the phase. The time dependence of transformed volume fraction shows that not only temperature but also water greatly enhances the transformation rate (Fig. 2). In the olivine-wadsleyite transformation, the grain-boundary reaction is the dominant mechanism. The results of the fitting of the obtained kinetic data using the Avrami rate equation indicate that the saturation of nucleation site occurs at the initial stage of the transformation and the overall transformation rate is controlled only by growth. In this case, we can estimate the growth rate in the transformation as shown in Fig. 2.

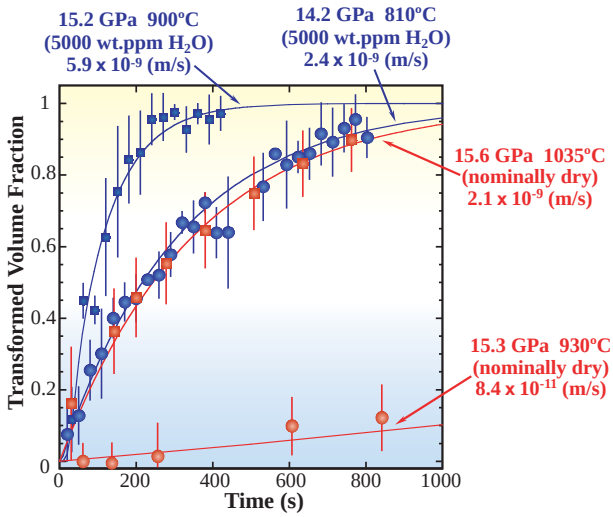

Fig. 2. Time dependence of transformed volume fraction and estimated values of growth rate in olivine-wadsleyite transformation.

Growth in a polymorphic transition is controlled by interface kinetics. The growth rate law can be described as follows;

$$\dot{x} = ATC_{OH}{}^{n} \exp\left(-\frac{E^* + PV^*}{RT}\right)\left[1-\exp\left(\frac{-\Delta G_r}{RT}\right)\right]$$

where A is a pre-exponential factor, T is the absolute temperature, C_{OH} is the concentration of hydroxyl, n is the OH content exponent, E^* is the activation energy for growth, P is pressure, V^* is the activation volume for growth, R is the gas constant, and ΔG_r is the free energy change of the transformation. By fitting this rate equation to the growth rate data, pressure, temperature, and OH content dependences on the growth rate were determined as shown in Fig. 3. The results demonstrate that the growth rate in the olivine-wadsleyite transformation is proportional to the OH content to the power of about 3.

Because the depth of the olivine transformation in cold subducting plates is controlled by growth kinetics [2], the effects of water on growth kinetics must be considered to estimate the fields of metastable olivine. We have calculated changes in the depth of the transformation with the OH content in a cold subducting plate on the basis of the growth kinetics determined in this study (Fig. 4). It is clearly shown that the depth of the olivine transformation drastically changes with water content. The metastable olivine can survive greater than the 650 km depths in cold plates containing the water of less than 500 wt·ppm H_2O, which is identical to the depth of the deepest seismicity. Whereas, in cold slabs containing water of 5000 wt·ppm H_2O, the depth of the transformation is reduced to about 450 km depth even in the cold plates. Thus, water would control the field of the metastable olivine and the dynamics of the subducting cold plates.

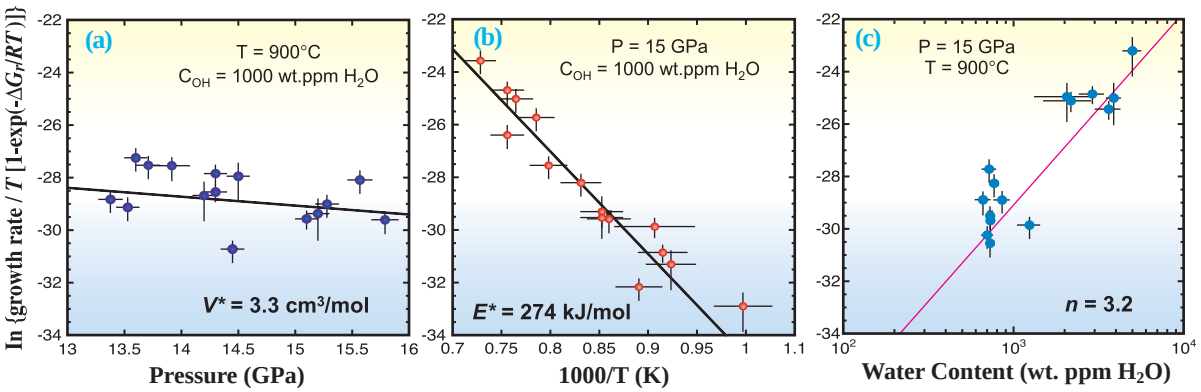

Fig. 3. Pressure **(a)**, temperature **(b)**, and water content **(c)** dependences on growth rate in olivine-wadsleyite transformation.

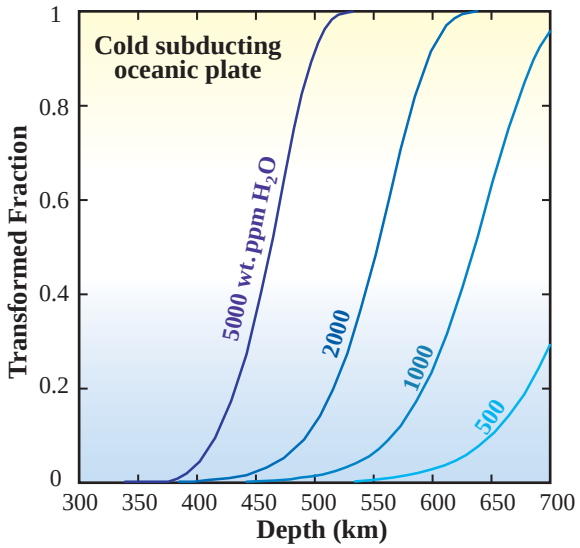

Fig. 4. Depths of olivine transformation with water contents in cold subducting oceanic plate.

Tomoaki Kubo[a,*], Tomofumi Hosoya[b] and Eiji Ohtani[b]

[a] Department of Earth and Planetary Sciences, Kyushu University
[b] Institute of Mineralogy, Petrology and Economic Geology, Tohoku University

*E-mail: kubotomo@geo.kyushu-u.ac.jp

References

[1] C.M. Sung and R.G. Burns: Tectonophysics **31** (1976) 1.
[2] J.L. Mosenfelder *et al.*: Phys. Earth Planet. Inter. **127** (2001) 165.
[3] T. Kubo *et al.*: Science **281** (1998) 85.
[4] T. Kubo *et al.*: Am. Miner. **89** (2004) 285.
[5] *T. Hosoya, T. Kubo, E. Ohtani, A. Sano and K. Funakoshi: Geophys. Res. Lett.* ***32*** *(2005) L17305; doi:10.1029/2005GL023398.*

Density Measurements of Silicate Magma under Pressure by X-ray Absorption Technique

Magma, which is generated by the melting of rocks at the deep interiors of the Earth and other planets, is involved not only in volcanism but also in 4.5 billion years evolution of the Earth's and planetary interiors. The ascending or descending migration of magma is driven by buoyant force. Chemical stratification in planetary interior is thought to be formed by the gravitational separation of crystal from magma ocean at the early stage of planetary formation. Density is the primary factor controlling these magmatic processes. However, the density of magma has not been clarified especially at high pressure due to experimental difficulties. Recent advances in synchrotron radiation-based high-pressure and high-temperature technique allow us to approach directly the physical properties of silicate magma, such as structure, viscosity, and density, under high pressure [1]. We introduce, here, the application of the X-ray absorption technique to measure the density of magma under pressure.

High-pressure X-ray absorption technique has been developed for the measurement of the density of a liquid metal by Katayama *et al.* [2]. They confined metallic liquid in a hard sapphire ring and determined its density from the X-ray absorption profile using the Lambert-Beer law $I/I_0 = \exp(-mrt)$ (Fig. 1). It is, however, difficult to apply this method to magma, because magma is a silicate melt with low X-ray absorption. The high melting temperature (nearly 2000 K) and high chemical reactivity of magma also raise the challenge level of this experimental study. As diamond is the only material that can be used to overcome these difficulties, we use a diamond ring as a sample capsule for magma (Fig. 1). Diamond is X-ray transparent rather than silicate and the hardest material which is uniformly deformed under pressure. The chemical inertness and the extremely high-melting point of diamond also assure the advantage of diamond capsule for X-ray absorption experiments of magma.

It is necessary for high-pressure X-ray absorption experiments to use a multi-anvil high-pressure apparatus generating hydrostatic pressure in a large sample volume (about 0.1 cm^3) and a stable brilliant monochromatic X-ray. We choose beamline **BL22XU** wherein a cubic-type press (Fig. 1) and an in-vacuum undulator with a liquid nitrogen cooling monochromator are available. The silicate sample placed in the diamond cylinder and pistons is pressurized to several GPa and heated above its melting point by an internal graphite heater, and then the intensities of the incident and transmitted X-rays (I and I_0) are measured by ion chambers. The X-ray absorption profile (Fig. 2) is surprisingly clear and has

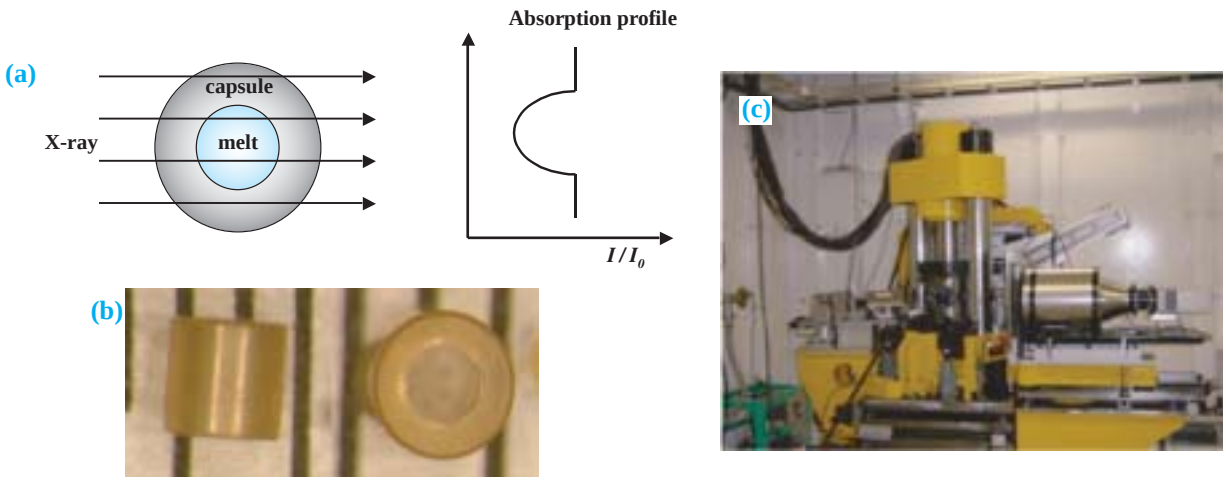

Fig. 1. **(a)** Concept of high-pressure X-ray absorption technique. **(b)** Diamond capsule for silicate magma made of synthesized single crystal. **(c)** Cubic-type high-pressure apparatus SAMP1 installed at BL22XU.

a good quality to yield a density of magma with a meaningful precision, although silicate magma mainly consists of light elements, such as Si, Al, Mg, and O.

Our study on magma density is carried out in two ways: one is to determine the density of simple end-member silicate melt, and the other is the density measurement of natural complex silicate magma. We could determine the isothermal compression curve of basaltic magma, yielding the bulk modulus of basaltic magma with high precision comparable with crystal. Thus, the thermal equation of the state of magma can be evaluated from density measurements. We also study the density of silicate glass at low temperature, which gives an insight into the relationships between the structure and the density of magma. Figure 3 shows an example of the density variation of $Na_2FeSi_2O_6$ glass with increasing temperature. We can see a clear increase in glass density with temperature at constant pressure, which is the opposite of the thermal expansion of a common material. This anomalous behavior is an inherent feature of glass and melt, in which their structures change with temperature and pressure. The structure of $Na_2FeSi_2O_6$ glass is expected to change from a low-pressure one into a high-pressure dense one with temperature closing to the glass transition point.

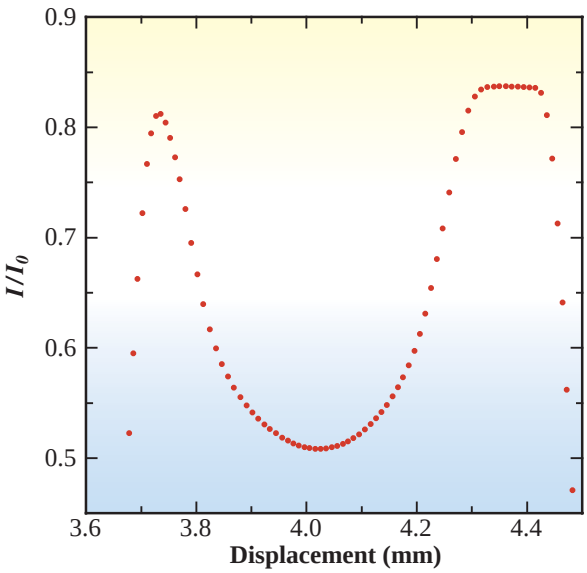

Fig. 2. X-ray absorption profile traversing the radial direction of $Na_2FeSi_2O_6$ melt at 2.5 GPa and 1400 K is obtained by moving the SMAP1 perpendicular to the X-ray beam.

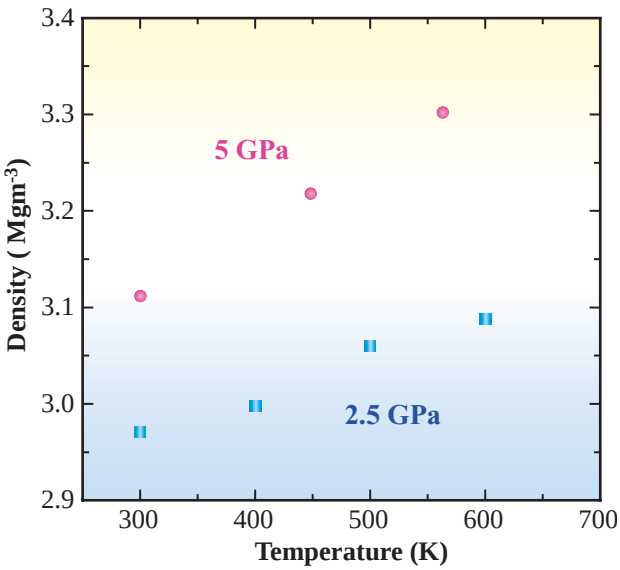

Fig. 3. Densification of $Na_2FeSi_2O_6$ glass at high pressure. This indicates that the structure of glass is relaxed into a high-pressure one by increasing temperature.

Satoru Urakawa[a,*], Eiji Ohtani[b] and Yoshinori Katayama[c]

[a] The Graduate School of Natural Science and Technology, Okayama University
[b] The Graduate School of Science, Tohoku University
[c] SPring-8 / JAEA

*E-mail: urakawa@cc.okayama-u.ac.jp

References

[1] *E. Ohtani, A. Suzuki, R. Ando, S. Urakawa, K. Funakoshi and Y. Katayama: High-Pressure Technology for Geophysical Applications, Elsevier, Amsterdam, 2005.*
[2] Y. Katayama *et al.*: J. Synchrotron Rad. **5** (1998) 1023.

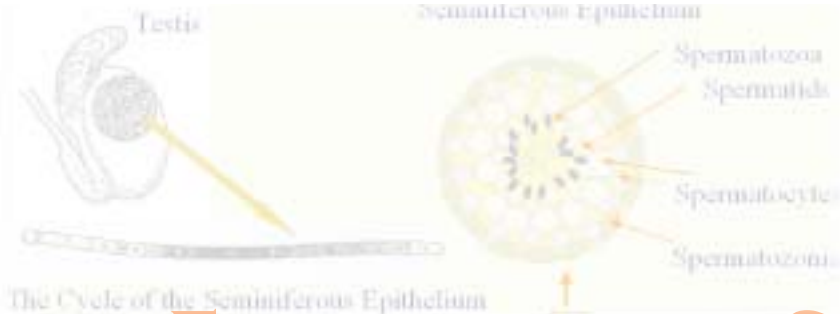

Environmental Science

X-ray analysis using SPring-8 synchrotron radiation is a powerful method for environmental sciences. The fields of application are extending, and applications to experiments are increasing. I'm very glad to report excellent results. Regrettably, we can only report on five topics from many great results.

Takeda *et al.* detected Sn in spermatozoa of rats exposed to tributyltin chloride. They showed that high-energy SR-XRF analysis using a microprobe would be a powerful technique for investigating elemental dynamics in tissues with complex structures.

Nakai *et al.* applied micro-XRF imaging and micro-XANES to an arsenic hyperaccumulator fern. Arsenic in root tissues of the Chinese brake fern exists as a mixture of As(III) and As(V) and the As(III)/As(V) ratio increases in the inner cortex and the boundary between the cortex and central cylinder. These techniques could be used in the analysis of the mechanism of phytoremediation.

Yamaguchi *et al.* showed the transformation of iodine species in soil under upland field and submerged paddy field. In agricultural soils, the reduction of IO_3- resulted in the formation of I_2. Soil organic matter in upland field and the development of reduction conditions attributable to microbial activity in submerged paddy field are responsible.

Akiho *et al.* are characterizing trace elements in a complicated mixture. Standard mercury materials, gypsum and a mercury/gypsum mixture were prepared as follows: mixed gas consisting of N_2, $C0_2$, 0_2 and Hg^{2+} was fed into 9.3wt% gypsum slurry at 313 K. Their XAFS spectra showed that gaseous mercury was captured in gypsum slurry as $HgS0_4$.

Fujita *et al.* developed an *in situ* liquid cell that was applied to the observation of the reduction of Pd-supported catalysts. Using this cell and quick XAFS, they analyzed it with a formaldehyde solution.

Masayuki Kunugi

Environmental Chemistry Division
National Institute for Environmental Studies

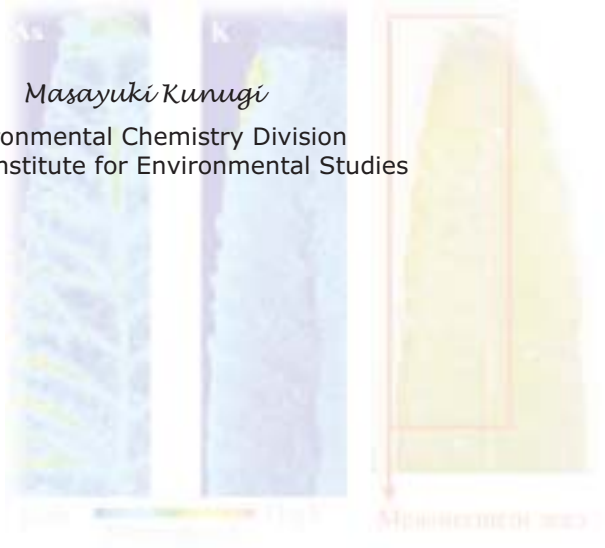

Cell-selective Determination of Sn in Spermatozoa of Rats Exposed to Tributyltin Chloride by Synchrotron Radiation X-ray Fluorescence Analysis (SR-XRF) using Microprobe

Marine pollution due to organotin compounds added to ship bottom paints or fishnet antifoulants and the contaminated food have been a recent concerns as the pollutants are potential endocrine disruptors. Organotin compounds exhibit reproductive toxicity in experimental animals but the dynamics of Sn in reproductive organs is poorly understood.

Seminiferous tubules of rat testis contains a few spermatogonia, which are primitive germ cells, along the basement membrane, one or several layers of spermatocytes farther inside, and groups of spermatids next to the lumen of the tubule (Fig. 1). These types of germ cell undergo a series of developmental processes, which are further classified into 14 stages, and become spermatozoa. Germ cells at different stages of seminiferous tubules respond differently to exogenous stimuli. A novel technique, therefore, is expected to reveal cell-specific profiles of trace elements in the testis.

Sensitive analysis by analytical methods in common use is difficult for trace Sn. Synchrotron radiation X-ray fluorescence analysis (SR-XRF) using a microprobe is a simple and useful method of investigating the precise distribution of elements in tissues. The use of high-energy incident X-rays is suitable for detecting small amounts of Sn in biological samples because it excites the XRF of the Sn K-line, which is not interfered by major elements, such as calcium and potassium, unlike the Sn L-line. In the present study, we applied the analytical method for the cell-selective determination of Sn in the testis of Wistar male rats exposed to tributyltin chloride (TBTC) [1].

SR-XRF measurements were performed at beamline **BL37XU**, using an energy dispersive SR-XRF system with monochromatic X-rays [2]. Spermatozoa in a seminiferous tubule stage VIII, which is the final stage of spermatogenesis in the

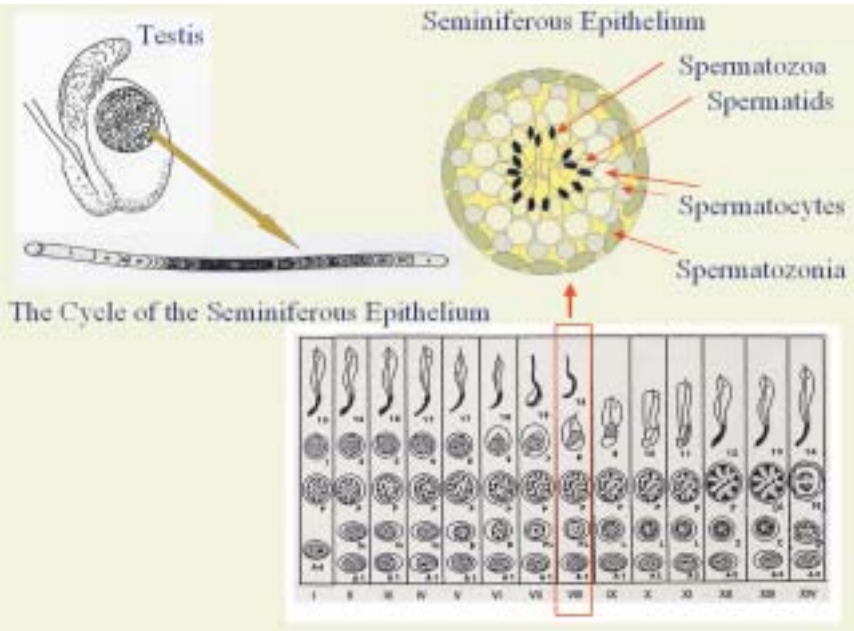

Fig. 1. Structure of rat testis. The illustration on the lower part is a arrangement of germ cells in the seminiferous epithelium. Rat seminiferous tubules are classified into 14 stages in the order of development. The specific associations in the vertical columns represent specific stages (Roman numerals) of the epithelium cycle. The illustration on the upper part is a cross section of a stage VIII tubule.

testis, were subjected to cell-selective Sn determination (Fig. 2). X-rays (37.5 keV; beam size, 3 × 3 μm^2) were used to irradiate spermatozoa of the testicular specimen. The analytical position was confirmed by comparison with the Zn imaging of the stage VIII seminiferous tubules because Zn concentration is higher in spermatozoa than in other types of germ cells at this stage as reported previously [3].

Four days after the first injection of TBTC (45 μmol/kg per day for 3 days, *p.o.*), Sn was detected in spermatozoa in the innermost area of the tubule. It indicates that an investigation of toxic effects after TBTC exposure on not only spermatogenesis but also spermiogenesis should be performed. High-energy SR-XRF analysis using a microprobe can be a powerful technique for investigating the elemental dynamics of Cd, Mo, U, and Cs as well as Sn in tissue with complex structures.

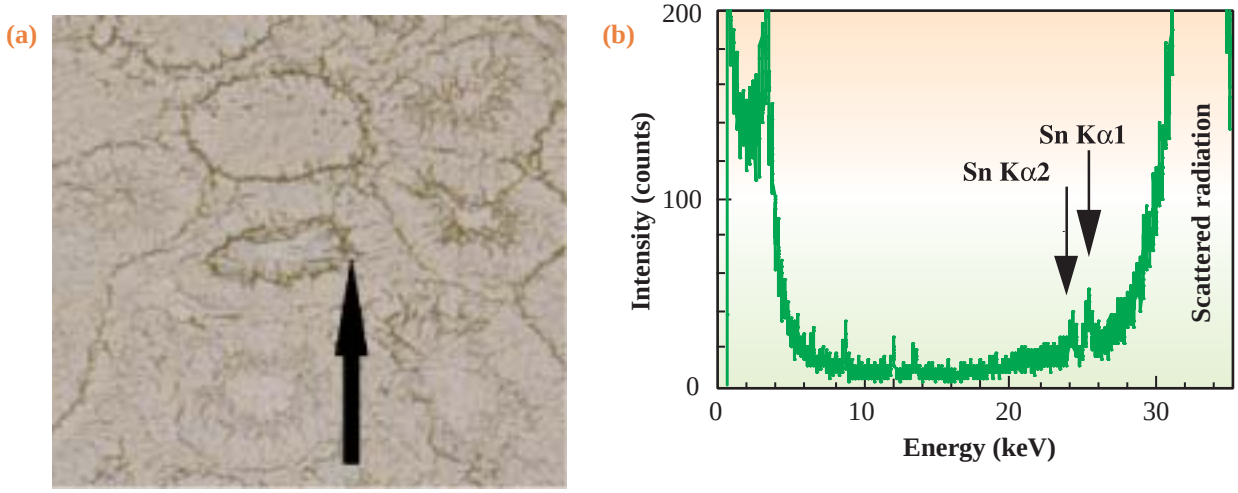

Fig. 2. Light microscopy of the testicular specimen **(a)** and X-ray fluorescence spectrum of the spermatozoa in the stage VIII seminiferous tubule **(b)**. A cryosection (30 μm) was obtained from the testis 1 day after TBTC administration (45 μmol/kg per day for 3 days, *p.o.*). The stage VIII seminiferous tubule has spermatozoa in its innermost. The arrow indicates the position of SR-XRF spot analysis. The Sn concentration of the testis was 0.5 μg/g wet weight.

S. Homma-Takeda

Environmental Radiation Protection Research Group, National Institute of Radiological Sciences

E-mail: shino_ht@nirs.go.jp

References

[1] *S. Homma-Takeda, Y. Nishimura, Y. Terada, S. Ueno, Y. Watanabe and M. Yukawa: Nucl. Instrum. Meth. Phys. Res. B* ***231*** *(2005) 333.*
[2] Y. Terada *et al.*: AIP Conference Proc. **705** (2004) 376.
[3] S. Homma-Takeda *et al.*: J. Radioanal. Nucl. Chem. **259** (2004) 521.

Arsenic Distribution and Speciation in Arsenic Hyperaccumulator Fern by Micro-XRF Imaging and Micro-XANES Analysis

It has been known for a long time that some plants accumulate heavy metal elements such as Mn, Ni, Cu, and Pb. Recently, such heavy-element-hyperaccumulator plants have been attracting much attention because of their application to phytoremediation. Phytoremediation is a technology that uses plants to remove, destroy, or sequester hazardous substances from the environment [1]. It is an emerging technology for environmental remediation that offers promise as a low-cost, versatile technique suitable for use against a number of different types of contaminant in various media. Some specific kinds of plant are known to be heavy metal hyperaccumulators; in particular, the Chinese brake fern (*Pteris vittata* L.) has been reported to accumulate large amounts of arsenic (As: *ca.* 22,000 $\mu g \cdot g^{-1}$ dry weight) in pinnae when it is grown on contaminated soil [2]. It has not yet been determined how this fern efficiently extracts a toxic heavy element such as arsenic from soil into their fronds. As a result, the chemical forms of arsenic and arsenic distribution are being studied with great eagerness [3].

In the present study, we have applied a synchrotron radiation (SR) microbeam to elucidate the elemental distribution and the oxidation state of arsenic in root tissues at sub-cellular levels [4,5]. The XRF imaging of As in a pinna with a nonfocused beam is shown in Fig. 1, which clearly indicated the distribution of As in the fern tissue for the first time. Cells in plant roots are microscopic and fragile (see Fig. 2); therefore, the introduction of a microbeam to XRF imaging and the XANES spectrum of root tissues should provide us new knowledge about the arsenic accumulation mechanism in the Chinese brake fern. Conventional SEM-EDS mapping is not suitable for this purpose because of the low sensitivity of electron beam analysis for heavy elements such as arsenic though SEM is suitable for obtaining clear three-dimensional images of a plant cell.

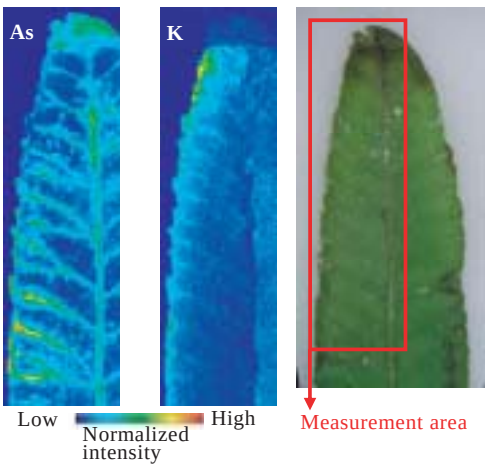

Fig. 1. XRF imaging of As and K in pinna of Chinese brake fern. X-ray energy: 15.0 keV, beam size: 50 μm × 50 μm, measurement points: 60 × 205 points, measurement time: 0.5 s/point.

Pteris vittata seedlings, cultivated from spores for six months on soil, were transferred to hydroponic culture after removing soil from roots carefully. Following two weeks of preculture without arsenic, the nutritional solution was changed to a 10 mg L^{-1} arsenic-containing solution prepared with potassium arsenate. New roots that elongated during the preculture, were used for analyses. Each root cut from the root system of the fern was placed on dry ice immediately and frozen rapidly. Then the root was sliced using a razor blade with *ca*. 200 μm thickness to obtain horizontal cross sections. Sliced root samples were freeze-dried and placed on a mylar film on a sample holder, and then subjected to X-ray microbeam analysis.

SR-μ-XRF imaging and μ-XANES analysis were performed at beamline **BL37XU**. X-rays from the undulator were monochromatized with a Si(111) double crystal monochromator and focused with a Kirkpatrick-Baez (K-B) mirror to 1.1 μm × 1.3 μm at an X-ray energy of 12.8 keV. The sample holder was set on an X-Y-axis stepping-motor-driven stage. X-ray fluorescence intensity was measured with a silicon drift detector (SDD). The step size was set at 1.0 μm, and spectral acquisition times were varied to ensure adequate counting statistics (typically 0.1 s). The measurement was carried out in air. Integrated intensity for each element was calculated from the spectrum, and an elemental image was obtained. XRF intensity was normalized by incident X-ray intensity (I_0).

Fig. 2. SEM image of the root tissue of Chinese brake fern.

After XRF imaging, μ-XANES analysis was carried out to investigate the oxidation state of arsenic at the cellular-level spatial resolution. Arsenic *K*-edge (11.867 keV) X-ray absorption spectra were measured as the fluorescence mode by monitoring the X-ray fluorescence intensities of the As Kα line (10.543 keV). The XANES spectrum of the sample was measured over the energy range from –20 eV to +40 eV from the absorption edge with a step size of 1 eV. The measurement time for each point was varied from 2 to 10 s depending on As level. All data were collected at room temperature in air. The measurement points were selected and controlled precisely using an X-Y-axis stepping motor.

Figure 3 shows the result of the XRF imaging of a cross section of a fern root. Arsenic was detected in the entire root tissue; however, a relatively lower intensity of arsenic signal was observed within a central area (points g and h in Fig. 3 (b)). A comparison of the XRF image with its optical microscope image suggests that this area corresponds to the central cylinder (a tissue which includes the vascular bundle as the pathway of water and substance transportation).

Figure 4 shows a comparison of XANES spectra of eight measured points shown in Fig. 3(b) with those of the reference compounds of $AsIII_2O_3$ and H_3AsVO_4. Although arsenic was added to the culture media as As(V), both As(V) and As(III) exist in root tissues. At points *a* to *d* in the outer cortex, it was found that As(V) was the more dominant species than the As(III) form. It seems to be the general tendency that the As(III)/As(V) ratio increases from the surface to center: the central cylinder and the inner cortex contain a certain amount of As(III). This result indicates that there is reduction activity in the inner cortex or the boundary between the cortex and central cylinder in root tissues.

In conclusion, the arsenic distributions in cross sections were successfully measured by SR-μ-XRF analysis. A comparison of XANES spectra of eight points in the root tissue with high As level with those of the reference compounds (As_2O_3 and H_3AsO_4) revealed that arsenic in root tissues exist as a mixture of As(III) and As(V) and the As(III)/As(V) ratio increases in the inner cortex and the boundary between the cortex and central cylinder.

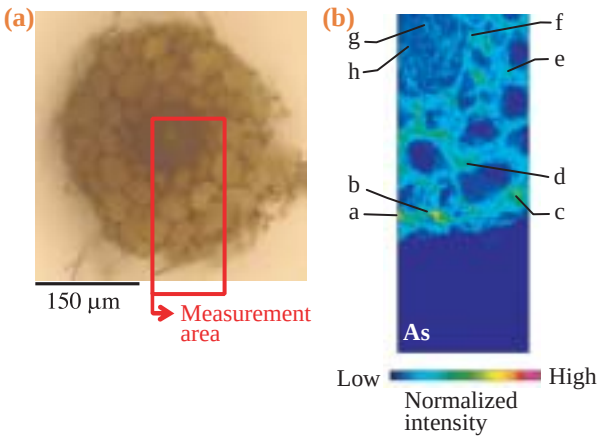

Fig. 3. Optical microscopic image of cross section of fern root **(a)** and μ-XRF imaging of As in root tissue **(b)**. Beam size: 1.1 μm × 1.3 μm, measurement points: 501 × 201 points, measurement time: 0.1 s/point.

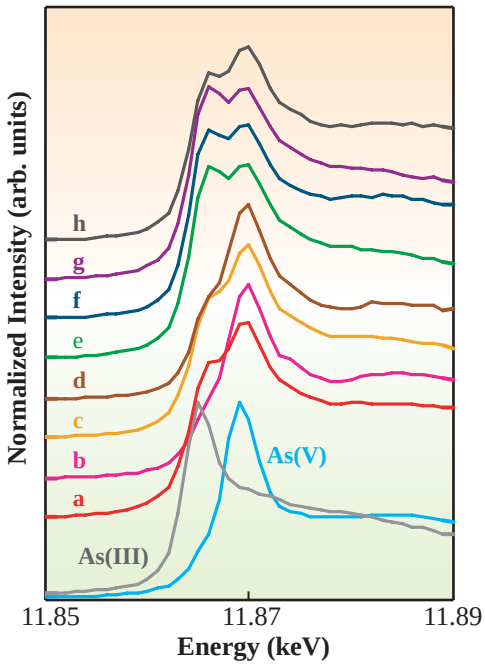

Fig. 4. μ-*K* edge-XANES spectra of As accumulated in root tissue. The measurement points are shown in Fig. 3.

Akiko Hokura[a], Nobuyuki Kitajima[a,b], Yasuko Terada[c] and Izumi Nakai[a,*]

[a] Department of Applied Chemistry, Tokyo University of Science
[b] Fujita Co.
[c] SPring-8 / JASRI

*E-mail: inakai@rs.kagu.tus.ac.jp

References

[1] I. Raskin and B.D. Ensley: Phytoremediation of Toxic Metals: Using Plants to Clean Up the Environment, John Wiley & Sons, Inc. (1999).
[2] L.Q. Ma *et al.*: Nature **409** (2001) 579.
[3] *A. Hokura, R. Omuma, Y. Terada, N. Kitajima, T. Abe, H. Saito, S. Yoshida and I. Nakai: J. Anal. At. Spectrom.* ***21*** *(2006) 321.*
[4] N. Kitajima *et al.*: Proc. XRM2005, IPAP Conf. series - in press.
[5] N. Kitajima, R. Onuma, A. Hokura, Y. Terada and I. Nakai: Adv. X-Ray Chem. Anal. **37** (2006) 301.

Transformation of Iodine Species in Soil under Upland Field and Submerged Paddy Field Conditions

Elevated radioiodine level is observed in atmosphere and soil around nuclear-fuel reprocessing plants. Exposure to radioiodine is hazardous, particularly for children, because radioiodine is accumulated in the thyroid gland. For food safety, considerable attention should be paid to the behavior of radioiodine in the agricultural environment. Once long-half-life ^{129}I (1.6×10^7 y) enters the cycle of biogeochemical systems, it will behave in the same way as stable ^{127}I. Major iodine species in soil include iodide (I^-), iodate (IO_3^-), and organically bound iodine. Only small amounts of iodide can bind to soil components, so that iodide dissolveds in water and thereby absorbed by plants and migrates into groundwater. Iodate is relatively immobile in soil because it can be adsorbed onto soil minerals.

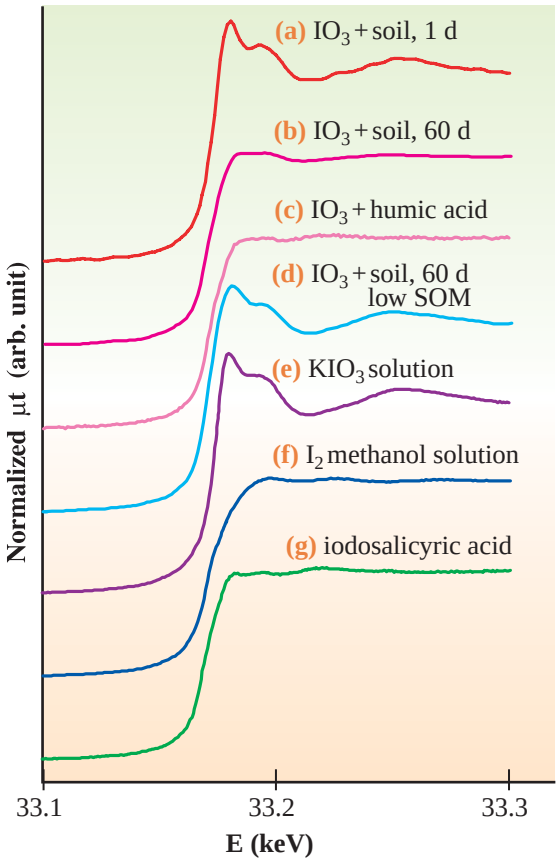

Fig. 1. I *K*-edge XANES spectra after incubation with humic acid and soils of different organic matter contents under upland field conditions **(a-d)** and XANES spectra of reference iodine compounds **(e-g)**.

Besides, organically bound iodine is considered as sink of iodine in soil. The iodine concentration in paddy field soil was substantially lower than that in upland fields and forest soils [1]. This suggests that agricultural practices strongly influence the speciation and mobility of iodine in soil. We investigated whether the transformation of the iodine occurs in agricultural soil systems and thereby affect their fate in the soil environment.

To simulate iodine transformation in upland fields, potassium iodate (KIO_3) dissolved in deionized distilled water was sprayed on mixture of soil and humic acid extracted from volcanic ash soil. The moist soil/iodate mixtures were then incubated at 308 K for 1 d and 60 d. Iodine *K*-edge (33.2 keV) XANES data acquisition was conducted at beamline **BL01B1** in the fluorescence mode. The post-edge feature of IO_3^- remained after 1-d incubation (Figs. 1(a) and 1(e)); however, it disappeared after 60-d incubation (Fig. 1(b)). The XANES post-edge feature of iodine after 60-d incubation appeared similar to that of I_2 or organoiodine (Figs. 1(f) and 1(g)). This indicated that IO_3^- in contact with soil was transformed to I_2 or organoiodine after 60 d under upland field conditions. The post-edge feature of IO_3^- also disappeared when IO_3^- was incubated with humic acid extracted from soil (Fig. 1(c)). The sterilization of soil by γ-ray irradiation did not affect XANES spectra after 60-d incubation, suggesting that microbial activity was not important for iodine transformation under upland field conditions. On the contrary, the post-edge feature of IO_3^- remained after 60-d incubation in soil of low soil organic matter (SOM) content (Fig. 1(d)). Therefore, SOM such as humic acid has a role in reducing IO_3^- to I_2. The highly volatile I_2 cannot remain in soil when it is present as I_2. Since I_2 is highly reactive with organic compounds, the formed I_2 likely associates with SOM as organoiodine in upland fields.

To simulate iodine transformation in paddy fields, KIO_3 dissolved in irrigation water was added to non-sterilized and γ-ray-sterilized soil at a soil-to-solution ratio of 1:1.5. The submerged soil was incubated for 30 d. The post-edge feature of IO_3^- totally disappeared after incubation for 30 d when the soil was not sterilized (Fig. 2(a)). On the other hand, the post-edge feature of spiked IO_3^- remained in sterilized

soil after 30 d of incubation (Fig. 2(b)). As a result, the consumption of oxygen attributable to biological activity and the subsequent development of anaerobic conditions could be the causes for the disappearance of IO_3^- in paddy soil. The post-edge feature of iodine in non-sterilized soils after 30 d of incubation appeared similar to that of reference I_2 or organic iodine. Iodide dissolves in solution in contact with soil and iodine associates with paddy soils either as I_2 or organoiodine under anaerobic conditions [2].

In conclusion, reductive reaction of IO_3^- caused the formation of I_2 in agricultural soils. In upland fields, SOM is responsible for the reductive reaction. In submerged paddy fields, the development of reduction conditions attributable to microbial activity is responsible for the reductive reaction. Because I_2 is highly reactive with organic compounds, the formed I_2 may associate with SOM as organoiodine. I_2 or organoiodine is a potential source of iodine absorbed by plants (Fig. 3).

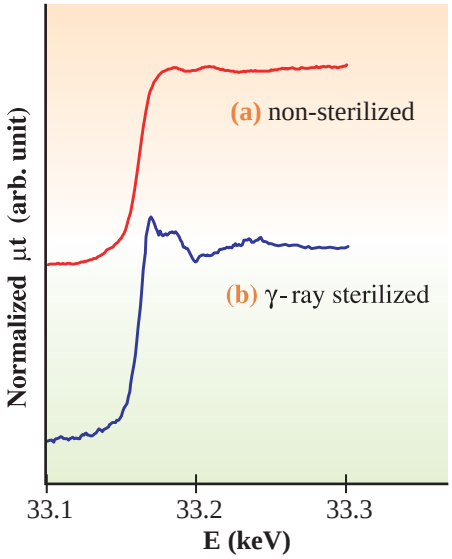

Fig. 2. I *K*-edge XANES spectra after 30-d incubation with soil under submerged paddy field conditions.

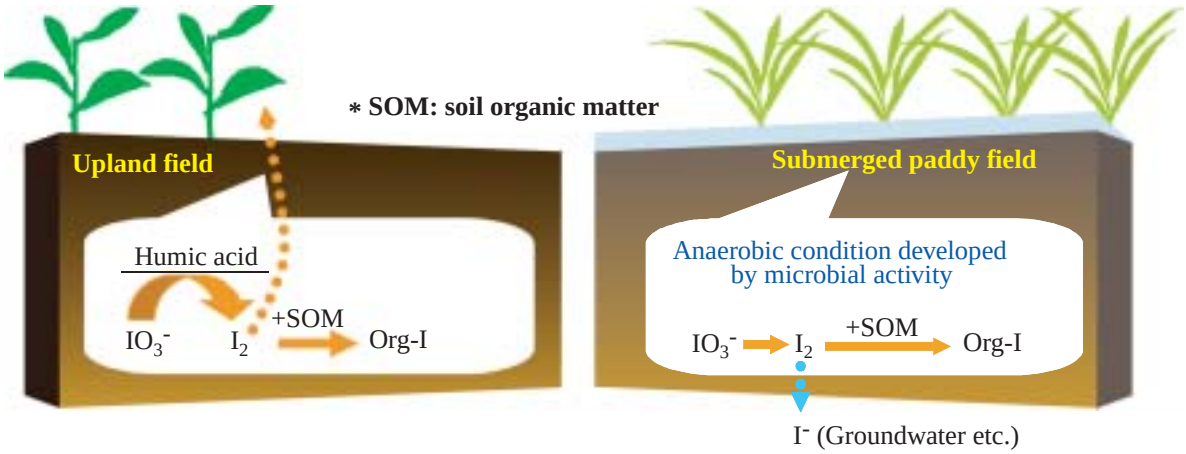

Fig. 3. Iodine transformation in upland and submerged paddy field soils.

N. Yamaguchi[a,*], M. Nakano[b] and H. Tanida[c]

[a] Soil Environment Division National Institute for Agro-environmental Sciences
[b] Research Institute of Soil Science and Technology
[c] SPring-8 / JASRI

*E-mail: nyamag@affrc.go.jp

References

[1] K. Yuita: Soil Sci. Plant Nutr. **38** (1992) 281.
[2] *N. Yamaguchi, M. Nakano, H. Tanida, H. Fujiwara and N. Kihou: J. Environmental Radioactivity* ***86*** *(2006) 212.*

Trace Metallic Elements in Coal, Coal Ash and Gypsum Measured by Fluorescence X-ray Absorption Near-edge Structure

Coal combustion plants are widely utilized as a source of thermal and electric energy. Coal, which consists of organic compounds and inorganic minerals, contains trace elements. As shown in Fig. 1, these trace elements are emitted into the flue gas as gaseous compounds or particle-bound forms in coal combustion processes. In a flue gas stream, trace elements are fixed in ash particles and in by-products such as gypsum and sludge if wet flue gas desulfurization (wet-FGD) unit is equiped. To understand their chemical forms in coal ash and by-products is very useful for utilization and disposal of these products. Conventional X-ray analysis, however, is not effective because the concentrations of these elements are generally very low. In this research, ultra-brilliant X-ray source of SPring-8 was applied to X-ray absorption fine structure (XAFS) spectra analysis to characterize trace elements in these complex systems.

We have attempted to measure the XAFS spectra from trace elements such as arsenic (As), selenium (Se) and chromium (Cr) in the NIST standard samples (NBS1632c: bituminous coal, NBS1633b: fly ash) at beamline **BL16XU**. Figure 2 shows X-ray absorption near-Edge structure (XANES) spectra at an As *K*-edge and a Se *K*-edge [2,3] from the NIST standard samples, several As and Se compounds. The XANES spectra of the NIST standard samples were detected using a wavelength-dispersive fluorescence X-ray spectrometer installed in the experimental station as shown in Fig. 3, which avoids the influence of coexisting elements and background. The XANES spectra of As and Se compounds were measured by the ordinary transmission method. XANES spectra are element specific and sensitive to the local structure and physical state of the element. It is easy to understand the oxidation and chemical states of the element by

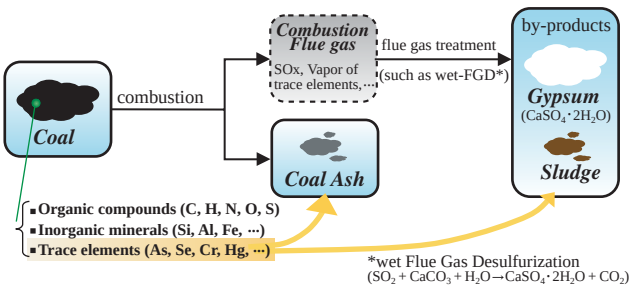

Fig. 1. Behavior of trace elements in coal combustion and flue gas stream.

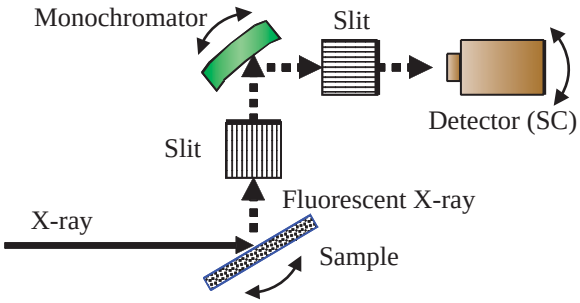

Fig .2. As-*K* edge and Se-*K* edge XANES spectra of NIST standard samples, arsenic and selenium compounds. (NBS1632c: As 6ppm, Se 1 ppm NBS1633b: As 136 ppm, Se 10 ppm)

comparison with the spectrum of a standard compound. As and Se exist in the environment in several oxidation states. The most common oxidation states of As are three and five, whereas those of Se are primarily four and six. In this study, the position of the maximum X-ray absorption energy is clearly related to the oxidation states of As and Se. We conclude that the oxidation states and ratios of As and Se in coal ash are higher than those in coal. We are able to predict that these elements exist in coal ash as the chemical forms of arsenate (AsO_4^{3-}), arsenite(AsO_3^{3-}), selenate (SeO_4^{2-}), and selenite (SeO_3^{2-}). In addition, we are able to understand that As and Se in coal are a mixture of at least three different oxidation states. We think that As and Se coexist in a more reduced form as a substituted pyrite(FeAs(Se)S)-like substance in coal.

We attempted the transmitted type and two kinds of fluorescence XAFS measurements. It became clear that fluorescence XAFS measurement using solid state detector (SSD) was applicable to the characterization of trace elements in a range above 10 mg/kg. In addition, XAFS measurements become capable of detecting a few mg/kg of trace elements using the WD-XRF spectrometer, as shown in Fig. 4 [3]. It was difficult to detect XAFS signal of mercury in the NIST standard samples because the concentrations of mercury are very low.

We have also attempted to measure the XAFS spectra of mercury captured in gypsum to investigate the chemical forms of mercury [3,4]. A mixed gas consisted of N_2, CO_2, O_2 and Hg^{2+} was fed into 9.3wt% gypsum slurry at 313 K to make a mercury/gypsum mixture. The XAFS spectra of seven pellet samples: five standard materials ($HgCl_2$, HgO, silver amalgam, HgS, and $HgSO_4$), a mixture of

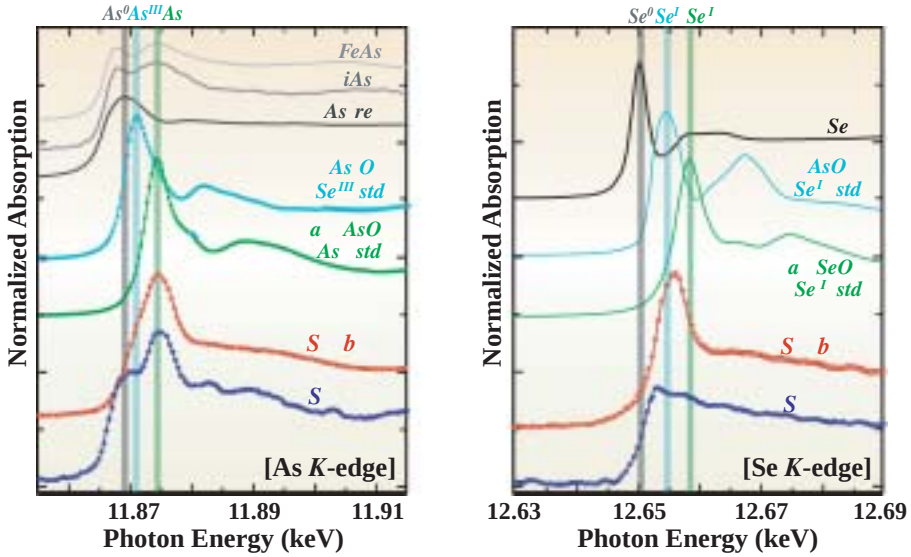

Fig. 3. Schematic diagram and photograph of wavelength-dispersive fluorescence X-ray (WD-XRF) system.

standard $HgSO_4$ and gypsum, and the above-mentioned mercury/gypsum mixture were measured. Figure 5 shows the Hg-L_{III} XANES spectra of those samples. The XANES spectra of the mercury/gypsum mixture and standard $HgSO_4$/gypsum mixture were detected using the wavelength-dispersive fluorescence X-ray spectrometer. The XANES spectra of the other five standard materials were measured by the ordinary transmission method. These XANES spectra reflect the chemical forms of the samples. The spectrum of the mercury/gypsum mixture is overwritten on the spectrum of the standard $HgSO_4$/gypsum mixture as shown in Fig. 5. Since the spectrum of the mercury/gypsum mixture is similar to the spectrum of the standard $HgSO_4$/gypsum mixture, mercury in the gypsum exists as $HgSO_4$ [4].

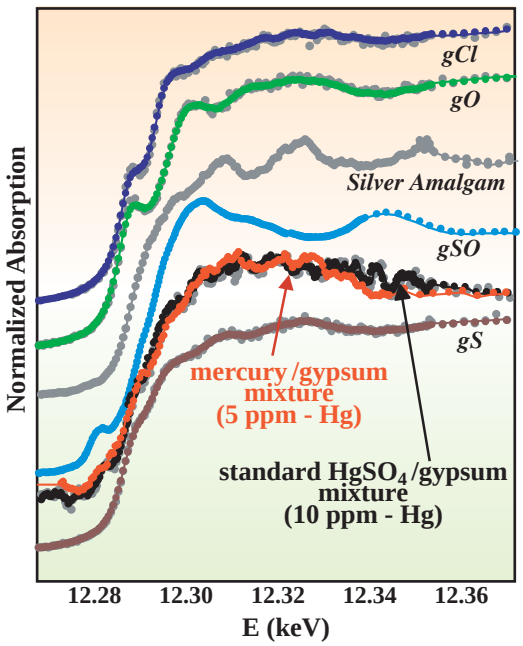

Fig. 5. Hg-L_{III} XANES spectra of mercury/gypsum mixture and standard materials.

The XAFS measurement technique will be applied to characterize the chemical forms of trace elements in liquid samples at beamlines BL16XU and BL16B2.

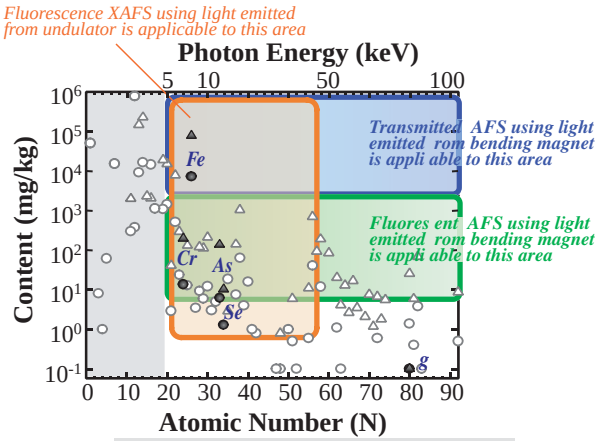

Fig. 4. Capability of XAFS analysis of various elements in NIST standard samples.

Hiroyuki Akiho* and Toru Yamamoto

Central Research Institute of Electric Power Industry (CRIEPI)

*E-mail: akiho@criepi.denken.or.jp

References

[1] N. Awazi and T. Yamamoto: Jpn. J. Appl. Phys. **39** (2000) L1252.
[2] T. Yamamoto *et al.*: CRIEPI Report, W01027 (2002) (in Japanese).
[3] T. Yamamoto *et al.*: CRIEPI Report, W03034 (2004) (in Japanese).
[4] H. Akiho, M. Nunokawa and H. Shirai: J. Jpn. Institute of Energy **83** (2004) 924.

In Situ Structural Analysis of Heterogeneous Noble Metal Catalysts in Solvent under Reduction-Oxidation Conditions by Quick XAFS

Reduction-oxidation reactions catalyzed by noble metals are industry important and environmentally friendly processes. Among the metal catalysts, palladium has been widely and intensively studied and applied to various industrial fields. We have studied reduction-oxidation reactions catalyzed by heterogeneous palladium in the liquid phase. In the course of the investigation, we expected that the local structure of palladium would change during chemical interaction between catalysts and the solvent, taking into account that reaction and deterioration rates were significantly dependent on reactants, solvents and temperatures. Herein, we report the structural change of the palladium catalyst suspended in a solution using an *in situ* cell developed by us. Generally, the measurement of a solid catalyst suspended in a liquid is difficult because of the inhibition by cell windows or solvents. In this respect, the absorption of the X-ray beam is small at the energy of the Pd *K*-edge, which renders the measurement of XAFS of a solid catalyst in a liquid cell.

The illustration and photograph of our reaction cell are shown in Fig. 1. The *in situ* reactor cell made of stainless steel could be operated under an inner pressure of 1 MPa and a temperature of up to 100 ºC. The stainless cell was placed on a hot plate and the solvent was stirred with a magnetic stirrer. The temperature of the solvent was measured with a thermocouple inserted into the center of the reactor cell. The solid catalyst loaded onto a pipe (3 cm in length) was placed on the X-ray path. Polycarbonate disks with a thickness of 1 cm were used as windows of the cell. Pressure inside the cell could be monitored using a gauge. The reducing agent (an aqueous formaldehyde solution) was poured from the vessel connected to the upper part of the cell.

In the initial stage of our research, it was difficult to obtain good spectra with a high S/N ratio due to the interference of a high background count, which was caused by air bubbles generated during stirring. To improve the quality of spectra, the shape and construction of the reaction cell, and experimental conditions were improved to decrease the number of bubbles. The most effective improvement was the optimization of the rotation of stirring.

The *in situ* cell was applied to QXAFS measurement in the course of the reduction of Pd with a formaldehyde solution. In the measurement, the 10wt% Pd/Al_2O_3 catalyst was placed on the path of an X-ray beam and Pd *K*-edge XAFS spectra were collected every 5 min in N_2 atmosphere.

Figure 2 shows examples of Pd *K*-edge Fourier transforms of Pd/Al_2O_3 measured in the formaldehyde/water solvent at a temperature ramping

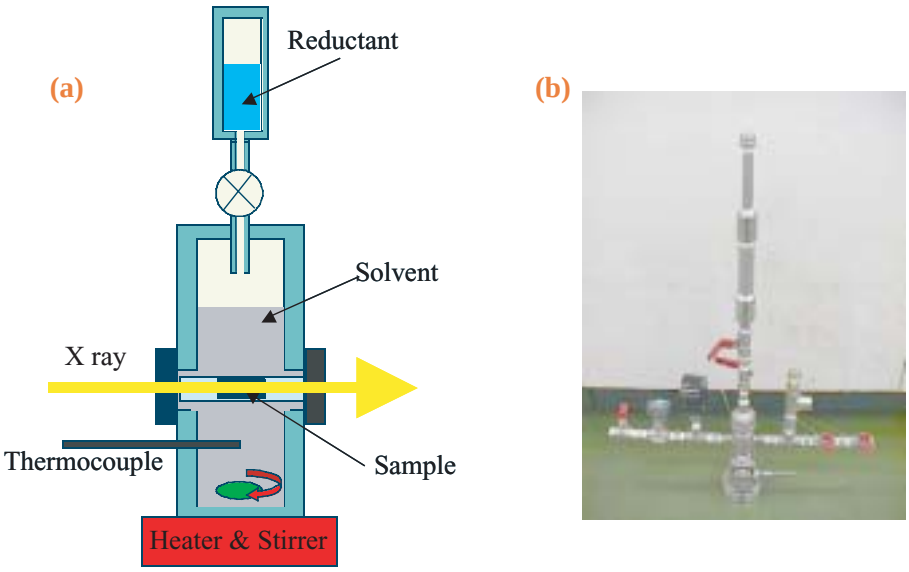

Fig. 1. Illustration **(a)** and photograph **(b)** of new reactor cell.

rate of 10 K/min. In the Fourier transforms, the Pd-O peak appeared at 1.6 Å, indicating that palladium was oxidized at the initial stage. The intensity of the peak of Pd-O decreased accompanied by the reduction of PdO in the temperature range between 50 and 70 ºC. Then the Pd-Pd peak ascribed to the Pd metal appeared at 2.7 Å above 70 ºC.

The structural change of Pd was monitored sequentially at 65 ºC immediately after the addition of the formaldehyde solution from the upper vessel. The spectrum was collected every 5 min. As can be seen from the figure, the reduction of palladium progressed with time and the growth of the Pd metal continued over 30 min from the beginning of the reaction, after which it progressed slowly.

In summary, a new *in situ* liquid cell was applied to the observation of the reduction of Pd-supported catalysts. By using this technique, we could demonstrate the applicability of the cell in the measurement of solid catalysts suspended in a solution.

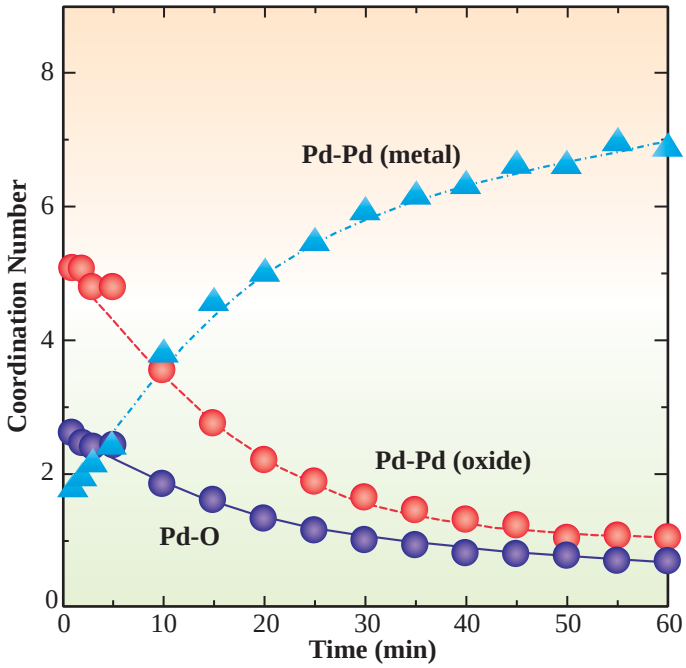

Fig. 2. Pd *K*-edge EXAFS Fourier transforms of 10wt% Pd/Al_2O_3 measured during reduction with formaldehyde in N2 atmosphere. Temperature was changed stepwise from 30ºC to 80ºC.

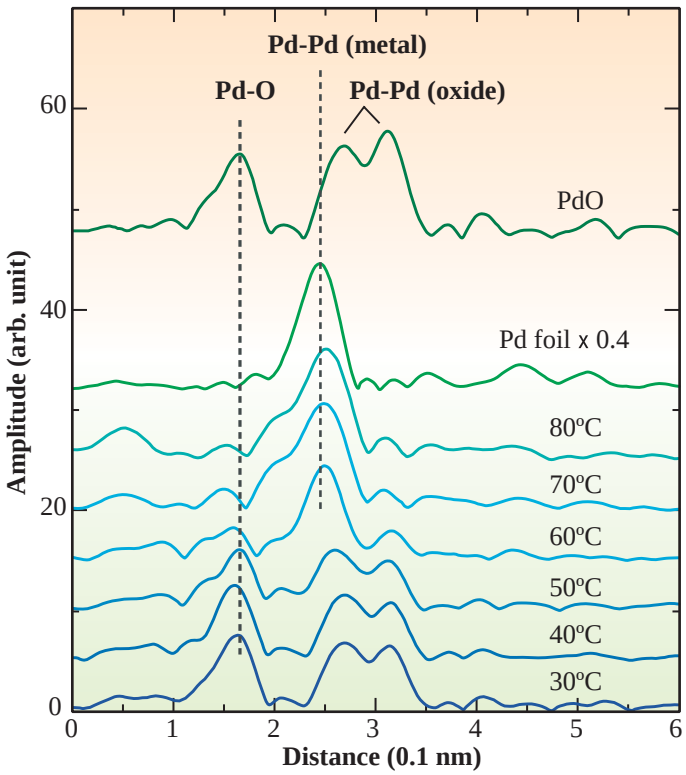

Fig. 3. Coordination numbers of Pd-O, Pd-Pd (oxide) and Pd-Pd (metal) of 10wt% Pd/Al_2O_3 plotted as function of reaction time. Formaldehyde solution was used as the reductant. Temperature, 65 ºC.

Tsutomu Fujita[a,*], Kazu Okumura[b] and Yasuo Takenaka[a]

[a] Mitsubishi Rayon Co. Ltd.
[b] Faculty of Engineering, Tottori University

*E-mail: fujita_ts@mrc.co.jp

Industrial Applications

The fact that the number of users from industries and that of industrial companies at SPring-8 have been dramatically increasing shows that the utilization of synchrotron radiation has already become a commonly used technique in various industrial fields. This situation holds true not only for the public beamline but also for contract ones. Such an increase in the number of users from industry may be partially attributed to the recent intentional funding by government for the "Trial Use Program" aiming at the education of and assistance for industrial newcomers to SPring-8. In some technological areas like fluorescence analyses or X-ray reflectivity measurements, the present state of the activities for industrial application has become more advanced as compared with those in a few years ago in terms of measurement accuracy.

Some of the outstanding work recently achieved in industry is introduced here. Although major expert users have previously belonged to electronics, many researchers from other industrial fields, such as cars, new materials for functional devices, construction and cosmetics, are now joining SPring-8.

In the electronics field, which still supplies the majority of users, various types of memory or high-capacity storage devices, such as flash memory, digital versatile disk-random access memory (DVD-RAM) and magnetic hard discs (HDD), have been continuously popular materials for characterization, mainly by XPS, XRD and X-ray reflectivity measurements. As long as the crystal structures in bulk materials or at interfaces are sometimes closely related to the device performance and life or the production yield, research activities for those materials should continue for another decade.

Studies on the structures of or stresses in thin surface layers with and without coating films have also become popular as part of research into surface strengthening and the prevention of corrosion, rusting or crack formation. As examples of such studies the analytical results of toxic hexavalent chromium in metal coating layers, stress measurement results of laser-peened metals and X-ray diffraction results of dynamic phase transition in arc-welding metal layers will be introduced.

In the field of construction concrete strength, or its durability, is also a key issue since Japan often suffers from large earthquakes. It is effective to directly see the internal structure of concrete by an X-ray imaging technique to understand the deterioration mechanism of the concrete more clearly.

One of the industries that is more directly related to the people's lives is cosmetics. Hair treatment materials are of special interest to the cosmetic industry. Thus, the research of structures in treated hair using SAXS combined with an X-ray microbeam would be a rewarding target to elucidate how those materials affect hair, not only from the viewpoint of the industry's sales but also from that of human health.

Junji Matsui
Center for Advanced Science and Technology
Hyogo

Interfacial Structure of Tunnel Oxynitride Films in Flash Memory

Flash memory is a kind of electrically erasable programmable read only memory (EEPROM). The name flash describes the technology's operation because it takes less than one second to erase a large number of cells at the same time. Flash memory has two major applications: one is nonvolatile memory integration in microprocessors to allow software updates, and the other is to create storing elements like *removable flash memory cards*. All of these applications require flash reliability in which a cell can be erased and programmed for a sufficient number of cycles without degradation of device functionality.

Electron trapping in charge-transfer dielectrics is known to be a limiting factor of the program/erase cycling endurance of nonvolatile floating-gate memory. In flash memory cells, which use channel hot-electron injection for programming and Fowler-Nordheim tunneling for erasing, electron trapping in the tunnel oxide reduces the electric field during erase operations, resulting in a gradual degradation of erase characteristics and the closure of the memory cell threshold window. The understanding of the charge trapping mechanism is therefore needed for the development of optimized program/erase schemes.

Oxynitrides (SiON) have drawn great attention as a candidate tunnel dielectric for nonvolatile memory due to the small charge-trapping amount [1]. The effect of nitrogen incorporation, however, was reported as exhibiting process-condition dependence rather than nitrogen-concentration dependence [2]. This implied the chemical state of nitrogen atoms playing a critical role in the dielectric characteristics. In this study, two kinds of 7-nm-thick SiON films with a significant difference in charge trapping behavior were prepared by thermally annealing oxide (SiO_2) film in either NO or N_2O ambient. The chemical depth profile of nitrogen atoms in the SiON films was studied by angle-resolved photoemission spectroscopy (AR-PES), which was carried out at beamline **BL15XU**. The excitation energy was chosen as 3 keV ± 0.3 eV on the basis of the balance of the detectable depth and photoelectric cross section.

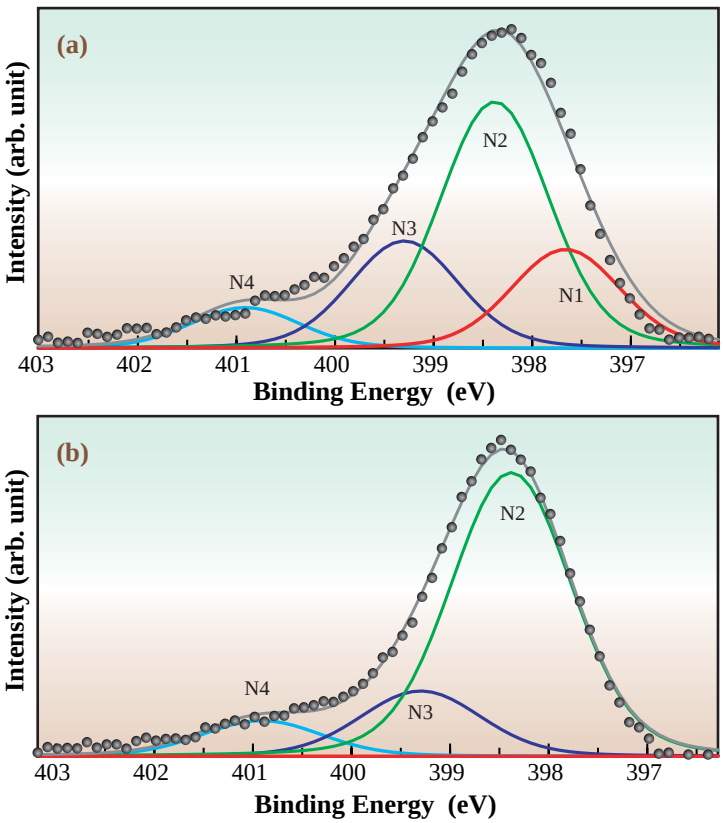

Fig. 1. N1*s* photoelectron spectra of SiON tunnel films prepared by annealing oxide in **(a)** NO and **(b)** N_2O ambient. The solid line shows the fitting results and the dots show the experimental results.

N1*s* spectra obtained from SiON films in normal emission (Fig. 1) were decomposed into four components, N1-N4. Both N1 and N2 were assigned to the [N-Si_3] group with either the mixture of nitrogen and Si atoms (N1) or all oxygen atoms (N2), respectively, bound as second-neighbor atoms. N3 and N4 were attributed to Si_2NO and $SiNO_2$, respectively [3,4]. The significant difference in the N1s spectra is that the N1 state is only detected from the NO-annealed film (Fig. 1(a)). To determine the depth distribution of N1-N4, the peak intensities normalized by the O1*s* peak were plotted as a function of the emission angle. The tendency of the angle dependence suggests that N1 and N2 exist closer to the SiO_2/Si interface, while N3 and N4 are distributed more homogeneously within the films. Moreover, an analysis result of the depth profile indicated that N1 is localized in the interface layer, while N2 is distributed further into the near-interface region (Fig. 2). Comparing the electrical properties suggests that the NO-annealed film contains a significantly higher number of electrically active electron traps existing mainly in the interface region than the N_2O-annealed film. We thus demonstrate that the source of interfacial electron trap generation might be related to interfacial nitrogen detected as the N1 component by AR-PES.

We have investigated the difference in interface structure of two SiON films by hard X-ray ARPES. We propose that SiON film with a nitrogen-free interface atomic layer is a promising tunnel film in flash memory for the improvement of program/erase cycling endurance.

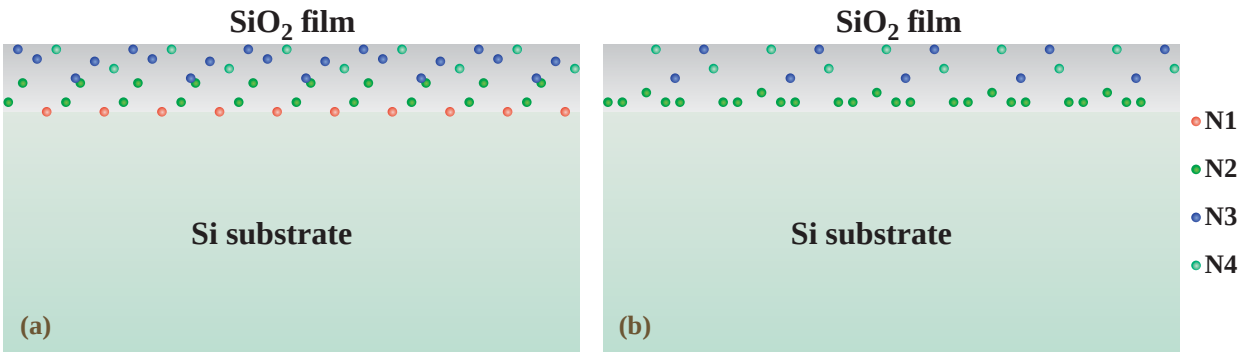

Fig. 2. Illustration of depth profile of nitrogen atoms decomposed as N1-N4 components in **(a)** NO-annealed and **(b)** N_2O-annealed SiON films.

Ziyuan Liu* and Takashi Ide

NEC Electronics Corporation

*E-mail: z.liu@necel.com

References

[1] F. Jong *et al.*: IEEE EDL. **18** (1997) 343.
[2] J. Kim *et al.*: 35th Annual Proc. IRPS (1997) 12.
[3] S. Toyoda *et al.*: Appl. Phys. Lett. **83** (2004) 5449.
[4] J. Ushio *et al.*: Appl. Phys. Lett. **81** (2002) 1818.
[5] Z. Liu *et al.*: to be published.

Structural and Electrical Properties of Optical Phase-change Materials GeTe and $Ge_8Sb_2Te_{11}$

In a rewritable phase-change optical disk such as a digital versatile disc - random access memory (DVD-RAM), information is recorded using the change in optical property, such as reflectivity or transmissivity, that results from the phase transformation of the material between the crystal (erase) and amorphous (record) states [1]. Today, the GeTe-Sb_2Te_3 (GST) pseudobinary compound, typically $Ge_8Sb_2Te_{11}$ or $Ge_2Sb_2Te_5$, is the most widely used rewritable phase-change optical recording material. These materials are of considerable importance since compounds in this system are used not only for rewritable optical storage but also for future non-volatile electronic memories. However, the crystal structures and electrical properties of these materials have not been investigated in detail. We therefore investigated those of the two materials, GeTe and $Ge_8Sb_2Te_{11}$, by electric measurements, and X-ray powder diffraction and photoemmision spectroscopy using synchrotron radiation at beamlines **BL02B2** and **BL47XU** [2].

GeTe and $Ge_8Sb_2Te_{11}$ have high- and low-temperature crystalline phases. The former phase has a NaCl-type cubic structure. Ge and Sb cations are located at the 4(*b*) site in the space group $Fm\bar{3}m$; on the other hand, Te anions occupy the 4(*a*) site (see Fig. 1). The latter phase has a rhombohedrally distorted NaCl-type structure (*R3m*), in which two kinds of ions migrate away from each other along the [111] axis, leaving the equilibrium positions, (0 0 0) and (1/2 1/2 1/2), that they had occupied in the high-temperature phase. Both compounds lie in these low-temperature phases at room temperature. The crystallographic data obtained by Rietveld analyses are shown in Table I, in which the *g*-parameter indicates the atom occupancy in each site. As seen in this table, a high density of about 2% Ge vacancies (4×10^{20}/cm^3) was present at the Na sites in the GeTe crystal. This indicates that the single-phase region of the GeTe binary compound sits on the Te-rich side of the GST pseudobinary line in the Ge-Sb-Te ternary system [3]. On the other hand, the atomic occupation for the $Ge_8Sb_2Te_{11}$ compound was about (8+2)/11, which indicates that this compound contains almost no excess vacancies, and that its single-phase region lies on or very near the pseudobinary line.

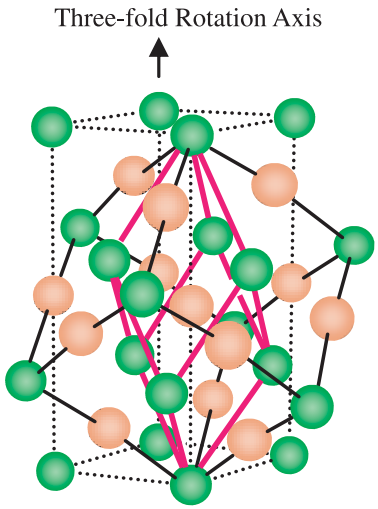

Fig. 1. Structure of GeTe or $Ge_8Sb_2Te_{11}$ low-temperature phase shown with both rhombohedral (thick lines ━) and hexagonal (dotted lines •) unit cells. Green circles indicate Te atoms, whereas orange ones represent Ge/Sb atoms and vacancies. The NaCl-type cubic structure of the high-temperature phase, shown by thin solid lines, is slightly deformed in the low-temperature phase.

It is known that in the GST pseudobinary NaCl-type structure, when its composition is exactly located on the pseudobinary line, the valence band is fully occupied by all the outermost electrons of the three kinds of constituent atoms; on the other hand, the conduction band is completely empty, irrespective of their compositions [4]. Figure 2 shows the electrical resistance measurement results for GeTe and $Ge_8Sb_2Te_{11}$ polycrystalline thin films undertaken at temperatures ranging from 4 - 280 K. It can be seen in this figure that the electrical resistivity obtained for GeTe has a positive correlation with temperature, showing fairly low values, which demonstrates that this film is a metal-like substance. On the other hand, the electrical resistance of the $Ge_8Sb_2Te_{11}$ film showed a slightly negative temperature dependence. This means that, unlike GeTe, $Ge_8Sb_2Te_{11}$ is a semiconducting substance. Our Hall effect measurements performed on the GeTe film at room temperature showed *p*-type electrical conductivity with a high carrier density of up to 5×10^{20} cm^{-1}. We have revealed by molecular orbital calculation that Te atoms have received 0.30 electrons (/atom) from Ge atoms, and that this crystal tolerates an ionic bonding nature [2]. In other words, about 0.3 holes are formed per single Ge vacant site in the Madelung field to retain electrical neutrality, which means that the above-mentioned Ge vacancies present in the GeTe

Table I. Refined structural parameters for **(a)** GeTe and **(b)** $Ge_8Sb_2Te_{11}$ low-temperature phases at room temperature. Standard deviations are shown in parentheses. The final *R*-factors and lattice parameters for GeTe are R_{wp} = 8.42%, R_p = 5.81%, R_I = 1.29%, R_{wp} expected = 2.15% and a = 4.2806(4) Å and α = 58.259(5)°, respectively, and those for $Ge_8Sb_2Te_{11}$ are R_{wp} = 4.03%, R_p = 2.53%, R_I = 1.33%, R_{wp} expected = 2.88% and *a* = 4.2511(4) Å and α = 59.580(4)°, respectively.

(a) atom	**site**	***g***		***y***		**(Å^2)**
Ge	1:1(*a*)	0.977(5)	0.5238(2)	*x*	*x*	1.52 (6)
Te	2:1(*a*)	1.0	0	0	0	0.74 (3)
(b) atom	**site**	***g***		***y***		**(Å^2)**
$Ge_{8/11}Sb_{2/11}$	1:1(*a*)	1.024(3)	0.5154(4)	*x*	*x*	2.49 (5)
Te	2:1(*a*)	1.0	0	0	0	0.94 (2)

crystal can generate up to 1×10^{20} (electroconductive) holes /cm^3. This estimated density shows good agreement with the carrier density measured on our crystalline GeTe film. We therefore hold that this GeTe film is a metallic substance. The Hall effect measurement on the $Ge_8Sb_2Te_{11}$ polycrystalline film showed that this substance has a lower carrier density (up to 1×10^{19} cm^{-1}) at room temperature than GeTe. In addition, the measurement indicated that the carries had no clear polarity (positive or negative). We have clarified above that no *excess* vacancies are present in the $Ge_8Sb_2Te_{11}$ crystal, unlike the GeTe crystal. In other words, the abovementioned interesting difference in electrical properties between GeTe and $Ge_8Sb_2Te_{11}$, is decided by the presence of excess vacancies in these pseudo-binary crystals. The valence-band spectra obtained by the synchrotron radiation photoemission spectroscopy at room temperature are shown in Fig. 3. The energies are expressed in terms of the spectrometer Fermi level. As seen in the spectra, the top energies of the valence bands are different from each other; the Fermi level in the GeTe spectrum lies at the top of the valence band, whereas that in $Ge_8Sb_2Te_{11}$ sits above it. These observations support our conclusion that the GeTe polycrystalline film is a metallic substance, but the film of the $Ge_8Sb_2Te_{11}$ pseudobinary polycrystalline compound is a semiconductor.

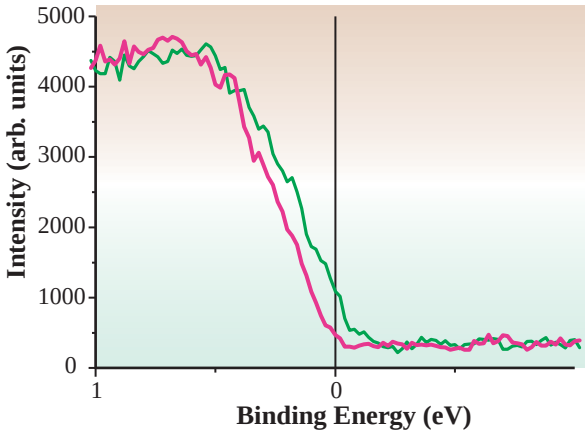

Fig. 3. Electron emission spectra near Fermi level of GeTe (green line) and $Ge_8Sb_2Te_{11}$ (pink line) crystalline films taken at room temperature by high-resolution hard X-ray photoemission spectroscopy.

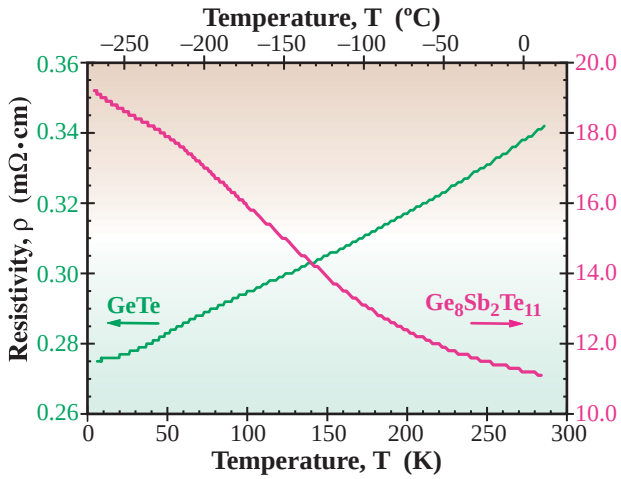

Fig. 2. Temperature dependence of electrical resistivity for GeTe (green line) and $Ge_8Sb_2Te_{11}$ (pink line) polycrystalline films.

Toshiyuki Matsunaga

Characterization Technology Group,
Matsushita Technoresearch

E-mail: matsunaga.toshiyuki@jp.panasonic.com

References

[1] N. Yamada *et al.*: J. Appl. Phys. **69** (1991) 2849.
[2] *T. Matsunaga, H. Morita, R. Kojima, N. Yamada, K. Kifune, Y. Kubota, Y. Tabata, J. Kim, M. Kobata, E. Ikenaga and K. Kobayashi: submitted to Nature Material.*
[3] N.Kh. Abrikosov *et al.*: Semiconducting II-VI, IV-VI, and V-VI compounds, Plenum, New York, 1969.
[4] *T. Matsunaga, R. Kojima, N. Yamada, K. Kifune, Y. Kubota, Y. Tabata, M. Takata: Inorg. Chem.* ***45*** *(2006) 2235.*

X-ray Reflectometry for Absolute Thickness Measurement of Perfluoro-polyether Lubricant on Hard Disk Surface

In a hard disk drive, magnetic write/read heads fly with a spacing of about 10 nm over the magnetic disk surface at very high speed. Therefore, direct contact between head and disk sometimes makes irreversible damage on a recording surface. Perfluoro-polyether (PFPE) liquid lubricant is widely used as a protective coating against fatal damage (Fig. 1).

Precise measurement of the absolute thickness of liquid lubricant film is a very important issue to understand the mechanism of lubricity and to design a high-performance lubricant layer. X-ray reflectometry at beamline **BL19B2** was applied to measure the absolute thickness of PFPE on a Si wafer in the nm range. A standard laboratory X-ray is not suitable for this purpose, since the brightness of the X-ray is not enough to analyze nm range thickness from X-ray reflectivity.

In this study, we have chosen two differently structured PFPE oils on Si wafer as typical thin film lubricant on a hard disk surface (Table 1).

We used a multi-axis diffractometer installed in BL19B2 for the measurement. The sample coated on a Si wafer was mounted in a chamber filled with He gas with a cover of Kapton film for reducing the background noise from air scattering.

Reflectivity of the Si wafer with lubricants was measured as a function of the reflection angle 2θ.

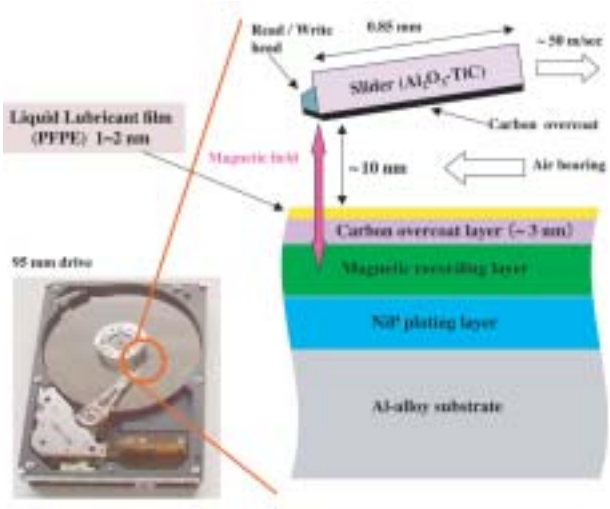

Fig. 1. Cross section of head-disk interface of hard drive.

Table 1. Molecular structure of PFPE lubricant

Fomblin Z-Dol-2000"	$H\text{-}O\text{-}CH_2CF_2O(CF_2CF_2O)_m(CF_2O)_nCF_2CH_2\text{-}O\text{-}H$
A20H"	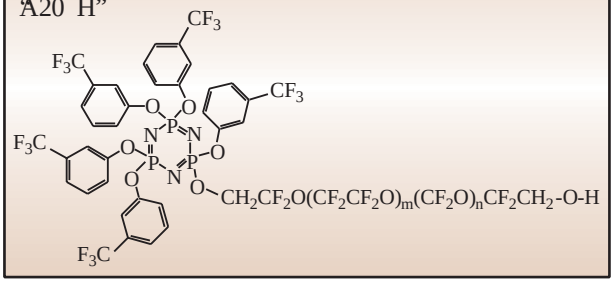

Absolute thickness was calculated by a curve fitting method with computer simulation based on the multilayered film model (Fig. 2). The lube thickness of each sample was also measured by ellipsometry for comparison.

At first, for the measurement of the no-lube sample, a model of two native oxide silicon layers was necessary for suitable matching of the experimental reflectivity and simulated curves. Therefore, in cases of lubricated sample measurements, the same model of two oxide silicon layers was applied for a lubricant layer simulation. The simulation was performed on a multilayered thin film model that is simulated with three parameters for each layer. Film thickness, electron density and interface roughness were adjusted as parameters. For example, in the case of the lubricant A20H in Fig. 2, calculated parameters for each layer are shown in Table 2.

A correlation between the thickness calculated from X-ray reflectivity and the thickness measured by ellipsometry is shown in the Fig. 3. Both measurements have a good relationship in thickness.

Table 2. Simulation results for A20H film on Si

A20H	Thickness [nm]	Electron Density	Roughness [nm]
Lubricant	1.14	1.58	0.288
SiO_2 (1)	0.84	1.51	0.091
SiO_2 (2)	1.30	2.28	0.182
Si wafer	∞	2.33	0.009

Thus, the ellipsometry that has been widely used in the hard disk industry can be applied even in a very thin thickness range below 5 nm. However, the absolute thickness of lubricant measured by X-ray reflectometry is 1.56 times thicker than that measured by ellipsometry. Therefore, the ellipsometry should be calibrated by X-ray reflectometry in order to obtain precise values. Reflectometry gives electron density and interface roughness simultaneously. They are also very important information to evaluate thin film properties in the nm range.

In this study, a Si wafer was chosen as the base substrate for PFPE lubricant in order to obtain high reflectivity for an X-ray. However, on an actual hard disk, PFPE lubricant is coated on a diamond-like-carbon (DLC) overcoat. The interaction between lubricant molecules and a DLC surface will be different from that between lubricant molecules and a Si surface. Therefore, X-ray reflectometry will be tried on a disk DLC surface directly in a subsequent experiment.

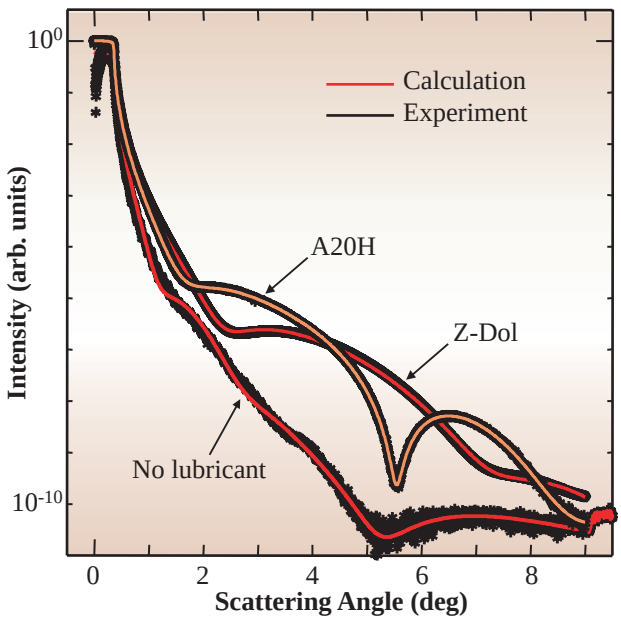

Fig. 2. X-ray reflectivity spectra.

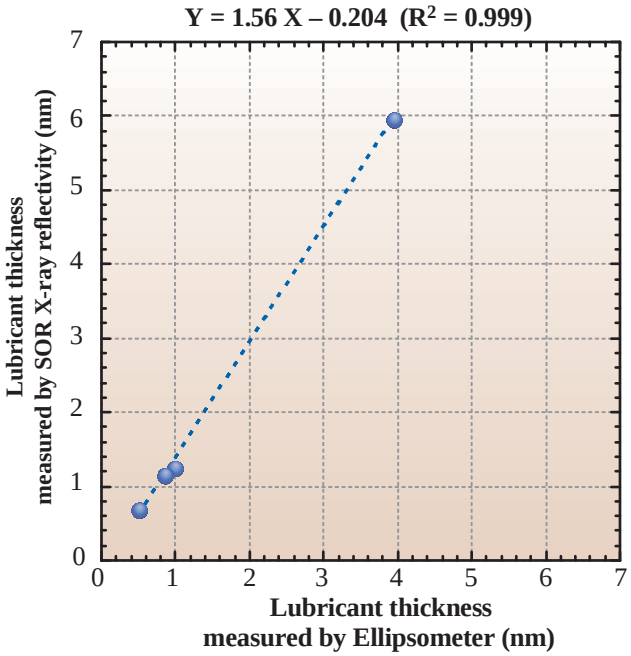

Fig. 3. Correlation between ellipsometry and X-ray reflectometry.

Yasuo Sakane†

Matsumura Oil Research Corp. (MORESCO)

E-mail: sakane@mac.com

†Present address: Komag Inc., Japan Office

References

[1] M. F. Toney and S. Brennan: J. Appl. Phys. **66** (1989) 1861.
[2] M. F. Toney and C. Thompson: J. Chem. Phys. **92** (1990) 3781.

Nondestructive Measurement of Hexavalent Chromium in Chromate Conversion Coatings using X-ray Absorption Near-Edge Structure

Chromate conversion coatings (CCCs) have been widely used for electrical components and mechanical parts, made of brass, aluminum, copper or galvanized iron, to prevent rust formation at a reasonable cost. CCCs have often contained a hexavalent chromium (Cr^{6+}) in addition to a trivalent chromium (Cr^{3+}). Cr^{6+} is known to be toxic and soluble in water. In contrast, Cr^{3+} is nontoxic and mostly insoluble in water. In connection with RoHS (Restriction of the use of certain Hazardous Substances) regulation [1], components containing Cr^{6+} will not be allowed to be used in the electric and mechanical products. Therefore, it is important to analyze the chemical state of chromium (Cr) and to estimate the concentration of Cr^{6+} in a CCC.

The X-ray absorption near-edge structure (XANES) is known to provide useful information on the chemical bonding state of the materials. Recently, Shaffer *et al.* and Tsuyumoto *et al.* investigated chromium in soil [2] and in Portland cement [3], respectively. In comparison with these bulk materials, a CCC is a thin layer of thickness less than 1 μm. In the following, we describe the development of an evaluation technique for Cr^{6+} in the thin coating layer, including the depth distribution of Cr^{6+}.

For the high-sensitive detection of fluorescent X-rays from CCCs, we used a silicon drift detector (SDD) with seven elements. The measurements were performed at beamline **BL16B2**. In Fig. 1, we show the normalized Cr-K XANES spectra for black, yellow, colored and nonhexavalent CCCs. In the figure, the spectra were normalized by the intensity at 6150 eV where the complex oscillation structure coming from the chemical structure is already smoothed out. The inset shows the pre-edge peak, which is the resonant absorption that corresponds to the 1s to 3*d* transition, which allowed for Cr^{6+} and forbidden for Cr^{3+} [4]. The black, yellow and colored CCCs showed the pre-edge peak that indicates the existence of Cr^{6+} in contrast to the absence of the peak in nonhexavalent CCCs. On the other hand, the fluorescence intensity at the normalization point of 6150 eV, Cr at any valence state, contributes to the fluorescent yield and can be used to estimate the total amount of Cr in a CCC.

To quantify the percentage of Cr^{6+} in a CCC, we used the integrated intensity of the pre-edge peak to minimize the effects from the variation of the spectral shape on the quantification. In the integration, the background was removed by using the profile of the nonhexavalent chromium sample. The percentage of Cr^{6+} can be obtained by multiplying the integrated peak intensity by the calibration constant obtained from the reference sample of CrO_3 as a pure Cr^{6+}.

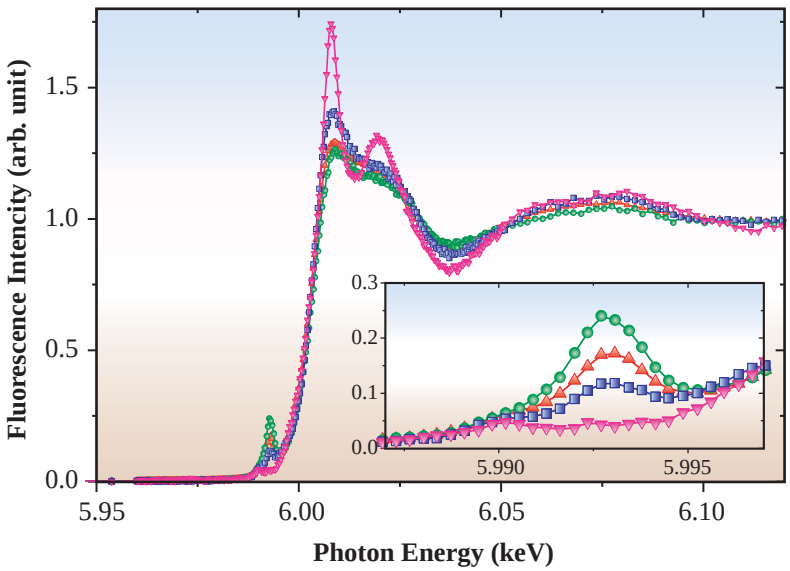

Fig. 1. Normalized Cr-*K* XANES spectra of black (▲), yellow (●), colored (■) and nonhexavalent (▼) CCCs. The inset shows an enlarged view of the Cr^{6+} peak area.

This method gives the percentages of Cr^{6+} in the black, yellow, colored and nonhexavalent CCCs, which are 10.5 ± 1.1, 19.3 ± 1.9, 3.5 ± 0.4 and 0%, respectively.

To evaluate the depth distribution of Cr^{6+} in a CCC, we performed grazing incidence X-ray fluorescence (GIXRF) measurements using the wavelength-dispersive detector system at beamline **BL16XU**. We measured the incident angle dependence of the fluorescence yield, which reflects the depth distribution of the element, at 5993 eV and at 6150 eV, which correspond to the pre-edge peak of Cr^{6+} and the total Cr, respectively. The measurement results are shown in Fig. 2(a) where we can see a clear difference in the fluorescent profiles between Cr^{6+} and the total Cr. In the data analysis, we developed an optimization program that is based on the multilayer reflectivity calculation where the fluorescence intensity is calculated from the electric field in the layer and the depth distribution for Cr^{6+} and the total Cr [5]. Since the surface roughness was large, we sliced the CCC into thin layers and the mass density of each layer, which is proportional to the total Cr density, was optimized. Furthermore, the dispersion of the incident angle due to the rough surface was taken into account by assuming the divergence of the incident angle of X-ray to be around 0.1 degree in the calculation. The result of the optimization for the measured X-ray intensity is shown by the solid line in Fig. 2(a). The corresponding depth profile is shown in Fig. 2(b) and the inset figure is the schematic image of Cr^{6+} concentration. The percentage of the Cr^{6+} concentration turned out to decrease along the surface of the yellow CCC. The conventional CCC process includes a water rinse after the formation of a coating. It is possible that the Cr^{6+} around the surface was deoxidized or eluted in the water [6].

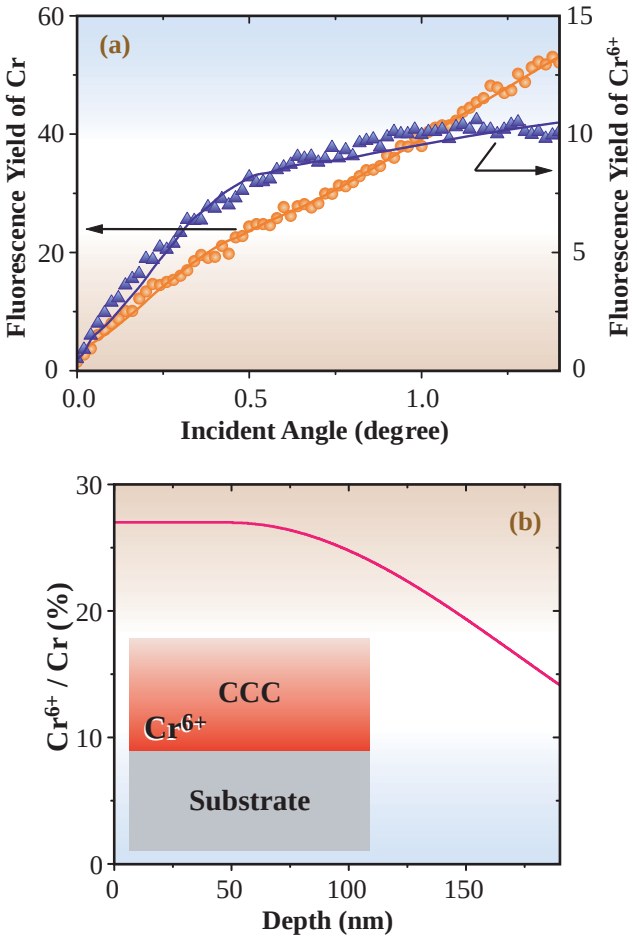

Fig. 2. **(a)** Incident angle dependence of Cr-Kα fluorescence from the total Cr (●) and at Cr^{6+} pre-edge peak (▲) for yellow CCC. The solid line represents the calculation based on the multilayer model. **(b)** Depth profile of Cr^{6+} ratio. The inset in **(b)** shows a schematic image of Cr^{6+} concentration.

K. Nomura* and N. Awaji

Fujitsu Laboratories LTD.

*E-mail: nomura.kenji@jp.fujitsu.com

References

[1] Official Journal of the European Union **37** (13 February 2003) 19.
[2] R.E. Shaffer *et al.*: Anal. Chim. Acta **442** (2001) 295.
[3] I. Tsuyumoto and H. Uchikawa: J. Ceram. Soc. Jpn. **111** (2003) 608.
[4] S. Bajt *et al.*: Anal. Chem. **65** (1993) 1800.
[5] N. Awaji: Spectrochim. Acta, Part B **59** (2004) 1133.
[6] *K. Nomura and N. Awaji: Jpn. J. Appl. Phys. Lett.* ***45*** *(2006) L304.*

Evidence of Surface Compression and Stability of Laser-peened Material without Coating

Laser peening without coating (LPwC) is an emerging surface enhancement technology. The effects of eliminating stress corrosion cracking (SCC) susceptibility and enhancing fatigue strength for metal materials have been demonstrated through various experiments and applications [1]. However, it still remains as an open question how the surface layer can be compressive despite the possible thermal effect of LPwC, where intense laser pulses directly irradiate the material surface [2].

The purpose of this study is to present substantial evidence showing that the surface after LPwC is compressive and the residual stress imparted by LPwC is stable under thermal loading. For this purpose, we have applied a constant penetration depth (CPD) method, which can provide relevant information on the surface residual stress, because the method enables us to control the X-ray penetration depth constant for a series of exposures with various ψ angles [3]. By combining this method with the high energy and high brilliance X-ray of SPring-8, the residual stress depth profile in the surface layer can be precisely evaluated in a non-destructive manner.

Preliminary experiments were conducted to prove the effectiveness of the CPD method with a 25 keV X-ray at beamline **BL19B2**. Figure 1 shows an example of the so-called $\sin^2\psi$ diagram obtained by a conventional ψ-goniometer method for high tensile strength steel (JIS SHY685) with a huge stress gradient. Since the residual stress is supposed to be proportional to the slope of the diagram, the result is strongly affected by the range of ψ angles used in the measurement. The $\sin^2\psi$ diagrams obtained by the CPD method for various penetration depths of the same sample are shown in Fig. 2. There is no ambiguity in deducing residual stress since the data for each penetration depth make an almost straight line. Through the preparatory experiments above, it was concluded that the CPD method could allow us to properly evaluate the residual stress depth profile in the surface layer non-destructively.

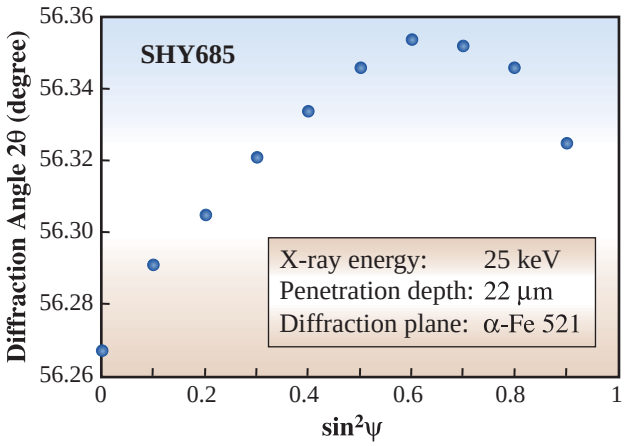

Fig. 1. $\mathrm{Sin}^2\psi$ diagram obtained by conventional ψ-diffractometer method.

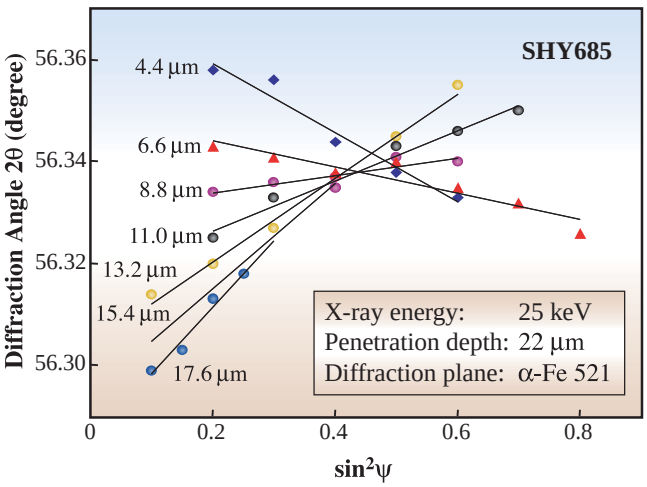

Fig. 2. $\mathrm{Sin}^2\psi$ diagram obtained by CPD method.

LPwC was applied to samples of 20% cold-worked austenitic stainless steel (JIS SUS304). The conditions of laser peening were a 60 mJ pulse energy, a 0.7 mm spot diameter and a 70 pulses/mm^2 density. The residual stress depth profile was evaluated by the CPD method before, during and after heat treatment at up to 673 K. The resulting residual stress depth profiles are shown in Fig. 3. It is evident that the surface layer is compressive despite the direct irradiation of laser pulses to the surface in LPwC. The heat treatment somewhat reduced the residual stress; however, the overall distribution was quite stable. This kind of measurement using the same sample could not be realized without the CPD method with the high energy X-ray of SPring-8.

LPwC was also applied to a ceramic material. Since the residual stress distribution in the surface region largely affects the mechanical property of brittle materials such as ceramics, it is important to evaluate

the depth profile without interference that might be introduced by machining or grinding. However, measuring the residual stress depth profile of ceramics is a difficult task because it is not easy to remove the surface layer due to its hardness. On the other hand, the density of ceramics is relatively low and consequently it makes the CPD method attractive for measuring the depth profile using a high energy X-ray that highly penetrates into ceramics.

Samples were prepared from finely ground Si_3N_4. LPwC was performed under conditions of a 40 mJ pulse energy, a 1.0 mm spot diameter and a 18 pulses/mm^2 density. The profiles of the ground and laser-peened samples were measured with 15 keV and 25 keV X-rays at BL19B2. The results obtained are shown in Fig. 4. Both profiles obtained at different X-ray energies well agree with each other. Because the laser peening conditions are much gentler than those for the metal material, the amplitude of compressive residual stress is relatively small and the depth is also shallow.

The strong evidence of surface compression on laser-peened SUS304 and Si_3N_4 without coating has been successfully obtained through the present experiments by the CPD method in conjunction with the high energy and high brilliance X-ray of SPring-8. The method is versatile and opens up new applications to many industrial materials and components.

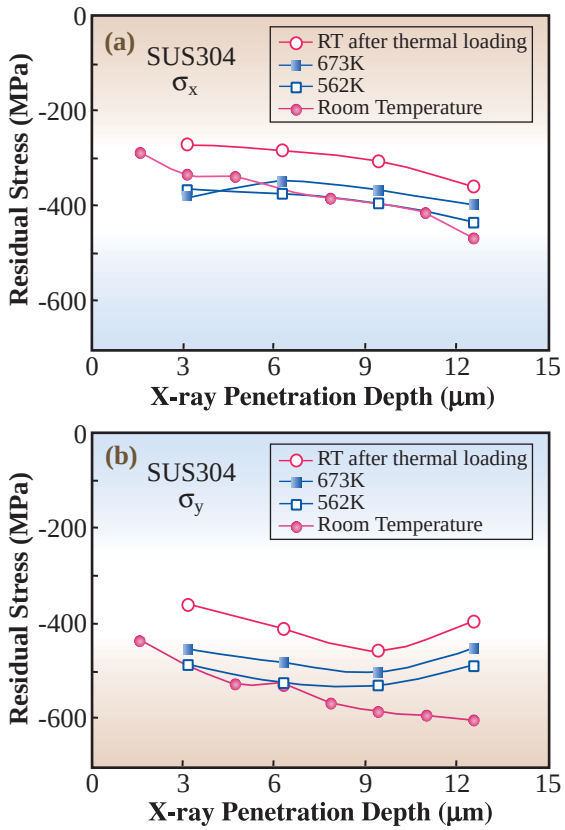

Fig. 3. Residual stress depth profile of laser-peened SUS304 obtained by CPD method.

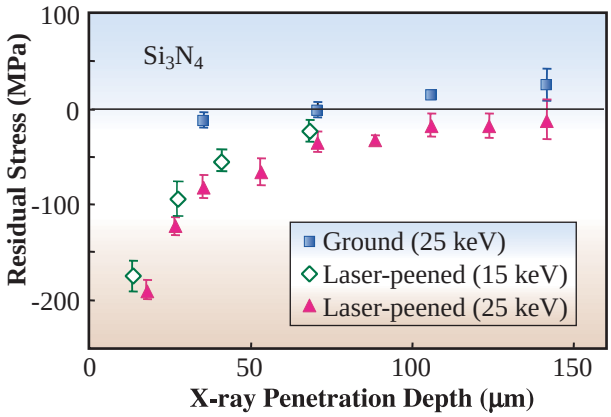

Fig. 4. Residual stress depth profile of laser-peened Si_3N_4 obtained by CPD method.

Yuji Sano[a,*] and Koichi Akita[b]

[a] Toshiba Corporation
[b] Musashi Institute of Technology

*E-mail: yuji.sano@toshiba.co.jp

References

[1] *Y. Sano, M. Obata, T. Kubo, N. Mukai, M. Yoda, K. Masaki and Y. Ochi: Mater. Sci. Eng. A* ***417*** *(2006) 334.*
[2] P. Peyre *et al.*: J. Mater. Sci. **33** (1998) 1421.
[3] M. Sato *et al.*: to be published in Proc. SRI2006 (Daegu, Korea).

Development of *In Situ* Observation Technique on Solidification Structure of Weld Metals by X-ray Diffraction

High-intensity heat sources used for fusion welding create steep thermal gradients in materials as they are rapidly heated and cooled to and from their melting points. The rapid thermal cycling that takes place induces melting and solidification in those parts of the weld where the liquidus temperature has been exceeded, as well as solid-state phase transformation on both heating and cooling during welding. Then, the weld metal suffers from a crack, known as a solidification crack, owing to the thermal strain in the solidification temperature range in which ductility remarkably decreases during welding. The solidification crack is a significant problem of austenite stainless steels during rapid cooling for industrial applications. *In situ* observation is essential for understanding these phenomena. X-ray diffraction analysis is often utilized as an *in situ* technique. In the case of welding, the physical dimensions of the weld depend on the welding conditions and transformation kinetics, and an X-ray probe must have a beam size finer than the dimensions of the transformation region. In this work, the experimental setup for time-resolved *in situ* observation of phase transformation during solidification and cooling (10 to 10^4 K/s) in a welding process using synchrotron radiation and the result for several kinds of steel welds are presented.

In our research group, an *in situ* phase identification system combined with an undulator beam and an imaging plate has recently been utilized at **BL46XU** beamline [1]. Furthermore, a two-dimensional pixel detector that the SPring-8 detector team has been developing in collaboration with the Paul Scherrer Institute (PSI) in Switzerland [2] was used to exclude the influence of preferred orientation as shown in Fig. 1. A photon energy of 18 keV was selected to maximize the number of observable diffraction peaks in the 2θ window. The gas tungsten arc-welding torch was moved in parallel to the upper surface of the specimen, which was set on the anode. These make it possible for phase transformation to be identified in real-time under conditions of one-directional solidification and a spatial resolution of 0.1 × 0.3 mm.

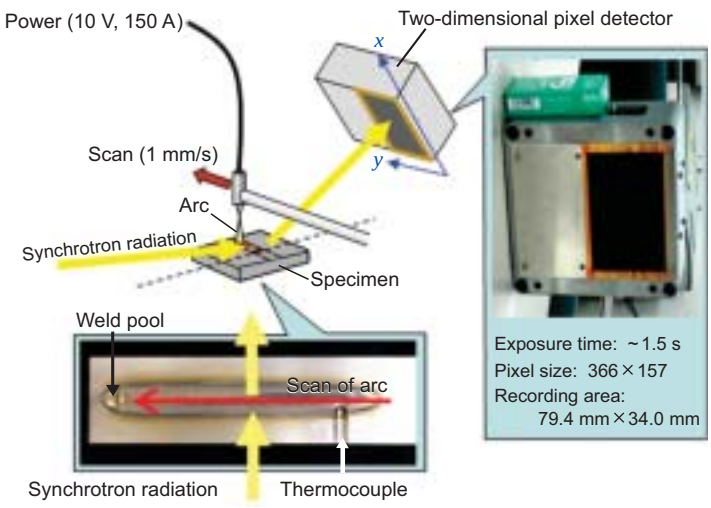

Fig. 1. Experimental setup for time-resolved *in situ* observation.

Figure 2 shows an example of X-ray diffraction pattern on the imaging plate obtained in the welding and an SEM observation of the rapid cooling microstructure of the stainless steel (Fe-20%Cr-14%Ni). The shift of the diffraction peak, mist-like pattern and periodic pattern of the primary γ phase were observed, suggesting an increase in crystallinity, the appearance of the nucleus of dendrites and the rotation of crystallites due to a drop in temperature. The crystal growth of γ phases was observed in detail with a time resolution of 0.1 s or less.

Figure 3 shows the change of the two-dimensional diffraction pattern for the austenite stainless steel (high alloy) (a-d) that is identical with the specimen in Fig. 2 and hypoeutectoid steel (low alloy) (e-h) during welding. In the high alloy, the diffraction patterns of the primary γ phase blink at a high temperature of more than 1400 ºC (a,b), suggesting the rotation of crystallites. The diffraction spots converge with the appearance of the secondary δ phase, suggesting the preferred orientation due to lattice matching. Consequently, the microstructure of the high alloy after solidification also has the preferred orientation normal to the specimen surface. In the low alloy, the δ, γ, and α phases appear at (e) about 1500 ºC, (f) 1450 ºC and (g) 600 ºC, respectively. Consequently, the diffraction peaks of residual γ and α phases mainly coexist. The comparatively random microstructure is formed as shown by the ring pattern (h).

This phenomenon corresponds to the miniaturization of the microstructure due to the solid transformation in the final stage.

This technique is quite useful for verifying experimentally whether ferrite or austenite is the primary phase that solidifies from the melt, and for following the dynamics of phase transformation during cooling in the fusion welds under a steep thermal gradient and non-isothermal heating and cooling conditions.

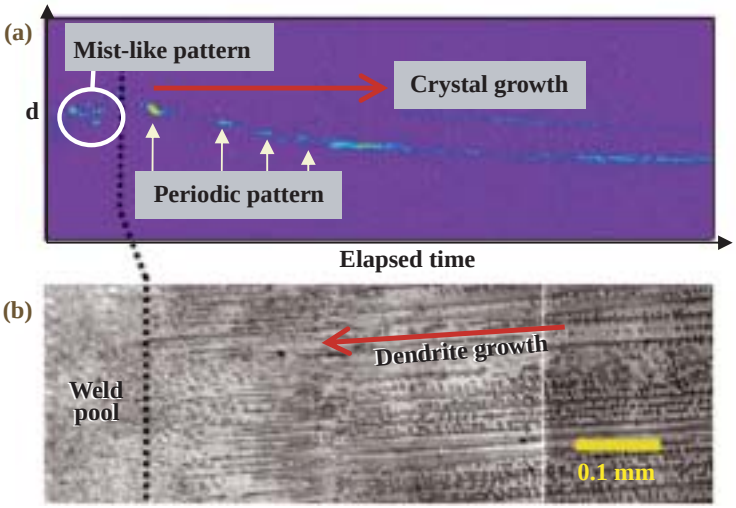

Fig. 2. X-ray diffraction peak on imaging plate and SEM observation of rapid-cooling microstructure.

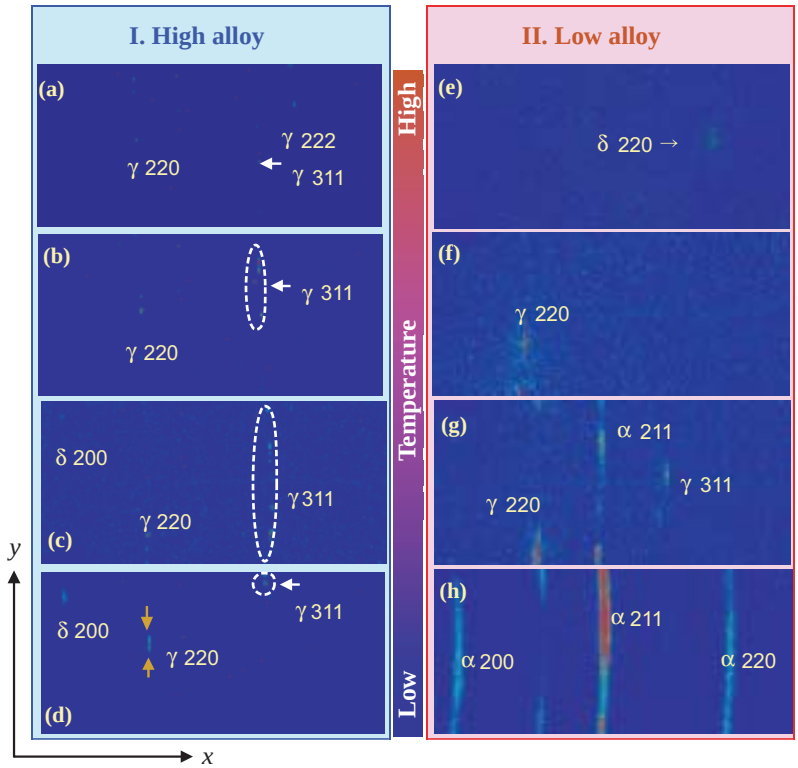

Fig. 3. Time-resolved two-dimensional diffraction patterns. The *x*- and *y*-axis corresponds to those in Fig. 1.

Mitsuharu Yonemura[a,*], Yu-ichi Komizo[b] and Hidenori Toyokawa[c]

[a] R&D laboratories, Sumitomo Metals Industries, Ltd.
[b] Joining & Welding Research Institute, Osaka University
[c] SPring-8 / JASRI

*E-mail: yonemura-mth@sumitomometals.co.jp

References

[1] *M. Yonemura, T. Osuki, H. Terasaki, Y. Komizo, M. Sato and A. Kitano: Mater. Trans.* ***47*** *(2006) 310.*
[2] H. Toyokawa: Abstract of The 8th SPring-8 Symposium (2004) p. 11.

Evaluation of Calcium Leaching in Concrete using High-intensity X-ray CT

Concrete is a widely used construction material that is normally very durable. However, it has been found that in some environments it deteriorates and breaks down. It is now understood that this deterioration results from ion elusion and invasion both internally and externally. Civil structures are normally expected to have long lifetime, sometimes more than one hundred years.

Deterioration due to leaching occurs gradually in structures in long-term contact with water. This results in the elusion of calcium, which is a major component of concrete, and is called leaching.

Leaching is described as follows. Concrete is a solidified mixture of cement and rock. The main components of cement are calcium and silicon. Cement solidification occurs with hydration, which generates calcium compounds. The resulting solidified cement structure is a porous material. Pores in the structure are connected and form a network. The calcium compounds are gradually dissolved in water that invades the pores. Dissolved and ionized calcium migrates into the concrete medium. As a result, in environments where the concrete is in contact with water, the solidified cement component of the concrete is gradually dissolved. This cement dissolution increases the porosity of the concrete structure. It is understood that concrete strength is correlated with its porosity.

This phenomenon of concrete leaching is currently considered to be the key to the long-term safety of structures. Due to the long-term nature of this process of at least a few decades, it is difficult to experimentally simulate it. Thus, an attempt has been made to predict the leaching rate by computer simulation. A leaching predictive simulator is constructed on the basis of diffusion equations.

There are complicated boundary conditions for concrete, which take into account various factors such as aggregate and cracks. The calcium diffusion rate with these conditions is determined in the simulation. Some of the aggregate and cracks are only a few tens of microns. To determine their distribution, observation by X-ray CT with a large visual field and high resolution in SPring-8, using beamline **BL20B2**, was necessary.

Calcium ion migration is described as a diffusion phenomenon. Thus, a diffusion coefficient for the concrete medium that fits the leaching conditions is indispensable. Understanding of the fine concrete structure is essential to understand the deterioration mechanism, including the diffusion coefficient. However, no observation method has been available, and fine structure study has relied on assumptions from macroscopic experiments. Thus, until now, a simulation-based fine concrete structure has been limited to a simple model.

Electron microscopy, the mercury injection method and X-ray CT, among others are now available for observing the fine concrete structure. Electron microscopy can allow us to only observe the surface, so it not suitable for structure observation. The mercury injection method can be used to measure the distribution of pore radius, but not to obtain the three-dimensional structure of the pores. The size of the picture element of the conventional X-ray CT is as large as over 10 microns. Furthermore, radiated X-ray energy is too large for concrete whose main components are light elements. Thus, conventional X-ray CT cannot be used to observe pore structure.

High parallelism and high brightness of the beam enable us to realize high resolution and high visibility for X-ray CT at beamline **BL47XU**. This accuracy cannot be obtained by other methods.

A cross-sectional image of the internal concrete obtained by X-ray CT is shown in Fig. 1. The

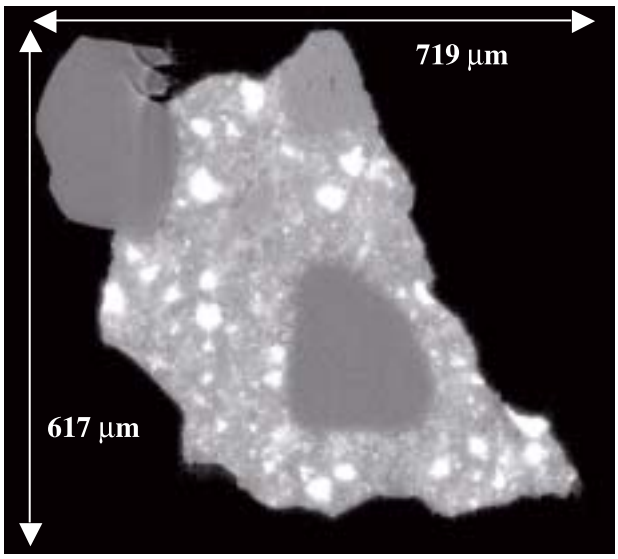

Fig. 1. Cross-sectional image of healthy mortar W/C 0.4.

specimen is made of concrete whose aggregate was removed under healthy conditions where no leaching occurred. The pores are shown as a dark color. The granular uniform structure shown in the figure is sand. The rock part and porous cement part can also be observed. A cross-sectional image of the concrete structure in which leaching occurred is shown in Fig. 2. It is found that the cement structure has many pores.

Digitization of these pictures enables us to capture the pores in the concrete cross section. Stacking of the pores in the cross section enables three-dimensional reconstruction. A three-dimensional image of the pores is shown in Fig. 3. The central part of Fig. 2 was three-dimensionally extracted and only the continuity of the cement structure was examined. The colored part in the region shows the pores that are vertically continuous in the scanned range.

Understanding of the three-dimensional structure of the pores enables us to determine the diffusion path of the ions that cause the concrete to deteriorate. Base data for estimating the diffusion coefficient of calcium and other ions are obtained from the diffusion path.

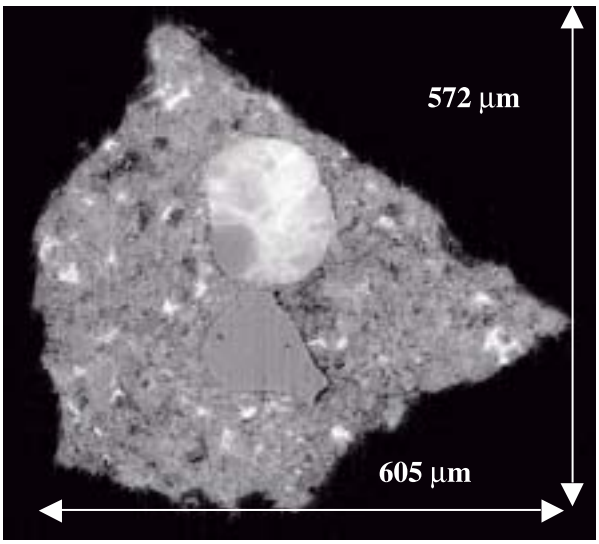

Fig. 2. Cross-sectional image of mortar W/C 0.4 with leaching.

It is impossible to capture independent air bubbles by the mercury injection method. Understanding of the independent air bubbles is essential in constructing a theoretical model that can predict changes in structures after deterioration occurs. Furthermore, the correlation between material strength and porosity would be clarified. Thus, the material strength at an arbitrary material age can be estimated from the degree of deterioration. Fine sampling is difficult because cement is a highly brittle material.

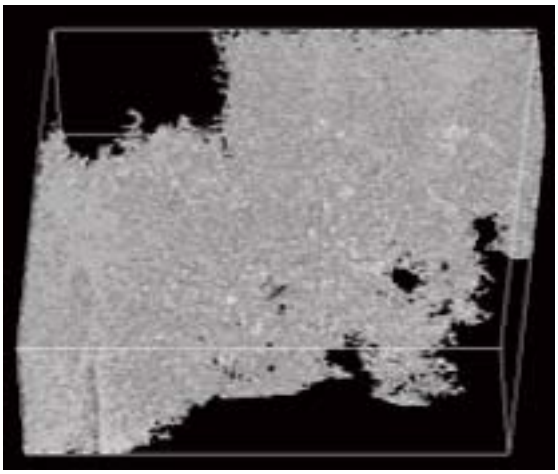

Fig. 3. Continuous pores of mortar W/C 0.4 with leaching.

Takashi Hitomi

Civil Material Laboratory, Obayashi Co.

E-mail: hitomi.takashi@obayashi.co.jp

Structural Analysis of Curly and Straight Human Hair Fibers by Scanning Microbeam SAXS

Human hair is one of many keratinous fibers and has a structure similar to that of wool. Figure 1 illustrates the structure of hair. The surface of a hair fiber is covered with thin scale-like cells (cuticles) and beneath the cuticle layers are the cortex and the medulla, which exists at the center of hair. The cortex dominates (*ca.* 80%) and is comprised of cortical cells. Figure 1 also shows the hierarchy structure of a cortical cell. It is filled with macrofibrils, which are composed of intermediate filaments (IFs) surrounded by matrix proteins.

Most wool fibers contain two (sometimes three) types of cortical cells, namely, orthocortex and paracortex (and mesocortex), and the bilateral distribution of these has been associated with the crimped structure of wool. It has been found by transmission electron microscope (TEM) observations that there are obvious differences in the geometrical arrangement of the IFs in these cortical cells. IFs seem to be oriented more parallel to the fiber axis in the para- and mesocortex, whereas they are twisted helically in the orthocortex [1]. The shape of wool fiber is curly, but that of human hair varies from curly to straight. There are some reports on cortical cell types for human hairs [2] but no information on their distributions or the relationship with the macroscopic hair shape. The purpose of this study is to analyze the IF arrangement of curly and straight hairs, in the intact condition, to elucidate the difference in macroscopic curl shape from the viewpoint of the internal nanostructure. Measurements have been performed for Asian, Caucasian and African hairs having various curl strengths, ranging from strong curly to nearly straight.

Small angle X-ray scattering (SAXS) experiments were carried out at beamline **BL40XU** of SPring-8 and BL-4A of Photon Factory (Tsukuba) [3,4]. Two-dimensional (2D) SAXS from different positions in the transverse direction of a fiber was measured. The diameters of measured hairs were larger than 50 μm, so the size of the microbeam used (less than 6 μm) was small enough to analyze the inner and outer sides of the curl separately. In this study, only the scattering patterns from the cortex have been analyzed.

Figure 2 shows typical 2D SAXS patterns of a curly human hair fiber. Major intensity maxima, which are observed along the equator (short arrows), are attributed to the lateral packing between IFs. A clear difference in these IF peaks is seen between the outer side (a) and the inner side (b) of the curl. The IF peaks of the inner side are strong and sharp but those of the outer side are weak and broad. This means the IF arrangements are different between the outer side and the inner side of the curl, suggesting the inhomogeneity of IF arrangement in the transverse direction. This inhomogeneity was observed for Merino wool, curly African, Caucasian and Asian hairs, but not for nearly straight Caucasian and Asian hairs.

Through analyses of equatorial scattering profiles with a model having closed packing of infinite cylinders [5], values of the IF diameter and the mean IF-IF distance are estimated. The degree of IF tilt against the fiber axis is also analyzed on the basis of the full-width at half maximum (FWHM) of the IF peak profile in the azimuthal direction. As a result, it has been found for curly hairs that the IF diameter is almost constant, but that the mean IF-IF distance decreases while the IF tilt angle increases from the inner side toward the outer side of the curl. These tendencies are consistent with those of wool fibers, which were speculated only qualitatively on the basis of TEM observation. In contrast, if the curl strength is very weak, not only the IF diameter but also the mean IF-IF distance and IF tilt angle are almost constant from the inner side to the outer side of the curl.

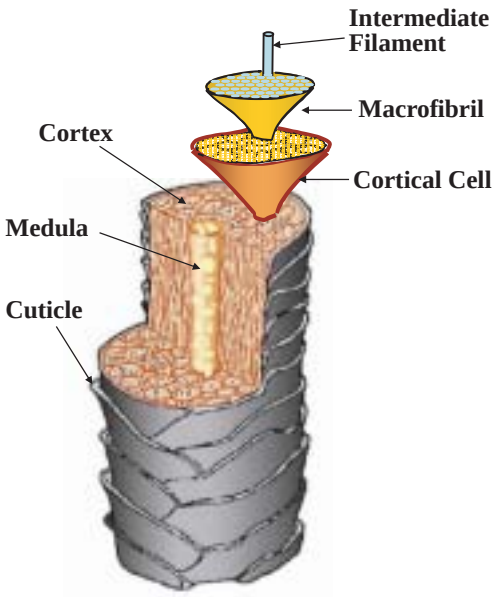

Fig. 1. Internal structure of human hair fiber.

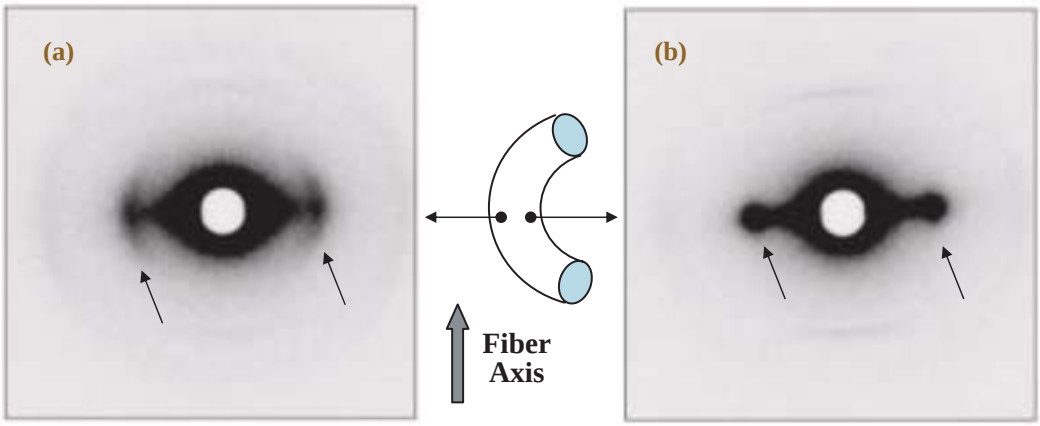

Fig. 2. SAXS patterns from outer side **(a)** and inner side **(b)** of strong-curl African hair.

In order to quantify the inhomogeneity in the transverse direction, we have introduced the index η, which represents the nanostructural difference based on the difference in the IF tilt angle between the inner side and the outer side of the curl. η is defined as the ratio of the averaged FWHM of the IF profile in the azimuthal direction in the outer side ($0.2 < P < 0.4$) to that in the inner side ($0.6 < P < 0.8$), where P is the relative position in the transverse direction from the outermost side ($P = 0$) to the innermost side ($P = 1$) of the curl. Data within the ranges 0.2 to 0.4 and 0.6 to 0.8 are likely to be a result of scattering from the cortex and will have no contribution from the cuticle or medulla.

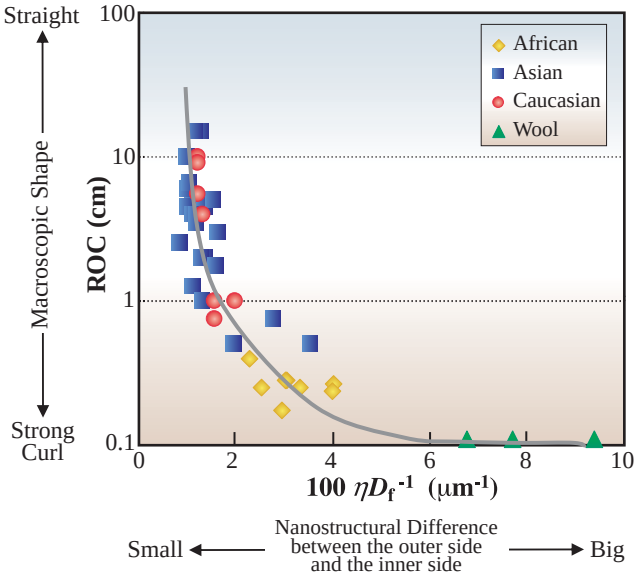

Fig. 3. Relationship between macroscopic curl strength (radius of curvature: ROC) and normalized η for microscopic inhomogeneity in transverse direction of fiber. ◆: African hair; ●: Caucasian hair; ■: Asian hair; ▲: Merino wool.

Figure 3 shows the relationship of macroscopic curl strength (radius of curvature: ROC) *vs.* η normalized by the fiber diameter D_f. The Caucasian and Asian hairs used in this study have a wide variety in their curl strength and overlap. The curls of African hairs are stronger than those of Caucasian and Asian hairs and Fig. 3 also includes the results for Merino wool fibers as an extreme case. It can be seen that the larger the nanostructural difference between the inner side and the outer side of the curl, the higher the macroscopic curl strength. Moreover, all the data points follow one smooth curve. This strongly suggests that the macroscopic curl strength depends on the microscopic inhomogeneity in the transverse direction of fibers, and that this relationship holds over all ethnic origins, including wool.

Takashi Itou[a,*], Yoshio Kajiura[a] and Yoshiyuki Amemiya[b]

[a] Hair Care Research Laboratories, Kao Corporation
[b] Department of Advanced Materials Science, The University of Tokyo

*E-mail: itou.takashi1@kao.co.jp

References

[1] W.G. Bryson *et al.*: Proc. 10th Int. Wool Text. Res. Conf. (2000) ST-P3.
[2] C.R. Robbins: Chemical and Physical Behavior of Human Hair, 4th Ed., Springer-Verlag, Chapter 1 and references therein.
[3] Y. Kajiura *et al.*: J. Appl. Cryst. **38** (2005) 420.
[4] *Y. Kajiura, S. Watanabe, T. Itou, K. Nakamura, A. Iida, K. Inoue, N. Yagi, Y. Shinohara and Y. Amemiya: J. Struct. Biol. - in press, (available to see at http://dx.doi.org/10.1016/j.jsb.2006.04.008).*
[5] F. Briki *et al.*: Biochimica et Biophysica Acta **1492** (1998) 57.

Structural Analysis of Human Hair Cuticle using Microbeam X-ray Diffraction: Relationship with Effects of Hair Dyeing

Hair treatments, such as permanent waving, hair bleaching and hair conditioning, are performed in wet conditions. Thus, in cosmetic research, it is important to understand how water-soluble products can penetrate into a hair fiber. The cuticle is the outermost layer of a hair fiber and is made up of a stack of several sheet-like cells (Fig. 1). This structure is thought to have a large effect on the permeation of substances into hair. The surface of the cuticle cell is covered by a thin layer of lipids called β-layer. Between adjacent cells, these lipids are separated by the δ-layer of proteinous components. This triple-layered structure between adjacent cells is called a cell membrane complex (CMC). CMC is the only substructure that continuously fills the intercellular spaces of a hair fiber. Therefore, it is considered to be an important pathway for the penetration of substances.

Recently, small angle X-ray scattering (SAXS) analysis using a microbeam has been reported to be useful for characterizing CMC structure [1]. We have characterized human hair samples using SAXS analysis and have detected changes in CMC structure that correlate with the penetration of molecules [2].

Using a 5-μm φ high flux beam (λ=0.083 nm), SAXS experiments were carried out at beamline **BL40XU** under an atmosphere of 30 ºC and 50% relative humidity. Each thickness of the β-layer and δ-layer was estimated from X-ray scattering patterns using an electron density model [3]. For SAXS experiments, hair strands were obtained from Japanese women who had not used any chemical treatments such as permanent waving or hair bleaching. The strands were subjected to extraction with four different solvents, namely, methanol, acetone, hexane, and a chloroform/methanol mixture (2:1 v/v), at 37 ºC for 6 hours. Because was reported that solvent extraction accelerated the dyeing rate of wool fiber [4], we planned to detect the influence of these extraction treatments on CMC structure.

The estimated thickness of the CMC structure of the hair samples is shown in Fig. 2. The thickness of the β-layer was decreased by extraction with acetone and hexane, while it was not changed by extraction with methanol or chloroform/methanol. In addition, the thickness of the δ-layer was decreased by extraction using methanol, acetone, and chloroform/methanol, and did not significantly change with hexane. Interestingly, these hair samples differed in the dyeing extent of Acid Orange 7 as an index of substance penetration.

Figure 3 shows the relationship between the CMC structure and the dyeing extent. There is a correlation between the thickness of the δ-layer and the dyeing extent, the larger decrease in δ-layer thickness resulting in a greater elevation of the dyeing extent. On the other hand, the thickness of the β-layer did not show a correlation with the dyeing extent. These results suggest that the δ-layer acts as a major pathway of acidic dye penetration.

SAXS analysis using an X-ray microbeam is a powerful tool for characterizing the CMC structure in the area of cosmetic research. The main advantage

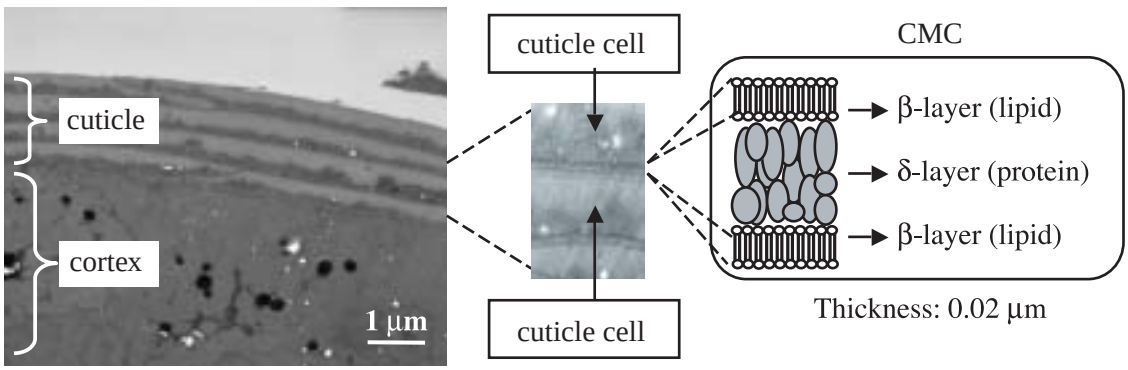

Fig. 1. Transmission electron micrographs of human hair and schematic diagram of CMC structure.

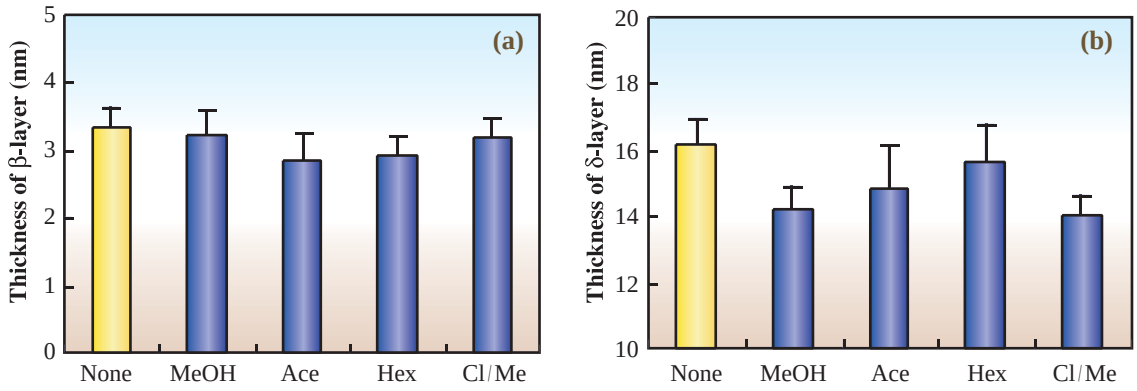

Fig. 2. Effects of extraction with solvents on thickness of β- and δ-layers. **(a)** β-layer. **(b)** δ-layer. None; nonextracted, MeOH; extracted with methanol, Ace; extracted with acetone, Hex; extracted with hexane, Cl/Me; extracted with mixture of chloroform and methanol (2:1).

of this method over transmission electron microscopy is the availability of hair analysis in natural conditions, as the hair samples do not require fixing, pre-staining or slicing. Therefore, we were able to detect structural changes in the CMC by solvent extraction. Fixing and pre-staining treatments would induce serious chemical changes of hair components that are comparable to the solvent extraction.

Our findings showed a correlation between dyeing extent and δ-layer thickness, both of which were changed by extraction with solvents. It has been speculated that hydrophilic molecules penetrate hair through the δ-layer, on the basis of histochemical observations of the CMC. Since the dye used in our study (Orange 7) was water-soluble, the relationship seen between the dyeing extent and the δ-layer thickness is in agreement with this speculation. Thus, we were able to detect changes in the CMC structure that correlated with the penetration of molecules using a microbeam SAXS method.

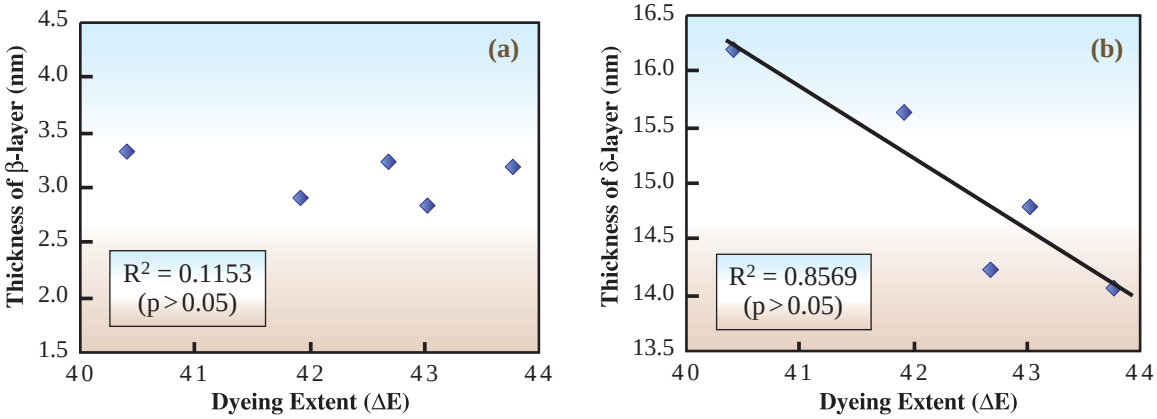

Fig. 3. Relationships between CMC structure and extent of dyeing. **(a)** Relationship between thickness of β-layer and dyeing extent. **(b)** Relationship between thickness of δ-layer and dying extent. ΔE; index of dyeing extent measured using a chromometer, R; correlation coefficient, p; level of significance.

Takafumi Inoue[a,*], Yoshimichi Iwamoto[b] and Noboru Ohta[c]

[a] Basic Research Laboratory, Kanebo Cosmetics
[b] Beauty Care Laboratory, Kanebo Home Products
[c] SPring-8 / JASRI

*E-mail: tinoue@kanebocos.co.jp

References

[1] L. Kleplak *et al.*: Biochim. Biophys. Acta **1547** (2001) 268.
[2] *T. Inoue, Y. Iwamoto, N. Ohta, K. Inoue and N. Yagi - in preparation.*
[3] N. Ohta, T. Oka, K. Inoue, N. Yagi, S. Kato and I. Hatta: J. Appl. Cryst. **38** (2005) 274.
[4] K. Joko *et al.*: Proc. 7th Int. Wool Text. Res. Conf. **5** (1985) 23.

Instrumentation & Methodology

Radiation from SPring-8 features the most powerful characteristic of having the world's highest brilliance. The low emittance operation that was back last year after an interval of three years has further increased brilliance three times higher than the former operation, and thus it has brought about new scientific opportunities not only in basic researches but also in technological developments, being combined with sophisticated top-up operation. In this issue, eight reports have been selected as outstanding results in the field of Instrumentation and Methodology.

Cavity resonance fringes have been successfully observed and Fabry-Perot resonators have been realized for the first time in the hard X-ray region using minute monolithic silicon crystal cavities. Commercially available nearly perfect large-area quartz wafers have been investigated and it has been confirmed that they have a great potential for inelastic X-ray scattering analyzers. A new algorithm using the maximum entropy method has been proposed for single-energy photoelectron holography and its effectiveness has been clearly demonstrated using a two-dimensional display type analyzer. Phase tomography by Talbot interferometry has been realized with thick gold gratings fabricated by X-ray lithography and gold electroplating using the LIGA beamline of NewSUBARU. A multilayer supermirror composed of platinum-carbon combination, which is for astronomical hard X-ray telescope, has been characterized by highly brilliant SR. High-energy X-ray PEEM has been able to achieve a probe depth ten times deeper than that using conventional soft X-ray PEEM. The phase modulation of the nuclear resonant synchrotron radiation for ^{181}Ta nucleus has been clearly shown. Ultrafine monochromatized X-ray beam for nuclear resonant scattering experiments has been generated by high-quality iron borate crystal heated at near Néel temperature.

Yasushi Kagoshima
Graduate School of Material Science
University of Hyogo

Realization of Fabry-Perot Resonators for Hard X-rays

Optical Fabry-Perot resonator has been frequently used in optics. In the case of X-rays, crystal resonators have long been thought of and proposed for nearly four decades [1]. The simplest two-plate crystal resonator has been mostly investigated theoretically. A variety of experiments in realizing X-ray resonators (cavities) have also been attempted.

An X-ray Fabry-Perot resonator, like the optical one, uses two crystal plates as reflecting mirrors. An incident X-ray beam is reflected back and forth coherently between the two plates via back diffraction, of which the Bragg angle is very close to 90º. Interference fringes due to cavity resonance are generated. In spite of that there have been many well documented theoretical studies of X-ray cavity resonance reported in the literature, the experimental conditions for such coherent interaction between the back-and-forth X-rays are however very difficult to be attained [2]. To overcome this difficulty, we first considered both the required temporal and spatial coherence of incident X-rays for cavity resonance in relation to the effective crystal gaps d, i.e., the longitudinal coherence length $\ell_L = [\lambda E/\Delta E] \geq 2d$ and the crystal size $\ell_C \geq \ell_T$ (the transverse coherence length), where d is the sum of the thickness and gap of the crystal plate. We then designed the following experiments [3]: We prepared several two- and multi-plate crystal cavities of a plate thickness ranging from 25 to 150 μm and a crystal-gap of 40-150 μm from a four-inch Si (001) crystal wafer using the microelectronic lithography process. The size of the crystal plates is 800 μm wide and 200 μm high. Cavities with plate numbers up to 8 were manufactured. To fulfill the coherence conditions for cavity resonance, a Si (111) double-crystal and a four-crystal ultrahigh resolution monochromators used yield the energy resolution $\Delta E = 2.5 \times 10^{-8}$ at 14.4388 keV, i.e., $\Delta E = 0.36$ meV [4].

The experiment was carried out at the Taiwan undulator beamline **BL12XU**. The incident X-rays, monochromatized by the monochromators mentioned hit at one of the cavities, which was sit at the center of an eight-circle diffractometer. The diffractometer allowed the crystal cavity to be rotated vertically and horizontally by adjusting the $\Delta\theta_v$ and $\Delta\theta_h$ angles, respectively, with a minimum step of 0.0005º. Energy scans were performed by tuning together the Bragg angles of the fourth-crystal monochromator with a minimum step of 0.005 arcsecond, equivalent to 58.548 μeV in energy.

The (12 4 0) reflection of silicon was used as the back diffraction. Both the forward-transmitted (000) and the back-reflected (12 4 0) beams were monitored by an ion chamber and a pin-diode detector, respectively. A 24-beam simultaneous diffraction, including (000) and (12 4 0), took place, because of the high energy X-rays used and the symmetry of the silicon crystal. These 24 diffractions belong to 9 sets of coplanar reflections of the same zone axes. Figure 1 shows the $\mu\theta_v$ -scans of (a) the forward-transmitted (000) beam and (b) the back-reflected (12 4 0) beam of the two-plate cavity at $\Delta E = 9$ meV off the exact

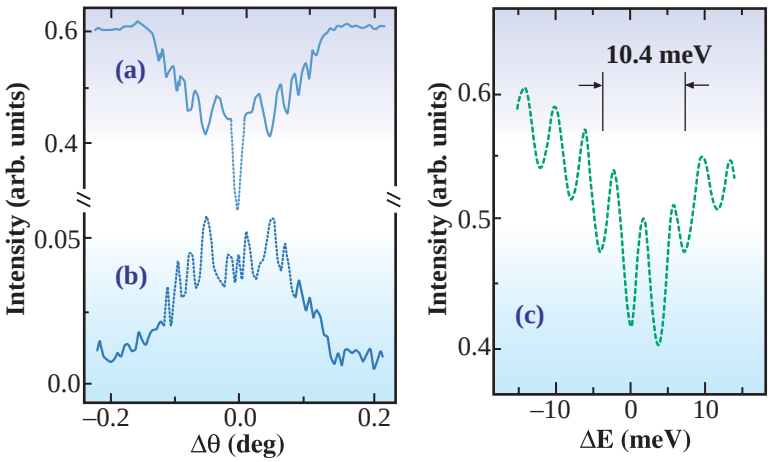

Fig. 1. Angle-scans of the forward-transmitted **(a)** and back-reflected beams **(b)**; **(c)** Energy scan [3].

energy, 14.4388 keV, and 0.002º per step for a two-plate cavity of 70 μm thickness with a 100 μm gap. Figure 1(c) shows the energy scan. The region of broad width shown in Fig. 1(a) is the total reflection region, which corresponds to the energy gap in energy scans. The intensity dip in the middle of Fig. 1(a) results from the 24-beam diffraction. Interference fringes due to cavity resonance are clearly seen. The expected cavity resonance fringes in the energy-scans are also observed. The energy range about 10.4 meV is the energy gap (Fig. 1(c)). The fringe spacing, namely the E_d is about 3.60 meV, in agreement with the calculated value 3.65 meV from the relation $E_d = hc/2d$, where E_d is the so-called free spectral range of a cavity.

Figure 2 shows the intensity distributions of resonance interference at ΔE = 12 meV off the exact photon energy: (a) Angular $\Delta\theta_v - \Delta\theta_h$ distribution of the transmitted (000) intensity I_T of the two-plate crystal cavity in a linear scale; (b) Two-dimensional contour map of Fig. 2(a); (c) Calculated map of (b) without angle and energy integrations. The three-dimensional plot, Fig. 2(a), reveals the interference intensity distribution. The two-dimensional fringes in Fig. 2(b) show concentric rings of alternating maxima and minima and the straight lines are due to the coplanar diffractions denoted as Lines L1 - L9.

In summary, we have realized Fabry-Perot resonators for hard X-rays. Interference fringes due to crystal cavity resonance are clearly observed.

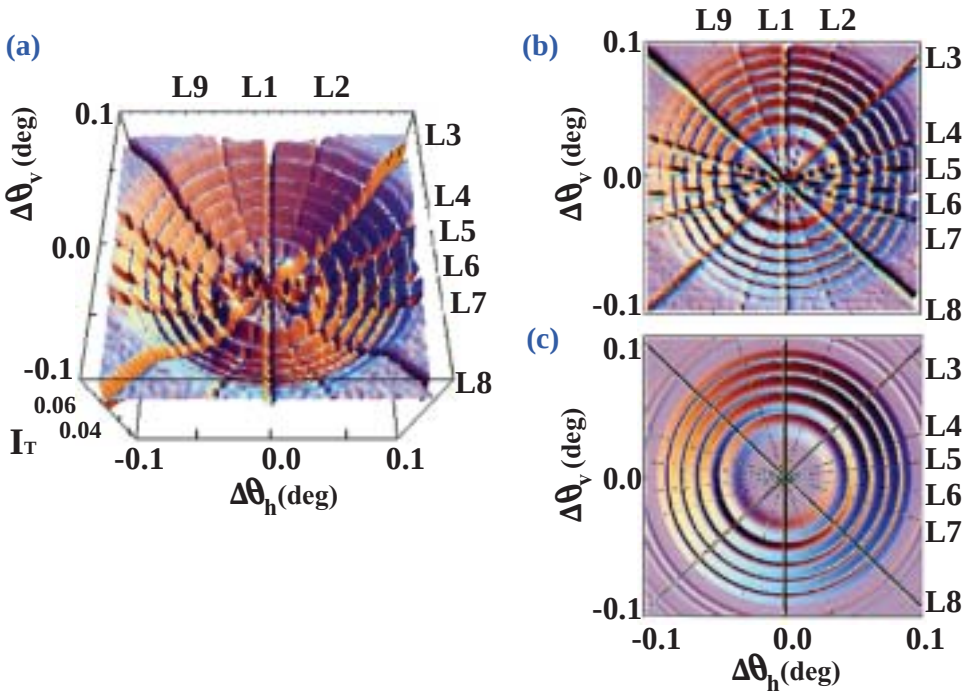

Fig. 2. Intensity distributions of resonance interference: **(a)** three-dimensional, **(b)** two-dimensional, and **(c)** calculated two-dimensional maps [3].

Shih-Lin Chang[a,b,*], Yuriy Stetsko[b] and Mau-Tsu Tang[b]

[a] Department of Physics, National Tsing Hua University, Taiwan
[b] National Synchrotron Radiation Research Center

*E-mail: slchang@phy.nthu.edu.tw

References

[1] W. L. Bond *et al.*: Appl. Phys. Lett. **10** (1967) 216.
[2] K. D. Liss *et al.*: Nature **404** (2000) 371.
[3] *S.-L. Chang, Y.P. Stetsko, M.-T. Tang, Y.-R. Lee, W.-H. Sun, M. Yabashi and T. Ishikawa: Phys. Rev. Lett.* ***94*** *(2005) 174801.*
[4] M. Yabashi *et al.*: Rev. Sci. Instrum. **72** (2001) 4080.

Backscattering Topography of Large, Nearly Perfect Quartz Crystals

Many synchrotron radiation beamlines that produce hard X-rays use optical elements made from perfect crystals of silicon. However, silicon is limited in certain ways by its highly symmetric cubic lattice structure. Quartz, with a non-centrosymmetric trigonal lattice, has shown potential, especially for inelastic X-ray scattering (IXS) energy analyzers. These must provide not only good energy resolution, but also large angular acceptance and large area for efficient collection of the low and diffuse scattered flux. Large perfect silicon wafers oriented to Bragg reflections near backscattering ($\theta_B \approx 90^\circ$) have fulfilled these needs, but large perfect quartz wafers, if available, would make IXS feasible under a wider range of conditions [1]. While no silicon backscattering reflection below 12 keV offers a bandpass below 9 meV, quartz can go as low as 1 meV, making phonon measurements feasible at lower energies. Quartz also offers backscattering reflections at 184 distinct energies for photons of 5-12 keV, while silicon offers them at only 22. Absorption and emission spectroscopy and nuclear resonant scattering, which require a photon beam of specific energy, benefit from this.

Large-area measurements are needed to find out whether obtainable quartz wafers are indeed good enough. Backscattering from quartz has been investigated with a small-area beam [2], but not with the large-area beams needed for a topograph. Non-backscattering topographic images of quartz also exist [3] but may be outdated and do not show whether the energy resolution requirements for IXS are fulfilled. Therefore, both topographic images and reflectivity scans of two quartz wafers have been made using the (7 -4 -3 4) reflection of 9.979 keV photons (θ_B = 89.77°, Darwin width 2.0 meV). These "A grade" wafers are 40 mm in diameter, 2.0 mm thick, and are polished on both sides.

The measurements were performed at beamline **BL29XU**. A high-resolution monochromator with a calculated bandpass of 1.91 meV, built using the design in [4], was placed downstream of the inbuilt high-heat load monochromator, but still near the source.

The quartz wafers were placed in the 1-km hutch because the beam size increases many times over this distance. Reflectivity curves as a function of photon energy were made using an APD; topographic images were recorded on a CCD camera using an 8 × 8 mm^2 beam.

The image in Fig. 1(a) is a composition of topographs covering most of the first quartz wafer. It shows both a distinctly reduced reflectivity in the lower left-hand side of the wafer and defects of smaller area scattered throughout the wafer. The graph in Fig. 1(b) shows two curves of reflectivity *versus* photon energy that

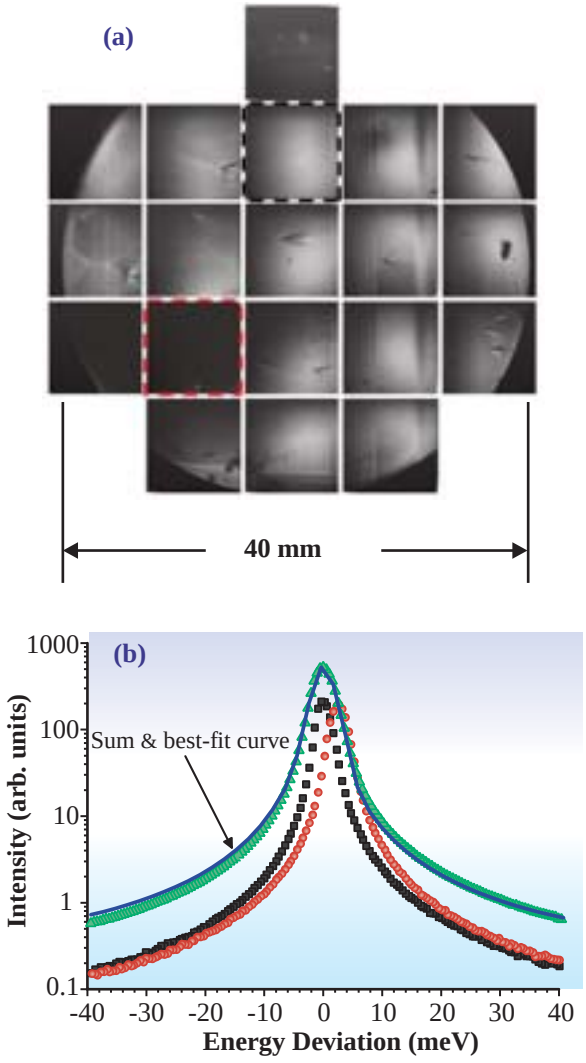

Fig. 1. **(a)** Topograph of quartz wafer. **(b)** Comparison of energy curves in two regions (outlined with corresponding colors at the top) and sum of energy curves over all regions. The best-fit curve to the sum is a Gaussian of FWHM 4.17 meV centered at +0.39 meV plus a Lorentzian of FWHM 3.64 meV centered at -0.48 meV. The peak amplitude of the Gaussian is 0.994 times that of the Lorentzian.

were measured at each region of the wafer. The peak widths of these curves lay between 2.9 and 4.0 meV. The reflectivity curves of the top and lower left-hand regions of the wafer are similar but are shifted by 2.5 meV, indicating a lattice spacing variation of 2.5 meV / 9.979 keV = 0.25 ppm. The same graph also shows the sum of the reflectivity curves over all the imaged regions. Properly accounting for temperature drifts, one finds a FWHM of 4.0 meV, which includes the resolution function of the high-resolution monochromator since no deconvolution was performed.

Figure 2 shows the 1 × 1 mm^2 area around one small defect of the second wafer with a defect-free region of the same wafer. The weaker and broader reflectivity curve at the defective region shows that its lattice structure is strongly distorted. The observed area density of these small defects was 2 per cm^2 in the first wafer and 5 per cm^2 in the second wafer.

In summary, nearly perfect large-area quartz wafers are commercially available. Low defect concentrations are found even over areas of 10 cm^2, while reflectivity curves have shown a bandpass of 4.0 meV. Quartz thus shows great promise as a material for IXS analyzers and other X-ray optical elements.

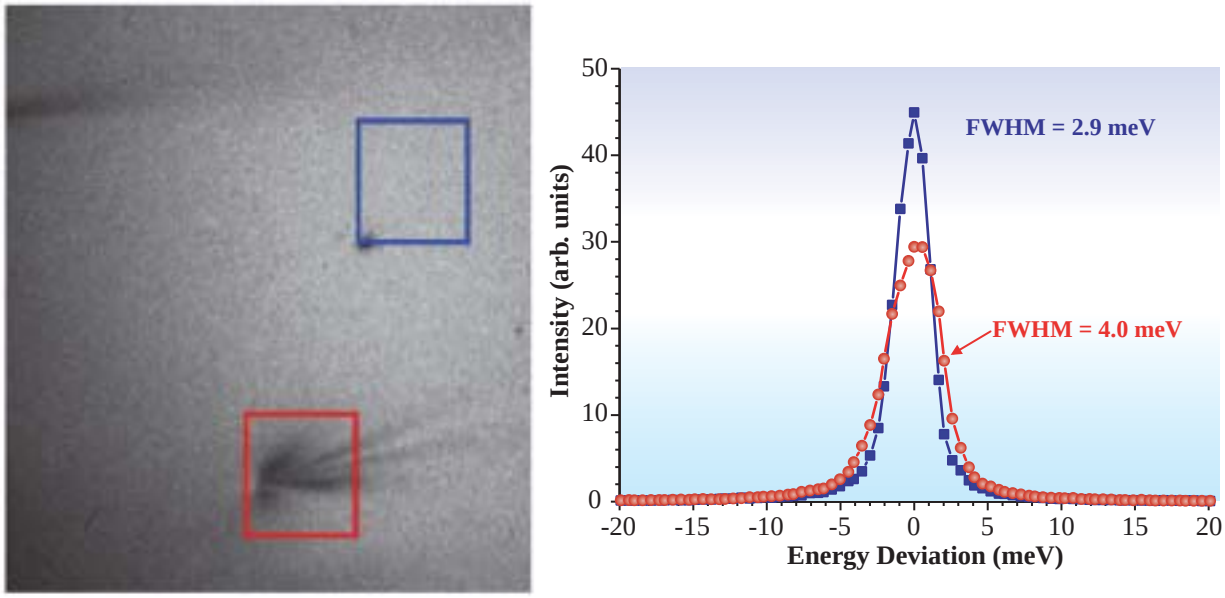

Fig. 2. Comparison of defective and defect-free areas of quartz wafer. For details, see text.

John P. Sutter[a,*,†], Alfred Q.R. Baron[b] and Tetsuya Ishikawa[a,b]

[a] SPring-8 / JASRI
[b] SPring-8 / RIKEN

*E-mail: John.Sutter@diamond.ac.uk

[†] Present address: Diamond Light Source Ltd, Rutherford Appleton Laboratory, UK

References

[1] *J.P. Sutter, A.Q.R. Baron, T. Ishikawa and H. Yamazaki: J. Phys. Chem. Solids* ***66*** *(2005) 2306.*
[2] Y. Imai *et al.*: SPring-8 User Experiment Report No. 8 (2001) p. 70; No. 9 (2002) p. 74.
[3] J. Yoshimura *et al.*: J. Cryst. Growth **46** (1979) 691.
[4] M. Yabashi *et al.*: Rev. Sci. Instrum. **72** (2001) 4080.

Photoelectron Holography: Maximum Entropy Reconstruction Scheme

Holography utilizing the wave nature of electrons was originally proposed by Gabor [1] for the electron microscope. In his technique, a point source, i.e., a highly focused electron beam is utilized, and the size of the point source correlates with spatial resolution. Sz_ke pointed out that atomic resolution holography can be realized by utilizing a wave emitted from an atom [2] (characteristic X-ray, photoelectron or Auger electron), which is an atomic scale point source. A schematic view of photoelectron holography is shown in Fig. 1. The emitted wave is partially scattered by the potentials of surrounding atoms, and an interference pattern between the unperturbed and scattered waves is observed in the angular distribution. The pattern is interpreted as a hologram recording the three-dimensional atomic arrangement. It has been expected that the local atomic structure around the target atomic site can be directly obtained from the hologram, since an emitter atom is selective by choosing the photoelectron energy characteristic to the element and chemical state. Barton proposed a numerical algorithm on the basis of the Fourier transform [3] to reconstruct a three-dimensional atomic arrangement from an electron hologram. However, the image from an actual single-energy hologram was unclear, due to the forward scattering effect, i.e., strong intensity of forward focusing peak and the frequency shift around the forward scattering region prevent the simple Fourier analysis. To avoid the effect of forward focusing peaks, many techniques have been developed such as the multi-energy method [4], and differential hologram [5] among others. However, the reconstruction from a single-energy hologram has been quite difficult.

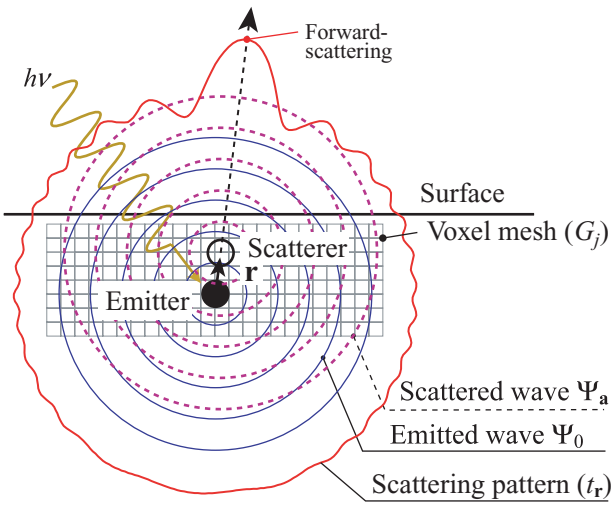

Fig. 1. Schematic view of photoelectron holography.

We have proposed a new algorithm using the maximum entropy method to single-energy photoelectron holography. It is composed of the scattering pattern matrix and the maximum entropy method [6,7]. The idea is quite simple. We have defined a new mathematical expression of the hologram as

$$\chi(\vec{k}_i) \equiv I(\vec{k}_i) - |\Psi_0(\vec{k}_i)|^2,$$
$$\cong \sum_j t_{\vec{a}_j}(\vec{k}_i) \cdot G_j$$

where $\chi(\vec{k})$ is the hologram function, $I(\vec{k}_i)$ is the measured intensity, $\Psi_0(\vec{k}_i)$ and is the photoelectron wavefunction from the emitter (reference wave). $t_{\vec{a}_j}$ is a scattering pattern caused by a scatterer atom located on $\vec{a}_j$. Here, the real space voxel is defined as **G**, and its element located on $\vec{a}_j$ is described as G_j. When the elements G_j located on scatterer positions are set to $1/|a_j|$ and the others are set to 0, this formula gives the hologram pattern. This equation can be interpreted as a simple linear simultaneous equation.

Therefore, to obtain the atomic arrangement from the hologram, it is necessary to solve this linear simultaneous equation. However, it is difficult to solve it using commonly used gradient methods, because the amount of the unknown elements G_j is larger than that of the linear equations. We have found that the maximum entropy method of iterative scaling algorithm is effective for solving this equation.

To demonstrate the effectiveness of the algorithm, we measured a photoelectron hologram of Si(001) using a two-dimensional display type analyzer at beamline **BL25SU** [8]. The unique analyzer can measure an angular distribution of ±60° at once. Therefore, it can measure the photoelectron hologram within 1 sec ~ several minutes, which is quite fast. The kinetic energy of photoelectron from Si 2*p* core level was set to 800 eV. The obtained hologram is

shown in Fig. 2. Although symmetrical operation has not been applied to it, four-fold symmetry is clearly seen in the figure.

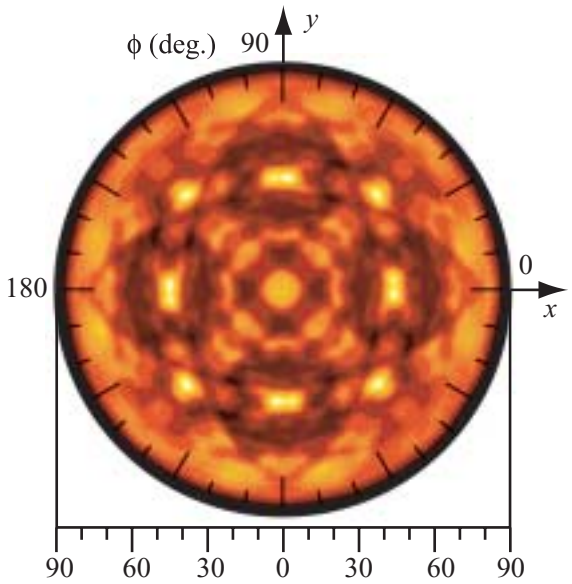

Fig. 2. Photoelectron hologram of Si(001). The initial state is Si 2*p* and the kinetic energy is 800 eV.

We applied the simple Barton algorithm (Fourier transform) and our algorithm, which are shown in Fig. 3 and Fig. 4, respectively. The simple Barton algorithm cannot reconstruct atomic image. On the other hand, the image using our algorithm is quite clear. This indicates the effectiveness of the new algorithm.

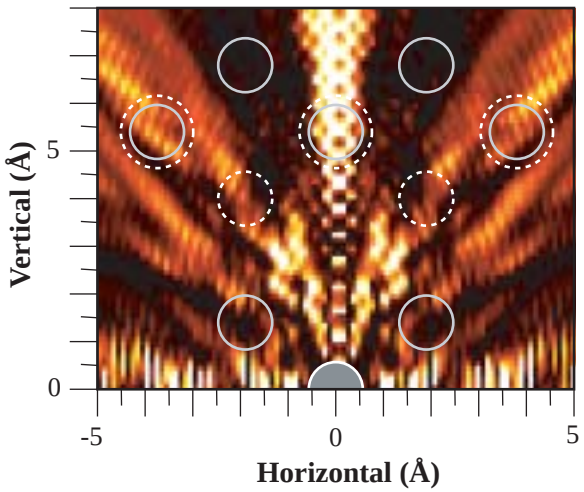

Fig. 3. Real space image of (110) plane reconstructed by simple Barton algorithm.

The combination of this algorithm and 2D-PES enables us to measure local structure around a target atomic site in real-time. This algorithm is expected to become a powerful tool for measuring atomic arrangement around a target atom.

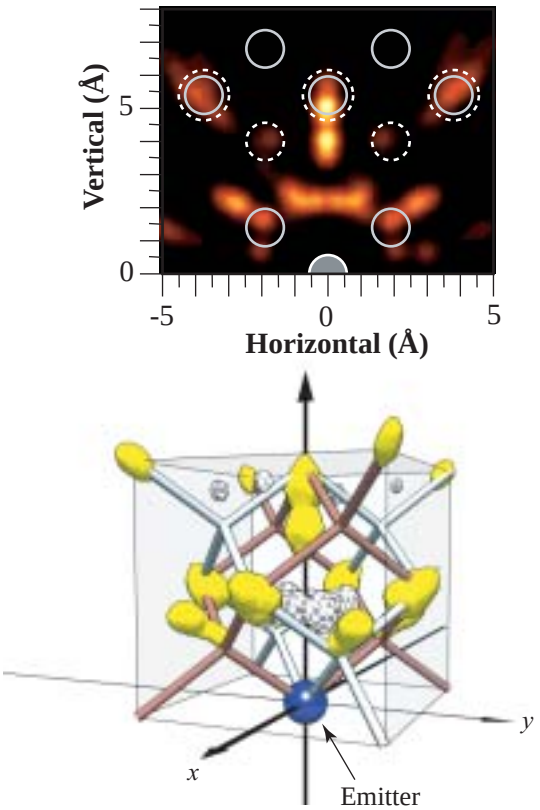

Fig. 4. Real space image of (110) plane and three-dimensional image reconstructed by new algorithm.

T. Matsushita

SPring-8 / JASRI

E-mail: matsusita@spring8.or.jp

References

[1] D. Gabor: Nature **161** (1948) 777.
[2] A. Szöke: AIP Conf. Proc. No. 147 (1986) 361.
[3] J.J. Barton: Phys. Rev. Lett. **61** (1988) 1356.
[4] J.J. Barton: Phys. Rev. Lett. **67** (1991) 3106.
[5] S. Omori *et al.*: Phys. Rev. Lett. **88** (2002) 055504.
[6] T. Matsushita *et al.*: Europhys. Lett. **65** (2004) 207.
[7] *T. Matsushita, A. Yoshigoe and A. Agui: Europhys. Lett.* ***71*** *(2005) 597.*
[8] M. Kotsugi *et al.*: Nucl. Instrum. Meth. Phys. Res. A **467-468** (2001) 1493.

Phase Tomography by X-ray Talbot Interferometry

X-ray phase imaging is attractive for the observation of weakly absorbing materials, such as soft materials and biological tissues. In the past decade, several techniques of X-ray phase imaging were reported and demonstrated [1]. Recently, we have developed an X-ray Talbot interferometer for novel X-ray phase imaging, including phase tomography. This method is unique in that transmission gratings are used to generate differential phase contrast (Fig. 1). Two gratings are aligned along the optical axis with a specific distance determined by the X-ray wavelength λ and the grating pitch *d*. The influence of refraction on the sample placed in front of the first grating is observed just behind the second grating. The detailed principle of the contrast generation is described in Refs. [2,3].

A critical key for realizing X-ray Talbot interferometry is the fabrication of an amplitude grating that is used as the second grating. However, it is not straightforward because a tall stripe pattern must be formed so that X-rays are fully blocked by the pattern. Gold gratings were therefore fabricated by X-ray lithography, which is advantageous in forming tall patterns, and gold electroplating, using the LIGA beamline of NewSUBARU, SPring-8. A SEM (scanning electron microscope) image of the grating is shown in Fig. 1. The pitch and pattern height were 8 μm and 30 μm, respectively.

Through the quantitative measurement of the differential phase shift by the sample, extremely high-sensitive three-dimensional imaging, that is, X-ray phase tomography, is attainable by X-ray Talbot interferometry [3]. We demonstrated this with biological samples using monochromatic undulator X-rays at beamline **BL20XU**. Figure 2 shows a rabbit liver tissue with VX2 cancer observed by X-ray phase tomography using a CCD-based X-ray image detector whose effective pixel size was 3.14 μm [4]. The cancerous lesion is depicted with a darker gray level than the surrounding normal liver tissue. The bright islands in the cancerous lesion indicate necrosis. The spatial resolution of this image was evaluated to be 15 μm. The phase tomogram approximately maps the difference in mass density, and the detection limit of the density deviation was estimated to be 1.3 mg/cm^3 from noise in the tomogram. Another observation result that was obtained for a mouse tail [4] is shown in Fig. 3. Bones and soft tissues, such as skin,

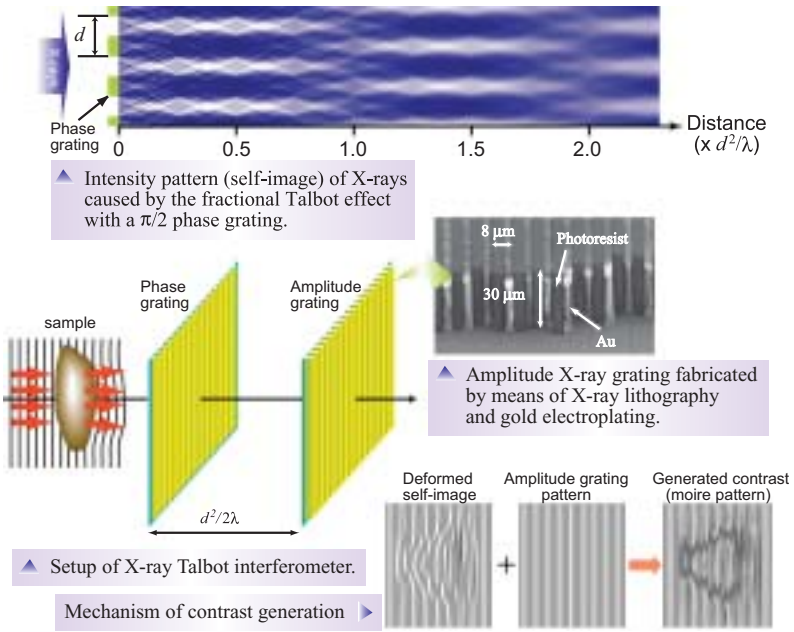

Fig. 1. Illustration showing principle of X-ray Talbot interferometry. The pattern of a phase grating is converted into an intensity pattern (self-image) by the fractional Talbot effect at a specific position from the grating. The self-image is deformed correspondingly to the refraction at the sample. A moiré pattern that involves information of the refraction is observed by the superposition of the deformed self-image and an amplitude grating.

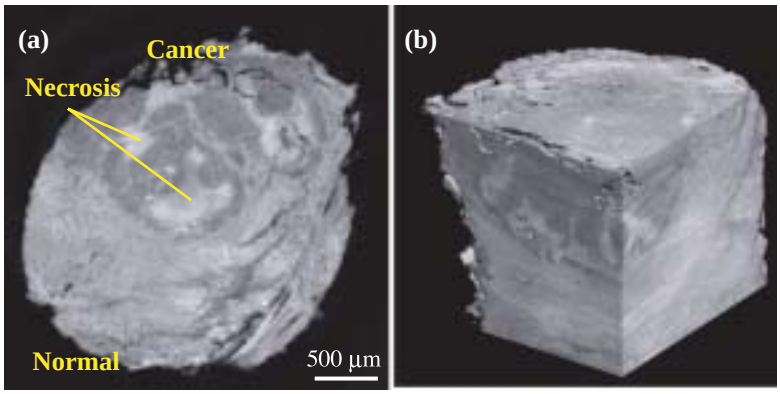

Fig. 2. Phase tomogram of rabbit liver tissue with VX2 cancer. The cancerous lesion is clearly differentiated from the surrounding normal tissue, and necrosis is depicted as bright islands in the cancerous lesion.

muscle, ligament, and intervertebral disc (cartilage), are depicted in the same view although some artifacts particularly caused by the bones remain. The images in Fig. 2 and Fig. 3 were measured with 12.4-keV and 17.7-keV X-rays, respectively, and the Talbot interferometer functioned up to 31 keV, which was confirmed by observing the sample identical to that in Fig. 3. The samples were courtesy of Drs. T. Takeda and J. Wu of the University of Tsukuba.

Three-dimensional observation by X-ray phase tomography is thus feasible for biological samples. Here, it should be emphasized that the implementation of X-ray Talbot interferometry outside synchrotron radiation facilities may be possible in the future. This is because a cone beam with a broad energy band width is available in principle owing to the use of gratings. It is also pointed out that this interferometer is much less sensitive to vibration than the Bonse-Hart crystal X-ray interferometer, and therefore it is easy to operate. Thus, imaging applications not only with synchrotron radiation as presented here but also with a compact X-ray source are expected for future practical application such as mammography, provided that a grating with a thicker pattern for higher-energy X-rays than the grating in the present study is fabricated with a wider effective area.

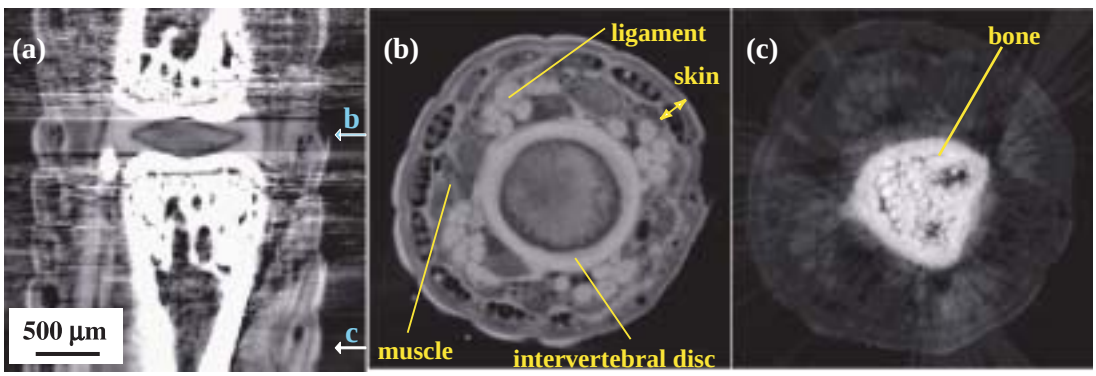

Fig. 3. Phase tomogram of mouse tail. The positions of axial images **(b)** and **(c)** are indicated by the arrows in the sagittal image **(a)**. Bones and soft tissues, such as skin, muscle, ligament, and intervertebral disc (cartilage), are depicted. The grayscale range of **(c)** is 3.5 times wider than that of **(b)**.

Atsushi Momose[a,*], Wataru Yashiro[a] and Tadashi Hattori[b]

[a] Graduate School of Frontier Sciences, The University of Tokyo
[b] Laboratory of Advanced Science and Technology for Industry, University of Hyogo

*E-mail: momose@exp.t.u-tokyo.ac.jp

References

[1] A. Momose: Jpn. J. Appl. Phys. **44** (2005) 6355.
[2] A. Momose *et al.*: Jpn. J. Appl. Phys. **42** (2003) L866.
[3] A. Momose *et al.*: SPIE Proc. **5535** (2004) 352.
[4] *A. Momose, W. Yashiro, Y. Takeda, Y. Suzuki and T. Hattori: Jpn. J. Appl. Phys.* ***45*** *(2006) 5254.*

Development of Astronomical Hard X-ray Telescope and Its Characterization using High-brilliance Synchrotron Radiation Facility

It is usually thought that astronomers observe the sky with high resolution, much finer than our naked eyes. Unfortunately, it is not the case in some span of electromagnetic spectrum, where one cannot even tell the difference between the moon and a star, because of a lack of spatial resolution. In our research, we aim to bring optics into the hard X-ray spectrum region, where no one has ever observed the Universe with high spatial resolution. The key technologies of "hard X-ray telescope" are multilayer-supermirror hard X-ray reflector and multi-nested high-efficient grazing incidence optics.

An X-ray telescope utilizes grazing incidence optics called Wolter-I system. The principle of X-ray reflection is the total external reflection that occurs only at grazing incidence. Since the late 1970s, many X-ray telescopes have been installed on orbiting satellites and facilitated scientific achievements. These telescopes were, however, only sensitive below 10 keV, due to the practical limit of the use of total external reflection in terms of aperture efficiency and field of view.

Instead, Bragg's reflection by multilayer is the effective principle of reflection beyond 10 keV. When the periodic length of a multilayer is graded in the depth direction, the so-called "supermirror," Bragg's condition is satisfied in a wide range of X-ray energies at a fixed angle. Wide energy and angular response are key requirements for astronomical instruments. Developments have been underway since the mid-1990s by several research groups in the world, as one of key technologies for the next generation X-ray observatories. See Yamashita *et al.* [1] for general reviews, as well as some of our initial works.

We chose platinum-carbon combination as the multilayer supermirror, because of platinum's high-electron number density and carbon's sharp interface against platinum. Multi-nested thin-foil optics is employed to achieve high efficiency. Technical details have been reported in previous papers [1-3]. Figure 1 shows a photograph of the hard X-ray telescope thus fabricated. The aperture diameter, height and focal length are 40 cm, 20 cm and 8 m, respectively. 255 pairs of optics are nested coaxially and con-focally in the telescope housing. About 2000 segmented reflectors are used for one telescope.

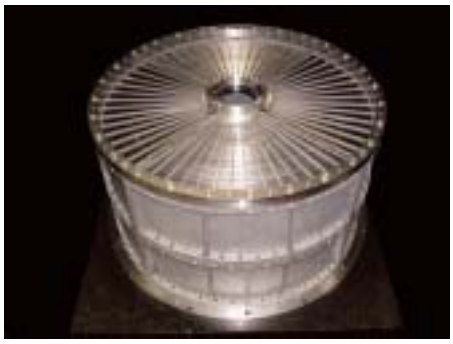

Fig. 1. Multilayer supermirror hard X-ray telescope.

The telescope was first characterized at beamline **BL20B2**. This characterization part of the study is quite important. Otherwise, telescope performance will remain unknown and data observed from the sky will remain difficult to interpreted. In addition to synchrotron light brightness, BL20B2 has a 200-m-long transport tube. Therefore, large-sized and less divergent beam is available, which is a crucial requirement for measuring large aperture optics.

Figure 2 shows an example of an X-ray image focused by our hard X-ray telescope and measured using a CCD-based hard X-ray imager at 30 keV. Such measurement was performed with 10 to 80 keV X-rays. The measurement showed that hard X-rays are successfully focused, with a quality of 2.5 arcmin in terms of Half Power Diameter. The number is almost the same as that measured at 8 keV prior to this experiment. This is an experimental proof that the same quality of angular resolution as in the soft X-ray region is attained by our method.

The high brightness of the beam at SPring-8 enables us to perform microscopic measurement of the telescope. It is important to "diagnose" the telescope and not just to "characterize" it to know how current performance is established, or what prevents the telescope from performing better than its present performance.

Figure 3 is what we call as "local brightness distribution" measured at various energies. We divide the telescope aperture into about 2000 local areas in r-φ plane, and each area is illuminated by X-rays. Focused images are measured for each area. The color coding of each figure indicates an X-ray flux obtained from each measurement. The wedge-shaped dark areas correspond to boundaries between neighboring mirror segments (quadrants). The radial slope of flux is observed, as well as the dependency of its steepness on energy. They agree well with the angular and energy reflectivities of supermirrors. Segment-to-segment

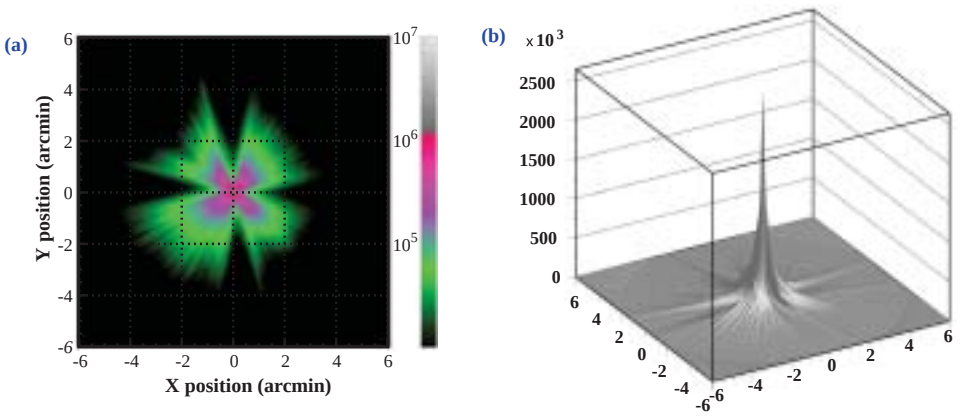

Fig. 2. Focused image of hard X-ray telescope at 30 keV. **(a)** Two-dimensional expression with color coding in log scale. **(b)** Three-dimensional expression. Horizontal axes are in arcmin.

difference comes from the difference of supermirror designs. These verifications are so-called "function check." In terms of "diagnostics," any local anomalies of brightness, for example, dark lanes in the upper-left and lower-right quadrants as seen in the figures, are indicative of reflectors not functioning well in these areas. Information obtained is enormous, and is used for understanding and improving the telescope. These functions are brought about by the bright light source, and cannot be totally attained without bright synchrotron light and a beamline with long baseline. Recent results are summarized in the study of Ogasaka *et al.* [4].

The telescope, the first of its kind when launched on the stratospheric balloon payload for its first flight in 2001, and still the largest in effective area as a single unit, was dedicated for successful scientific flight observation in 2004 [5]. The experiment was carried out by US-Japan international collaboration (InFOCμS project [6]). In this flight, we observed multiple astronomical objects from nearby black holes in our Milky Way galaxy, to distant (about one billion light years away) cluster of galaxies that harbor tens or sometimes even hundreds of galaxies like our own. Data analysis is underway, and part of the data confirmed the function of our telescope. Although we have many steps to go before we can establish truly epoch-making scientific results, a new window is now open in the hard X-ray spectrum region.

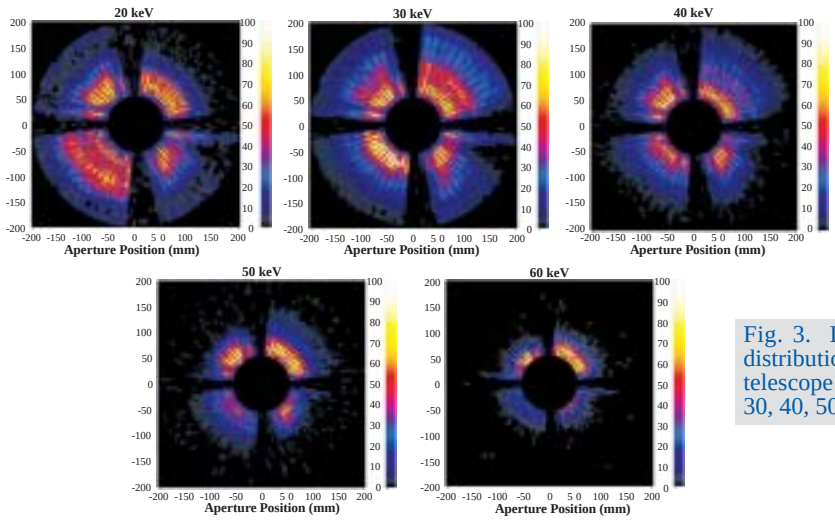

Fig. 3. Local brightness distribution of hard X-ray telescope measured at 20, 30, 40, 50 and 60 keV.

Yasushi Ogasaka*, Keisuke Tamura and Ryo Shibata

Department of Physics, Nagoya University

*E-mail: ogasaka@u.phys.nagoya-u.ac.jp

References

[1] K. Yamashita *et al.*: Applied Optics **37** (1998) 8067.
[2] T. Okajima *et al.*: Applied Optics **41** (2002) 5417.
[3] F. Berendse *et al.*: Applied Optics **42** (2003) 1856.
[4] *Y. Ogasaka, R. Shibata, K. Tamura, A. Furuzawa, R. Takahashi, T. Miyazawa, M. Sakashita, C. Sakai, K. Shimoda, N. Yamada, Y. Fukaya, H. Kunieda, K. Yamashita, E. Miyata, K. Uesugi and Y. Suzuki: Proc. SPIE* ***5900*** *(2005) 5900F.*
[5] *Y. Ogasaka, J. Tueller, K. Yamashita, P. Serlemitsos, R. Shibata, K. Tamura, A. Furuzawa, T. Miyazawa, R. Takahashi, M. Sakashita, K. Shimoda, Y. Tawara, H. Kunieda, T. Okajima, H. Krimm, S. Barthelmy, Y. Soong, K.-W. Chan, S. Owens, M. Rex, E. Chapin, M. Devlin: Proc. SPIE* ***5900*** *(2005) 5900R.*
[6] http://infocus.gsfc.nasa.gov

Development of NanoXAFS: New Use of Photoelectron Emission Microscope (PEEM) in Connection with Hard X-ray

Over the last decade, the photoelectron emission microscope (PEEM) has been successfully developed for surface science and related nanotechnologies. PEEM is a type of electron microscope that can magnify spatial information about secondary electrons photoemitted from a surface with the lateral resolution power of several ten nanometers. Its application has been particularly carried out in combination with soft X-ray. Here, we report a new use of PEEM in connection with hard X-ray. This technique offers two possible information: one is local structure analysis at the arbitrary pixel on an observed image; another is photoelectron information from the buried layers. We are developing the "NanoXAFS" technique for local structure analysis [1,2]. The concept of this measurement technique is entirely different from conventional spatially resolving X-ray absorption fine structure (XAFS) techniques established using the Fresnel's Zone plate or microbeam because the NanoXAFS technique does not need a focused X-ray beam and all the pixels in the observed image are acquired simultaneously.

X-ray absorption intensity is proportional to the intensity of a secondary electron photoemitted from the surface, and spatial resolved information of the secondary electron is projected on the screen of the PEEM analyzer; therefore, the intensity of each pixel in the observed image is proportional to the X-ray absorption intensity. XAFS represents element-specific information about electronic states, and the oscillatory signal in an extended range provides information about the local environment around the absorbing atom [3]. Furthermore, the excitation by hard X-rays creates high-energy Auger electrons with long penetration ranges. Thus, the combination of PEEM and hard X-ray provides spatial resolved information for the XY direction and information from the buried layers for the Z direction. Experiments were carried out at beamline **BL39XU**. Hard X-ray synchrotron radiation is available in a range of photon energies from 5 to 37 keV. PEEM SPECTOR (Elmitec, GmbH) was installed inside the experimental hutch.

We show successful examples measured on Gibeon iron meteorite at first. Gibeon iron meteorite exhibits a characteristic micrometer-sized structure known as the Widmanstätten structure that is considered a mixed multi-crystal composed of bcc-FeNi and fcc-FeNi. NanoXAFS images were continuously recorded by scanning the photon energy over the Fe and Ni *K*-absorption edges. The normalized spatial

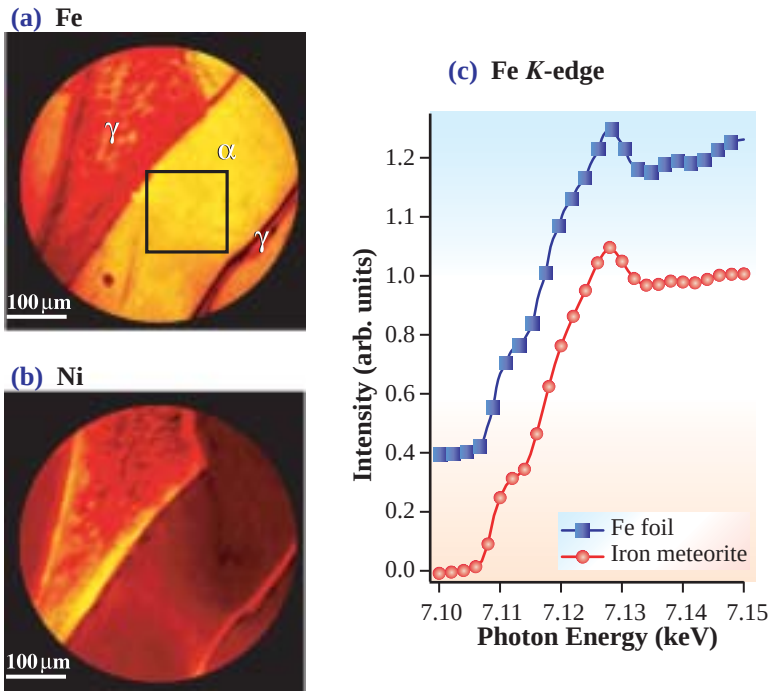

Fig. 1. Spatial distribution of XAS intensity in Gibeon iron meteorite, **(a)** normalized image for Fe composition **(b)** normalized image for Ni composition. **(c)** Averaged XAS intensity in iron meteorite (red line with circle) extracted from squared region in **(a)**. Fe absorption spectrum on reference specimen of Fe foil (blue line with square).

distributions for Fe and Ni compositions are shown in Figs. 1(a) and 1(b), respectively. The Ni distribution in a thick γ lamella is spatially non-homogeneous and rapidly increases when approaching the interface. Thin γ lamellae and uneven thick γ lamellae are separated by thick γ lamellae. This is likely the result of the interatomic diffusion of Fe and Ni in the core of a mother body when an asteroid has been cooled at an extremely slow rate. The averaged XAFS spectrum for Fe extracted from the square in Fig. 1(a) is shown in Fig. 1(c) as a red line with filled circles, and the blue line with filled squares is obtained from a reference specimen of the bcc-Fe foil. The sharp crest is recognized at the absorption edge of the iron meteorite. However, the spectrum of the synthetic bcc-Fe foil also shows a similar behavior. The shape of the crest in the synthetic Fe_xNi_{1-x} system is reported to commonly show a single peak when the crystallographic structure takes bcc below 25 at.% Ni [4]. Therefore, the result of the iron meteorite suggests that the γ lamella takes the bcc structure with spatially homogeneous composition.

Next, we evaluate the probing depth of this method. We used a patterned Co thin film on a Si substrate etchted by a focused ion beam (FIB). Figure 2(a) shows the schematic view of the multilayer of Pt/Co/Au/Cr deposited on the Si substrate. The thicknesses of the layers were 0.5, 50, 100 and 1 nm. Figure 2(b) shows the observed image at photon energy of 11.85 keV. The two dark square regions correspond to the Co patterns. Figure 2(c) shows the extracted NanoXAFS spectra over the Au L_{III}-edge from area 1 and area 2 marked by squares in Fig. 2(b). The former exhibits the signals from the bare Au layer, and the latter from the Au layer under the Co overlayer. We clearly see Au signals under the 50-nm-thick Co layer. The magnitude of the edge jump for the Au layer under the Co overlayer is 28% of that for the bare Au layer. To quantitatively discuss the probing depth, we used the calculation formula proposed by Erbil *et al.* [5]. This method revealed that the probing depth for total electron yield with hard X-rays is determined primarily by the penetration ranges of high-energy Auger electrons. Our calculation shows that the edge jump at Au L_{III} is 29% of that for the bare Au layer. This value is in excellent agreement with our experimental result of 28%. Using this formula, the maximum probing depth for NanoXAFS is concluded to be ten times deeper than that for conventional PEEM with soft X-ray.

Consequently, we indicate several results obtained by NanoXAFS and it has a potential to treat a wide variety of materials in surface science, nanotechnology and planetary science. More experience will be necessary to perfect NanoXAFS.

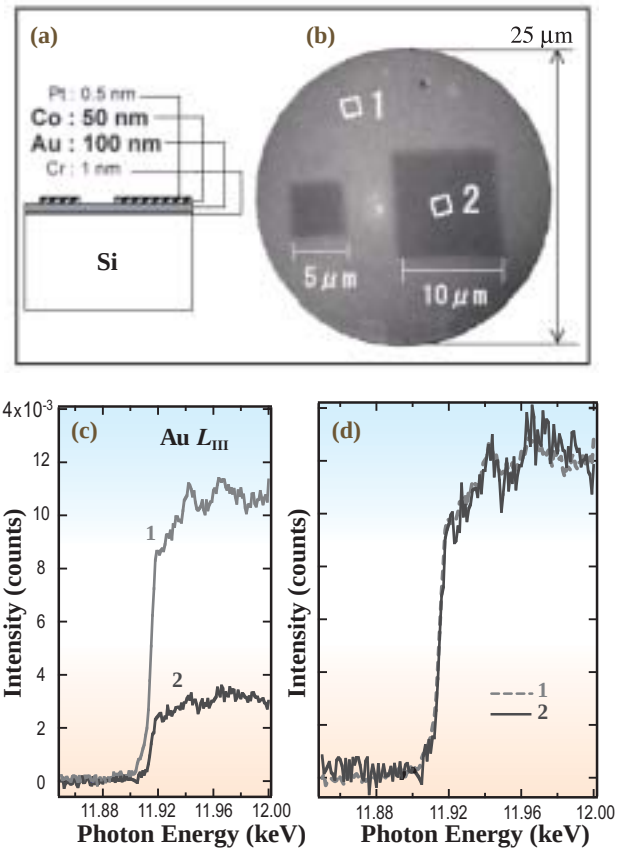

Fig. 2. **(a)** Schematic illustration of sample, showing its stacking sequence. **(b)** PEEM image of sample. The field of view is 25 μm. The sizes of the dots are 5 and 10 μm. **(c)** Total yield spectra near Au L_{III} edge of areas 1 and 2 marked with squares in **(b)**. **(d)** The same spectra as **(c)** normalized to integrated intensities.

M. Kotsugi[a,*], T. Wakita[b] and K. Ono[c]

[a] Hiroshima Synchrotron Radiation Center, Hiroshima University
[b] SPring-8 / JASRI
[c] High Energy Acceleration Research Organization

*E-mail: kotsugi@hiroshima-u.ac.jp

References

[1] T. Wakita *et al.*: Jpn. J. Appl. Phys. **45** (2006) 1886.
[2] *M. Kotsugi, T. Wakita, T. Taniuchi, K. Ono, M. Suzuki, N. Kawamura, M. Takagaki, M. Taniguchi, K. Kobayashi, M. Oshima, N. Ishimatsu and H. Maruyama: e-J. Surf. Sci. Nanotech. **4** (2006) 490.*
[3] J. Stöhr: NEXAFS Spectroscopy, Springer Verlag (Berlin).
[4] H. Sakurai *et al.*: J. Phys. Soc. Jpn. **62** (1993) 459.
[5] A. Erbil *et al.*: Phys. Rev. B. **37** (1988) 2450.

Phase Modulation of ^{181}Ta Nuclear Resonant Synchrotron Radiation

In nuclear γ-ray resonance spectroscopy, ^{181}Ta stands for the highest energy resolution at low energies, and the ^{181}Ta nuclear resonant elastic scattering with synchrotron radiation has been successively observed at beamline **BL09XU** utilizing a stroboscopic detection technique and the heterodyne setup [1,2]. In the stroboscopic detection technique and the heterodyne setup, two Ta foils are placed in the beamline and one of these foils is given a variable velocity, and the Doppler effect shifts the resonance energy. The spectra are then taken as a function of Doppler velocity between the two Ta foils. When the Doppler-shifted resonance energy is equal to the energy in the other foil, an enhanced intensity of the delayed forward scattered photons is observed and a Mössbauer-like spectrum is created. The propagation of the synchrotron radiation through the ensemble of the resonant nuclei is a single-photon event and it is possible to observe phase modulation due to the change in optical path length or the deflection of the radiation or the small angle diffraction of the radiation for nuclear resonance in ^{181}Ta.

As shown in Fig. 1, a rotating Lucite wedge, which has periodic positive and negative slopes in the thickness change, is inserted between the two Ta foils and the Mössbauer-like spectra have been observed as a function of rotation speed from 0 to 10,000 revolutions per minute (RPM). When the thickness of the Lucite wedge is D and its refractive index is $N = n + iK$, the phase change by the variation in D is given by:

$$\phi = \phi_0 + \frac{(1+N)\,\omega_0}{c}\cdot\frac{dD}{dt}\,.t \quad ,$$

where c is the speed of light. Time dependent phase change induces a slight shift in resonance frequency that is given by $[(1-n)\omega_0]/c \times (dD/dt)$ [3]. Since the positive and negative slopes in the thickness of the Lucite wedge induce the positive and negative time dependences of the phase change, the 0th order resonant Mössbauer-like spectrum splits into two resonant peaks depending on the rotation speed and the refractive index of the Lucite wedge. Figure 2 shows the Mössbauer-like spectra as a function of the rotation speed of the Lucite wedge. When the rotation speed of the Lucite wedge is zero, the 0th order stroboscopic resonance is shown as a single peak at zero Doppler velocity. When the rotation speed of the

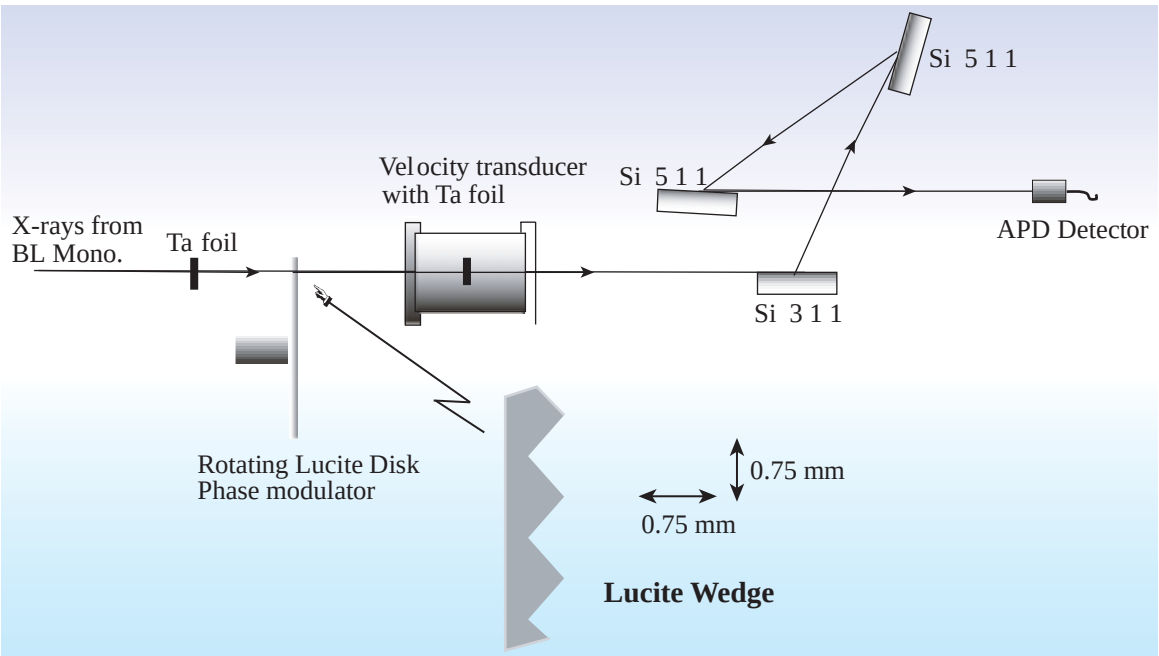

Fig. 1. Experimental setup for the phase modulation of the ^{181}Ta nuclear resonant synchrotron radiation. Rotation lucite disk is inserted between two Ta foils and the optical path length D for the 6.21 keV ^{181}Ta resonant radiation depends on the rotating speed.

Lucite wedge increases from 0 to 10,000 RPM, the split of the 0th order stroboscopic resonance has been observed clearly and the magnitude of the splitincreases with increasing rotation speed. Figure 3 shows the magnitude of the split of the 0th order stroboscopic resonance as a function of the rotation speed of the Lucite wedge. The split of the 0th order stroboscopic resonance depends linearly on the rotation speed. From the gradient of the line, the refractive index of the Lucite wedge (1-n) was determined to be $(7.11 \pm 0.14) \times 10^{-6}$ for 6.21 keV of ^{181}Ta nuclear resonance energy.

The present investigation clearly shows the phase modulation of the nuclear resonant synchrotron radiation for ^{181}Ta nucleus and will open a new field for exploring the fundamental properties of the radiation in the X-ray and γ-ray regions. We have available sufficient frequency resolution to reveal the spectral changes produced by variously generated modulation frequencies, just as we have at radio frequencies, and also now in the X-ray and γ-ray regions where quantum effects predominate.

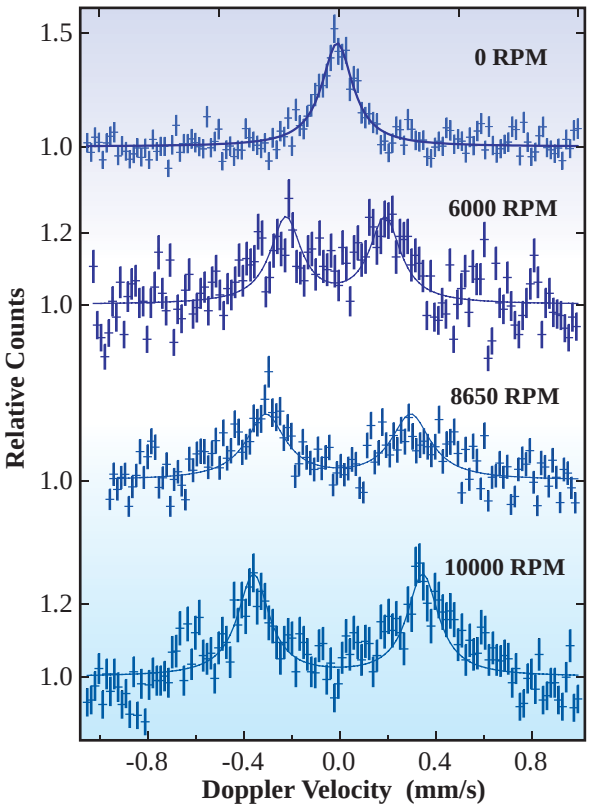

Fig. 2. Rotating Lucite wedge, which has periodic positive and negative slopes in the thickness change, has been inserted between two Ta foils and the 0th order stroboscopic spectra of the Ta foils have been shown as a function of the rotating speed (RPM) of the Lucite wedge. Doppler velocity is given for one Ta foil and the other foil is stationary.

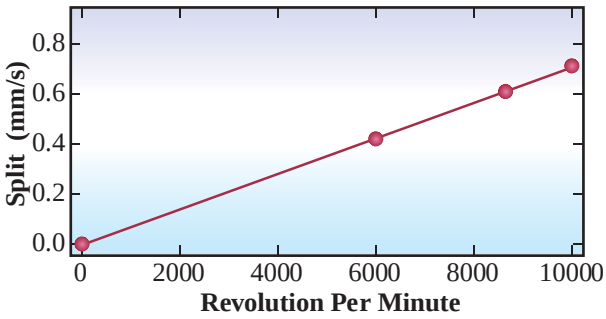

Fig. 3. Magnitude of split of 0th order stroboscopic resonance line as function of rotating speed (RPM) of the Lucite wedge. The magnitude of the split is twice that of the resonant shifts induced by the time dependent phase modulation.

Saburo Nasu[a,*], Shotaro Morimoto[a] and Yoshitaka Yoda[b]

[a] Prof. Emeritus, Graduate School of Eng. Science, Osaka University
[b] SPring-8 / JASRI

*E-mail: SabuNasu@aol.com

References

[1] *I. Serdons, R. Callens, R. Coussement, S. Gheysen, J. Ladriére, S. Morimoto, S. Nasu, J. Odeurs, Y. Yoda and G. Wortmann: submitted to Nucl. Instrum. Meth. (2006).*
[2] R. Callens *et al.*: Phys. Rev. B **67** (2003) 104423.
[3] L. Grodzins and E. A. Philips: Phys. Rev. **124** (1961) 774.

High Quality Iron Borate Crystal for Nuclear Resonant Scattering Experiment

^{57}Fe-enriched $FeBO_3$ single crystal is one of the most advantageous optical elements of the nuclear resonant scattering of synchrotron radiation (SR). Since pure nuclear Bragg scattering (NBS) in the vicinity of Néel temperature T_N can emit an extremely narrow band single-line X-rays on the order of 10^{-8} eV [1], this allows one to perform energy domain Mössbauer measurement using excellent SR properties (i.e., polarization, small beam size, etc.). However, high reflectivity and small divergence of NBS are achieved only when the nuclear monochromator crystal has crystallinity on few seconds order. Recently, we have successfully obtained a centimeter-sized very high-quality $^{57}FeBO_3$ single crystal by flux crystal growth [2]. Crystal perfection and magnetic domain structure were investigated by double-crystal topography using a non-dispersive (+,−) setting, i.e., asym-Si(331) × sym-$FeBO_3$ (444). As shown in Fig. 1, the measured rocking curve of $^{57}FeBO_3$ (444) reflection revealed that the value of full width at half maximum (FWHM) was only 4.48 arcsec for λ = 1.24 Å. This assures that this $^{57}FeBO_3$ crystal has an ideal crystal perfection suited for an optical element using NBS. Magnetic domain structure was observed using precise X-ray topograph. In the topograph recorded at the peak position, homogeneous X-ray diffraction contrast is obtained from almost the whole of the crystal (see Fig.1 (a)). This indicates that the crystal surface is free from serious lattice defects such as dislocations and inclusions. On the contrary, topographs recorded at low and high-angle positions of FWHM show many straight-line contrasts crossing over the crystal surface (see Figs. 1(b) and 1(c)). The line contrasts are caused by magnetostriction across 90º magnetic domain walls. They are composed many regularly arranged black and white diamond shaped strain sectors with a typical sector size of a few millimeters. Because the black and white contrasts of each sector have been reversed in Figs. 1(b) and 1(c) respectively, it is found that adjacent domains have a slight inclination to the opposite direction of each other with angular misorientation below a few arcsec. These results are the first observation of a unique case showing that regularly arranged multimagnetic domains play a vital role in the high-crystal perfection of $^{57}FeBO_3$.

The optics for the generation of ultrafine monochromatic X-rays at a SR facility are shown in Fig. 2. The experiment was performed at beamline **BL11XU**.

A high-resolution monochromator (HRM) was used for the monochromatization of SR X-ray. Then, the σ-polarized 14.4 keV X-ray of 2.5 meV bandwidth was incident on a $^{57}FeBO_3$ crystal that was mounted in a heater. An external magnetic field of 150 Oe was applied along the $^{57}FeBO_3$ (111) plane to magnetize it

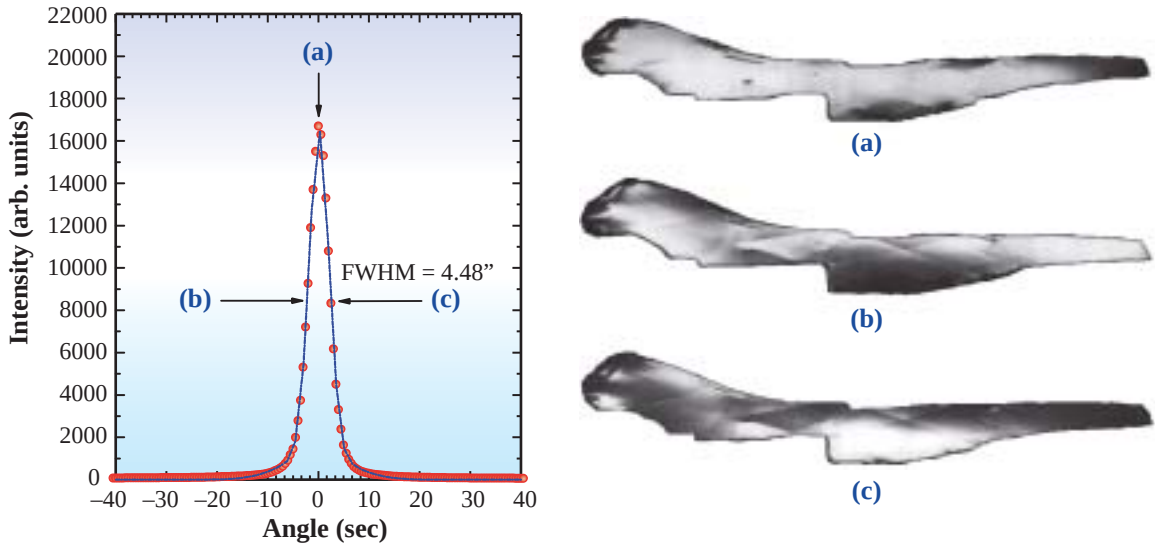

Fig. 1. Rocking curve and X-ray double crystal topograph of $^{57}FeBO_3$ (444) plane with X-ray illumination of whole sample in H_{ex} = 0 Oe. The dashed line is a Gaussian fitting curve. Topographs **(a)**, **(b)** and **(c)** are recorded at the following angles: **(a)** Δθ = 0.0 s, **(b)** Δθ = -2.24 s and **(c)** Δθ = +2.24 s.

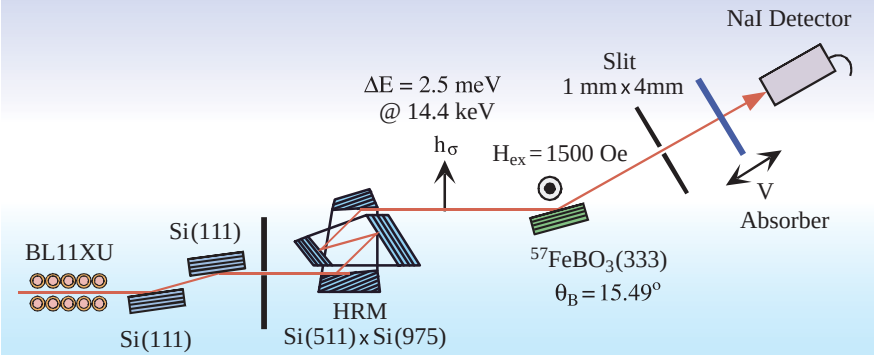

Fig. 2. Optics for ultrafine monochromatization of synchrotron radiation.

perpendicular to the scattering plane. In this optical system, a π-polarized ultrafine monochromatic X-ray beam could be emitted by the electronically forbidden pure nuclear Bragg reflection of $^{57}FeBO_3$ (333).

In Fig. 3, the Mössbauer spectra of a ^{57}Fe-enriched stainless steel foil are displayed at different temperatures in the range from room temperature up to the Néel temperature. This shows that narrow-band single-line X-rays are obtained at 75.8 deg. From the theoretical fitting on the absorption spectra of thin iron foils, it was estimated that the energy resolution is 15 neV. Intensity and angular divergence were evaluated by measuring a rocking curve of $^{57}FeBO_3$ (333). As the result, their values were 12,000 cps and 3.8 arcsec, respectively (see Fig. 4).

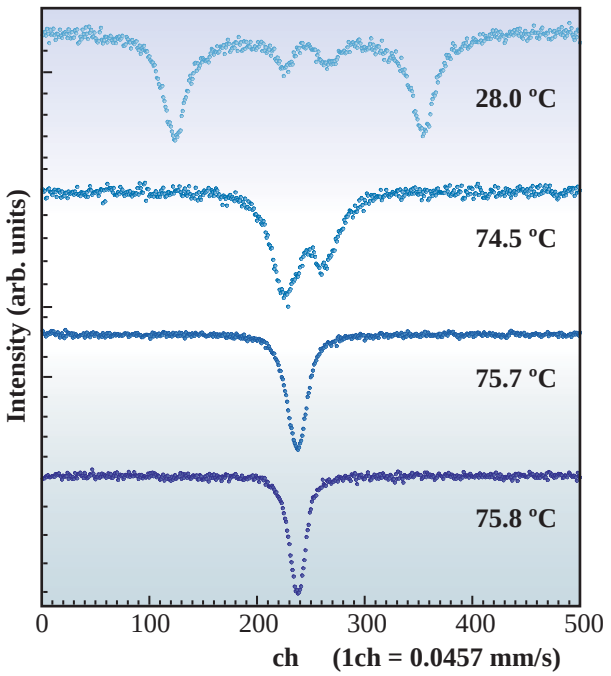

Fig. 3. Mössbauer absorption spectra of 2.5- μm-thick stainless steel foil (90% ^{57}Fe) measured with reflected Bragg radiation from $^{57}FeBO_3$ (333) at different temperatures.

These results indicate that our obtained ultrafine monochromatized X-ray beam has a very high quality. Therefore, by utilizing an excellent neV bandwidth probe beam, Mössbauer microanalysis, precise γ-ray optics, and other new techniques of SR neV spectroscopy will be greatly advanced.

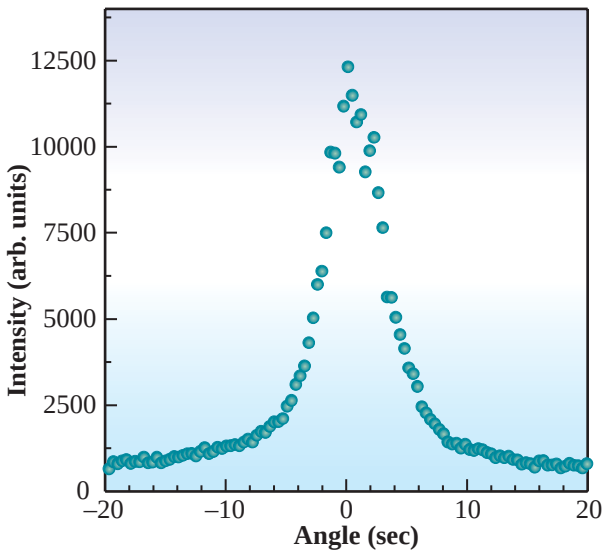

Fig. 4. Rocking curve of NBS from $^{57}FeBO_3$(333) at temperature of T = 75.8 deg.

Takaya Mitui

SPring-8 / JAEA

E-mail: taka@spring8.or.jp

References

[1] G.V. Smirnov *et al.*: Phys. Rev. B **55** (1997) 5811.
[2] *T. Mitsui, H. Takei, S. Kitao, M. Seto, T. Harami, X. Zhang, Y. Yoda and S. Kikuta: Trans. Mater. Res. Soc. Jpn.* ***30****(1) (2005) 7.*

Nuclear Physics

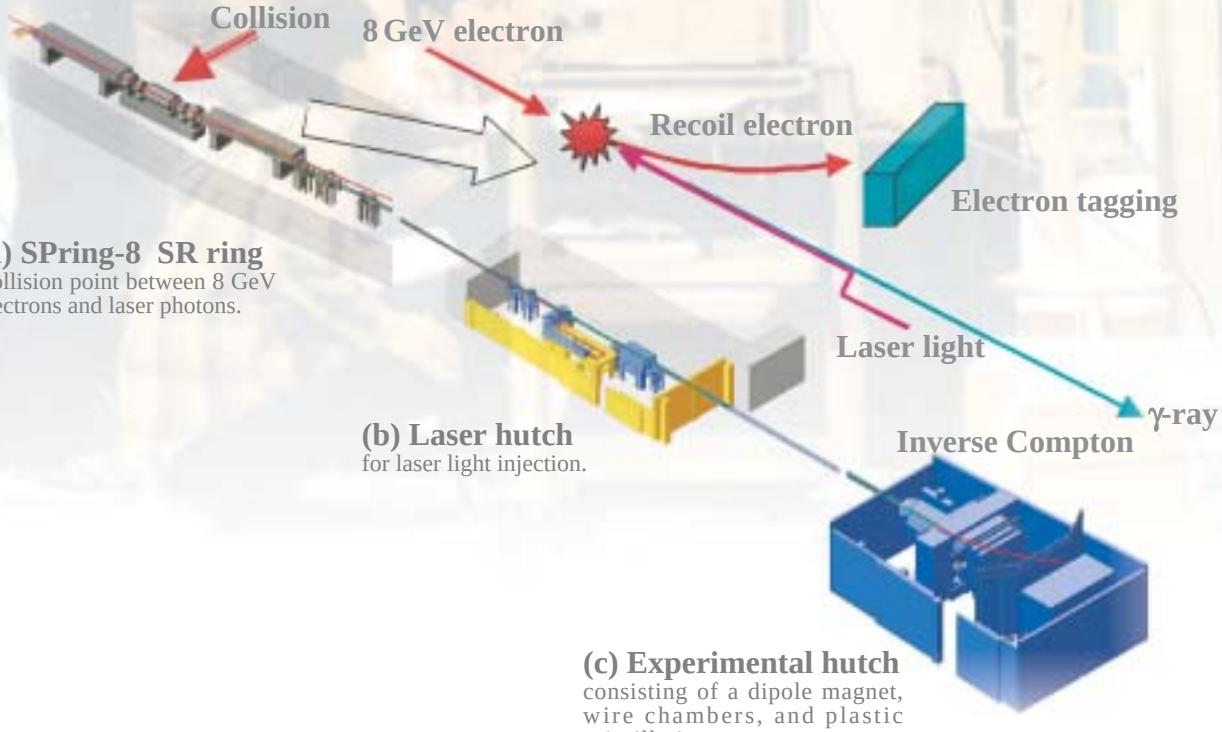

(a) SPring-8 SR ring
Collision point between 8 GeV electrons and laser photons.

(b) Laser hutch
for laser light injection.

(c) Experimental hutch
consisting of a dipole magnet, wire chambers, and plastic scintillation counters.

K^+ PHOTOPRODUCTION WITH LEPS AT BL33LEP

There are many nucleon resonances, N* and Δ*, which have been predicted by theoretical calculations, but have not been observed in πN and N(γ, π) reactions. These nucleon resonances are called 'missing resonances.' It has been realized that intermediate resonances to be studied in pionic reactions are limited [1]. Quark model studies suggest that a part of these missing resonances may couple to strangeness channels, such as KΛ and KΣ channels [1].

Measurements of the total cross section for the $\gamma p \rightarrow K^+ \Lambda$ reaction at ELSA/SAPHIR [2] and JLAB/CLAS [3] showed a new resonance-like structure around W = 1900 MeV (E_γ = 1.5 GeV) [4]. However, only cross section data are insufficient for establishing the missing resonances. There still remains a controversy in the theoretical description of the cross sections [5,6]. Additional observables are necessary for further studies. Photon beam asymmetry is useful to pin down the model to be used. Furthermore, there remains a significant discrepancy between the SAPHIR and CLAS data, particularly at forward angles [3]. Therefore, new cross section data are important for solving this discrepancy.

The LEPS experiment has been carried out using linear-polarized photons and a liquid hydrogen target at beamline **BL33LEP**. Photon beam asymmetries and differential cross sections of the $\gamma p \rightarrow K^+ \Lambda$ and $\gamma p \rightarrow K^+ \Sigma^0$ reactions have been measured in the photon energy range from 1.5 GeV to 2.4 GeV at forward angles of $0^\circ < \Theta^{K^+}_{cm} < 60^\circ$. The produced kaons were detected and identified using a magnetic spectrometer in an experimental hutch. The Λ and Σ^0 hyperons are identified using the missing mass calculation.

Figure 1 shows the experimental results of the photon beam asymmetries as a function of $\cos\Theta^{K^+}_{cm}$ for the $\gamma p \rightarrow K^+ \Lambda$ and $\gamma p \rightarrow K^+ \Sigma^0$ reactions, respectively. The statistical and systematic errors are included in the error bars in the data plots. The signs

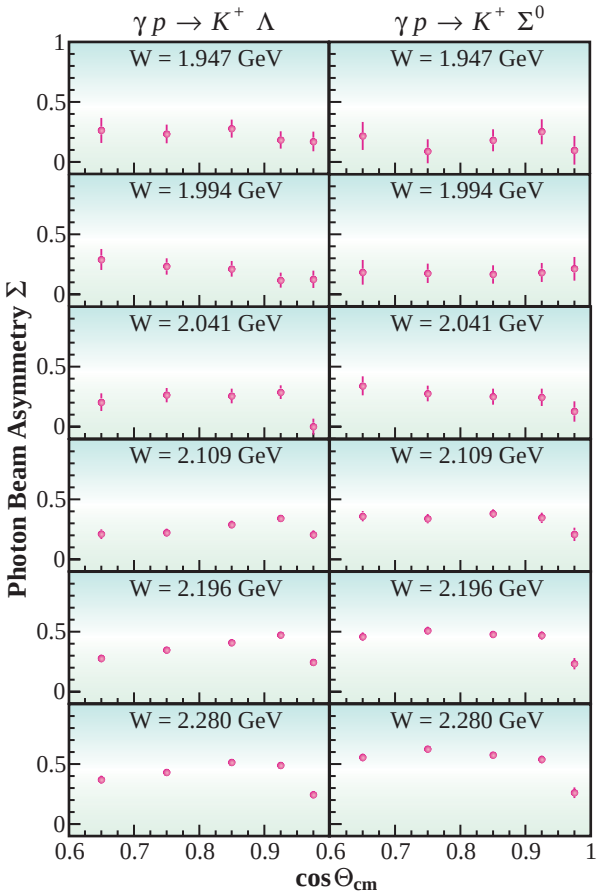

Fig. 1. Angular dependence of photon beam asymmetries for the $\gamma p \rightarrow K^+ \Lambda$ **(a)** and $\gamma p \rightarrow K^+ \Sigma^0$ **(b)** reactions. W is the total energy in GeV.

of the photon beam asymmetries are positive for both reactions in the measured kinematical region. The positive sign means that K^+ particles are emitted preferentially in the orthogonal direction to the photon polarization. The photon beam asymmetry for the both reactions increases as the photon energy increases. Figure 2 shows the differential cross sections as a function of $\cos\Theta^{K^+}_{cm}$ for the $\gamma p \to K^+ \Lambda$ and $\gamma p \to K^+ \Sigma^0$ reactions. The measured differential cross sections agree with the data measured by the CLAS collaboration at $\cos\Theta_{cm} < 0.9$ within the experimental uncertainties, but the discrepancy with the SAPHIR data for the $K^+ \Lambda$ reaction is large at $\cos\Theta_{cm} > 0.9$. In the $K^+ \Lambda$ reaction, the resonance-like structure found in the CLAS and SAPHIR data at W =1.96 GeV is seem. The differential cross sections at forward angles suggest a strong K-exchange contribution in the t-channel for the $K^+ \Lambda$ reaction, but not for the $K^+ \Sigma^0$ reaction.

None of theoretical models can reproduce the present data. The data will help develop the theoretical models.

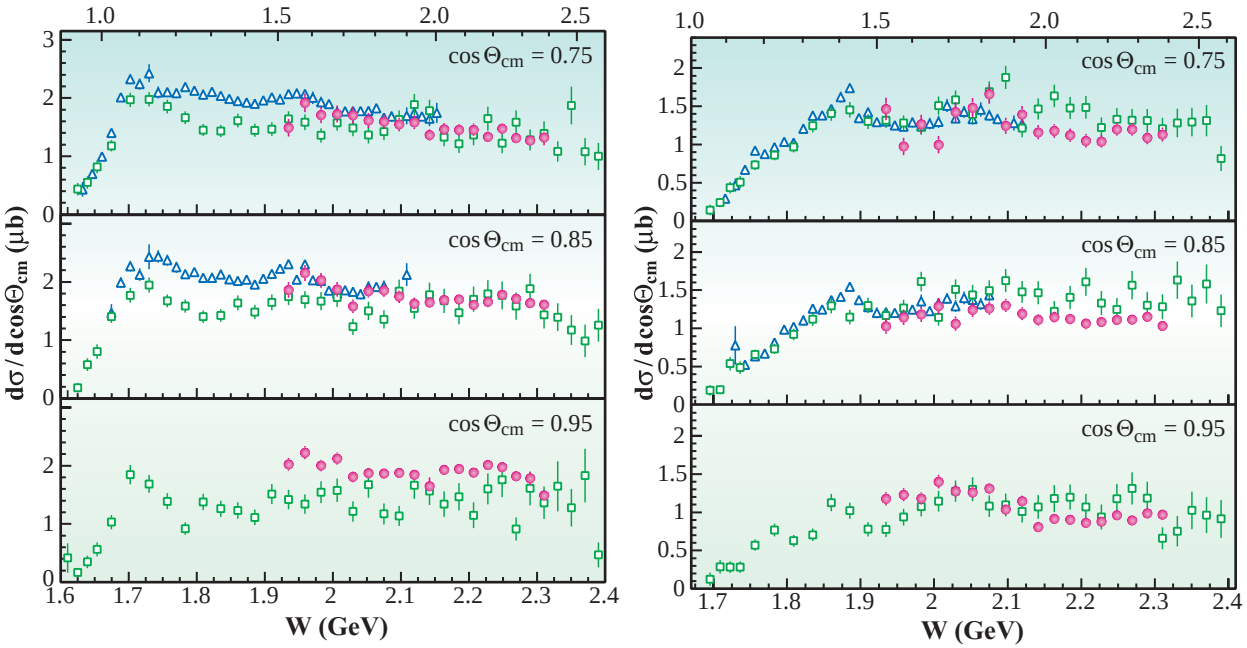

Fig. 2. Energy dependence of differential cross sections for the $\gamma p \to K^+ \Lambda$ **(a)** and $\gamma p \to K^+ \Sigma^0$ **(b)** reactions. The closed circles are the present results. The open squares and triangles are the data measured by the SAPHIR [2] and the CLAS [3] collaborations, respectively. Errors are only statistical one.

Mizuki Sumihama for LEPS Collaboration

Research Center for Nuclear Physics (RCNP), Osaka University

E-mail: sumihama@rcnp.osaka-u.ac.jp

References

[1] S. Capstick and W. Roberts: Phys. Rev. D **49** (1994) 4570; Phys. Rev. D **58** (1998) 074011.
[2] M.Q. Tran *et al.*: Phys. Lett. B **445** (1998) 20.
[3] R.A. Schumacher: Nucl. Phys. A **663-664** (2000) 440, nucl-ex/0305028 (2003).
[4] T. Mart and C. Bennhold: Phys. Rev. C **61** (1999) 012201.
[5] S. Janssen *et al.*: Phys. Rev. C **65** (2002) 015201.
[6] B. Saghai: nucl-th/0105001 (2001).

Energy Upgrade of Laser-Electron Photon Beam

A few GeV photon beam is a powerful tool for investigating hadron interactions at the quark-nuclear scale ($\hbar c$ ~ 0.2 GeV·fm). A high energy photon couples to a pair of quark and antiquark interacting with a nucleon or a nucleus in a target material. The LEPS Collaboration has carried out experiments on photoproductions of hyperons [1], pentaquarks [2] and ϕ mesons [3,4] by using 1.5 – 2.4 GeV photons. If a higher energy photon beam is available, the kinematical regions for extracting cross sections and spin asymmetries can be expanded. In addition, other physics possibilities, including the search for ω-mesic nuclei [5] and the photoproductions of heavier hadrons like K*(892) will become feasible.

A laser-electron photon (LEP) beam was produced by injecting ultraviolet (UV) laser light into the storage ring at beamline **BL33LEP**, as shown in Fig. 1. The UV light was focused 35 m downstream by the expander optimized for the wavelengths of 280 nm and 351 nm. The laser light was back scattered by 7.960 GeV electrons at the straight section of the storage ring (Backward Compton Scattering or BCS). Here the energies of the laser photons are magnified by an order of 10^9. The maximum energy of the LEP beam (k_{max}) is calculated by:

$$_{\max} = \frac{(E_e + P_e)\, k_{\text{laser}}}{E_e - P_e + 2k_{\text{laser}}} \cong \frac{4E_e^2\, k_{\text{laser}}}{m_e^2 + 4E_e\, k_{\text{laser}}}$$

where E_e, P_e, and m_e are the energy, momentum and mass of the electrons in the ring, respectively. So far, the Ar laser with multi-wavelengths around 351 nm (k_{laser} = 3.5 eV) has been used in order to get the maximum LEP energy of 2.4 GeV. The LEP beam intensity was ~10^6/s with the laser power of 6 W. Recently, high power CW lasers with the wavelengths of 257/266 nm (k_{laser} = 4.8/4.7 eV) have become commercially available because of the doubling of the frequencies of visible lasers by second harmonic generation with a BBO crystal. These deep UV lasers were introduced to extend the maximum LEP energy to 3.0/2.9 GeV.

The energy upgrade was first tested with the 266 nm laser ('DeltaTrain' produced by Spectra-Physics). Figure 2 shows the energy spectrum measured using the tagging system. The tagging system analyzes the momenta of recoil electrons from BCS by means of the bending magnet of the storage ring. It was calibrated on the basis of the relation between gamma-ray energies and recoil-electron momenta in the bremsstrahlung radiations from the residual gas. Here the gamma-ray energy was measured at the forward spectrometer by adding momenta of pair-created electron and positron. The Compton edge of the energy spectrum was confirmed at 2.9 GeV. The lower side of the spectrum was limited because of the acceptance of the tagging system. Recently the 257 nm laser ('Sabre MotoFreD' produced by COHERENT) has been introduced for a long-term operation. A 20 W Ar laser (visible) pumped up the UV output of 1.0 - 1.5 W. The spot on the BBO crystal from which UV light was emitted was damaged in several days at the maximum power, and the crystal was mechanically shifted to different positions. The maximum laser power was maintained with the power tracking system. The typical LEP intensity was 2×10^5/s as expected from the ratio to the Ar laser power. Currently, the Ar laser (351 nm) or the deep UV laser (257 nm) is operated depending on a purpose of the physics program.

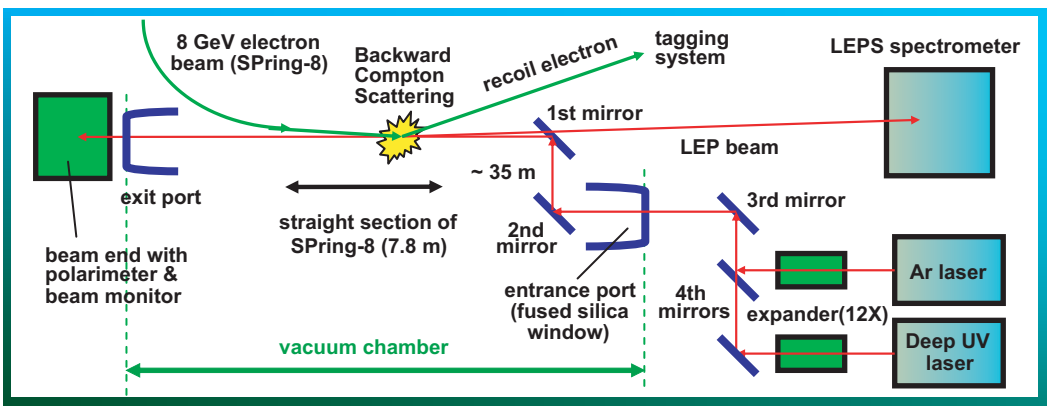

Fig. 1. Schematic view of the LEP beam production.

The search for the ω-mesic nuclei is one of the physics programs involving the deep UV laser. The chiral symmetry broken in vacuum is theoretically expected to be restored partially at the nuclear density. The medium modification of ω-meson potential results in the mass reduction or nuclear bound state of the ω meson. A 2.75 GeV photon reacts with a nucleon, producing a rest ω meson, and has an advantage to form the bound state inside a nucleus. After one week test experiment with the 266 nm laser, the 257 nm laser was operated for four months. Carbon targets (~0.2 radiation lengths) were set with the forward spectrometer, which was used to detect a high momentum proton in the reaction $\gamma^{12}C \rightarrow p\omega\ ^{11}B$. In the latter experiment a time projection chamber was additionally placed around the target to detect ω meson decays. Figure 3 shows the distributions of the missing mass MMp(γ,p) with a carbon and a CH_2 target in the test experiment. The size of the carbon data was scaled to the LEP counts in the CH_2 data. Free ω photoproductions from rest protons are seen. The existence of the signals is being identified in the carbon data by seeking events below the energy threshold of the free ω photoproduction.

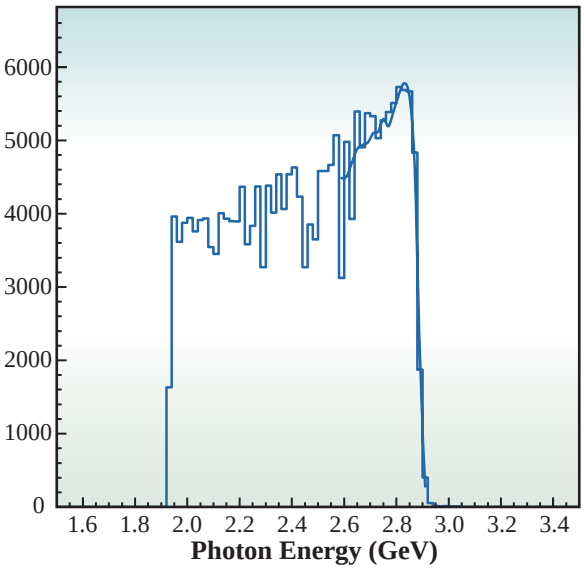

Fig. 2. LEP energy spectrum obtained with deep UV laser.

In summary, the maximum LEP energy has been extended to 3.0 GeV using the deep UV laser (257 nm). This energy is the highest among the world BCS facilities. The LEP intensity reached 2×10^5/s. In the future, a higher intensity beam will be tested with a technique to generate a laser beam collimated in a long distance by interference. In addition, a new optical system to inject multi-lasers is under consideration. The upgraded LEP beam is useful for exploring new fields in photoproduction experiments.

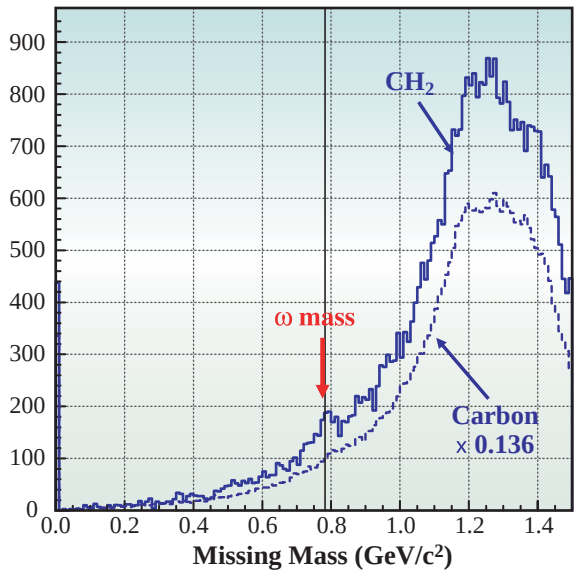

Fig. 3. Missing mass assuming the reaction p(γ,p)X.

Norihito Muramatsu for the LEPS Collaboration

Research Center for Nuclear Physics (RCNP), Osaka University

E-mail: mura@rcnp.osaka-u.ac.jp

References

[1] M. Fujiwara: SPring-8 Research Frontiers 2001B/2002A (2003) p.122.
[2] T. Nakano: SPring-8 Research Frontiers 2003 (2004) p.130.
[3] T. Mibe *et al.*: SPring-8 Research Frontiers 2004 (2005) p.147.
[4] T. Ishikawa and M. Fujiwara: SPring-8 Research Frontiers 2004 (2005) p.149.
[5] E. Marco and W. Weise: Phys. Lett. B **502** (2001) 59.

Accelerators & Beamlines

Frontiers

BEAM PERFORMANCE

Developments and Upgrades of Storage Ring

Orbit Stability

In 2005, the entire user operation was performed in the top-up mode. Accordingly, the beam orbit stability was excellent compared with the previously used decay mode. The remaining problem is the relatively large orbit variation over a long period, which we will mention below.

Low emittance optics have not small linear dispersion at the source points of insertion devices (IDs) and, hence, the photon axes of the ID beamlines suffer serious orbit variation by earthquakes. The dedicated feedback system, which precisely detects the circumference variation and adjusts the RF frequency of the RF acceleration with a resolution of 0.01 Hz, is under development.

To suppress the orbit drift at the restart of user operation, we have investigated the mechanical stability of beam position monitors (BPMs). The stability during beam operation was measured using several inductive displacement sensors. The measurements show that the displacements in the top-up operation are less than 2 μm, including a measurement error. However, they also show that at the restart of operation, the maximum horizontal and vertical drifts reach ~12 and ~7 μm, respectively. The stored electron beam directly and indirectly heats the vacuum chamber and, hence, a thermal expansion of the aluminum vacuum chamber occurs depending on the beam filling condition and stored current. The estimated thermal expansion of the chamber where a BPM is mounted well explains the measured data. To reduce the thermal expansion, the flow rate of the cooling water fed to the chamber was increased four times, which resulted in the horizontal and vertical displacements decreasing to a half of the previous values, ~7 and ~3 μm, respectively. Figure 1 shows the horizontal and vertical displacements of two BPMs during user operation after the cooling improvement.

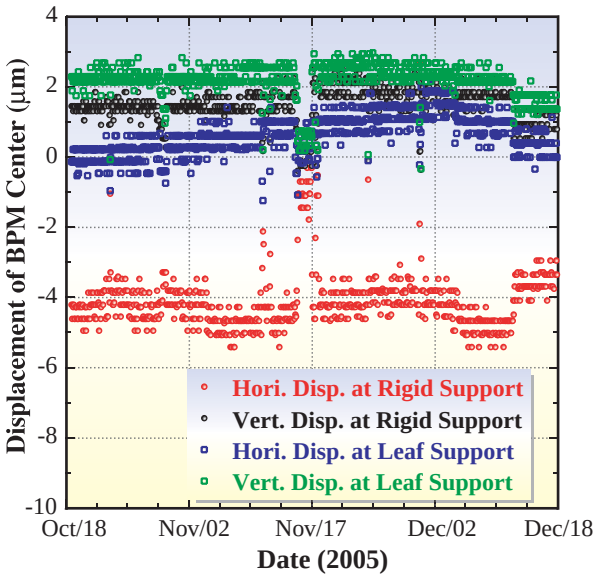

Fig. 1. Long-term stability of two BPM mechanical positions with different support methods. The red and black circles represent the horizontal and vertical displacements for the BPM fixed with the rigid support, respectively. The blue and green squares represent the horizontal and vertical displacements for the BPM fixed with the leaf support, respectively.

After introducing the top-up operation, the one-day orbit variation appears clearly in the variation of the field strengths of high-resolution steering magnets (HRSTs) used in the periodic closed orbit distortion (COD) correction. We have thus been investigating the mechanism of this pseudo-periodic variation. By analyzing the setting current data (corresponding to the field strength) of HRSTs, we have recently identified the error source locations, each of which has a tunnel or a trench under the floor of the machine tunnel. We selected one source location where the SSBT tunnel runs under the floor and carried out the systematic measurement of, for example, environmental parameters, the deformation of the girder, and the displacements of the magnets on the girder. At present, the results suggest an interesting mechanism: The fluctuation of AC voltage varies the air flow rate from the fan-coil unit and this flow rate change causes the deformation of the machine tunnel. The local deformation of the floor causes two central focusing quadrupole magnets on the second girder of cell 44 to incline. Figure 2 shows the correlation among these parameters. To clarify the mechanism, the systematic measurements and investigation are being continued.

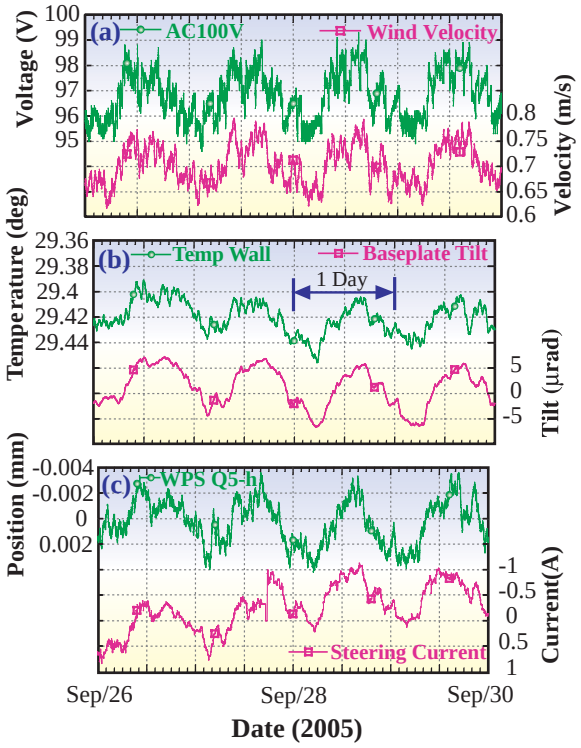

Fig. 2. Deformation of machine tunnel at cell 44 by variation of AC voltage. **(a)** correlation between AC voltage of fan-coil unit at cell 44 and velocity of circulating air from fan-coil unit, **(b)** correlation between surface temperature of inner wall of machine tunnel (experimental hall side) and tilt of central base plate at cell 44, and **(c)** correlation between horizontal displacement of QF5 at cell 44 and current of HRST at cell 43.

Top-up Operation

Top-up operation with a low emittance electron beam was started in September 2005 [1]. From the measurements of the photon fluxes of monochromatized X-rays emitted from the long undulator at BL19LXU, it is found that the peak flux in the new operation is 2.7 times larger than that in the previous operation, which is well explained by the calculation based on the design. The brightness enhancement is greatly beneficial for user experiments, and not only reduces the measurement time but also improves the data accuracy. A method of reducing the emittance employed at the SPring-8 storage ring is explained in ref. [2]. The emittance is reduced by breaking the achromatic condition imposed on the original double-bend achromat optics. In this situation, the dispersion function is nonzero at IDs and the energy spread of an electron beam enlarges the lateral beam extent through the dispersion function. The dispersion function is then optimized so that the phase space volume including the effect of the energy spread at a straight section of an ID takes the minimum value, as shown in Fig. 3.

Operation with a low emittance electron beam was first available for user experiments in November 2002 [3]. Although the low emittance electron beam provided brilliant X-rays, an extremely short beam lifetime due to the high electron density caused a significant variation in X-ray intensity, which disturbed precise experiments. First of all, the enormously short lifetime decreases the integrated or average brilliance against the expected end of the low emittance optics. Moreover, since the aborted electron beam damaged part of the vacuum chamber at the beam injection section, operation with the low emittance electron beam was suspended in October 2003. By improving the design of the vacuum chamber and introducing top-up injection [4-9], the problems for stable operation were resolved.

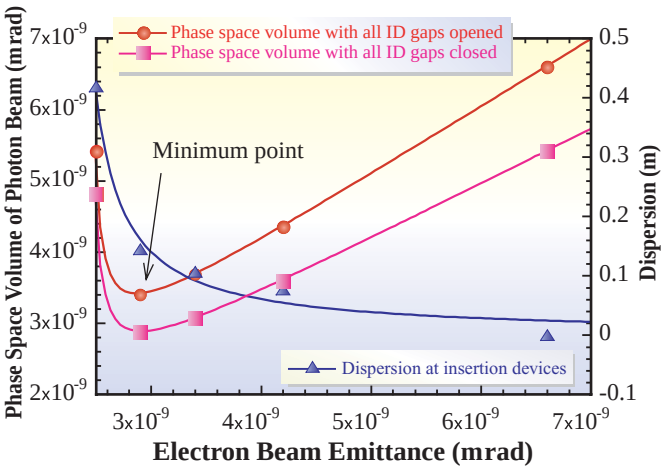

Fig. 3. Dependence of phase space volume of photon beam (vertical axis left) and dispersion at each insertion device (vertical axis right) on electron beam emittance (horizontal axis).

Development of New BPM Electronics

New signal processing electronic circuits for SPring-8 storage ring BPMs are under construction to improve the performance of the BPMs: faster measurement with the same level of resolution or better resolution with the same measurement time as the presently used electronics. The present circuits are scheduled to be replaced with the new circuits during the summer shutdown of 2006.

The present circuit was optimized for small signals so that the orbit could be measured with the small amount of stored electrons at the commissioning stage. Larger signals than those corresponding to 1 mA of stored current are attenuated before input to the RF amplifier stage to avoid nonlinear effects induced by large signal amplitudes. However, the signal-to-noise ratio (S/N) cannot be improved for a stored current larger than 1 mA, in spite of the increase in signal strength, because the input signal level to the RF amplifier is kept constant for a signal larger than the signal corresponding to 1 mA of stored current.

The design of the new circuits was optimized for 100 mA of stored current. The typical signal strength of 100 mA of stored current at the circuit input is -20 dBm for the single 508.58 MHz spectral component. 508.58 MHz is the acceleration RF frequency and also the detection frequency of the BPM signal processing circuits. The target resolution is in the sub-μm range; the stability must also be in the same range. A multiplexing method was employed to fulfill the stability condition. Ambient temperature stabilization is also planned and will employ a temperature controlled cabinet enclosure for stability, so the effects of temperature dependent drift are expected to be small. One set of the circuit consists of the following components: a filter-switch module to attenuate unnecessarily high frequency components for the protection of switching elements and to multiplex signals from BPM electrodes, an RF amplifier module having a narrow-band band-pass filter with a 3-dB bandwidth of less than 400 kHz at the center frequency of 508.58 Mhz, a mixer to down convert the signal to a 250 kHz IF (intermediate frequency) signal, an IF amplifier to adjust the signal level for the subsequent ADC, an ADC module to sample and digitize the IF signal, and a DSP module as a VME board to calculate the beam positions. Figure 4 shows a simplified block diagram of one set of the new circuits. One of the features of the new circuit is that the IF signal is sampled with a 16-bit 2MSPS ADC to achieve a good linearity. Most of the nonlinearity of the present circuit comes from the demodulation stage. Since the nonlinearity is the dominant factor in the stored current dependence of the measured position data, an improvement of the stored current dependence is expected to be achieved by the IF sampling method.

Block Diagram of R&D Electronic

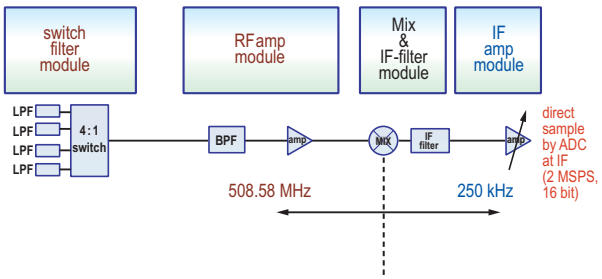

Fig. 4. Simplified block diagram of new electronics.

An example of data taken with a prototype of the new circuits is shown in Fig. 5. Data taken from two kinds of signal sources are compared: one is a signal generator with a CW output and the other is the beam signal. The signal generator output was divided by four, input to the circuit and processed. The processed signals were converted to the equivalent beam position data. The data taken with the signal generator show that the resolutions of 1 μm pk-pk (less than 0.3 μm in standard deviation) in both the horizontal and vertical directions are expected. However, data taken with actual beams show resolutions of 15 μm pk-pk (3.5 μm in standard deviation) in the horizontal direction and 10 μm pk-pk (1.9 μm in standard deviation) in the vertical direction, which are several to ten times worse than expected from the signal generator data. The discrepancy is due, at least partially, to the motion of the beam. The realization of the full performance of the BPM system requires the separation of the effect of the beam motion on the position measurements. Further study should be carried out to achieve the expected sub-μm resolution for the actual beam.

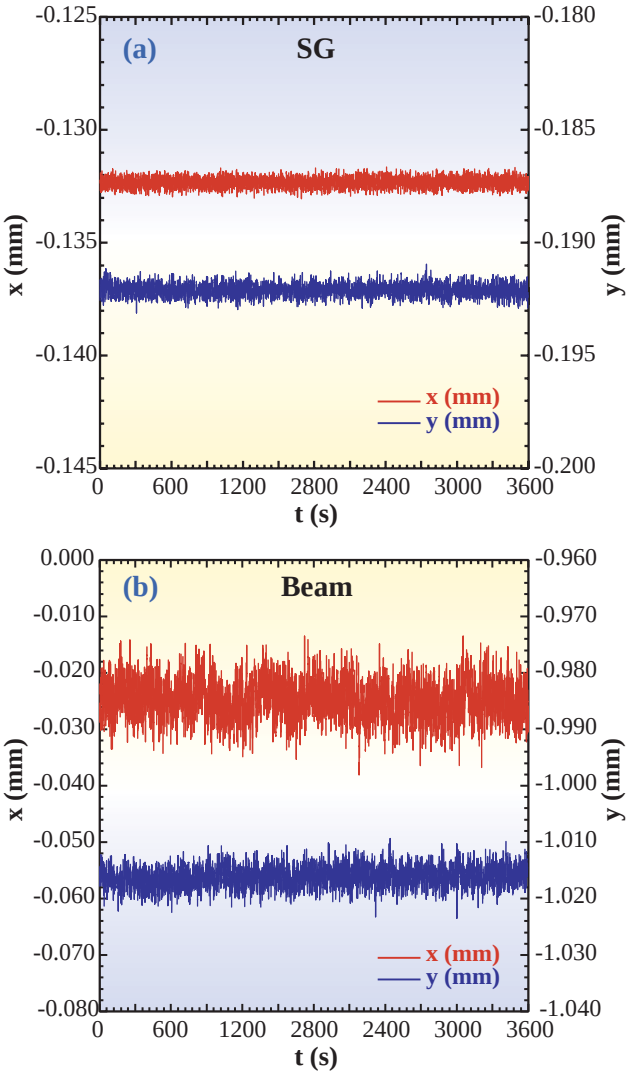

Fig. 5. Example of position data taken with prototype of new electronic circuits. **(a)** The signal source is a signal generator. **(b)** The signal source is the beam.

Improvement of Bunch-by-bunch Feedback

A new bunch-by-bunch feedback processor has been developed for planned advanced operation modes of the SPring-8 storage ring and for the ease of tuning of the system by simplifying the architecture and making the system USB-controllable with a Linux-based PC. The system can also handle two 20-tap FIR filters or one 50-tap FIR filter that enable single-loop two-dimensional transverse feedback with a newly developed method for the calculation of FIR filter coefficients. This scheme can suppress horizontal and vertical beam instabilities using one single loop; one diagonal pair of electrodes at a skewed position as a beam position monitor, one stripline at a skewed position as a kicker to detect and kick the beam horizontally and vertically, and one feedback processor, as shown in Fig. 6. This makes feedback systems easy to tune and highly cost-effective.

The single-loop two-dimensional feedback with new SPring-8 feedback processors is employed by Photon Factory at KEK and Taiwan Light Source at NSRRC, Taiwan, and are in user operation.

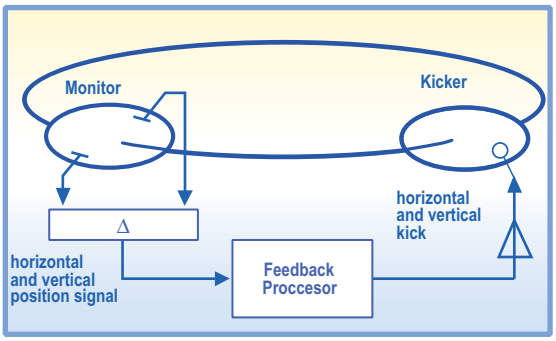

Fig. 6. Single-loop two-dimensional feedback using new SPring-8 feedback processor.

Development of Accelerator Diagnostics Beamlines

A schematic layout of the accelerator diagnosis beamline I (BL38B2) is shown in Fig. 7. The light source of the beamline is a bending magnet, and synchrotron radiation (SR) in a wide spectral range from visible light to X-rays can be utilized. Visible SR is used for the diagnostics of the longitudinal properties of the source electron beam, such as bunch length and bunch purity [10]. X-rays are used for emittance diagnostics of the electron beam using an X-ray beam imager (XBI) based on a Fresnel zone plate (FZP) and an X-ray zooming tube [11].

The accelerator diagnosis beamline II (BL05SS) is the second diagnostics beamline that is under construction. It has a straight section of the storage ring for an ID. The beam diagnostics and

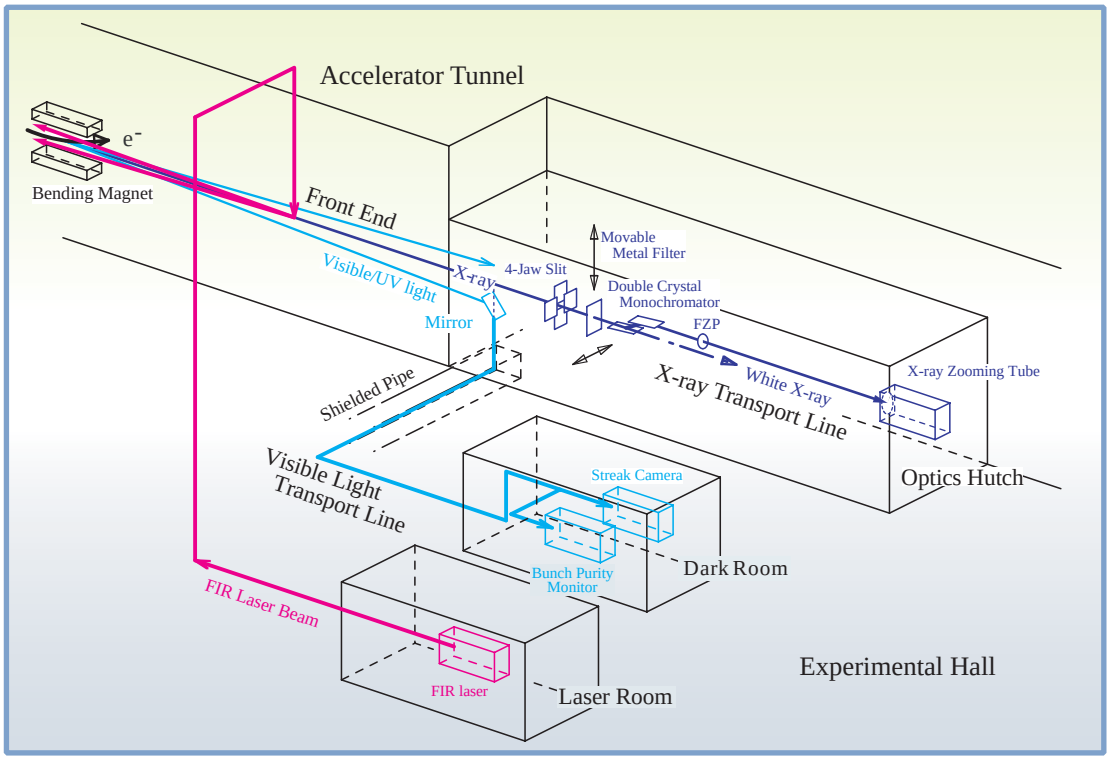

Fig. 7. Schematic view of accelerator diagnosis beamline I (BL38B2).

R&Ds of accelerator components are planned utilizing SR from the ID. The ID was developed and installed in the accelerator tunnel of the storage ring in 2005. The magnet array presently mounted on the ID is of the multipole wiggler (MPW) type and is designed to produce high-power SR. Studies of radiation damage to accelerator components and the development of high-thermal-load components such as photon absorbers are planned, utilizing SR from the MPW. A compact photon absorber developed to withstand the high heat load of the SR from the MPW was installed in the front-end in 2005. Designs of vacuum components for the X-ray transport line to be installed in the radiation shielding hutches of the diagnosis beamline II are in progress. For example, a differential pumping system was developed, which is necessary to connect the ultra high vacuum section in the range of 10^{-8} Pa and the low vacuum section in a range of 10^{-4} Pa directly without any vacuum partitions such as beryllium windows.

The study of the production of γ-ray photons in the energy range of 10 MeV is in progress at BL38B2 and BL05SS. The MeV γ-rays are generated by the backward Compton scattering of optically pumped far-infrared laser photons from 8 GeV electrons in the storage ring [12].

Improvement of Pressure Measurements

The abnormal actions of a Bayerd-Alpert type ionization gauge were observed. Gauges on the downstream end of the straight section chamber and on the crotch chamber are installed very close to the photon absorber. Therefore, these gauges are influenced by photoelectrons and radiation from the photon absorber. By precise measurement, three origins of abnormal action were confirmed as follows: the effects of (i) radiation on the gauge head, (ii) electron inflow on the gauge head, and (iii) radiation on gauge cable. (i) was also reported at ELETTRA, Italy [13]. (ii) is a well-known effect in accelerators. (iii) occurred owing to radiation induced current, and in this case the reading pressure was lower than the actual pressure. The following measures were made: (i) the shielding of the gauge head's casing with lead of 3 mm

thickness, (ii) the additional installation of a U tube or a permanent magnet upstream of the gauge head port, and (iii) the replacement of damaged cable with new cable, and the shielding of cables with lead tube of 3 mm thickness.

Figure 8 shows the normalized pressure rise (ΔP/I) and the product of the beam current (I) and beam lifetime (τ) as a function of the beam dose. I・τ increased with the integration of beam dose. SC1 shows ΔP/I at the middle of the straight section where the amount of radiation is very low. AB3 and CR1 show ΔP/I near the photon absorber. ΔP/I of SC1 decreased constantly in proportion to (beam dose)$^{-0.8}$. On the other hand, ΔP/I of AB3 and CR1 decreased negligibly after 10 Ahr of beam dose. ΔP/I of AB3 and CR1, however, decreased rapidly after 1014 Ahr of beam dose, because of the above-mentioned measures. ΔP/I of AB3 and CR1 were almost equal to that in SC1.

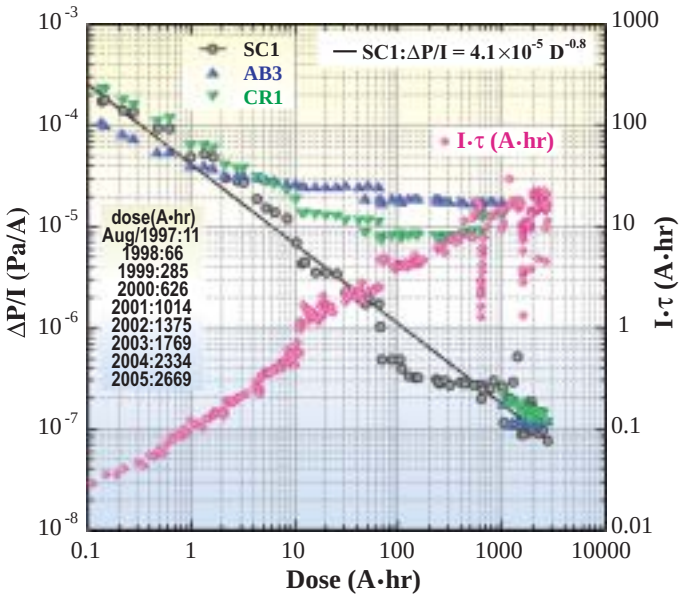

Fig. 8. Normalized pressure rise (ΔP/I) and product of beam current (I) and beam lifetime (τ) as a function of beam dose.

Study on Local Modification of Optics at Long Straight Section for Installing Superconducting Wiggler

The generation of high-energy SR in the MeV range using a 10 T superconducting wiggler (SCW) has been studied. High-energy SR from the SCW can be applied to new research fields such as nuclear astrophysics experiments, etc. [14-18].

To make use of the SCW in user operation at 100 mA, we have to solve the problems of high heat load, radiation shielding, non-negligible effects on the stored beam, etc. For example, when the SCW is excited in the storage ring, the emittance changes with the values of the horizontal betatron function and dispersion function at the place of installation of the SCW. A drastic increase in the emittance can be avoided by changing the storage ring optics locally and making a low-beta insertion at the SCW. A possible place for installation is one of four magnet-free long straight sections (LSSs) of about 30 m. In Fig. 9, we show an example of the local modification of optics. If we make such a local modification of optics, the periodicity of cell structure, especially of the sextupole field distribution, is broken and the symmetry of the ring becomes low. As a result, the dynamic aperture becomes narrow, and the beam injection efficiency and beam lifetime deteriorate.

To recover the periodicity of cell structure and hence the dynamical stability, we developed a method of “counter-sextupoles.” In this method, additional sextupole magnets are placed within the matching section to cancel the nonlinear kick due to the sextupole magnets for local chromaticity correction, which are located in the arc of the matching section. The betatron phase between the counter-sextupoles and the sextupoles for local chromaticity correction is chosen to be as close as possible to π to make such a cancellation. To check the effectiveness of this scheme, we installed additional quadrupole and sextupole magnets in one of the four LSSs, as shown in Fig. 9. We measured beam parameters for the modified optics and checked the effectiveness

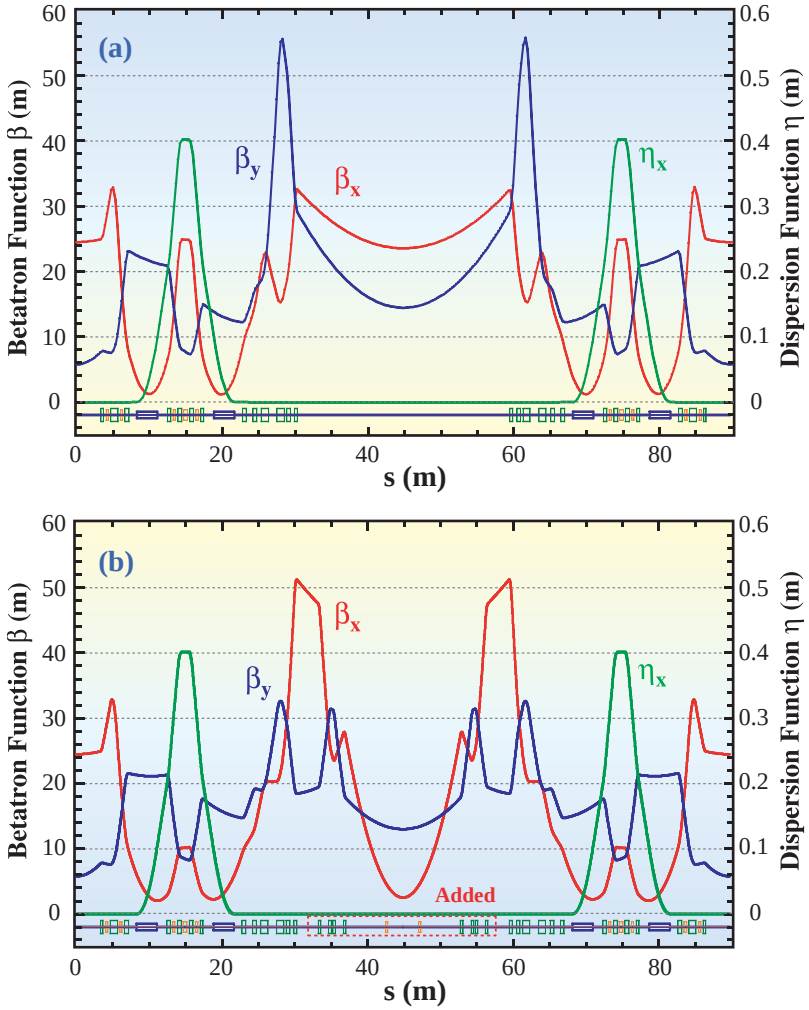

Fig. 9. Optics of matching section **(a)** before and **(b)** after local modification. Bending, quadrupole and sextupole magnets are shown by blue, green and orange rectangles, respectively.

of the above scheme. We, however, could not fully recover the degree of stability because the rest of the LSS's were remained unchanged and the kick due to the sextupole magnets was not canceled in these sections. We are now planning to install counter-sextupoles in all four of the LSSs and this will improve the beam performance in routine user operation. It is also expected that, with this scheme of counter-sextupole independent tuning of local optics at each LSS, it will become possible to insert devices other than the SCW.

Developments and Upgrades of Booster Synchrotron

Beam Storage Operation of Booster Synchrotron

To improve the performance of the booster synchrotron, especially for the high duty operation of top-up injection, it is important to understand the detailed characteristics of the booster synchrotron. Beam storage operation is effective for measuring various parameters, such as HOM in the RF cavity

at 1 GeV, COD at each energy, and emittance at each energy, which are difficult to measure in normal energy ramping operation.

For a test operation of the beam storage, it was necessary to modify the timing system. In booster operation, all pulsed magnets are operated at 1 Hz. Other magnets and RF acceleration voltage are operated ramping up and down at 1 Hz. For storage operation, the timing system was modified to stop its chain at the desired time. In this test operation, a beam lifetime of 2.7 hours at a stored beam current of 8.6 mA was achieved.

Measurement of Demagnetization of Undulator Magnet

Permanent magnets are the main components of undulators. The demagnetization of the magnets in a highly radioactive environment is a serious problem. For the experimental use of the SPring-8 booster synchrotron, instead of beam injection into the storage ring, we investigated the demagnetization of an undulator magnet by irradiating the magnet with the electron beam to in January 2005.

A 40-mm-thick copper block was placed in front of the magnet and the electron beam was irradiated onto the block. The electron beam irradiation was carried out at the beam dump of the booster synchrotron. After the beam irradiation, the magnetic field distribution of the undulator magnet was measured using a Hall probe. The electron beam was injected into the target Cu block, passing through a 1-mm-thick aluminum vacuum window and a fluorescence screen for beam position monitoring. The electron dose was monitored by DCCT in the booster synchrotron.

The repetition rate of beam irradiation was 1 Hz, and the beam irradiation dose was 1.4×10^{15} electrons for each sample magnet. Various beam energies were used: 4 GeV, 6 GeV and 8 GeV, respectively. The result of the experiment, the beam energy dependence of demagnetization, was observed. Data analysis is now in progress.

Developments and Upgrades of Linac

Beam Stabilization [19]

The SPring-8 linac has been improved to realize stable top-up injection into the SPring-8 and the NewSUBARU storage rings. A long-term beam energy instability of 0.02% rms was achieved by the following stabilizations (1998 - 2005): RF amplitude and phase stabilization, the synchronization of beam timing and the linac's 2856 MHz RF, and the installation of an energy compensation system (ECS). Beam feedback controls compensate for the residual long-term variation of beam trajectory and energy.

Air temperature fluctuations in the linac klystron gallery have reappeared since 2002 because of the electric power saving of the linac. The temperature variations have resulted in RF phase fluctuations in a 100-m-long waveguide that drives eleven klystrons. The improvement of an air conditioning system has stabilized the temperature fluctuations less than 1ºC, as shown in Fig. 10. In addition, the long waveguide is covered with thermal insulation and warm water (27±1ºC) is circulated in pipes inside the cover. The air temperature fluctuations inside the insulation have been consequently reduced to 0.23ºC.

To improve the long-term stability, we introduced the following feedback controls: (i) beam position stabilization at three beam transport

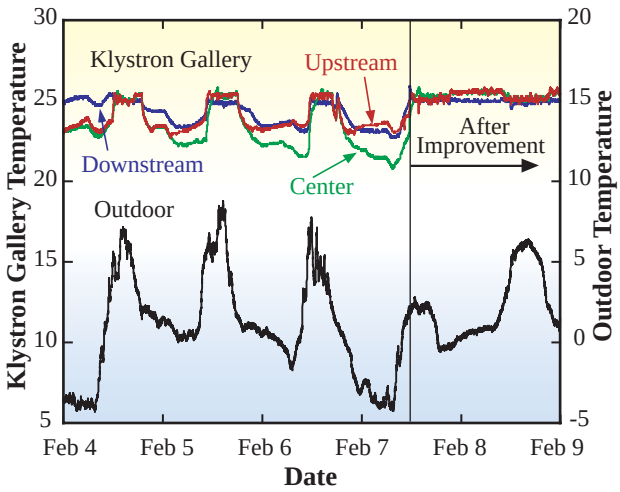

Fig. 10. Variations of klystron gallery temperatures before and after improvement.

lines, and (ii) beam energy stabilization by adjusting the ECS. Beam position control is carried out at the following three points in the linac: (i) a drift space in the injector, (ii) the drift space of a transport line to the NewSUBARU storage ring, and (iii) a transport line between the ECS and a bending magnet downstream. These straight parts respectively contain two sets of steering magnets upstream and two sets of BPMs downstream. The control program adjusts the steering magnets and maintains beam positions within the position window at reference BPMs. The position window was determined to be ±30 μm, which is nearly double the standard deviation of the measured values.

Beam energy is stabilized as follows: it is measured by BPMs installed at the dispersive sections of the beam transport line to the NewSUBARU or to the booster synchrotron. The program adjusts the RF phase of the ECS so that energy error remains within the energy window of ±0.03%.

Development of Photocathode RF Gun

A study of a photocathode RF gun, which is expected to be a highly qualified electron beam source for producing future X-ray light sources, has been in progress since 1996 at SPring-8. We have promoted the development of basic technologies especially for producing low emittance beams with a single-cell type RF gun [20]. The next step in this R&D project is to verify the beam performance, particularly the beam emittance, in the higher beam energy region because a single-cell cavity can only accelerate beams up to 4.1 MeV and the emittance can easily grow in this energy region. To enhance the beam energy, a 3-m-long traveling wave structure has been added after the RF gun, as shown in Fig. 11 [21], and thus the approved maximum beam energy has been increased from 4.1 MeV to 30 MeV. At present, the beam emittance is evaluated by the variable quadrupole magnet method, which often underrates the actual emittance. An emittance measurement system based on the double slit scanning method, which generally enables a more accurate emittance evaluation, is now under construction.

An electron bunch having a uniform density distribution is expected to minimize the nonlinear space charge effect, which causes the emittance growth. Hence, we have developed optical systems to control the spatial and temporal shapes of laser light pulses to realize such ideal charge distributions. We employed a computer-aided deformable mirror as a spatial shaper [22]. This deformable mirror consists of 59 small hexagonal mirrors with center-to-center distances of 1.75 mm. A control voltage between 0 and 250 V, in increments of 1 V, is applied to each mirror, making it possible to shape any laser spatial profile, with a total of 25059 (~10141) forming possibilities. Thus, this spatial shaping method needs a sophisticated algorithm to control the deformable mirror. As a result, the laser profile on the cathode surface was spatially shaped to have a quasi-flattop profile (right-hand side of Fig. 12). The laser beam diameter was estimated to be 1.0 mm.

The copper cathode was illuminated by this shaped laser pulse at normal incidence. The measured horizontal normalized emittance of the accelerated beam was 1.74 π mm·mrad at its minimum with a net charge per bunch of 0.09 nC/bunch [22].

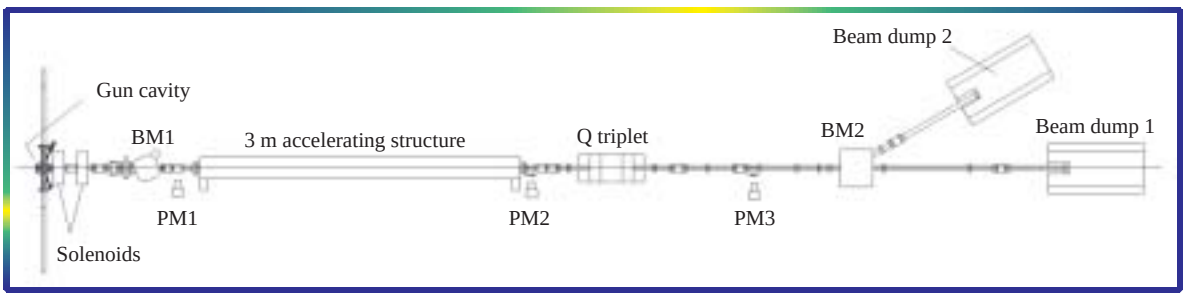

Fig. 11. Layout of 30-MeV linac with photocathode.

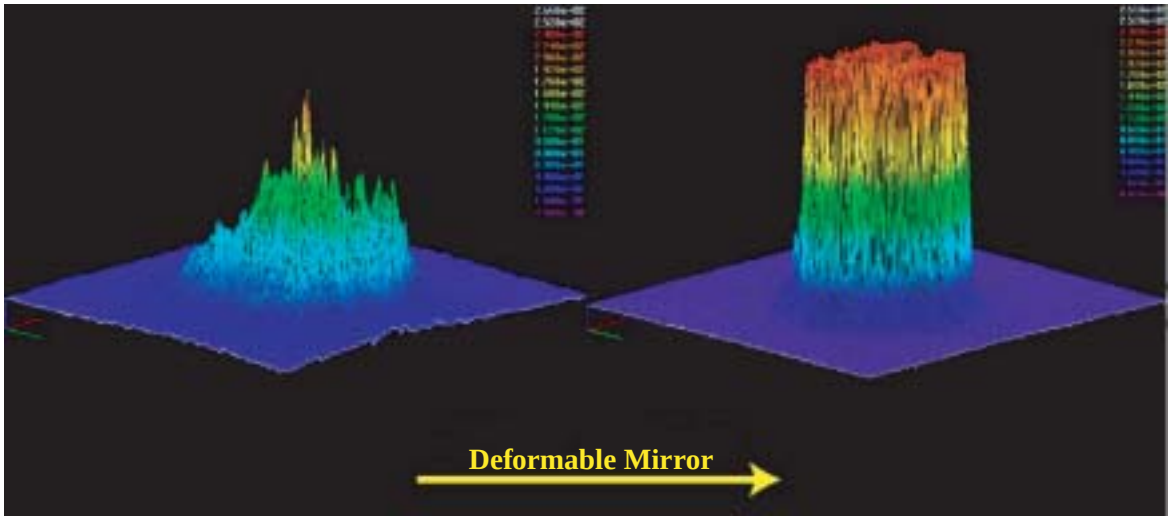

Fig. 12. Spatial shaping results using deformable mirror and genetic-algorithm-based optimizations.

Haruo Ohkuma*, Hiroto Yonehara,
Hirofumi Hanaki and Noritaka Kumagai

SPring-8 / JASRI

*E-mail: ohkuma@spring8.or.jp

References

[1] H. Tanaka *et al.*: to appear in Proc. EPAC06, Edinburgh, UK.
[2] H. Tanaka *et al.*: Nucl. Instrum. Meth. A **369** (1996) 312.
[3] M. Takao *et al.*: to appear in Proc. APAC04, Gyeongju, Korea.
[4] H. Tanaka *et al.*: Proc. of EPAC 2004, Lucerne, Switzerland, 222.
[5] M. Takao *et al.*: Proc. of EPAC 2004, Lucerne, Switzerland, 417.
[6] K. Fukami *et al.*: to appear in Proc. of APAC 2004, Gyeongju, Korea.
[7] T. Ohshima *et al.*: Proc. of EPAC 2004, Lucerne, Switzerland, 414.
[8] H. Tanaka *et al.*: Proc. of EPAC 2004, Lucerne, Switzerland, 1330.
[9] H. Tanaka *et al.*: Nucl. Instrum. Meth. A **539** (2005) 547.
[10] K. Tamura *et al.*: Proc. 1st Annual Meeting of Particle Accelerator Society of Japan and Proc. 29th Linear Accelerator Meeting, Funabashi, Japan, 2004, p.581.
[11] S. Takano *et al.*: Nucl. Instrum. Meth. A **556** (2006) 357.
[12] H. Ohkuma *et al.*: to appear in Proc. EPAC06, Edinburgh, UK.
[13] J. Miertusova: Vacuum **51** (1998) 61.
[14] H. Yonehara *et al.*: SPring-8 Internal Report B2004-001 (2004) (in Japanese).
[15] H. Utsunomiya *et al.*: Nucl. Phys. A **738** (2004) 136.
[16] H. Utsunomiya *et al.*: Nucl. Instrum. Meth. A **538** (2005) 225.
[17] A. Ando *et al.*: J. Synchrotron Rad. **3** (1996) 201.
[18] D.A. Gryaznykh *et al.*: Nucl. Instrum. Meth. A **448** (2000) 106.
[19] H. Hanaki *et al.*: Nanobeam2005, Uji, Japan.
[20] H. Dewa *et al.*: Proc. ICFA Workshop "The Physics and Applications of High Brightness Electron Beams", Sardinia, Italy, 2002, p.28.
[21] T. Taniuchi *et al.*: FEL'04, Trieste, Italy.
[22] H. Tomizawa *et al.*: FEL'05, Stanford, USA.

Impacts of the Top-up Operation to SR experiments

Of particular desire for synchrotron radiation (SR) experiment user is to attain a stable and no time decay X-ray beam. The top-up operation in SPring-8 has been realized to bring great advantages for user experiments.

The merits of the top-up operation for SR experiments are summarized as follows: (a) Increase in time averaged photon flux: The top-up operation achieved an expected increase in total photon flux, which leads to a high counting statistic measurement due to constantly high beam intensity. In addition, a continuous operation without shut down for refilling beam current excluded not only a shut down time loss but also a time loss for the warm-up of optics. Consequently, for multi bunch experiments, the top-up operation provides about 1.5 times higher intensity measurement in total while for the single bunch experiment 3 times higher intensity were provided, since a preferential beam filling for the use of a single bunch has an electron with shorter lifetime than that in the case of multi-bunch filling. (b) Current stability within 0.1% fluctuation: The minimized current fluctuation of a stored beam leads to a constant heat load for optics including monochromators, which enables the achievement of a virtually absolute measurement with intensity monitor free. (c) No interruption by refilling of beam: The operation without shut down for electron refilling allows us planning of long time stable measurement.

Here, we describe the merit of the step-scan measurement in a diffraction experiment as an example. In the case of step-scan measurement, the time dependent decay and fluctuation of incident X-ray intensity were used to be corrected by monitoring incident X-ray intensity. However, the precise top-up operation succeeded in the elimination of ambiguity over the step-scan measurement caused by a data correction based on the monitored intensity at each measurement step. This enhances the data reliability of the diffraction experiment.

The diffraction data of amorphous silica measured at the high-energy X-ray diffraction beamline **BL04B2** with 61.6 keV high-energy X-rays is shown in Fig. 1. Since the scattered intensity drastically decreases with an increase in scattering angle as shown in this figure, it is necessary to obtain the correct intensity profile in the high-angle region to place the observed data on an absolute scale. To obtain the correct intensity profile of disordered materials up to large values of scattering vector Q, the measurement is performed using $\theta - 2\theta$ step-scans with an intrinsic Ge detector over a period of 4 – 12 hours. Therefore, the incident flux of photons should have a high stability for a long time scan over a wide range of Q values.

Figure 2 (a) shows high angle data of amorphous silica measured in the conventional non-top-up mode. Here, it can be seen that the difference in scattering intensity between the first and second scans is due to the fluctuation of the incident beam flux. On the other hand, the two intensity profiles measured in the top-up mode are nearly identical, as shown in Fig. 2 (b). Figure 2 (c) shows the difference in scattering intensity between the first and second scans. In the case of the top-up mode, the difference is almost equal to zero, which demonstrates that a heat load on the monochromator of BL04B2 remains equal to a steady value owing to the constant stored beam current of the storage ring.

To clarify the effect of the top-up operation on

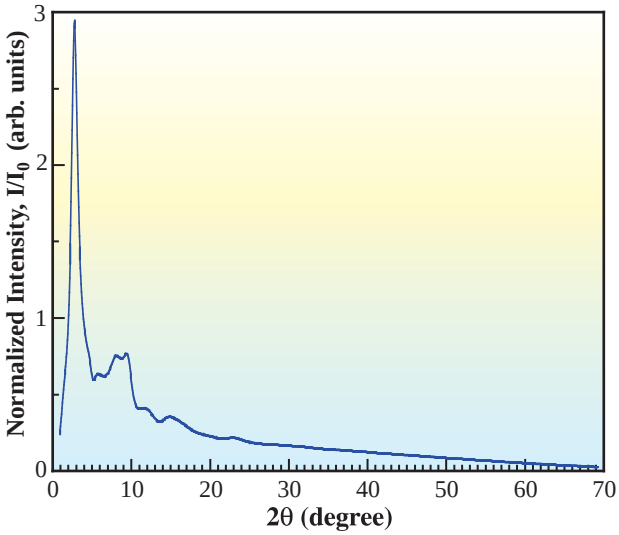

Fig. 1. X-ray diffraction pattern of amorphous silica.

the structural analysis of disordered materials, both of the diffraction data are normalized to the total structure factors $S(Q)$ and Fourier transformed to the total correlation functions in real space, $T(r)$. The $S(Q)$ of amorphous silica obtained in the top-up mode exhibits proper oscillations up to Q = 32 Å^{-1}, as shown in Fig. 3(a), whereas $S(Q)$ obtained in the conventional mode exhibits some artificial declination below $S(Q)$ = 1.0 in the high-Q region (Q > 20 Å^{-1}), which produce significant ripples in the correlation function, $T(r)$, as shown in Fig. 3(b), at r < 1 Å.

The top-up operation of SPring-8 allows us to very accurately measure diffraction data of disordered materials up to a high-Q. It is particularly well suited for detecting small differences in structure between two isotopically substituted amorphous samples such as an isotopic quantum effect in water [1].

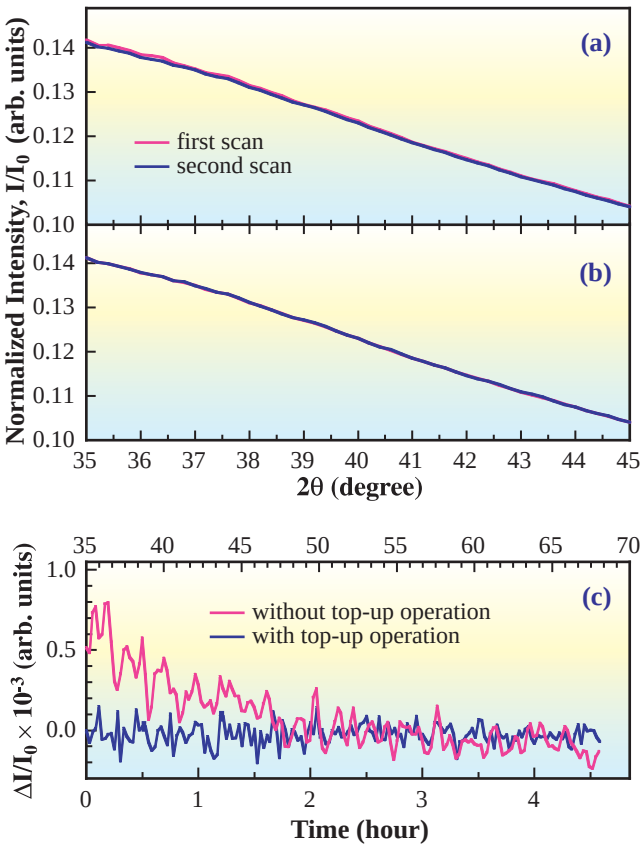

Fig. 2. X-ray diffraction patterns of amorphous silica without top-up operation **(a)** and with top-up operation **(b)**; the difference of first scan and second scan **(c)**.

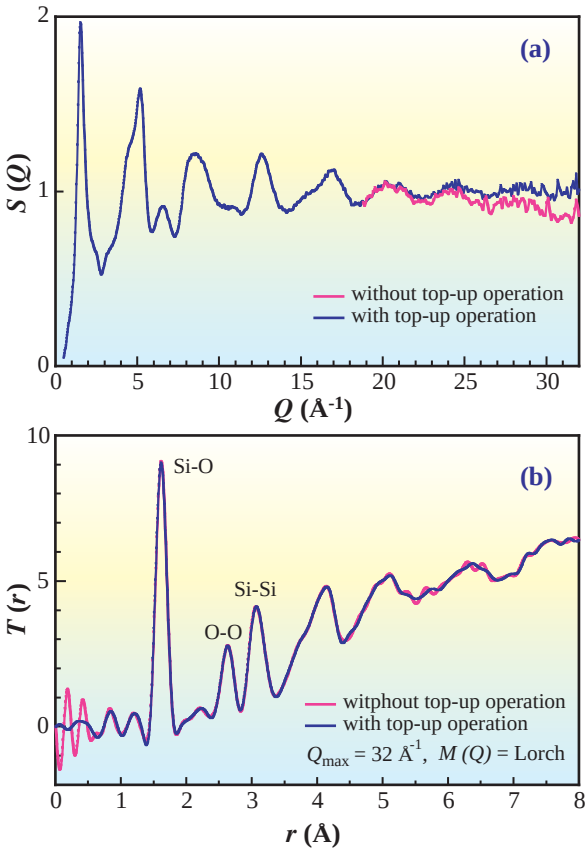

Fig. 3. Total structure factor $S(Q)$ **(a)** and total correlation function $T(r)$ **(b)** of amorphous silica.

Masaki Takata[a,b,*] and Shinji Kohara[a]

[a] SPring-8 / JASRI
[b] SPring-8 / RIKEN

*E-mail: takatama@spring8.or.jp

References

[1] R. Hart *et al.*: Phys. Rev. Lett. **94** (2005) 047801.

UNDULATORS WITH HIGH-TEMPERATURE SUPERCONDUCTING PERMANENT MAGNETS

Introduction

Periodic magnetic fields in undulators are usually generated by rare earth permanent magnets (REPMs). The performance of the REPM material is thus important for undulator development and is in fact improved yearly. It should be noted, however, that there is a theoretical limit to the remanent field of REPM materials, which means that the achievable magnetic field in an REPM undulator also has a theoretical upper limit.

To go beyond the limit, superconductors can be used instead of REPMs. In practice, undulators equipped with superconducting coils (superconducting undulators: SCUs) have been constructed and under development for about 20 years [1]. These SCUs can produce much higher fields than achieved by REPM undulators at the same magnet gap. Note, however, that the construction and operation of SCUs would be more difficult for shorter periodic lengths since they should operate at around liquid helium temperature at narrower gap values.

There is another way of utilizing superconductors as magnets. Because the resistivity of superconductors is exactly zero, a current loop induced by Faraday's electromagnetic induction law is not damped at all and flows forever (persistent current). Thus, such a "magnetized" superconductor works as a permanent magnet with a much stronger field than REPMs and is called a superconducting PM (SCPM). In particular, SCPMs fabricated from bulk-type high temperature superconductors (HTSCs) have better performances than REPMs. We have proposed two schemes for applying such SCPMs to shorter-period undulators. Their principles and results of demonstration experiments are presented in the following sections.

Cryoundulator plus

The cryoundulator plus (CU*plus*) [2] is an extension of the cryoundulator concept [3], in which REPMs are cooled to improve the magnetic performance, i.e., the remanent field and coercivity. Ring-shaped HTSCs are mounted on REPM arrays to enhance the magnetic field. Before operation, the magnet arrays are fully closed at room temperature. By reducing the temperature of the magnet arrays and opening the gap to a certain value, the HTSC rings are magnetized to keep the flux inside, resulting in a field enhancement. To demonstrate the principle, experiments were carried out with magnet modules composed of an HTSC ring made of GdBaCuO and three pieces of REPMs made of NdFeB as shown in Fig. 1(a).

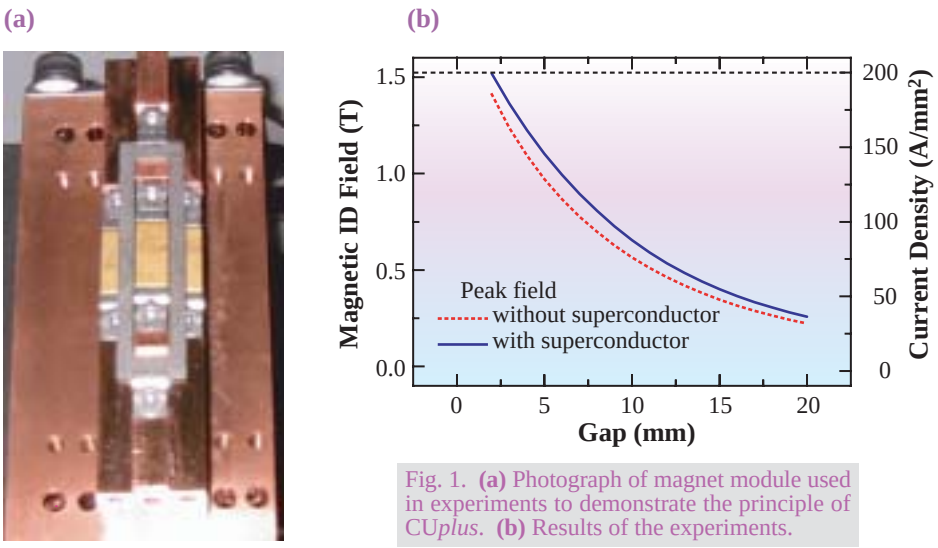

Fig. 1. **(a)** Photograph of magnet module used in experiments to demonstrate the principle of CU*plus*. **(b)** Results of the experiments.

Two of the rings were placed face-to-face and immersed in liquid nitrogen. Then the gap was opened to insert a Hall probe and measure the peak field as a function of the gap value. Figure 1(b) shows the results with and without the HTSC rings, clearly showing field enhancement by HTSC rings. We encountered one problem brought about by a mechanical weakness of the HTSC ring [4] during the experiment: magnetic performance degraded after several trials. R&D to improve the mechanical strength of the HTSC ring is now in progress.

proposed two methods of realizing the concept described above. For details, refer to [5].

To demonstrate the principle described above, experiments were carried out using three pieces of HTSC made of GdBaCuO and a normal conducting electromagnet to magnetize the HTSCs and eliminate field offset. The results are shown in Fig. 3, in which the magnetic field distributions generated by the three HTSCs pieces magnetized by the electromagnet are plotted. We can find periodic fields with three periods, i.e., the number of HTSC piece.

Superconducting Permanent Magnet Undulator

In the CU*plus* scheme, the magnetic field is generated mainly by REPMs and the HTSC plays only a minor role. To take full advantage of the magnetic performance of HTSCs, all the REPMs should be replaced with SCPMs. The most straightforward way of realizing this concept is to place SCPMs with opposite polarities side by side. However, it is easy to understand that this scheme is impractical. Now, let us consider the case when all SCPMs have identical polarities, as shown in Fig. 2(a). Such a situation is realized by magnetizing the HTSC array using an external uniform field. The magnetic field generated by the SCPM array is schematically shown in Fig. 2(b) and is composed of a uniform field (field offset) and a periodic field that reflects the periodic structure of the SCPM array. If the field offset can be eliminated by some measures, the remaining periodic field can work as an undulator field. The undulator period (λu) in this case corresponds to the length of the HTSC piece. We have so far

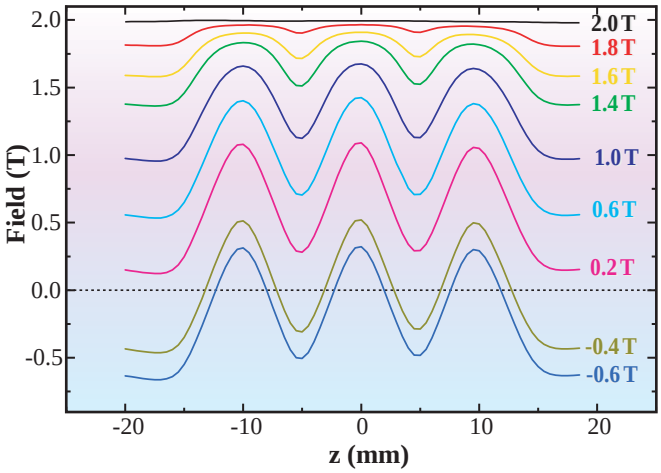

Fig. 3. Results of experiments for demonstrating the principle of SCPMU.

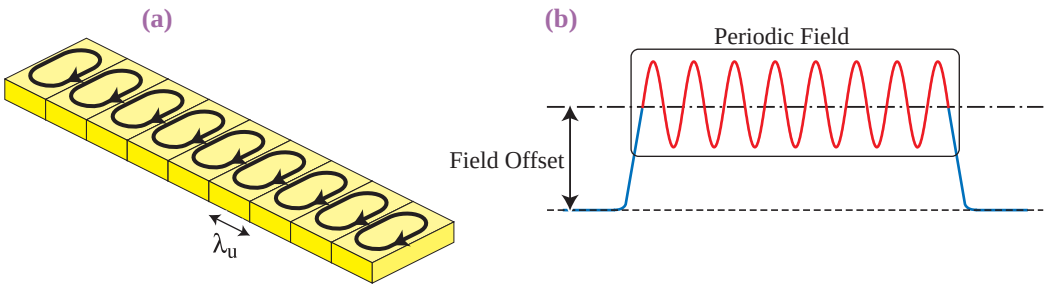

Fig. 2. **(a)** SCPM array with identical polarity and **(b)** its typical field profile.

Expected Performance

Now let us compare the expected performance of the proposed undulator schemes with those fo conventional ones. As an example, a periodic length of 14 mm and a gap value of 5 mm are taken for undulator parameters. Figure 4 shows the calculated peak fields achievable in the proposed undulator schemes as functions of the critical current density of the HTSC material (*jc*). In the same figure, peak fields in the other undulators, i.e., SCU, cryoundulator and conventional PM undulator, are indicated. We can find a criterion for *jc* whether or not the undulators with SCPMs are practical. The performance of the proposed undulators, i.e., the CU*plus* and SCPMU, can exceed that of the existing SCU, if *jc* is higher than 1 kA/mm^2, which is not difficult to achieve with the state-of-the-art technology in HTSC materials science.

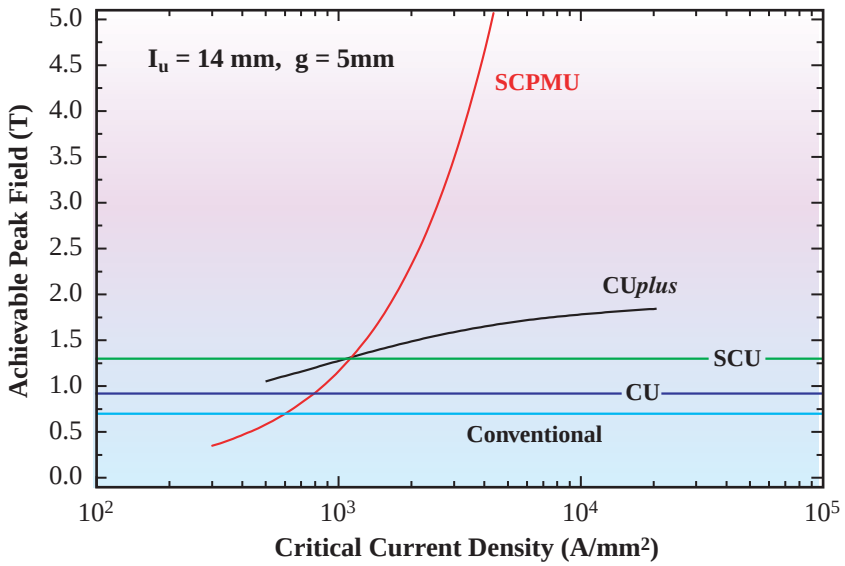

Fig. 4. Expected performance of proposed undulator and comparison with that of existing undulators.

Takashi Tanaka

SPring-8 / RIKEN•JASRI

E-mail: ztanaka@spring8.or.jp

References

[1] B. Kostka *et al.*: Proc. PAC2005 (2005) 2559.
[2] T. Tanaka *et al.*: Phys. Rev. ST-AB **7** (2004) 090704.
[3] T. Hara *et al.*: Phys. Rev. ST-AB **7** (2004) 050702.
[4] *T. Tanaka, T. Hara, R. Tsuru, D. Iwaki, T. Bizen, X. Marechal, T. Seike and H. Kitamura: submitted to Supercond. Sci. Tech. (2006).*
[5] T. Tanaka, R Tsuru and H. Kitamura: J. Synchrotron Rad. **12** (2005) 422.

Detectors

Microgap Gas Detector RAPID

RAPID (Refined ADC Per Input Detector) is a two-dimensional gas multi-wire detector developed at CCLRC Daresbury Laboratory in the U.K. The major advantage of RAPID is its fast response, enabling one to measure up to 20 million photons per second. Additionally, since RAPID is a photon counting detector, its wide dynamic range and low noise are advantageous compared with integrating detectors such as an imaging plate and CCD-based detectors.

RAPID has two sets of electrodes arranged at right angles: one is a set of parallel copper tracks on a PC board which work as cathodes, the other is a parallel array of gold-plated 10-∝m-diameter tungsten wires separated by 0.8 mm spaced at 0.5 mm from the cathodes, which work as anodes (Fig. 1). An X-ray photon causes a discharge in the detector which is filled with an argon/xenon-based gas. The discharge induces electric pulses on both anodes and cathodes which are measured by analog-to-digital converters (fast flash ADC). The small distance (microgap) between the anodes and the cathodes ensures that the electric charges generated by a gas discharge dissipate quickly. This enhances the response time of the detector and increases the number of photons that can be counted per second. Usually the charges are induced on more than one electrode. The position of an X-ray photon is calculated by interpolation using signals from three neighboring electrodes. Signals from the anodes and cathodes are correlated to locate a photon two-dimensionally. The positions of photons are stored in a histogram memory. The detection area is 20· 20 cm^2, which is divided into 1000· 1000 channels.

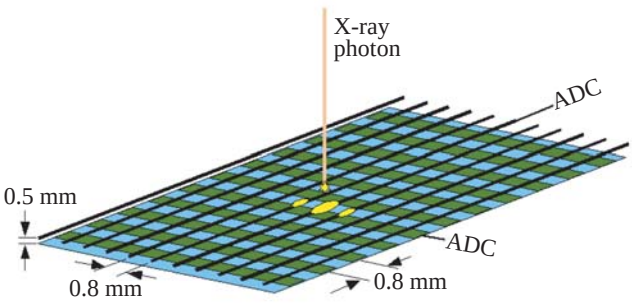

Fig. 1. Schematic drawing of the arrangement of electrodes in RAPID. An X-ray photon induces charges on both anodes (wires) and cathodes (strips).

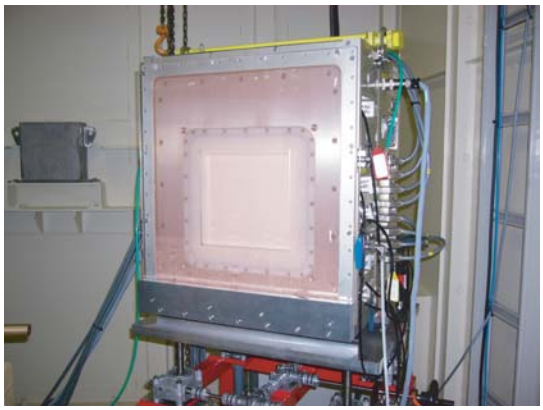

Fig. 2. RAPID detector installed in the experiment hutch of BL40B2.

A new model of RAPID was manufactured at Daresbury Laboratory for SPring-8, and has been installed at beamline **BL40B2** in May 2005 (Fig. 2). Its performance test proved that its wide dynamic range and low noise make it the most suitable detector for measuring diffraction and scattering from non-crystalline materials such as polymers and protein solutions (Fig. 3).

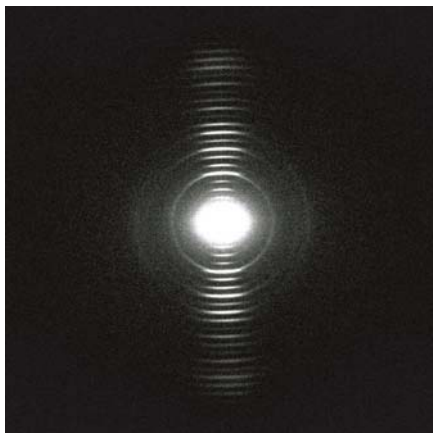

Fig. 3. Diffraction pattern of dried chicken tendon collagen recorded with RAPID.

Naoto Yagi* and Katsuaki Inoue

SPring-8 / JASRI

*E-mail: yagi@spring8.or.jp

References

[1] R.A. Lewis *et al.*: Nucl. Instrum. Meth. A **454** (2000) 165.

New Apparatus & Upgrades

Optimization of Beamline BL41XU for Measurement of Micro-Protein Crystal

A number of protein crystallography techniques have been improved in recent years. With this advancement, many kinds of not only soluble protein but also biological important molecule such as protein complexes and membrane proteins have been analyzed. When such proteins are crystallized, it is difficult to obtain a crystal with a suitable size for the diffraction experiment (~ 100 μm) though we commonly get a tiny crystal (~10 μm). Therefore, in order to extend the range of an applicable crystal size (< 20 μm), it is necessary to establish the data collection method for such micro-sized crystals. There are various difficulties in acquiring diffraction data with high accuracy from such crystals. However, it is very important to make the size of the beam irradiated to the crystal equal to or smaller than the size of the crystal to reduce the component of a cryoprotectant solution in background scattering. At beamline **BL41XU**, the highly brilliant beam made by undulator enables us to perform a structural analysis of a 30-μm-size crystal. However, it is not optimized to such crystals because the beam size usually used is about 100 × 100 μm^2. Therefore, we have optimized the beamline setting from the second half of 2004, evaluating beam shape at the sample position.

We tuned up the optical components, such as a monochromator, focusing mirrors and two sets of quadrant slits, by evaluating the direct beam. As a result, the beam size of 25 × 25 μm^2 at the sample position was formed to at 1 Å. However, the stability of beam intensity deteriorated markedly. The beam intensity in the beam size of 25 × 25 μm^2 decreased about 40% in 4 hours (Fig. 1) although the change in the intensity of the beam of 50 × 50 μm^2 is less than 2% within the same period. On the basis of results of the study, it is thought that this instability is caused by the thermal distortion of the double-crystal monochromator. Compton scattering generated by the first crystal heats and distorts the cradle of the second crystal. Therefore, we re-designed a "Compton shield" that was installed into the second cradle to remove such an effect, and introduced a new one (Fig. 2). Consequently, the change in beam intensity is suppressed to within 0.2% in 4 hours at the beam size of 25 × 25 μm^2 (Fig. 1). We also changed the aperture size of the front-end slit installed upstream of the monochromator. From the first half of 2005, the aperture size was reduced from 0.5 × 0.5 mm^2 to 0.3 × 0.3 mm^2 to improve the parallelity of the beam at a small beam size.

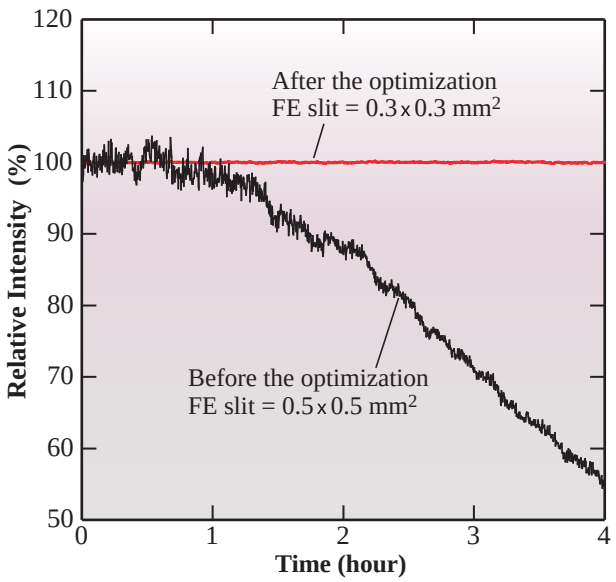

Fig. 1. Beam stability in beam size of 25 × 25 μm^2 at 1 Å. These data were measured using pin-photodiode installed at sample position, and the measurement interval was 10 s.

Fig. 2. Compton shield (KOHZU Precision Co., Ltd.) installed to second cradle.

As the result of these optimizations, the default beam size in BL41XU was changed from 100 × 100 μm^2 to 50 × 50 μm^2, and the 25 × 25 μm^2 beam became available for all users from the second half of 2005. Users can easily change the beam size only by selecting a target beam size from the GUI menu of the measurement software BSS [1]. The photon flux and photon density at the beam size of 25 × 25 μm^2 at 1 Å are 8.0 × 10^{10} photons/sec and 1.3 × 10^{14} photons/sec/mm^2, respectively. Figure 3 shows the beam shape at the sample position. The beam size was adjusted using two sets of quadrant slits. The color of the solution changed only at the place where X-ray was irradiated. We are now executing test measurements using some typical crystals with a size of about 20 μm. The change in beam size would contribute to the improvement of the ratio of signal to background of diffraction images. We are going to optimize the beamline performance further on the basis of those results.

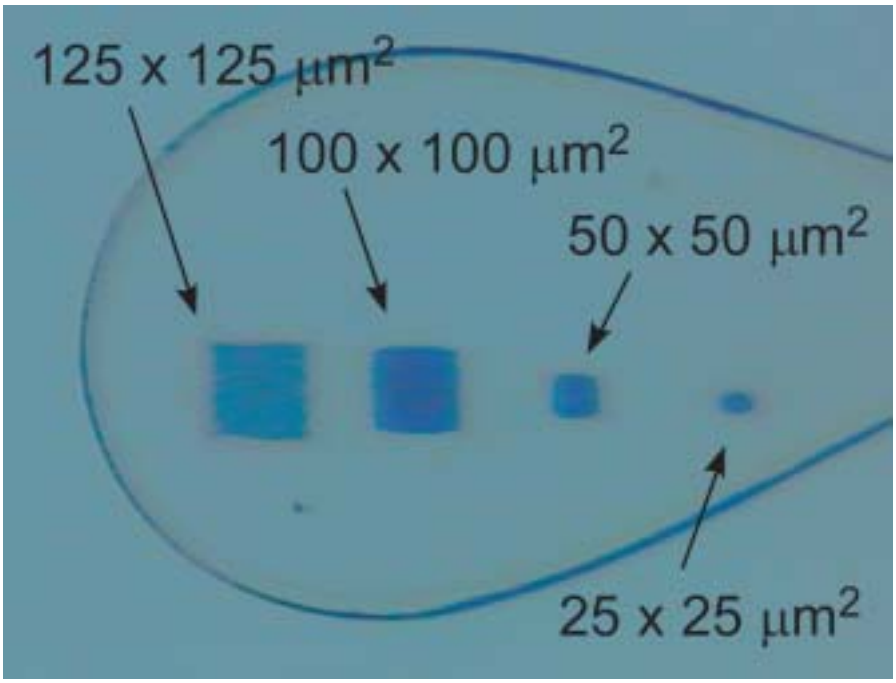

Fig. 3. Beam shape at sample position. This solution contains 30% glycerol and 30 % PEG4000.

Nobutaka Shimizu*, Kazuya Hasegawa and Masaki Yamamoto

SPring-8 / JASRI

*E-mail: nshimizu@spring8.or.jp

References

[1] G. Ueno, H. Kanda, T. Kumasaka and M. Yamamoto: J. Synchrotron Rad. **12** (2005) 380.

Powder Diffractometry for Time Resolved Charge Density Study

Photo-induced phase transition is a phenomenon in which feeble light produces a marked change in the physical properties of materials. Photo-induced phases range from transient to persistent. It is well known that the persistent photo-induced phase transition is often accompanied by a crystal structural change [1]. Therefore, it has been believed that structure investigation is important for revealing the mechanism of photo-induced phase transition. However, in particular transient photo-induced structures have been hardly determined. One of the reasons of the difficulties is that only a tiny fraction of specimen can be induced by photo-irradiation. Therefore, a very small amount of specimen should be used to increase photo-excitation efficiency.

Thus, the high flux beamline **BL40XU** was selected for the time-resolved diffraction experiment. Synchrotron radiation has the aspects of not only high brilliance but also ultra-short pulse width. A time-resolved experiment only realizes when the pulse feature is utilized. The electrons in the storage ring go around at a frequency of 508 MHz. A magnetic levitation type mechanical chopper, called the X-ray Pulse Selector (XPS), was installed to select the voluntary electron bunch. The XPS is synchronized with the frequency of bunches. The maximum frequency of the XPS is 1 kHz. The time window of the XPS is approximately 500 ns. By combining the chopper with the D-mode in SPring-8 as a bunch mode, a single bunch which has a pulse width of 40 ps can be extracted. The laser is triggered by the frequency of the XPS. The electric delay generator can control the delay time between the laser and X-ray. The schematic of this system is shown in Fig. 1.

BL40XU is not equipped with a monochromator, because this beamline adopts a quasi-monochromatic beam to maintain the photon flux. However, a monochromatic beam is indispensable for reduction of the powder profile's overlapping. Therefore a channel-cut monochromator is set up downstream of the chopper.

A monochromatic beam is irradiated onto the specimen on a powder diffractometer. The diffractometer for visualizing time-resolved charge densities was designed on the basis of the large Debye-Scherrer camera installed at beamline **BL02B2** [2]. The transient photo-induced phase has much instability. Whole powder patterns should be simultaneously measured. Accordingly, a two-dimensional detector, imaging plate, was attached to the camera. The mask with a 10-mm wide slit in front of the IP enables one to measure several data sets. By combining the multi-pattern recording system with the control program made by LabVIEW, the delay-time dependent data have been automatically obtained. Sample temperature is controlled from 90 K

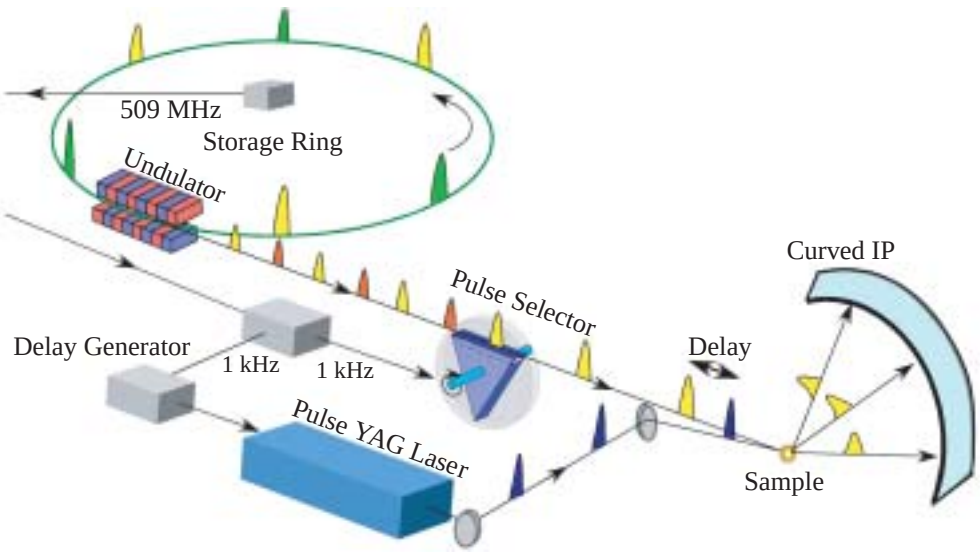

Fig. 1. Time-resolved experimental system using pump-probe method.

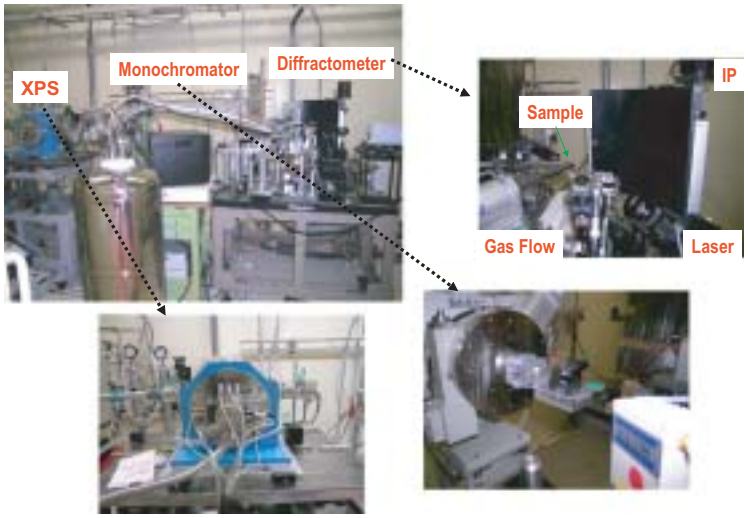

Fig. 2. X-ray pulse selector, channel cut monochromator and diffractometer installed at BL40XU.

up to 400 K using a nitrogen gas flow system.

Using the above time-resolved powder diffractometer shown in Fig. 2, we evaluated the reliability of the diffraction data obtained. As a result of Rietveld refinement for the standard sample CeO_2, the time-resolved data is fit for accurate structural analysis. The reliability factor based on Bragg intensity was 1.6% and the profile is both symmetrical and sharp as shown in Fig. 3.

We are now attempting to carry out time-resolved experiment with a 40 ps time resolution toward ultra-fast photo-sensitive materials at the charge density level.

The development of the experimental system has been performed during the long term proposal (Y. Moritomo *et al.*). The experimental know-how would be transferred to the CREST project (M. Takata *et al.*).

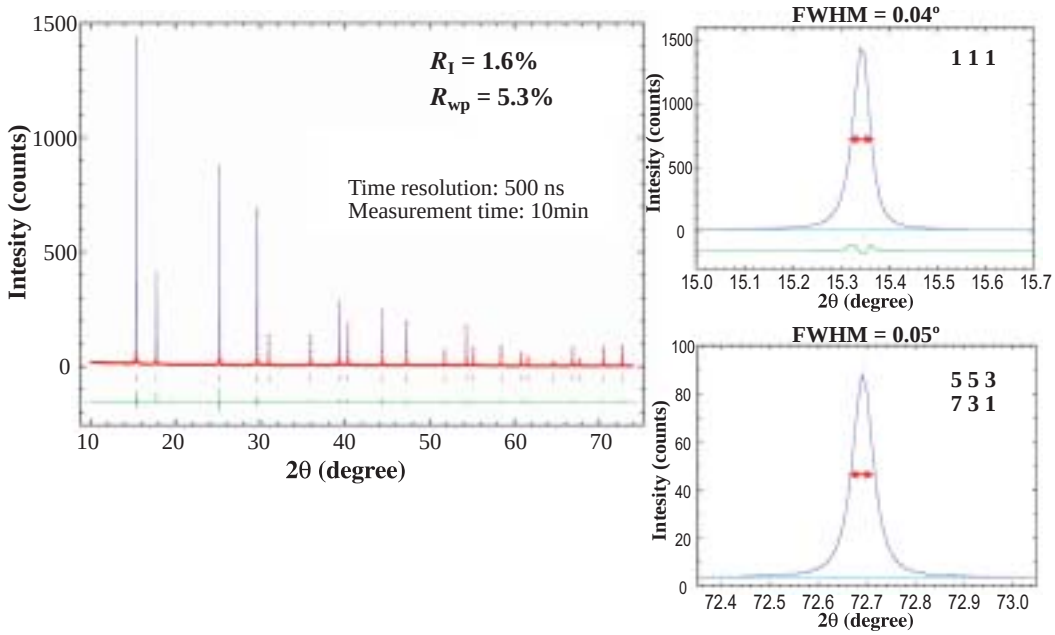

Fig. 3. The fitting results of Rietveld analysis for time-resolved data using standard sample, CeO_2.

Kenichi Kato[a,b]

[a] SPring-8 / JASRI•RIKEN
[b] CREST / JST

*E-mail: katok@spring8.or.jp

References

[1] Y. Moritomo *et al.*: Phys. Rev. B **68** (2003) 144106.
[2] *Y. Moritomo and K. Kato: SPring-8 Information* ***11*** *(2006) 168; K. Kato and M. Takata: KEK Proc. 2005* ***19*** *(2006) 114.*

Micro-area Reciprocal Space Map Measurements for Characterizing Strain Status of Epitaxial Layers

Among X-ray diffraction techniques, the measurement of the distribution of intensity in a reciprocal space, the so-called reciprocal space map (RSM) measurement, is effective for characterizing the strain status of an epitaxial layer because lattice tilt is separated from lattice spacing [1]. If we can measure RSMs using an X-ray microbeam, it is expected to be a more powerful tool for characterizing local strain behavior in detail.

Microdiffraction systems using a zone plate (ZP) are suitable for characterizing the strain status of epitaxial layers [2,3]. This is because a hard X-ray microbeam produced by a ZP has both a sub-micrometer beam size and a relatively low angular divergence on the sub-milliradian order. However, this angular divergence is not sufficient for precise RSM measurements. We therefore developed a new high-angular-resolution X-ray microdiffraction system for RSM measurements.

The new diffractometer was installed at beamline **BL46XU** (Fig. 1). On this diffractometer, we employed a phase ZP as a focusing device. It contains 500-nm-thick gold zones with an innermost zone radius of 4 μm and an outermost zone width of 100 nm. The diameter of the ZP is 160 μm and number of zones is 400. For X-rays with an energy of 15 keV, the ZP is designed to have a large focal length of 190 mm. The diffraction efficiency is about 3%. A 30-μm-diameter pinhole in a gold film was used as an order-sorting aperture (OSA). A 20-μm-wide slit was placed in front of the phase zone plate to partially irradiate the ZP. The center of the slit was off-placed 40 μm horizontally from the ZP center so that the OSA would eliminate unfocused and going-straight direct beam. This realized a focused beam with small size and small angular divergence. The beam size and angular divergence were measured to be 1.0 μm (horizontal) × 2.8 μm (vertical), and 75 μrad, respectively. The sample stage consists of high precision stepping motor-driven stages including a θ - 2θ rotation stage and XYZ linear stages, as well as two manual swivel stages on top. Those rotation stages have high angular resolutions of 1.7 and 8.7 μrad for the sample rotation (θ) and detector rotation (2θ), respectively. The linear stages have a minimum step size of 0.125 μm. To adjust the irradiation point on the sample precisely, the irradiation point was monitored using a long-focal-length optical microscope with a CCD camera. The maximum magnification of the microscope is 18 times. A detector was put on the 2θ arm. To improve the 2θ resolution, two sets of 20-μm-wide slits were placed in front of the detector.

Using this system, we tried to analyze the local

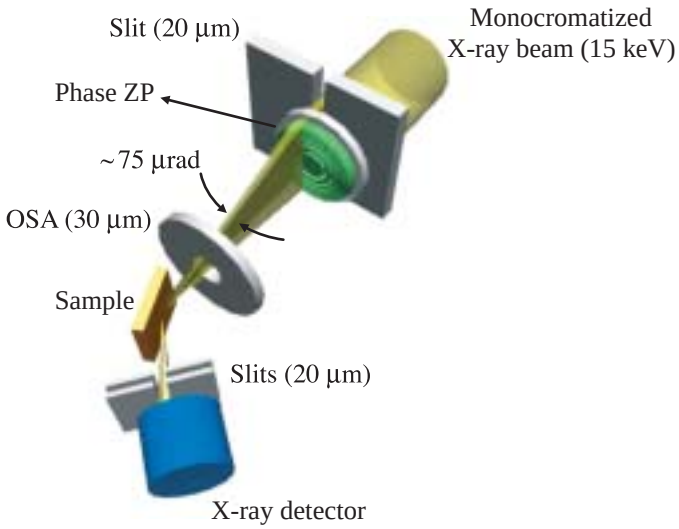

Fig. 1. Schematic figure of the experimental arrangement setup at BL46XU.

strain and crystalline texture of strain-relaxed SiGe epitaxial films on Si(001) substrates, which have recently been attractive as buffer layers for high mobility strained Si channel electronic devices [4]. For example, Fig. 2 shows the measured RSM around the SiGe 004 diffraction spots of the sample, which had a total 125-nm-thick $Si_{0.7}Ge_{0.3}$ layer on a Si(001) substrate. This is predominantly strain-relaxed with 60º misfit dislocations at the SiGe/Si(001) interface. It is found that every SiGe 004 diffraction peak broadens along the Qx direction. Furthermore, as shown by arrows in Fig. 2, several discrete peaks can be observed in the broadened SiGe 004 peak. These discrete peaks have never been observed without using the high-angular-resolution microdiffraction system. Detailed quantitative analysis revealed that crystal domains with sizes ranging from 100 nm to 140 nm at tilt angles from -0.18º to 0.42º with respect to the Si [001] direction are formed in the layer relaxed with 60º dislocations [4].

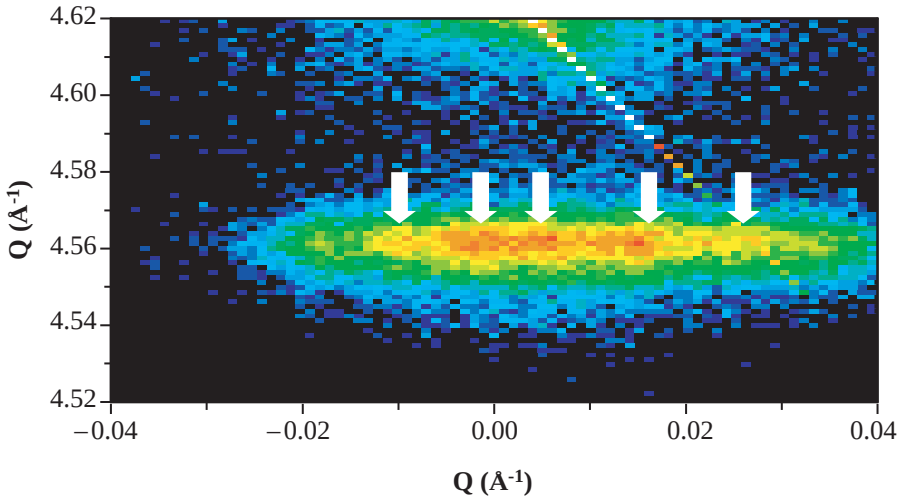

Fig. 2. Measured reciprocal space map around SiGe 004 diffraction spot.

Shigeru Kimura* and Shingo Takeda

JASRI / SPring-8

*E-mail: kimuras@spring8.or.jp

References

[1] For a review, P. Fewster: Semicond. Sci. Technol. **8** (1993) 1915.
[2] S. Kimura *et al.*: Jpn. J. Appl. Phys. **41** (2002) L1013.
[3] S. Kimura *et al.*: AIP Conference Proc. **705** (2004) 1275.
[4] *S. Mochizuki, A. Sakai, N. Taoka, O. Nakatsuka, S. Takeda, S. Kimura, M. Ogawa and S. Zaima: Thin Solid Films **508** (2006) 128.*

Development of Ultra-fast CT System with a Quasi-monochromatic Beam

An ultra-fast X-ray CT system was developed at beamline **BL40XU**. The beamline has a helical undulator as a light source and does not have any monochromator. Therefore, the bandwidth of the X-ray is 2 - 3 % and the total flux achieved is more than 10^{14} photons/sec, which is suitable for high-speed X-ray imaging. In particular, fast X-ray CT enables us to obtain four-dimensional information including time resolving ability. This is an important technology for all sciences.

The setup of the experiment is shown in Fig. 1. Two Pt-coated mirrors (200-mm-long) were placed in the experimental hutch. The mirrors were bent with a four-point bending mechanism. To make the X-ray field as even as possible, a beam diffuser was introduced upstream of the first mirror. This diffuser was made of a 5-mm-thick layer of graphite powder and rotated at speeds of 300 - 800 rpm. The image detector consisted of visible light conversion unit and a fast read-out CCD camera (Hamamatsu Photonics K.K.). The effective pixel size and format were 4.8 μm × 4.8 μm and 656 × 494 pixels, respectively. The minimum measurement time was 10 s for 312 projections. The shortest interval between each measurement was about 3 min because it was necessary to store images on a hard disc.

A volume rendered image was successfully obtained using a fast CT system (Fig. 2). The sample was a toothpick. It took 15 s for the entire measurement. The X-ray energy was 15 keV. The number of projections was 411. The exposure time for each projection was 33 ms.

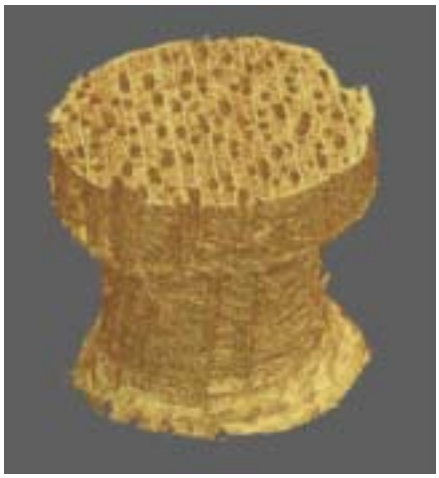

Fig. 2. Volume rendered image of part of a toothpick.

Kentaro Uesugi

SPring-8 / JASRI

E-mail: ueken@spring8.or.jp

References

[1] K. Uesugi *et al.*: J. Synchrotron Rad. (2006) - to be published.

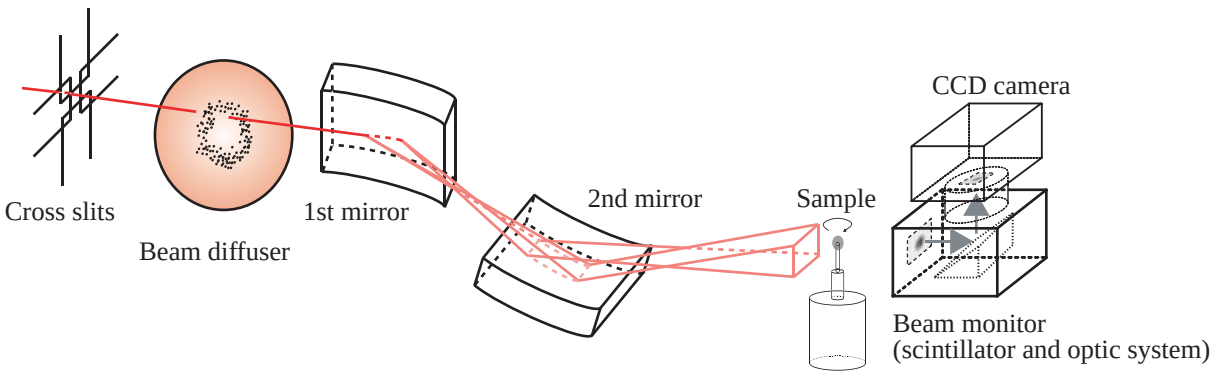

Fig. 1. Experimental setup.

Facility Status

Machine Operation

The operation statistics since the facility was opened to users are shown in Fig. 1. Recently, the SPring-8 storage ring has been operated on four- or five-week periods for one operation cycle. In 2004 and 2005, long-term operation cycles were also performed. In 2005, the total operation time of the accelerator complex was 5317.1 hours. The operation time of the storage ring was 4781.3 hours, of which 77.3% (3698.2 hours) was made available to the users. The down time due to failure accounted for 1.2% (59.7 hours) of the operation time of the storage ring; in 2005, there was no great loss of user time exceeding several hours. Since 2004, there has been no injection time because top-up injection was being introduced. For the user service operation, a high availability (ratio of net user time to planned user time) was achieved, e.g., 98.3% in 2005. The tuning and study time of 1559.2 hours was used for machine tuning, and the study of the linac, booster synchrotron and storage ring, and also used for beamline tuning and study. From January to March 2005, the storage ring operation was suspended because the roof of the storage ring building, which was damaged by typhoons in September 2004, was under full-scale repair. In 1559.2 hours, 522.4 hours of the beam study of the linac and the booster synchrotron were included during these periods of standstill of the storage ring operation.

The operations in three different filling modes were provided for the user time: 15.9% in the multi-bunch mode, 44.7% in the several bunch mode, such as the 203-bunch mode (203 equally spaced bunches) and 39.4% in the hybrid filling mode such as a 1/12-partially filled multi-bunch with 10-isolated bunches. For the hybrid filling mode, 0.7 or 1.5 mA is stored in each isolated bunch. An isolated bunch purity of better than 10^{-9} is routinely maintained in the top-up operation.

Table I presents a summary of the useful beam parameters of the storage ring. The ring optics was returned to 3 nm·rad low emittance optics in September 2005 for user time with a top-up operation. The low emittance optics was realized by breaking the achromatic condition in the unit cell.

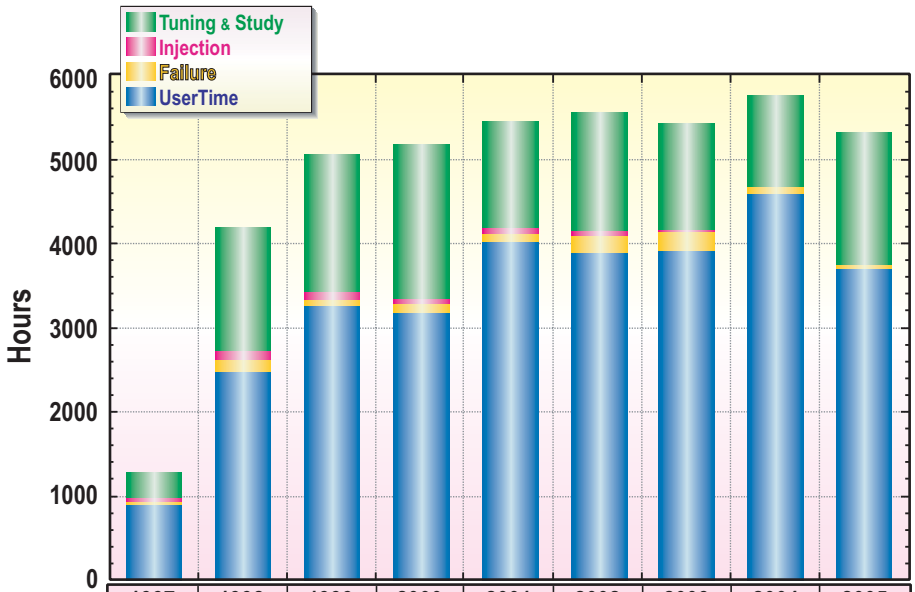

	1997	1998	1999	2000	2001	2002	2003	2004	2005
Accelerator Operation Time	1286	4189.6	5051.6	5167.5	5456.1	5542.9	5419.5	5759.2	5317.1
Storage Ring Operation Time	1270.6	4135.4	4863.9	4972.9	5340.6	5484.1	5328.5	5736.7	4781.3
Tuning & Study (Accel. & BL)	304	1457.6	1624.2	1815	1276.5	1394.9	1245.8	1085.9	1559.2
Injection	50	110	95.2	70.4	59.3	60.8	39.2	0	0
Failure	26	110	57.2	88.7	87.1	190.5	208.5	82.4	59.7
User Time	906	2512	3275	3193.4	4033.2	3896.7	3926	4590.9	3698.2
Planned Time	984	2712	3432	3352	4176	4152	4176	4680	3762
Availability (%)	97.2	96.7	98.2	97.4	98	95.3	95	98.1	98.3

Fig. 1. Operation statistics since the facility became available to users.

Table I. Beam parameters of SPring-8 storage ring.

Energy [GeV]	8
Number of buckets	2436
Tunes (ν_x / ν_y)	40.15 / 18.35
Current [mA]:	
single bunch	10
multi bunch	~100
Bunch length (σ) [psec]	13
Horizontal emittance [nm·rad]	3.4 *
Vertical emittance [pm·rad]	6.8 *
Coupling [%]	0.2
RF Voltage [MV]	16
Momentum acceptance [%]	±2.5 (= ±200 MeV)
Beam size[μm]: (σ_x / σ_y) [μm]	
Long ID section	294 / 10
ID section	301 / 6
BM section	107 / 13
Beam divergence [μrad]: ($\sigma_{x'}$ / $\sigma_{y'}$) [μrad]	
Long ID section	13 / 0.7
ID section	12 / 1.1
BM section	56 / 0.6
Operational chromaticities: (ξ_x / ξ_y)	+2 / +2 **
Lifetime [hr]:	
100 mA (multi bunch)	~ 200
1 mA (single bunch)	~ 15
Horizontal dispersion [m]:	
Long ID section	0.103
ID section	0.107
BM section	0.032
Fast orbit stability (0.1 – 200 Hz)[μm]:	
horizontal (rms)	~ 4
vertical (rms)	~ 1

* Assuming that 0.2% coupling for "Low Emittance Optics"
** With bunch-by-bunch feedback

BEAMLINES

The electron storage ring of the SPring-8 accelerator complex can potentially accommodate 62 beamlines (34 insertion devices, 4 long undulators, 23 bending magnets and 1 infrared). Occupying about 75% of its full capacity, there are 48 beamlines currently in operation as shown in Beamline map (Fig. 2) and List of beamlines (Table II).

These beamlines are primarily categorized into following four groups;
(1) Public Beamlines,
(2) Contract Beamlines,
(3) RIKEN Beamlines, and
(4) Accelerator Beam Diagnosis beamlines.

Constructed by JAERI[1] and RIKEN with governmental grants, Public Beamlines have been operated for public use. Now there are 25 public beamlines in operation; 22 X-ray beamlines, two soft X-ray beamlines and one infrared beamline. Among them, three beamlines had been specifically used for R&D. According to the recommendation made by R&D Beamline Review Committee, however, all the R&D beamlines have changed their status to general use since the period of 2005A, although one of them (BL46XU) is still kept for R&D programs as an interim measure.

The contract beamlines are installed, owned,

Table I. Beam parameters of SPring-8 storage ring.

Energy [GeV]	8
Number of buckets	2436
Tunes (ν_x / ν_y)	40.15 / 18.35
Current [mA]:	
single bunch	10
multi bunch	~100
Bunch length (σ) [psec]	13
Horizontal emittance [nm·rad]	3.4 *
Vertical emittance [pm·rad]	6.8 *
Coupling [%]	0.2
RF Voltage [MV]	16
Momentum acceptance [%]	±2.5 (= ±200 MeV)
Beam size[μm]: (σ_x / σ_y) [μm]	
Long ID section	294 / 10
ID section	301 / 6
BM section	107 / 13
Beam divergence [μrad]: ($\sigma_{x'}$ / $\sigma_{y'}$) [μrad]	
Long ID section	13 / 0.7
ID section	12 / 1.1
BM section	56 / 0.6
Operational chromaticities: (ξ_x / ξ_y)	+2 / +2 **
Lifetime [hr]:	
100 mA (multi bunch)	~ 200
1 mA (single bunch)	~ 15
Horizontal dispersion [m]:	
Long ID section	0.103
ID section	0.107
BM section	0.032
Fast orbit stability (0.1 – 200 Hz)[μm]:	
horizontal (rms)	~ 4
vertical (rms)	~ 1

* Assuming that 0.2% coupling for "Low Emittance Optics"
** With bunch-by-bunch feedback

BEAMLINES

The electron storage ring of the SPring-8 accelerator complex can potentially accommodate 62 beamlines (34 insertion devices, 4 long undulators, 23 bending magnets and 1 infrared). Occupying about 75% of its full capacity, there are 48 beamlines currently in operation as shown in Beamline map (Fig. 2) and List of beamlines (Table II).

These beamlines are primarily categorized into following four groups;
(1) Public Beamlines,
(2) Contract Beamlines,
(3) RIKEN Beamlines, and
(4) Accelerator Beam Diagnosis beamlines.

Constructed by JAERI[1] and RIKEN with governmental grants, Public Beamlines have been operated for public use. Now there are 25 public beamlines in operation; 22 X-ray beamlines, two soft X-ray beamlines and one infrared beamline. Among them, three beamlines had been specifically used for R&D. According to the recommendation made by R&D Beamline Review Committee, however, all the R&D beamlines have changed their status to general use since the period of 2005A, although one of them (BL46XU) is still kept for R&D programs as an interim measure.

The contract beamlines are installed, owned,

operated and maintained by university, companies, and other organizations for exclusive use by contractors. Currently there are 14 contract beamlines in operation, including JAEA beamlines[2]. The experimental stations of BL22XU and BL23SU are located at JAEA's RI Laboratory, and are dedicated to research utilizing radioactive isotopes and actinide materials. National Synchrotron Radiation Research Center of Taiwan (NSRRC) was the first foreign organization that constructed contract beamlines at SPring-8, i.e., BL12B2 and BL12XU.

There are seven RIKEN beamlines for their exclusive use to promote RIKEN's own research activities, although 20% of beamtime is reserved for public use. RIKEN BL19LXU is the only beamline instrumented with a long undulator, realizing the highest brilliance. BL26B1 and BL26B2 are the beamlines used for high throughput protein crystallography, closely related with the human genome project. BL29XU has two experimental stations, one located in the experimental hall, and the other at the end of the 1 km beamline.

Dedicated to studying the characteristics of the electron beam accumulated in the storage ring, the accelerator beam diagnosis beamlines are currently under the exclusive use of JASRI accelerator group.

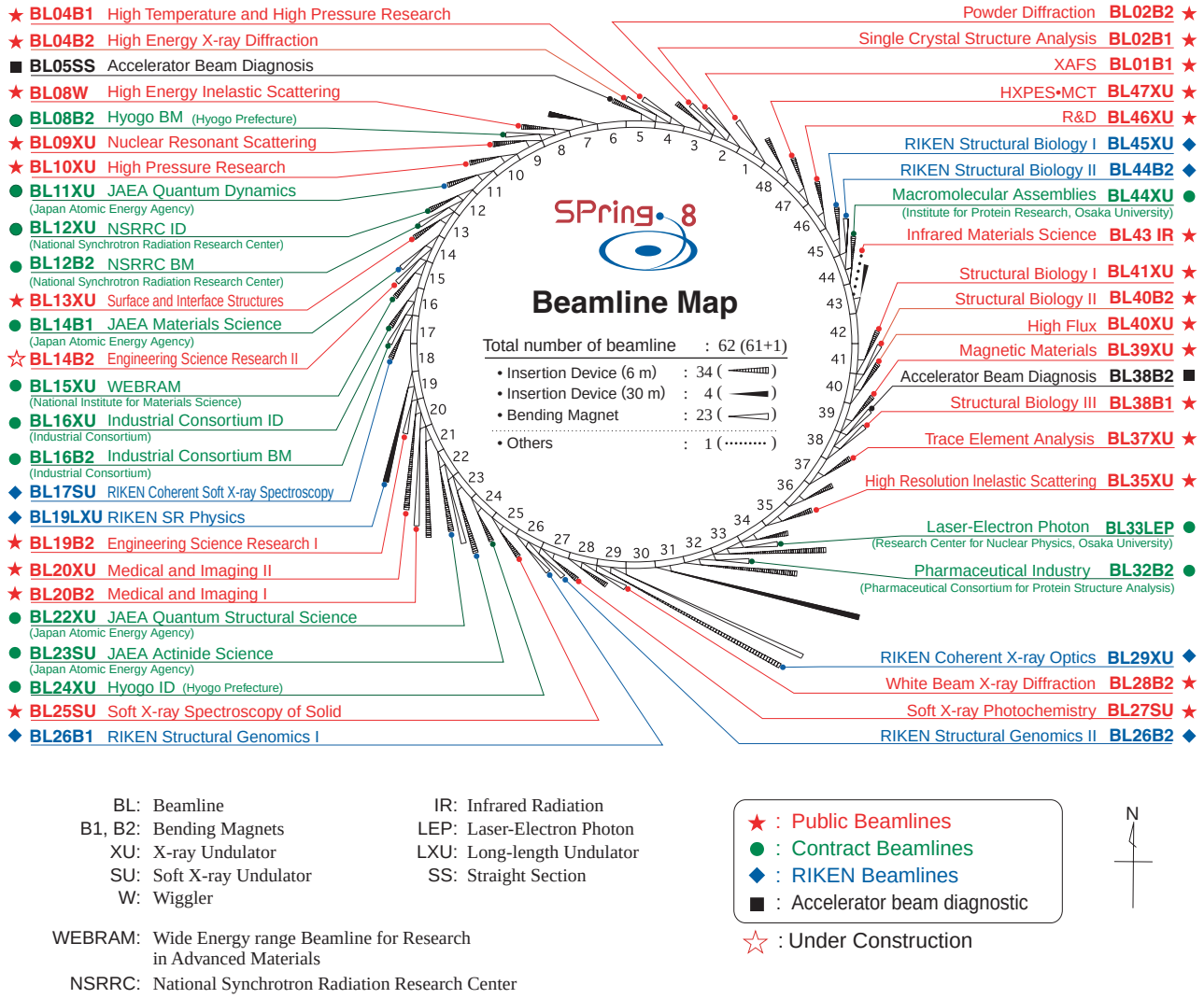

Fig. 2. Beamline map.

[1] Japan Atomic Energy Research Institute (JAERI) was transformed into an independent administrative institution now called Japan Atomic Energy Agency (JAEA) October 1, 2005.

[2] Due to the withdrawal of JAERI from the SPring-8 management October 1, 2005, JAEA beamlines, previously called JAERI beamlines, are now categorized into contract beamlines.

Table II. List of beamlines

(April, 2006)

BL #	Beamline Name	(Public Use)	Areas of Research
★ Public Beamlines			
BL01B1	XAFS	(Oct. 1997)	XAFS in wide energy region (3.8 to 113 keV). XAFS of dilute systems and thin films.
BL02B1	Single Crystal Structure Analysis	(Oct. 1997)	Structure physics using single crystal analysis. Precise structure analysis of photo-excited state.
BL02B2	Powder Diffraction	(Sep. 1999)	Accurate structure analysis of crystalline materials using powder diffraction data by Rietveld refinements and MEM (maximum entropy method).
BL04B1	High Temperature and High Pressure Research	(Oct. 1997)	Mineral physics at high temperature and high pressure. Energy-dispersive X-ray diffraction and X-ray radiography using the large-volume press.
BL04B2	High Energy X-ray Diffraction	(Sep. 1999)	Structural analysis of glass, liquid, and amorphous materials. X-ray diffraction under ultra high-pressure. Precise single crystal structure analysis
BL08W	High Energy Inelastic Scattering	(Oct. 1997)	Magnetic Compton scattering. High-resolution Compton scattering. High-energy Bragg scattering. High-energy fluorescent X-ray analysis.
BL09XU	Nuclear Resonant Scattering	(Oct. 1997)	Time domain Mössbauer spectroscopy. Lattice dynamics study using nuclear resonant scattering.
BL10XU	High Pressure Research	(Oct. 1997)	Structure physics and earth science under ultra high pressure using DAC.
BL13XU	Surface and Interface Structures	(Sep. 2001)	Atomic-scale structure analysis of an ultra-thin film, nanostructure and surface, using in-air measurements (room temperature to 500 °C) and in-vacuum measurements (20 to 1300 K).
BL19B2	Engineering Science Research	(Nov. 2001)	Industrial application using XAFS in wide energy region, residual stress measurement, structural analysis of thin film, surface and interface, powder diffraction, and X-ray imaging.
BL20XU	Medical and Imaging II	(Sep. 2001)	Medical application: Microangiography, refraction-enhanced imaging. / Micro-imaging: Scanning microscopy, imaging microscopy, microtomography, X-ray holography and X-ray optics. / Ultra-small angle scattering.
BL20B2	Medical and Imaging I	(Sep. 1999)	Medical application: Micro-radiography, micro-tomography and refraction-enhanced imaging. / Micro-imaging: R&D of optical elements for novel imaging techniques.
BL25SU	Soft X-ray Spectroscopy of Solid	(Apr. 1998)	High resolution photoemission spectroscopy. Photoelectron diffraction and holography. Magnetic circular dichroism (MCD). Photoelectron emission microscope (PEEM).
BL27SU	Soft X-ray Photochemistry	(May 1998)	Industrial research of functional material. Atomic and molecular spectroscopy by high resolution electron spectroscopy. Surface analysis and solid state physics.
BL28B2	White Beam X-ray Diffraction	(Sep. 1999)	White X-ray diffraction. Time-resolved energy-dispersive XAFS (DXAFS) .
BL35XU	High Resolution Inelastic Scattering	(Sep. 2001)	Material dynamics on ~ meV energy scales using inelastic X-ray scattering (IXS) and nuclear resonant scattering (NRS).
BL37XU	Trace Element Analysis	(Nov. 2002)	X-ray microbeam spectrochemical analysis. Ultra trace element analysis. High energy X-ray fluorescence analysis.
BL38B1	Structural Biology III	(Oct. 2000)	XAFS. R&D of optics and detector. Macromolecular crystallography.
BL39XU	Magnetic Materials	(Oct. 1997)	X-ray magnetic circular dichroism (XMCD) spectroscopy. Element-specific magnetometry. X-ray emission spectroscopy and its magnetic circular dichroism. Resonant or non-resonant magnetic scattering.
BL40XU	High Flux	(Apr. 2000)	Time-resolved diffraction and scattering experiments. X-ray speckle. X-ray fluorescence trace analysis.
BL40B2	Structural Biology II	(Sep. 1999)	Macromolecular crystallography. Small angle X-ray (solution) scattering.
BL41XU	Structural Biology I	(Oct. 1997)	Biological macromolecular crystallography.
BL43IR	Infrared Materials Science	(Apr. 2000)	Infrared microspectroscopy. Magneto-optical spectroscopy. Infrared surface science. Absorption and reflection spectroscopy. Time-resolved experiments with pulsed laser and SR (pump and probe).
BL46XU	R&D	(Nov. 2000)	Insertion devices R&D. Resonant and non-resonant magnetic scattering structural analysis.
BL47XU	HXPES•MCT	(Oct. 1997)	R&D of microtomography and microbeam technique. High energy photoemission spectroscopy.

(April, 2006)

BL #	Beamline Name	(First Beam)	Areas of Research
	● Contract Beamlines		
BL08B2	**Hyogo BM** (Hyogo Prefecture)	(Jun. 2005)	XAFS in a wide energy region. Small angle X-ray scattering for structural analyses of polymer and nano-composite materials. X-ray topography. Imaging. Powder diffraction with a high angular resolution.
BL12XU	**NSRRC ID** (National Synchrotron Rad. Res. Center)	(Dec. 2001)	High resolution non-resonant or resonant inelastic X-ray scattering. High resolution near-edge X-ray Raman scattering. Phase transitions under high-pressure, low and high temperatures. High-resolution X-ray absorption and emission spectroscopy. X-ray physics and optics.
BL12B2	**NSRRC BM** (National Synchrotron Rad. Res. Center)	(Oct. 2000)	X-ray absorption spectroscopy. Powder X-ray diffraction. High resolution X-ray scattering. Protein crystallography.
BL15XU	**WEBRAM** (National Institute for Materials Science)	(Jan. 2000)	High resolution X-ray photoemission microscopy. High energy excitation X-ray photoelectron spectroscopy. High resolution X-ray emission spectroscopy. Highly precise X-ray powder diffraction and ultra-small angle scattering.
BL16XU	**Industrial Consortium ID** (Industrial Consortium)	(Oct. 1998)	Characterization of thin films for ULSI and magnetic devices, catalysts, functional materials, and structural materials by X-ray diffraction, fluorescence X-ray analysis, X-ray magnetic circular dichroism, and imaging with X-ray microbeam.
BL16B2	**Industrial Consortium BM** (Industrial Consortium)	(Oct. 1998)	Characterization of industrial materials, such as metal and oxide films, semiconductor crystals by XAFS, topography and other methods.
BL24XU	**Hyogo ID** (Hyogo Prefecture)	(May 1998)	Structure analysis of small bio-crystals for industry. Surface/interface analysis for industry by fluorescent X-ray analysis, strain measurements and grazing incidence X-ray diffraction. Microbeam formation studies for materials and life sciences.
BL32B2	**Pharmaceutical Industry** (Pharmaceutical Consortium for Protein Structure Analysis)	(Apr. 2002)	Protein structure analysis for structure-based drug design: Design and optimization of new leading compounds based on pharmacodynamic action mechanism elucidated at the molecular level which obtained from a detailed interaction analysis of receptor-drug complexes.
BL33LEP	**Laser-Electron Photon** (RCNP, Osaka University)	(Jun. 1999)	Meson photoproduction from nucleon and nucleus. Photoexcitation of hyperons, nucleon resonances, and other exotic states. Photonuclear reactions. Beam diagnoses. Test and calibration of detectors with GeV photon beam.
BL44XU	**Macromolecular Assemblies** (IPR, Osaka University)	(May 1999)	Crystal structure analysis of biological macromolecular assemblies (e.g. membrane complexes, protein complexes, protein-nucleic acid complexes, and viruses).
BL11XU	**JAEA Quantum Dynamics**	(Oct. 1998)	Nuclear resonant scattering. Surface and interface structure with MBE. Inelastic scattering. XAFS.
BL14B1	**JAEA Materials Science**	(Dec. 1997)	Materials science at high pressure. Structure physics.
BL22XU	**JAEA Quantum Structural Sci.**	(May 2002)	Materials science at high pressure. Resonant X-ray scattering (activity at RI laboratory).
BL23SU	**JAEA Actinide Science**	(Feb. 1998)	Surface chemistry with supersonic molecular beam. Biophysical spectroscopy. Photoelectron spectroscopy (activity at RI laboratory). Magnetic circular dichroism (activity at RI laboratory).
	◆ RIKEN Beamlines		
BL17SU	**RIKEN Coherent Soft X-ray Spectroscopy**	(Sep. 2003)	Spectroscopy of multiply charged ions. Angle-resolved photoemission spectroscopy (ARPES). Soft X-ray emission spectroscopy.
BL19LXU	**RIKEN SR Physics**	(Oct. 2000)	Any research field requiring the highly brilliant X-ray beam.
BL26B1/B2	**RIKEN Structural Genomics I & II**	(Apr. 2002)	Structural genomics research based on single crystal X-ray diffraction.
BL29XU	**RIKEN Coherent X-ray Optics**	(Dec. 1998)	X-ray optics, especially coherent X-ray optics.
BL44B2	**RIKEN Structural Biology II**	(Feb. 1998)	Macromolecular crystallography.
BL45XU	**RIKEN Structural Biology I**	(Jul. 1997)	Macromolecular crystallography. Time-resolved structures of non-crystalline biological materials using small-angle scattering and diffraction technique.
	■ Accelerator Beam Diagnosis		
BL05SS	**Accelerator Beam Diagnosis**	(Mar. 2004)	Accelerator beam diagnostics. R&D of accelerator components.
BL38B2	**Accelerator Beam Diagnosis**	(Sep. 1999)	Accelerator beam diagnostics. R&D of accelerator components. Production of MeV γ-ray photons.

Proposal Scheme and Utilization Statistics

General Proposals

JASRI invites General Proposals twice a year. Those proposals submitted are reviewed by the SPring-8 Proposal Review Committee (PRC). In the scheme of General Proposal, the PRC approved 390 proposals from 655 proposals for 2004B and 380 from 644 for 2005A. In the scheme of Priority Field Proposal, 172 proposals were adopted from 231 proposals for 2004B and 167 from 234 for 2005A. In total, 3851 hours of beamtime was allocated for users from 2004B through 2005A.

SPring-8 user operation statistics for the period from 1997B to 2005A is shown in Table III. This table summarizes the beamtime available to users and the numbers of users as well as the number of experiments conducted at both public and contract beamlines, which are also illustrated in Fig. 3. The numbers of experiments conducted in the reserved beamtime at RIKEN beamlines and Priority Research Proposals are included in the table and the figure.

In 2004B and 2005A, SPring-8 provided users with 1,971 and 1,880 hours of beamtime in four and five operation cycles, respectively. As for 2004B, 3,546 individuals utilized the public beamlines in 554 independent experiments, while 1,154 individuals the contract beamlines in 146 experiments. In 2005A, 3,741 individuals utilized the public beamlines in 560 independent experiments, while 1,185 individuals the contract beamlines in 146 experiments. From October 1997, when SPring-8 was opened to the public, through 2005A, a total of 53,515 users conducted 8,028 experiments at public and contract beamline.

Figures 4 and 5 indicate the numbers of approved proposals with the affiliation of applicants and the research fields from 1997B to 2005A. As can be seen from the charts, as for the classification by affiliation, universities have accounted for approximately 66%, and other organizations have made up the rest almost equally. The percentage of approved proposals from overseas was 5.2% for 2004B and 6.5% for 2005A. The ratio of Life Science, Diffraction & Scattering and the others has been approximately 1:1:1 since the inauguration of SPring-8. The ratio of XAFS, Spectroscopy and Method & Instrumentation, all of which are categorized as “the others,” has also approximately been 1:1:1.

Research Term	User Time (hours)	Public BL		Contract BL	
		Experiments	Users	Experiments	Users
1997B: 1997.10 - 1998.03	1,286	94	681		
1998A: 1998.04 - 1998.10	1,702	234	1,252	7	
1999A: 1998.11 - 1999.06	2,585	274	1,542	33	467
1999B: 1999.09 - 1999.12	1,371	242	1,631	65	427
2000A: 2000.02 - 2000.06	2,106	365	2,486	100	794
2000B: 2000.10 - 2001.01	1,558	382	2,370	88	620
2001A: 2001.02 - 2001.06	2,381	473	2,915	102	766
2001B: 2001.09 - 2002.02	1,893	486	3,277	114	977
2002A: 2002.02 - 2002.07	2,093	545	3,246	110	1,043
2002B: 2002.09 - 2003.02	1,893	538	3,508	143	1,046
2003A :2003.02 - 2003.07	2,244	632	3,777	172	1,347
2003B: 2003.09 - 2004.02	1,844	548	3,428	154	1,264
2004A: 2004.02 - 2004.07	2,095	568	3,756	163	1,269
2004B: 2004.09 - 2004.12	1,971	554	3,546	146	1,154
2005A: 2005.04 - 2005.08	1,880	560	3,741	146	1,185
TOTAL	28,878	6,495	41,156	1,535	12,359

Table III. SPring-8 user operation results.

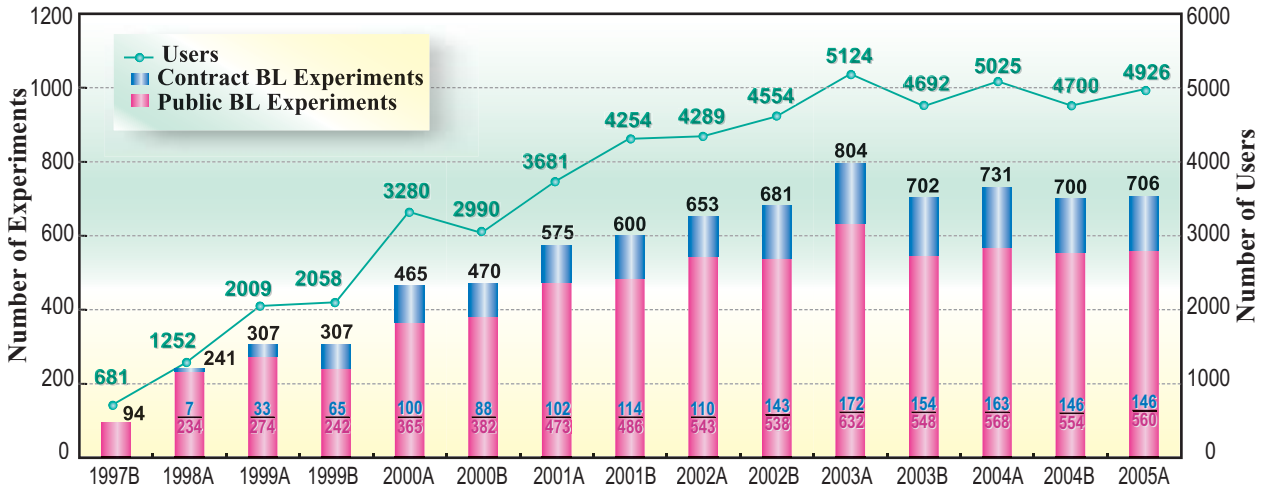

Fig. 3. Number of users and experiments conducted.

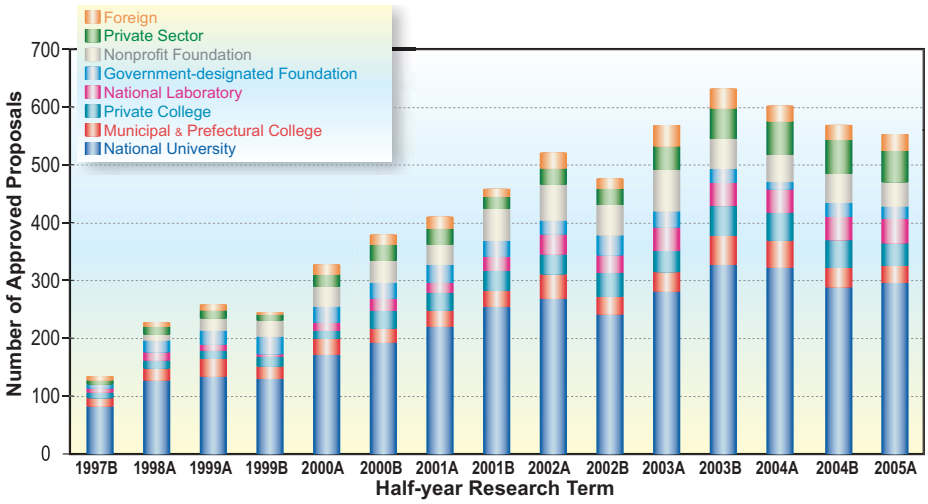

Fig. 4. Number of selected proposals by affiliation of applicants (public beamlines).

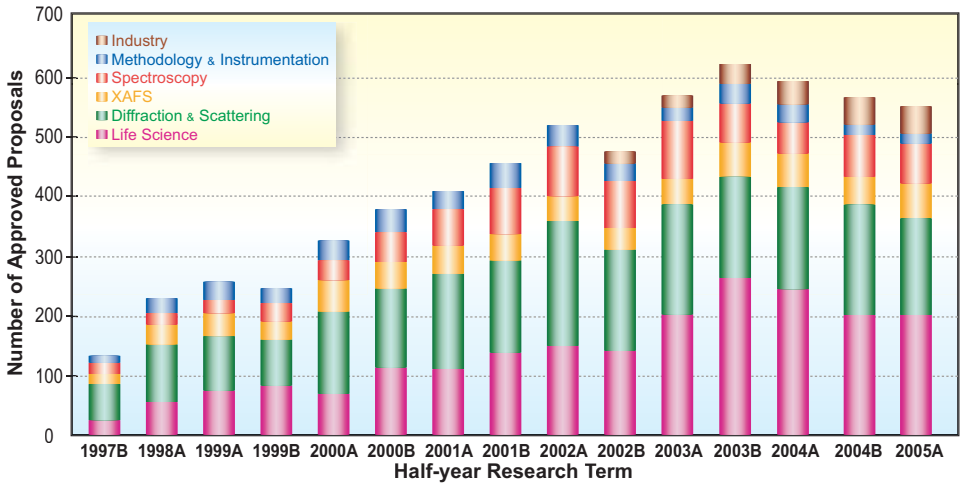

Fig. 5. Number of selected proposals by research fields (public beamlines).

Long-term Proposal

Being independent from General Proposals, JASRI has created a novel proposal scheme for the long-term use of beamlines, where beam access is guaranteed for up to three years. This system aims to further promote research that is expected to produce outstanding results in the field of science and technology, to pave the way for new research areas and research methodology and to help improve the technology for industrial base significantly by making the best use of SPring-8 characteristics. In 2005A, one proposal was selected from four applied. Six proposals are carried out by the end of 2005A.

Urgent Proposal

Since 1999A, the scheme of Urgent Proposal has been established in order to adequately respond to requests of conducting experiments as urgent as possible. Upon receiving an Urgent Proposal of non-proprietary use, the Proposal Review Committee promptly reviews it electronically on its necessity and urgency as well as on the basis of those criteria for General Proposals of non-proprietary use.

Proprietary Research Proposal

Users conducting proprietary research are charged beamtime fees of 472,000 yen/shift. Proprietary research is essential when users have commercially confidential information in their experiment or sample and do not want to disclose their research results. In 2004B, 23 proprietary experiments were performed at public beamlines and 26 at contract beamlines (22 at BL32B2, three at BL24XU and one at BL16XU); in 2005A, 29 experiments were conducted at public beamlines and 25 experiments at contract beamlines

(22 at BL32B2 and two at BL24XU), and one at BL16XU. During the period from 1999B, when the system was introduced, to 2005A, a total of 317 proprietary experiments have been carried out at both public and contract beamlines. The Pharmaceutical Consortium has spent about 94% of their beamtime on proprietary research at their contract beamline BL32B2, in 2005A.

Proprietary Time-designated Proposal

Since 1999B, JASRI has established a utilization scheme for those who wish to take the sole possession of their results, and to perform experiments during a specific time period with a beamtime fee of 708,000 yen/shift, which is increased by 50% to that for Public Beamlines as premium. In this utilization scheme, users can specify the preferred time period in their Proprietary Time-designated Proposal, which will be promptly reviewed once submitted.

Priority Research Proposal

Until FY2002, there were only (i) General Proposals and (ii) Long-term Proposals and (iii) the proposals using beamtime reserved for JASRI. In FY2003, the new scheme for the management of public beamlines was established, based on the report on SPring-8 by the governmental review committee. The report called on SPring-8 to further promote the use of public beamlines to produce more research results. The important point of the report was to launch the Priority Research Program. The new scheme is shown in Fig. 6. As can be seen from the figure, beamtime not exceeding 50% is allocated to the Priority Research Proposals and proposals using beamtime reserved for JASRI, so that more than 50% of the total user beamtime is guaranteed for General and Long-term proposals. The scheme for Priority Research Program is intended to make the best use of SPring-8 and to produce more research results. The Priority Research Proposals are tentatively categorized into the following three groups:

- Priority Field Proposal,
- Power User Proposal, and
- Strategy Proposal.

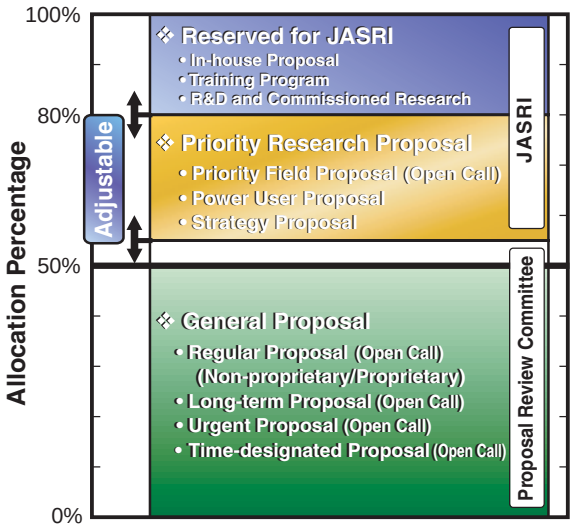

Fig. 6. Beamtime allocation scheme for public beamlines.

Priority Field Proposal

In this particular proposal scheme, JASRI strategically designates research fields in order to promote excellent research outcome from those areas in scientific and/or industrial domains with high strategic significance. The Priority Field Proposals are further categorized into three subgroups: Nanotechnology Support, Protein 500 and Industrial Use. These proposals are reviewed before General Proposals at the review committees designated for each priority field. The outline of each priority research field is as follows:

Nanotechnology Support

This research field is to support the development in nanotechnology, using 12 beamlines at SPring-8. Nanotechnology Support at SPring-8 had already started in 2002 under the Nanotechnology Researchers Network Project (Nanonet Project) of MEXT (Ministry of Education, Culture, Sports, Science and Technology), and was consolidated into the Priority Research Program in FY2003. In 2004B and 2005A, a total of 107 proposals were selected from 210 submitted proposals. This Project is valid until FY2006.

Protein 500

Just as Nanotechnology Support, Protein 500 at SPring-8 started shortly after MEXT launched the Protein 3000 Project in 2002 as a post-human genome program to analyze 3,000 kinds of protein structures, and was taken over as the Priority Field Program in FY2003. Under the Project, three of SPring-8 structural biology beamlines are assigned to analyze 500 kinds of protein structures, and 30% of their beamtime is allocated every year. In 2004B and 2005A, a total of 204 proposals were selected. This Project is valid until FY2006.

Industrial Use

As part of industrial use, the Trial Use Program originally ran from 2001B to 2002A, for the purpose of attracting new users to SPring-8 mainly from industries, and was restarted as one of the Priority

Field Proposals in 2003A. In 2004B, 15 Trial Use proposals were selected from 30 proposals. In 2005A, 13 Trial Use proposals were selected from 21 proposals.

Medical Biology

Since November, 2005, JASRI has further designated Medical Biology as a priority fields to expand the users in this field by organizing a trial use from 2006A.

Power User Proposal

This category refers to proposals of user groups who have full knowledge of beamline instrumentation, and are highly likely to produce outstanding research results in the future as well. Such user groups are designated as Power Users (PUs) by JASRI and expected to provide support for general users. In return for their support, up to 20% of beamtime of relevant beamlines can be used by the PUs. Five groups were designated as PUs in May, 2003. There have been 10 research subjects executed including the five running subjects from 2004B and 2005A.

Strategy Proposal

Strategy Proposals are expected to contribute to promoting research at SPring-8 including the development of new technologies necessary for the facility operation. JASRI will conduct such research by itself, or jointly with other organizations. There were three strategies research subjects designated in January, 2005 as follow:

- Analysis of Nanocomposite Materials
- Development of a New Application Technology for Powder Diffraction Experiments
- X-ray Pinpoint Structure Measurement

Beamtime Reserved for JASRI

There is 20% of the total beamtime reserved for JASRI to conduct its own research programs, to flexibly accept the Urgent Proposals mentioned above, to modify and adjust the instruments according to user's request, and to maintain the beamlines.

Industrial Research

As well as the promotion of research activities in the field of basic science, the contribution to the reinforcement of the technological base in industry has been one of the main pillars of the SPring-8 Project. In 2005, JASRI established Industrial Application Division, by promoting Industrial Application & Utilization Support Group. In this particular year, the division has intensively carried out the Advanced Large-Scale Research Facilities Strategic Utilization Program of MEXT, and has succeeded in doubling the number of new users conducting their experiments at SPring-8. The total number of proposals adopted for industrial applications has reached higher than 20% of the entire use.

The coordinator system, introduced in FY2000 to support industrial use mainly through consultation, continues to play a crucial role for exploring and acquiring new users from industrial domains. Trial Use Program is also making significant contribution for revitalizing local industries and for creating and promoting new industries. Public beamline BL19B2, Engineering Science Research Beamline, which was built to promote SR use by industries, has been the primary beamline used for the Trial Use Program. There are three contract beamlines, which were constructed by Industrial Consortium and Pharmaceutical Consortium, for the use by the consortium members. There have been workshops and training courses organized to introduce a variety of research fields and SR instrumentation, which were attended by a total of 292 people for FY2005.

Research Outcome

SPring-8 users are not charged for non-proprietary research as long as they submit an experiment report within sixty days after their experiments. When their results are disclosed in scientific journals or any other form of publication, the project leaders are required to report to JASRI and have the results registered with JASRI. As of September 30, 2005, the number of refereed publications (journals, proceedings and dissertations) is 3,688, among which 2,409 were attributed to public use, 543 to contract beamlines and 442 to RIKEN beamlines; where those publications related to two or more beamlines are counted at each beamline. Figure 7 displays the number of refereed publications annually counted.

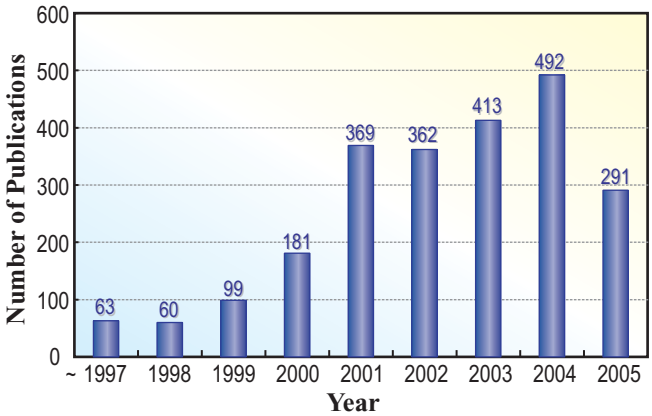

Fig. 7. Annual record of refereed publications as of Sep. 30, 2005.

Budget and Manpower

SPring-8 consisting of accelerators, beamlines and facilities for users, was constructed by the JAERI/RIKEN Project Team during the period from 1991 through 1997 at the total cost of about 110 billion yen. In 1994, JASRI was designated by the Law regarding Promotion of Common Use of the Synchrotron Radiation Facility (SPring-8) as the Organization for the Promotion of Synchrotron Radiation Research to be responsible for managing SPring-8. As a result, the SPring-8 research complex has been formed by JAERI Kansai Research Establishment, RIKEN Harima Institute and JASRI. JASRI has been entrusted by JAERI and RIKEN with the operation, maintenance, improvement, upgrading, R&D and safety management of SPring-8 as well as the technical support for the new beamline construction since the construction of main facilities and buildings at SPring-8 was completed and the public use started in 1997. As mentioned before, JAERI withdrew from SPring-8 management on September 30, 2005, becoming an independent administrative institution called Japan Atomic Agency (JAEA). Since then, SPring-8 has been managed by the two-party, i.e., RIKEN and JASRI.

About 80% of the total budget of JASRI comes from the Government through JAERI and RIKEN to be appropriated for the above-mentioned missions of JASRI and the remaining 11% comes directly from the Government in the form of a grant for user support. Figure 8 illustrates the budget at SPring-8. It shows that the total budget for JASRI for FY2005 was 9,651 million yen, and the total budget for RIKEN was 2,374 million yen. As can be seen from the figure, the budgets for JAERI and RIKEN have reduced since FY2001. It is because the construction such as utility facilities is approaching completion; meanwhile construction of beamlines is stopped due to lack of budget.

In FY2005, the total number of JASRI staff was 504. The total number of SPring-8 staff amounts to 1,172 when the number of staff at JAEA Kansai Research Establishment and RIKEN Harima Institute is combined with the number of JASRI staff. The numbers of staff by the types and fields of employment are illustrated in Fig. 9.

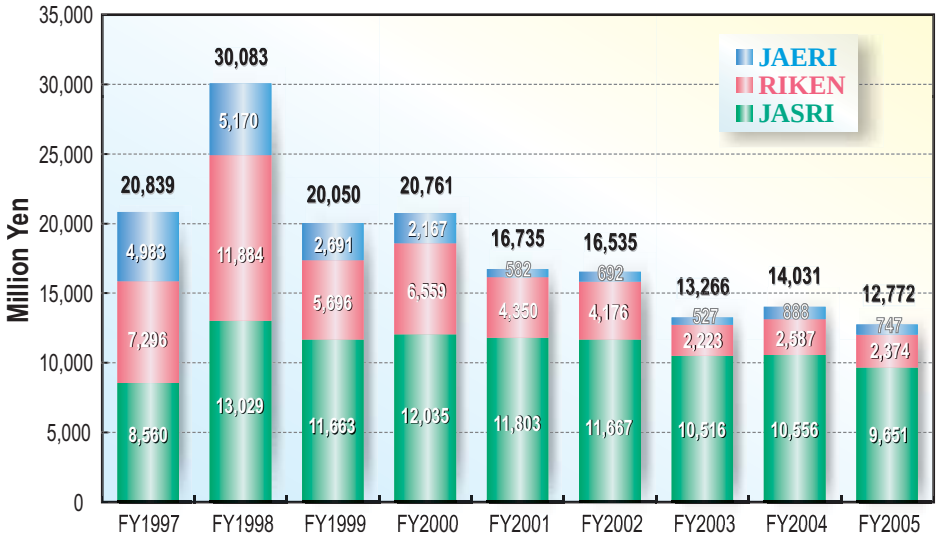

Fig. 8. Budget at SPring-8: JASRI, JAERI and RIKEN.

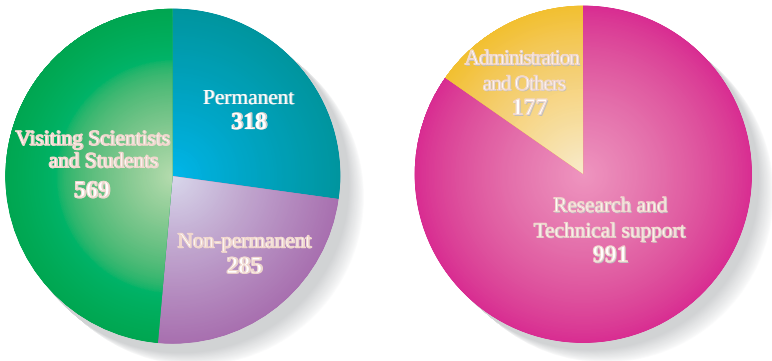

	by Type			by Field		Total
	Permanent	Non-permanent	Visiting Scientists and Students	Research and Technical Support	Administration and Others	
JASRI	220	152	132	361	141	**504**
JAERI	36	17	14	54	9	**67**
RIKEN	62	116	423	576	25	**601**
	318	**285**	**569**	**991**	**177**	**1172**

Fig. 9. Manpower at SPring-8: JASRI, JAERI and RIKEN (FY2005).

Organization

The SPring-8 research complex is composed of JASRI, JAEA Synchrotron Radiation Research Center, and RIKEN Harima Institute, all of which are on site. Research activity of JAEA stays intact at SPring-8, although it has administratively withdrawn from SPring-8 management. As mentioned before, JASRI is entrusted by RIKEN with the operation maintenance, improvement, upgrading, R&D and safety management of SPring-8. Since SPring-8 is a facility open to the public, user support is also one of the important tasks of JASRI. The organization that JASRI has formed to accomplish those missions is shown in Fig. 10. Organization of JAEA and RIKEN are shown in Fig. 11 and Fig. 12, respectively.

April, 2005.

Japan Synchrotron Radiation Research Institute (JASRI)

Director General A. Kira
Senior Exec. Director H. Ohno
Managing Exec. Director M. Yamada, M. Nagata, M. Hattori
Administration Consultant O. Shimomura

Research Sector

- **Accelerator Div.** — N. Kumagai
  - Operation & Beam Dynamics — H. Ohkuma
  - Linear Accelerator — H. Hanaki
  - Circular Accelerator — H. Yonehara
  - Control — R. Tanaka
- **Beamline Div.** — T. Ishikawa
  - Insertion Device & Front End — H. Kitamura
  - Optics & Transport Channel — S. Goto
  - Control — R. Tanaka
  - Instrumentation Development — Y. Asano
  - Technical Support — T. Ishikawa
- **Research Utilization Div.** — H. Suematsu
  - Materials Structure I — M. Takata
  - Materials Structure II — J. Mizuki
  - Materials Structure III — N. Yagi
  - Spectroscopy I — H. Suematsu
  - Spectroscopy II — T. Kinoshita
  - Structural Biology I — M. Yamamoto
  - Imaging — Y. Suzuki
- **Industrial Application Div.** — S. Komiya
  - User Support II — S. Komiya

Administration Sector

- **Facility Management Div.** — N. Kumagai
- **General Affairs Div.** — Y. Senge
- **Research Coordination Div.** — O. Shimomura
- **User Administration Div.** — T. Matoba
- **Public Relations Office** — M. Hara
- **Planning Office** — M. Moriyama

Safety

- **SPring-8 Safety Office** — J. Tada

Figure 10

April, 2005.

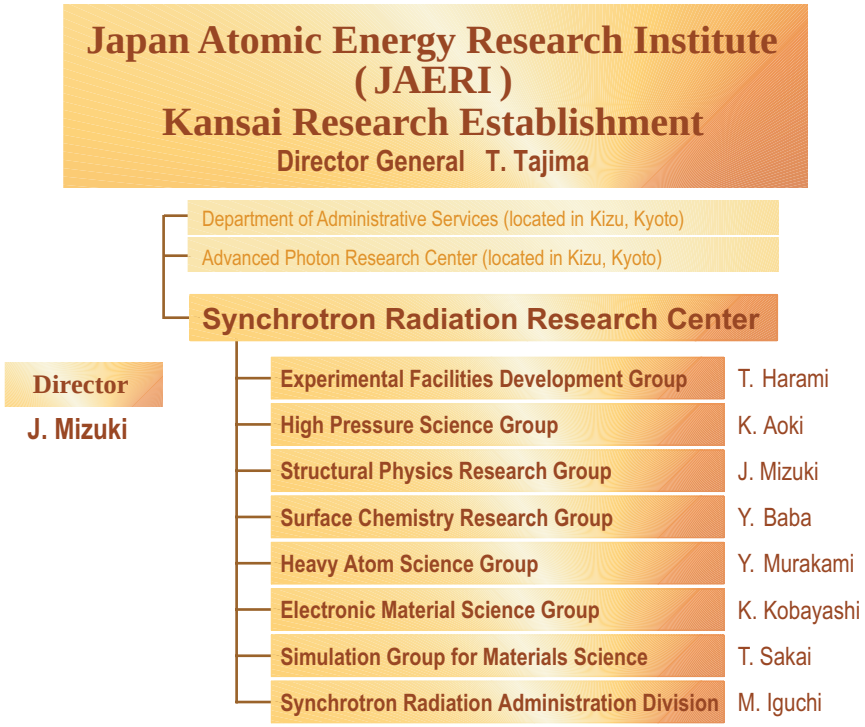

Figure 11

Figure 12

SPring-8 User Society

In order to advance the research activities of users at SPring-8, the SPring-8 Users Society was established in May, 1993, in such a way that the users can cooperate in SPring-8 construction and upgrading, facilitation and promotion of SPring-8 utilization, and can communicate and exchange information with each other as well as the facility. The number of the members in the Society amounted 1400 as of April, 2005.

For promoting utilization by the industrial users of SPring-8, SPring-8 Industrial User Society has been established in September 1990, and has been investigating and deliberating on the improvement of SPring-8 utilization system and on the SPring-8 utilization by the industry and makes recommendations. The number of the companies and the corporations joining the Society amounted 70 as of April, 2005.

International Conferences and Workshops

The International Conferences and Workshops sponsored by SPring-8 (JASRI, JAERI/JAEA, RIKEN) held in 2005 are listed below.

- XRM2005, The 8th International Conference on X-ray Microscopy
  July 26-30, 2005 – Egret, Himeji, Japan

- 2nd US-Japan Workshop on Synchrotron Radiation and Nanoscience
  April 4-6, 2005 – Humphrey's half Moon Inn & Suites, San Diego, USA

Users' Meeting

The Users Meeting sponsored by SPring-8/JASRI held in 2005 is listed below.

- First SPring-8 Users Meeting
  March 15-16, 2005

- 9th SPring-8 Symposium
  November 17-18, 2005

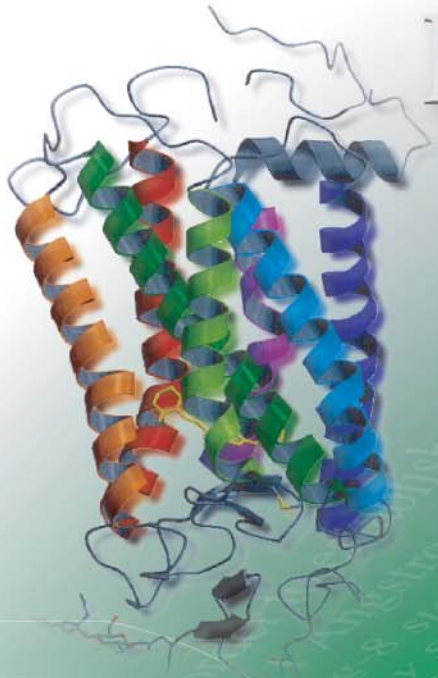

Project XFEL

SPRING-8 COMPACT SASE SOURCE PROJECT

SCSS SPRING-8 COMPACT SASE SOURCE

X-ray FEL Project at RIKEN/SPring-8

The steady and continuous evolution of synchrotron light sources has convinced us that they are indispensable to contemporary science and technology. A decade since the inauguration of the 3rd generation light source facilities, ESRF, APS and SPring-8 have helped solve a wide variety of mysteries in nature and a number of issues in industry. In addition, partially coherent, as well as short pulsed X-rays available have been found to be of great use; thus, motivated us to develop a new generation source which can deliver more coherent and shorter-pulsed X-rays.

It is believed that if we have X-rays FEL based on SASE principle, requests of both more coherent and shorter pulsed X-rays will be satisfied with the ultra-short pulse structure, extremely high peak power level and lateral full coherence of X-rays.

Figure 1 shows a computer image of the completed X-ray FEL machine, which will be constructed next to the existing 1 km beamline. After five years of construction, starting from the 2006 fiscal year (FY2006), we hope to start the operation of the XFEL in 2010. In the design, a low emittance electron beam will be generated by an electron gun located at the bottom-left corner, which will be accelerated to a high energy of 8 GeV by a high gradient C-band accelerator 400 m long, followed by an undulator section 80 m long, where FEL action will take place. The lased X-ray beam will be transported to the user facility, flying in free space in a vacuum pipe 100 m long, then in a beam safety shutter, an attenuator, and a monochromator, if necessary. In the first stage of the project, we will construct one undulator line and one user beamline. The rest of the beamlines will be constructed later. At the end of the C-band main linac, one branch will be connected to the booster-to-synchrotron transport line, which will directly inject an 8 GeV beam into SPring-8. It will provide a low emittance and a very short bunch beam, which will generate short X-ray pulses in the femto-second range for 100 turns before bunch spreading due to radiation damping. This type of short pulse radiation will be used to investigate the time response of materials by exciting them with a femto-second laser and then tracking the structural changes using the X-ray after the excitation.

It is believed that an X-ray FEL with wavelength shorter than 1.5 Å can only be accomplished by a scheme named SASE-FEL: self amplified spontaneous emission type free electron laser. Figure 2 shows the schematic configuration of SASE-FEL, which is quite simple: an electron source, an accelerator and an undulator. The undulator converts the kinetic energy of the electrons into X-ray radiation. In our machine design, we specially employ three key elements, a low emittance electron injector, a high gradient C-band accelerator and a short period in-vacuum undulator, which makes the system compact as compared with other projects, such as LCLS at SLAC, or XFEL at DESY.

Fig. 1. Computer image of SCSS-XFEL, (left straight facility, 700 m total length), which will provide extremely intense X-ray radiation: pulsed peak power > 1 GW, pulse length < 100 fs, repetition rate 60 pps. The designated wavelength is 1 Å at 8 GeV electron beam energy. The large circular building is the existing 8 GeV synchrotron radiation facility (500 m in diameter).

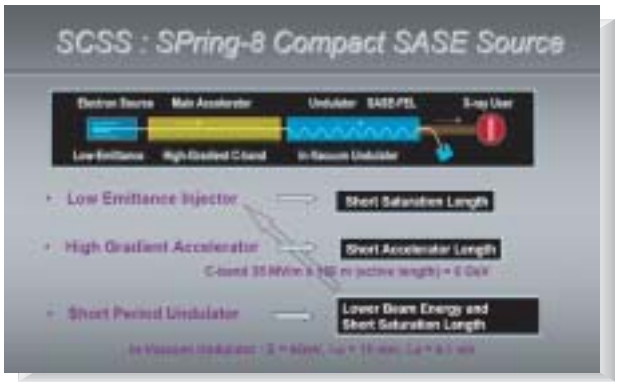

Fig. 2. Configuration of SASE-FEL and SCSS: SPring-8 Compact SASE Source concept. It is based on three key components: **(1)** low emittance electron gun, **(2)** high gradient C-band accelerator and **(3)** short period in vacuum undulator, which reduce the total length of the machine, and fit within the available site length at SPring-8.

Figure 3 shows the basic physics of FEL. It uses the radiation of electrons in free space, not orbital electrons in atoms; hence, it is named as free electron laser. In a non-FEL machine such as SPring-8 SR-ring, which is schematically indicated by the left illustration, when an electron bunch runs through the undulator, each electron generates a sinusoidal transverse electric field according to the magnetic field arrangement. It is called undulator radiation. Since the longitudinal positions of each electron are random, radiations sometimes cancel each other out, or contribute constructively, resulting in a non-coherent radiation field, which is sometimes called spontaneous radiation. The total power of spontaneous radiation is given by $P_{\mathrm{spt.}} = N_e \cdot P_1$, where P_1 is the radiation power from a single electron, and N_e is the number of electrons. When the longitudinal positions of the electrons are aligned regularly in a radiation wavelength, all radiation fields constructively contribute; thus, the field intensity and power become extremely high, in the maximum case, $P_{\mathrm{coherent}} = N_e^2 \cdot P_1$. Since there are

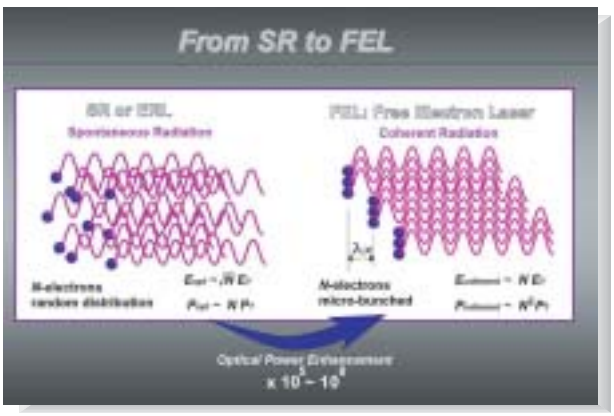

Fig. 3. What is FEL? Left-hand-side drawing shows undulator radiation of group of electrons in conventional SR and also proposed ERL. Right-hand-side is the FEL, where all electron positions are localized regularly at radiation wavelength. The peak power is enhanced drastically because of the constructive interference of all radiation.

10^8~10^9 electrons in one bunch, the power gain becomes 10^5~10^8 depending on the coherent length and the degree of electron density modulation. As you may imagine, the spectral narrowing of the X-ray laser and the transverse beam confinement (parallel beam) are due to the interference effect in time and space. Thus, the X-ray power amplification is identical phenomena as the growth of density modulation in an electron beam.

To realize XFEL, we need a high level of technology to generate low emittance electron beam, a highly stable acceleration field, a precise beam position monitor and a stable support system for equipment. We started the R&D of those key components in FY2001. In order to check the quality of developed hardware components, and demonstrate SASE-FEL at a soft-X-ray wavelength, we constructed the “SCSS test accelerator” in the R&D facility building during FY2004~2005, as shown in Fig. 4. The designed shortest wavelength is 50 nm at the electron beam energy of 250 MeV. Right after the beam commissioning, the first spontaneous light was observed at the visible to 100 nm wavelength in November 2005. We are now debugging the hardware and control software, which is currently the most important task of the prototype, and the first lasing test at the designed wavelength is scheduled in June 2006. All experience learned from the SCSS test accelerator will be fed back into the machine design and the operation of the 8 GeV X-ray FEL. For more details, please visit our website at http://www-xfel.spring8.or.jp/.

Fig. 4. SCSS test accelerator, prototype of X-ray FEL. Construction was completed in November 2005. First lasing test at 60 nm wavelength is scheduled in June 2006.

Tsumoru Shintake

SPring-8 / RIKEN

E-mail: shintake@spring8.or.jp

Editor
Seishi Kikuta
SPring-8 / JASRI

Editing & Layout
Marcia M. Obuti-Daté
SPring-8 / JASRI

Printing
ROKKO Publishing & Sale Co.

J A S R I
Library and Information
Users Administration Division

1-1-1 Kouto, Sayo-cho, Sayo-gun
Hyogo 679-5198 • JAPAN
Tel. +81-(0)791 58-2797 Fax. +81-(0)791 58-1869

frontiers@spring8.or.jp
http://www.spring8.or.jp/

August 2006

SPring-8

Japan Synchrotron Radiation Research Institute
1-1-1 Kouto, Sayo-cho, Sayo-gun, Hyogo 679-5198 JAPAN
http://www.spring8.or.jp